RICE UNIVERSITY

Synthetic Spin-Orbit and Light Field Coupling in Ultra-cold Quantum Gases

by

Lin Dong

A Thesis Submitted
in Partial Fulfillment of the
Requirements for the Degree

Doctor of Philosophy

Approved, Thesis Committee:

Dr. Han Pu, Chair
Professor of Physics and Astronomy

Dr. Randall G. Hulet
Fayez Sarofim Professor of Physics

Dr. Gustavo E. Scuseria
Robert A. Welch Professor of Chemistry
and Professor of Physics and Astronomy

Houston, Texas

March, 2017

Abstract

Ultra-cold quantum gases subjected to light-induced synthetic gauge potentials have become an emergent field of theoretical and experimental studies. Because of the novel application of two-photon Raman transitions, ultra-cold neutral atoms behave like charged particles in magnetic field. The Raman coupling naturally gives rise to an effective spin-orbit interaction which couples the atom's center-of-mass motion to its selected pseudo-spin degrees of freedom. Combined with unprecedented controllability of interactions, geometry, disorder strength, spectroscopy, and high resolution measurement of momentum distribution, *etc.*, we are truly in an exciting era of fulfilling and going beyond Richard Feynman's vision* of realizing quantum simulators to better understand the quantum mechanical nature of the universe, manifested immensely in the ultra-cold regimes.

In this dissertation, we present a collection of theoretical progresses made by the doctoral candidate and his colleagues and collaborators. From the past few years of work, we mainly address three aspects of the synthetic spin-orbit and light field induced coupling in ultracold quantum gases: a) The ground-state physics of single-particle system, two-body bound states, and many-body systems, all of which are subjected to spin-orbit coupling originated from synthetic gauge potentials; b) The symmetry breaking, topological phase transition and quench dynamics, which are conveniently offered by the realized experimental setup; c) The proposal and implications of light field induced dynamical spin-orbit coupling for atoms inside optical cavity. Our work represents an important advancement of theoretical understanding to the active research frontier of ultra-cold atom physics with spin-orbit coupling.

*See the footnote in Section 1.5 for more details

To my parents, for supporting me and encouraging me to pursue my dreams.
To my aunt Rufen (Lily) Gao, for her tenacious mindset fighting against cancer, always positive attitude towards life, and unfailing love to people around her.

Acknowledgments

First and foremost, I would like to thank my Ph.D. adviser Dr. Han Pu, for his excellent guidance for me along this invigorating research path. As I stumble my way through research works, Han has *always* treated me as an equal. His insightful yet concise, thorough yet patient, sharp yet compassionate approach to mentoring has prepared me to think and work as an independent researcher. He has given me time to develop technical tools I need to get things done, freedom to explore some of my own research ideas, and resources to establish great collaboration with other distinguished scholars around the globe. Very often, I am encouraged to confidently present my work at various conferences, self-promote my works to other like-minded physicists, and even defend comments/critics raised by journal referees for my submitted manuscripts in a scholarly way. Not only has Han been an excellent Ph.D. adviser but has also become a great mentor, a good friend and a spiritual leader for me throughout the past few years. I am truly thankful and grateful for his guidance, intuition and mentorship.

I would like to thank my collaborators and colleagues that I otherwise will not be able to know if not because of ultra-cold atomic physics research: Hui Hu, Biao Wu, Ming Gong, Xia-ji Liu, Ying Dong, Lei Jiang, Ram Bala, Lu Zhou, and Chuanzhou Zhu. I would also like to thank Dr. Pu's cohort of students and scholars: Hong Lu, Li Yang, Leslie Baksmaty, Shang-shun Zhang, Michael DeMarco, Hongyu Xiong, Wen Wen, Liming Guan, Xinghai Zhang, Youjiang Xu and Li Chen. I appreciate Dr. Qiyou Jiang's kind and dedicated support and guidance for my ever increasing computing needs, and Dr. Katerina Belik for her pragmatic way of teaching the effective communication class UNIV 601. I am very grateful to Dr. Randall G.

Hulet for his wisdom and commitment in teaching atomic physics course, which is essentially the underlying meat and bone of my theoretical endeavors. Dr. Hulet closely kept track of my academic achievements and extensively served on both of my Ph.D. advisory committee and defense committee, for which I am genuinely thankful. Dr. Hulet went through the draft of this thesis *VERY* carefully and made countless comments and annotations using his advanced iOS app on an iPad Pro, from which I am truly inspired and got greatly motivated to be a perfectionist in preparing for this dissertation. I am indebted to Dr. Anthony Arthur Chan's thoughtful and caring advises throughout my graduate career. Lastly, I would like to thank Dr. Gustavo Scuseria for being on my PhD defense committee, asking many thought-provoking questions at the time of thesis defense and helping me to further improve the quality and readership of this thesis.

I would like to take this brief moment to thank many other friends I have made at Rice University either academically or personally: Jiakui Wang, Yiting Xia, Yunxiang Liao, Chong Zhang, Zhentao Wang, Yang-Chi Chou, Aditya Shashi, Yinbin Ma, Mi Yan, Heng Ji, Ruoyu Chen, Ke Zhao, Mingjie Liu, Ming Luo, Yajing Li, Yun Li, Kai Lou, Ang Cai, Sitti Buathong, Vaideesh Loganathan, Jianxiong Chen, Yang Xia, Yue Zhang, Pu Han, Linglin Yu, Jianda Wu, Yuming Wang, Kai Li, Tianwu Zang, Zhen Wang, Xingcheng Lin, Xiaodi Deng, Jinmo Zhao, Bo Shuang, Pingfeng Yu, Jialu Xu, Ya He, Ya Liu, Lantao Yu, Ying Huang, Lin Tang, Lei Tang, Sidong Lei, Lifei Liu, Yang Zhou, Peng Wang, A Qia, Zhiming Peng, Kefeng Xin, Wei Chen, Jun Deng and Naili Qi, without all of whom my grad life could have been much tougher. I appreciate the friendship with my physics buddies that we have been in touch academically and personally: Huanglong Li, Mingyi Zhang, Ran Cheng, Xiao Ying, Biao Huang, Chao Gao, Yong Xu, Ran Wei. I have had true friendship and happiness with my "Panda" Ping-pong club members including Weihua Zheng, Songying Fang (Associate Professor at Department of Political Science, Rice University), Fanglu Sun, Di Du, Yimeng Zeng.

My "host family" at Houston, introduced via the greatest OISS office at Rice, have kept in close contact with me over the entire span of past seven years. They not only opened their and their extended family's house doors for me at holiday and weekend gatherings, but also greeted me with the most genuine friendship, helped me understand and even appreciate U.S. culture and western traditions. Most importantly, they heard me out, opened their hearts to love me, and revitalized me to keep going onward and upward. I consider this friendship very special and very beautiful, and look forward to establishing renewal of our friendship for the next few decades to come.

I am deeply inspired by my Aunt Rufen (Lily) Gao's tenacious mindset fighting against colorectal cancer, always positive attitude towards work, life and family, and her unfailing love to people around her. This dissertation is dedicated to her, without whom I could have had a lot less motivation for pursuing perfection in completion. I thank my Uncle Hualin Li for encouraging me to come to U.S. for graduate studies and my uncle Dr. Chen Dong, Dr. Yue Wang and aunts Dr. Ling Li, Dr. Xueling Wu, all of whom have successfully achieved Doctoral Degree in their respective fields, for taking good care of me and helping me to overcome cultural barriers.

I would never have made it to where I am today without the tremendous love, continual inspiration, and significant support of my family. Not only have my parents always been there for me, they have kept pushing me to follow my passions in life. My dad only had formal education in elementary school before his adulthood, but he managed to teach himself algebra, geometry, physics, chemistry, English, Chinese literature, and even circuit design before he successfully entered college for advanced studies as an electrical engineer. His passion for classical physics and advanced mathematics had deeply shaped me when I was a ten years old kid, and further motivated me to pursue advanced education and research frontiers of modern physics. My mom took great care of me and taught me the true meaning of hard work, caring and love for the family. Together as a happy couple and successful parents, they taught me

how to seek fulfilling life, separate pride from vanity, help others who are in need, and always be grateful and trustworthy to friends. I believe in them, their influence on me and wisdom passed down on me will continue to be invaluable throughout my life.

Last but not the least, I would like to thank the love of my life, my beloved fiancée Zhang (April) Zhang. In the past two years of my life, I have been lucky enough to get to know and fall in love with her. April is incredibly supportive in all of my very different endeavors, such as theoretical physics research, data science/machine learning self-studies, travel and photography, etc. We found out that we share a great deal of common purposes in life. Ever since we have been in love, we have grown together emotionally, intellectually, and spiritually. She is beautiful, genuine, my better half and she makes me become a better self. For these reasons and many more, I would like to thank April for helping me along this journey, for her commitment in us, for continuing to make it wonderful in the our future decades to come.

Publications

I hereby declare that except where specific reference is made to the work of others, the contents of this thesis are original and have not been submitted in whole or in part for consideration for any other degree or qualification in this, or any other university.

The following journal publications are (co-)authored and extensively reproduced by the Ph.D. candidate, **Lin Dong**, in this dissertation:

[1] **L. Dong**, L. Jiang, H. Hu, and H. Pu, "Finite–momentum dimer bound state in a spin–orbit coupled Fermi gas", Physical Review A, **87** (4) 043616, (2013).

[2] **L. Dong**, L. Jiang, and H. Pu, "Fulde–ferrell pairing instability in spin–orbit coupled Fermi gas", New Journal of Physics, **15**, (7) 075014, (2013).

[3] H. Hu, **L. Dong**, Y. Cao, H. Pu, and X.-J. Liu, "Gapless topological Fulde–Ferrell superfluidity induced by an in–plane Zeeman field", Physical Review A, **90**, (3) 033624, (2014).

[4] Y. Dong*, **L. Dong*** , M. Gong, and H. Pu, "Dynamical phases in quenched spin–orbit coupled degenerate Fermi gas", Nature Communications, **6**, 6103 (2015).

[5] **L. Dong**, L. Zhou, B. Wu, B. Ramachandhran, and H. Pu, "Cavity–assisted dynamical spin–orbit coupling in cold atoms", Physical Review A, **89**, (1), 011602 (2014).

[6] **L. Dong**, C. Zhu, and H. Pu, "Photon–induced spin–orbit coupling in ultracold atoms inside optical cavity", Atoms, **3**, 2, pp. 182194, (2015).

[7] C. Zhu, **L. Dong**, and H. Pu, "Effects of spin–orbit coupling on Jaynes–Cummings and Tavis–cummings models", Physical Review A, **94**, (5) 053621 (2016).

*with equal contributions

Contents

Illustrations

Chapter 1

Introduction and Outline

1.1 The Birth of Ultra-low Temperature Physics

Born in Groningen, Netherlands, a Dutch physicist named Heike Kamerlingh Onnes founded a very large cryogenics laboratory at University of Leiden in 1904. As a member of the Royal Netherlands Academy of Arts and Sciences, he was a very reputed figure in the scientific community. On July 10th. 1908, after following several methodological steps in his cryogenic experiments, he was able to successfully liquefy helium and lowered the temperature to -269 °C (4.2 °K). By further reducing the pressure of liquid helium, he managed to achieve a temperature near -271.65 °C (1.5 °K). These were the lowest possible temperatures ever achieved in the lab by human kind at the time. It was only five years later, on December 11th. 1913, he was awarded the Nobel Prize in Physics, "for his investigations on the properties of matter at low temperatures which led, inter alia, to the production of liquid helium" [1]. In his Nobel lecture, he noted "The Nernst heat theorem and, especially, Plancks quantum theory and zero-point energy theory have made measurements at *low temperatures* of prime interest to physicists" and "the density of the helium, which at first quickly drops with the temperature, reaches a maximum at 2.2 °K approximately, and if one goes down further even drops again. Such an extreme could possibly be connected with the *quantum theory*. At any rate, closer examination of the equation of state of the helium in relation to deviations from the law of corresponding states is very

promising, as it is the critical temperature precisely of this gas which approaches absolute zero so closely" [2].

Onnes did not stop the pursuit but rather kept focusing on the understanding of ultra-low temperature physics. He further used liquefied helium-4 to cool down mercury, and found that, at 4.2 °K, the resistivity of mercury metal abruptly dropped to very small values beyond accurate experimental measurement. In other words, the mercury became "superconducting". Other metals such as Tin ($_{50}$Sn) and Lead ($_{82}$Pb) all showed the same remarkable phenomenon, at 3.8 °K and 6 °K respectively. In a nutshell, the discovery of zero-resistance of metal at ultra-low temperatures essentially opened the door of studying superfluidity and superconductivity in an electron gas.

1.2 Quantum Statistics

We now know that every elementary particle can be divided into two categories: Fermions and Bosons. These two types of particle each obey distinctively different quantum statistics.

Fermions, such as electrons, cannot all occupy the same quantum state but rather need to arrange themselves in different quantum states, dictated by the Pauli exclusion principle. More formally, systems containing N identical particles which are totally antisymmetrical are said to satisfy Fermi-Dirac statistics:

$$P_{i,j}|\text{N identical fermions}\rangle = -|\text{N identical fermions}\rangle, \tag{1.1}$$

$$\text{Fermi-Dirac statistics:} \quad \langle N_i \rangle = \frac{g_i}{e^{(\varepsilon_i - \mu)/k_B T} + 1}. \tag{1.2}$$

where $P_{i,j}$ is the permutation operator that interchanges the ith and the jth particle with i and j being arbitrary; $\langle N_i \rangle$ denotes the expected number of particles with energy ε_i, g_i is the degeneracy of energy level i (in other words, the number of states with

energy ε_i), chemical potential μ is obtained from the particle normalization condition $\sum_i \langle N_i \rangle = N$ where N is the fixed total number of particles, k_B refers to Boltzmann constant and finally T denotes equilibrium temperature the ensemble of particles are at. Precisely because of the total antisymmetrical nature of fermions, a state like $|\psi\rangle_1 |\psi\rangle_2$ which is symmetrical under exchange of particle 1 and 2, is not possible for a fermions. The Pauli exclusion principle holds keys to solve many puzzles in the microscopic and even macroscopic world, and it is not an overstatement to say the principle paved ways to study atomic and molecular physics, as well as chemistry. In other words, when combined with the spin-statistics theorem, the spin of electrons results in the Pauli exclusion principle, which in turn underlies the periodic table of chemical elements.

Bosons, however, are totally symmetrical under the interchange of any pair and satisfy the so-called Bose-Einstein statistics:

$$P_{i,j}|\text{N identical bosons}\rangle = +|\text{N identical bosons}\rangle, \tag{1.3}$$

$$\text{Bose-Einstein statistics:} \quad \langle N_i \rangle = \frac{g_i}{e^{(\varepsilon_i - \mu)/k_B T} - 1}. \tag{1.4}$$

with the requirement of $\varepsilon_i > \mu$ and same notations used in Eq.1.2. A system made up of bosons, such as liquid helium-4, exhibits a tendency for all particles to get down to the same ground state (lowest possible eigen-energy solved from Schrödinger's equation) at extremely low temperatures. What Onnes and others did not realize at the time was that he was actually the first one to achieve Bose-Einstein condensation when liquid helium-4, being bosons obviously, is cryogenically cooled and vaporized at saturation pressure. To put it quantitatively, a typical density of liquid helium-4 has density of $n = 10^{22} cm^{-3}$. Assuming a uniform gas of helium atoms in 3-dimensions being very weakly interacting, the only energy scale that can be formed from relevant

quantities of particle mass m, number density n, and the Planck constant $2\pi\hbar$, is $\hbar^2 n^{2/3}/m$. Dividing this energy by the Boltzmann constant k_B, we get an estimate of superfluidity transition temperature $\frac{\hbar^2 n^{2/3}}{m k_B} \approx 3°\text{K}$, which is strikingly close to the famous λ-point temperature 2.17°K. From another perspective, by re-arranging terms a little bit, one can figure out that the critical temperature is only reached when the spacing between particles in 3-dimensions $n^{-1/3}$ becomes closely comparable to the thermal de Broglie wavelength $\sqrt{\frac{2\pi\hbar^2}{m k_B T}}$.

In layman's term, bosons are very sociable and they love to be in the same state, to the extent that tens of millions of bosonic atoms are routinely produced to hold "hands" and behave more or less like one giant atom in the recent experiments for alkali metals, such as ^{23}Na and ^{87}Rb. Fermions, on the other hand, are not at all sociable and they avoid each other to make sure they are not in the same quantum state.

It is important to note that, in space of three or more dimensions, fundamental particles and composite particles do not have a mixed symmetry. In 2-dimensional systems, however, quasiparticles can be observed that actually obey statistics ranging continuously between Bose-Einstein statistics and Fermi-Dirac statistics, as was first shown by Jon Magne Leinaas and Jan Myrheim of the University of Oslo in 1977 [3]. The operation of exchanging two identical particles may cause a global phase shift but still do not affect observables. This type of quasi-particles that only occur in 2-dimensional systems are called anyon. Anyons are generally classified as abelian or non-abelian. While the detected abelian anyons played a major role of explaining fractional quantum Hall effect, the non-abelian anyons are yet to be detected definitely in experiments and remain as an active area of research.

1.3 Quantum Spin

What is spin in quantum mechanics?

Spin is an intrinsic form of angular momentum, first inferred from observations such as the Stern-Gerlach experiment in which particles are observed to possess angular momentum that cannot be accounted for by orbital angular momentum alone [4]. In some ways, spin is much like a vector defined in Hilbert space; it has a definite magnitude, and it has a "direction" (but quantization makes this "direction" different from the direction of an ordinary mathematical vector). All elementary particles of a given kind have the same magnitude of spin angular momentum, which is indicated by assigning the particle a spin quantum number [5].

This internal degree of freedom has no classical counterpart. In contrast, a quantum particle's velocity, which is obtained by performing wave-function expectation on the velocity operator, is directly analogous to a classical particle's velocity. It is therefore without surprises that the object of quantum mechanical spin is a cornerstone for a variety of materials that can manifest quantum properties. Materials such as quantum magnets and topological insulators are fascinating to study and holds great application promises precisely because of the existence of quantum mechanical spin and the associated coupling with the momentum (or better known as "orbitals"). Typically, when the coupling strength is significant enough to increase energy scale of interests, various quantum effects are brought to the forefront manifestly. We will come back to address the origin and effect of the above mentioned coupling later in Section 1.5 of Chapter 1.

Remarkably, there is a deep connection between quantum spin of a particle and the quantum statistics obeyed by the particle: half-integer spin particles are fermions, and integer spin particles are bosons. In non-relativistic quantum mechanics, this

connection is accepted as an empirical postulate, a law of nature without known exceptions to-date. However, in the relativistic quantum theory, it can indeed be proved that half-integer spin particles cannot be bosons and integer spin particles cannot be fermions [6].

1.4 Dilute Ultra-cold Quantum Gases

In the 1920s, the Indian physicist Satyendra Nath Bose studied the quantum statistics of photons, for which the total number is not a fixed quantity and the particle is massless. He asked for comments from Albert Einstein on his manuscript before submitting it to a journal. Einstein immediately recognized the paper's importance and impact, and personally translated the paper and submitted it for publication at Zeitschrift für Physik [7]. Subsequently, Einstein extended Bose's treatment to massive particles, whose total number is a fixed quantity, and made a highly cited publication, the same year he published the important article on General Relativity [8]. Einstein considered a gas of non-interacting massive bosons and concluded that, below a critical temperature, there would be non-zero fraction of particles occupying the lowest energy single particle state [9]

In Section 1.1 and 1.2, we mentioned that liquid helium-4 was cooled below the λ-transition point and could flow frictionlessly, the very definition of superfluidity. However, the strong interaction strength between helium atoms reduces the the number of atoms in the zero-momentum state even at ultra-low temperatures, thus the condensate fraction is rather low, being around only 10%. The fundamental difficulties to realize weakly interacting Bose gases in ultra-cold temperatures (such that they can have high condensate fraction) came from a number of factors at the time. One important fact was that most substances at low temperatures do not re-

main gaseous (otherwise inter-particle scattering strength can be greatly reduced), but form solid structures (crystallization) or become liquefied (such as helium-4), so much so that the effects of interaction remain large. As laser cooling of alkali atoms made significant advances, it was finally made possible in the 1990s that a number of experiments became successful in producing gaseous Bose-Einstein condensate in the laboratories [10–12].

Since the exciting experimental realizations of Bose-Einstein condensate of ultracold quantum gases in the laboratories, the field of quantum gases or ultracold atoms is the fastest expanding and most interdisciplinary field in physics today. The experimental branch of this exciting new field uses the techniques of atomic, molecular and optical physics to study quantum phase transition, Bose-Einstein condensation (BEC), bosonic superfluidity, quantum magnetism, many-body spin dynamics, Efimov states, Bardeen-Cooper-Schrieffer (BCS) superfluidity and the BEC-BCS crossover, etc. These are condensed matter systems whose constituents have well-understood microscopic interactions. At sufficiently low temperatures, the long de Broglie wavelengths of the atoms allow these systems to exhibit quantum phenomena on a macroscopic scale. Ultracold atoms are also used in experiments for precision measurements enabled by the low thermal noise and, in some cases, by exploiting quantum mechanics to exceed the standard quantum limit. In addition to potential technical applications, such precision measurements may serve as tests of our current understanding of physics. The theoretical branch of this field is completely interdisciplinary, attracting top scientists from atomic, condensed matter, high energy and nuclear physics, as well as from quantum optics, quantum information, quantum simulation and quantum computation. It is of great interest in the context of condensed matter physics, where it may provide valuable insights into the properties of inter-

acting quantum systems. The ultracold atoms are used to implement an analogue of the condensed matter system of interest, which can then be explored using the tools available in the particular implementation. Since these tools may differ greatly from those available in the actual condensed matter system, one can thus experimentally probe otherwise inaccessible properties. Furthermore, ultracold atoms may even allow one to create exotic states of matter, which otherwise cannot be observed in nature. In short, ultracold quantum gases are proving to be a powerful model system for strongly interacting many-body systems [13–21].

1.5 Synthetic Gauge Field

Gauge fields are central in our modern understanding of physics at all scales. Electromagnetism is the simplest example, where the scalar and vector potentials together describe the coupling between charged matter and electromagnetic fields. In the standard model, interactions are mediated by more complex gauge fields which often are of a non-Abelian character. At the highest energy scales, the microscopic universe is governed by particles interacting with each other through the exchange of gauge bosons. At the largest length scales, our Universe is ruled by gravity, whose gauge structure suggests the existence of a particle, graviton, that mediates the gravitational force. At the mesoscopic scale, solid-state systems are subjected to gauge fields of a different nature: materials can be immersed in external electromagnetic fields, but they can also feature emerging gauge fields in their low-energy description. For example, the adiabatic motion of quantum particles with internal structure can be described in terms of an effective 'geometric' gauge potential. This property was first studied in molecular physics, where the Jahn-Teller effect revealed the geometric phases and corresponding vector potentials [22–24].

Atomic quantum gases are charge neutral, and therefore, they are not affected by external electromagnetic fields the way electrons are. However, atom-light coupling allows for the creation of versatile gauge potentials that effectively emerge in the atoms dynamics, allowing experimental access to a wide range of new phenomena at the quantum level. As such, atoms can be subjected to static Abelian gauge fields, offering a framework where synthetic electric and magnetic fields can be experimentally tuned with laser fields [25–27]. We noted in Section 1.4 that the laboratory realization of ultracold neutral atomic gases including Bose-Einstein condensates (BECs) [10–12] and degenerate Fermi gases [28] delivered remarkably versatile experimental systems that can faithfully simulate a wide range of real world materials. The newest addition to the quantum simulation vision* is just such: the static non-Abelian gauge fields have been tailored so as to reproduce the effects of Rashba-type spin-orbit couplings (SOCs) [30], as well as system of fermionic atoms in which lasers induce strong spin-orbit coupling [31, 32]. One can envision that this technique may be combined with Feshbach resonances [33] (which control the inter-atomic interactions) and optical lattices (which mimic the lattices in real materials), enabling the production of exotic states found in condensed-matter systems such as topological insulators. Even more importantly, one hopes to realize novel states of matter (e.g., "fractional topological insulators"), which are anticipated by many theoretical studies but are hard to create

*In 1981, Richard Feynman gave a famous keynote speech [29] about the possibility and potential consequences of "simulating physics with computers". The take-home message is that "nature is not classical and using classical computers to simulate quantum mechanics would be close-to impossible". Instead, one could think about solving these computationally and/or analytically intractable problems by constructing "quantum emulators/computers". In the meanwhile, "physicisits can get new ideas and explore new possibilities of understanding physical laws of nature", about which "we have to admit that we don't understand everything".

and analyze experimentally.

Spin-orbit coupling refers to the interaction between the spin and motional degrees of freedom of an electron. Consider a situation of 2-dimensional electron gas subjected to the uniform electric field perpendicular to the plane. According to special relativity, the electric field is seen as a magnetic field in the moving electrons' frame of reference. The magnetic field's strength and direction depend on the velocity of the electron, producing a correlation between the electrons' momentum and their spin states. At field strengths available in the laboratory this correlation can generally be neglected for any reasonable electronic velocities. However, strong spin-orbit coupling can be found in materials that contain heavier elements and lack inversion symmetry: the electron motion becomes relativistic near the ion cores, and the local electric field can be strong. While these relativistic effects can couple an electron's spin to its motion, coupling the spin and the center-of-mass motion of a neutral atom presents a challenge.

But we mentioned in the beginning of Section 1.5, that in the low-energy description gauge fields can still be emergent under certain situations. For instance, when the state vector of an atomic system evolves adiabatically in time, if the parameter space of the time-dependent Hamiltonian has cyclic geometric properties, the accumulated Berry phase becomes universally invariant, cannot be canceled, and consequently becomes an observable property of the system. These geometric vector potentials appear when each atom's external motion is described separately from its internal dynamics, yet the Hamiltonian governing the internal dynamics parametrically depends on the atomic position. In this context, when the local atomic internal states 'dressed' by the laser fields have degeneracies, effective non-Abelian gauge potentials can be formed, often manifesting as the spin-orbit coupling term that "heavy"

material systems would typically have due to relativistic correction to Schröndinger equation.

What typically happens in the cold atom experiments is the following: two hyperfine atomic states are singled out among many other internal degrees of freedom. Laser fields are properly aligned and designed in such a way that trapped atoms may mimic charged particles in a magnetic field with emergence of Lorentz-like force. Two counter-propagating laser beams are introduced to couple these states by a resonant stimulated two-photon Raman transition: by absorbing a photon from the left beam, and emitting it into the right beam, a $\uparrow$ spin atom will flip into the $\downarrow$ spin state. Since in the process the atom receives a momentum kick, this provides a mechanism by which spin and momentum become coupled. Using a group of degenerate (or quasi-degenerate) pseudo-spin eigenstates, non-abelian dynamics of cold atoms in light fields is generated, which effectively leads to the spin-orbit coupling for cold atoms, simulating the electronic counterpart in condensed matter. Here, synthetic SOC refers to the coupling between atom's pseudo-spins (i.e. hyperfine states) and COM motion, rather than the generic interaction between electron's spin (or magnetic moment) and angular/linear momentum operator in quantum mechanics.

Such spin-orbit coupling (SOC) in cold atoms has been realized in both bosonic [34, 35] and fermionic systems [31, 32], and has attracted tremendous attention in recent years [36]. In practice, to avoid spontaneous emission, SOC is induced between two hyperfine ground states of an atom via a pair of Raman laser beams. Due to its non-Abelian nature[†] , SOC not only significantly affects the physics of a single

[†] The form of SOC we discuss here can be expressed in terms of static gauge fields in the atomic Hamiltonian as $H = (p - \mathcal{A})^2/2m$. When the components of the vector $\mathcal{A} = (\mathcal{A}_x, \mathcal{A}_y, \mathcal{A}_z)$ mutually commutes with each other, the gauge field $\mathcal{A}$ is called Abelian gauge potentials. When they don't

atom, but, perhaps more importantly, also profoundly changes the properties of a many-body system. It is an essential ingredient underlying such diverse phenomena as topological superconductors/insulators, Majorana and Weyl fermions, spin-Hall effects, *etc.*

Experiments for both bosonic and fermionic gases are exciting, as each holds great and new promises for studying exotic states of matter. Due to the Pauli exclusion principle, fermions occupy a large number of momentum states, and are therefore sensitive to global (topological) features of the band structure. Spin-orbit-coupled fermionic gases would thus provide ways to explore a much richer phenomenology. Creating spin-orbit coupling in bosonic gases provides the first physical realization of an SO coupled bosonic system and therefore many new issues arise, such as "how does SO coupling affect the behavior of the superfluidity for bose gas". Cold atom systems are highly tunable and can be used for the purpose of quantum simulation. Making use of this tunability, on one hand, we can study physics like topological insulators and superconductors in a more flexible and disorder-free setting. On the other hand, we can reach certain parameter regimes that are not easy to access with conventional solid state materials, for instance, tuning the strength of spin-orbit coupling so that it is comparable with Fermi energy, where novel effects will be expected.

1.6 Quantized Light Field

When Jaynes and Cummings first studied the time evolution of a two-level atom in an electromagnetic field in a fully quantized way in 1960s [37], experimental realization of this ideal theoretical model was out of reach. It was made possible only with the advent of one-atom masers in late 1980s, by Rempe, Walther and

commute, for instance $\mathcal{A}_x\mathcal{A}_y \neq \mathcal{A}_y\mathcal{A}_x$, the gauge field $\mathcal{A}$ is called non-Abelian gauge potentials.

Klein [38], who experimentally studied the interaction of a single atom and a single resonant mode of electromagnetic field in a cavity. Jaynes-Cummings model (or J-C Model) serves to bridge our understanding of the relationship between quantum theory of radiation and semi-classical theory of atom-light interaction, and has become one of the most important models in quantum optics and cavity electrodynamics (CQED) and quantum mechanics was put to fundamental tests. In the experiment of Reference [38], a beam of atoms was used and the atom-light interaction was studied during the transient time when the atoms pass through the cavity. The intensity of the atomic beam is sufficiently low such that at any given time, no more than one atom is inside the cavity.

The field of CQED was further advanced by putting a single trapped cold atom [39], and more recently a condensate of ultracold atoms [40–42], inside an optical cavity. In addition, bright-state polaritons of four-wave mixing and six-wave mixing signals can be parametrically amplified [43]. In the J-C model, and other related CQED systems, the focus is the interaction and mutual influence between the cavity mode and the atomic internal degrees of freedom. The external degrees of freedom of the atom, *i.e.*, its center-of-mass (COM) motion, is generally neglected.

Unlike "hot" atoms, however, cold atoms' COM motion in general can no longer be neglected in this "atom + cavity" system, as the COM momentum of a cold atom will be significantly affected by photon recoil from emission and absorption of even a single photon. Therefore in a more complete description of the cavity system, one needs to take into account the interplay among the cavity photons, and both the internal and external atomic degrees of freedom. Because intra-cavity photon and atoms very frequently scatter off each other due to the geometric confinement, not only dipole force gets strongly enhanced but also atom's back-action *onto* light

becomes significant. For Bose-Einstein condensate (BEC), atoms occupy the same motional quantum state, and because of long-range cavity photon mediation, the internal states (pseudo-spins) are infinitely coordinated. The most famous example is the Dicke model [44], which has been realized in CQED as well [42]. Furthermore, when more than one atom is inside the cavity, one should also account for the cavity photon mediated long-range interaction between atoms. All of these make the "cold atoms + cavity" system extremely rich and interesting, and truly represent a new frontier in both CQED and cold atom research.

In Section 1.5, we mentioned that the synthetic gauge fields realized in cold atoms experiment provided a plethora of research opportunities for physicists. However, we should also note that all those schemes created *static* gauge fields, in the sense that they can be perfectly well described by adding additional terms in the bare atomic Hamiltonian. Whereas in nature, gauge fields as fundamental force carriers are naturally dynamical. Even in many-body physics, gauge fields are described by effective field theories and universally manifest themselves as dynamical: they are described by their own Hamiltonian and are not just imposed, in an *ad hoc* way.

In Chapter 5, we will describe in details about our proposal of realizing dynamical coupling between spin, orbit, and quantized light field. As a tidbit of this introductory chapter, the photon field affects both the internal states (via inducing a transition between different states of the atom) and the external center-of-mass motion (via photon recoil) of the atom, and at the same time more importantly, the photon field experiences back-actions from the atomic states. Such a simple feedback between atom and photon field leads to dramatic modification of the atomic dispersion relation, instability of the entire system, and exotic behaviors of the photon field. We will conclude that the synthesis of cavity QED and spin-orbit coupling is not a trivial

combination and interesting new physics emerges in this setting.

1.7 Outline of the Dissertation

The above sections conclude the introductory part in Chapter 1. The rest of the dissertation is divided into three parts, which are largely drawn from the published works while the author pursues the doctoral degree of physics at Rice University.

Chapter 2 and 3 addresses the novel features of ground-state physics, of spin-orbit coupled cold gases. We note that spin-orbit coupling effectively changes the band structure of single particle Hamiltonian [45, 46], may favor pairing at finite center-of-mass momentum for two body bound state [45], and induces Fulde-Ferrell type of Cooper pairs for many body systems [46].

Chapter 4 touches the surface and frontier of research progresses made in topological condensed matter physics and quantum dynamics of non-equilibrium physics. To make progresses, we considered specific physical realizations [47], discussed consequences of introducing spin-orbit coupling into well-known and well-studied model Hamiltonians [47,48], and presented numerically simulated non-trivial dynamical evolution [48].

Chapter 5 is dedicated to the proposal and study of another even more exotic type of spin-orbit coupling. We propose to put atoms into optical cavity, and let the trio of pseudo-spin, center-of-mass "orbit" (or orbital degrees of freedom for harmonic trap if present), and quantized cavity light field be mutually coupled. The full system may involve rather sophisticated experimental setup, but the physics from theoretical point of view is rather rich, and we will discuss a few realizations that promise surprising and interesting physics [49–52], which have never been conceived before.

Finally, in Chapter 6, we summarize the thesis and present concluding remarks.

Chapter 2

Synthetic Spin-Orbit Coupling

2.1 Single-Particle Physics with Spin-Orbit Coupling

We start by formulating the single-particle Hamiltonian for a non-interacting homogeneous Fermi gas in three dimension:

$$\mathcal{H}_0 = \frac{\hbar^2 \mathbf{k}^2}{2m} + \sum_{i=x,y,z} (v_i k_i + \Lambda_i)\, \sigma_i \,, \tag{2.1}$$

where we have defined SOC strength vector $\mathbf{v} = (v_x, v_y, v_z)$, and Zeeman field vector $\mathbf{\Lambda} = (\Lambda_x, \Lambda_y, \Lambda_z)$. $\boldsymbol{\sigma} = (\sigma_x, \sigma_y, \sigma_z)$ are Pauli matrices acting on the atomic pseudo-spin degrees of freedom. This description is a general model valid for various coupling schemes. The single-particle spectrum can be straightforwardly obtained as $E^{\pm}_{\mathbf{k}} = \epsilon_{\mathbf{k}} \pm \sqrt{\sum_{i=x,y,z}(v_i k_i + \Lambda_i)^2}$ with $\epsilon_{\mathbf{k}} = \hbar^2 \mathbf{k}^2/(2m)$. The superscripts '$\pm$' define the two helicity bases which are related to the original spin basis by the transformation

$$\begin{bmatrix} |\mathbf{k}+\rangle \\ |\mathbf{k}-\rangle \end{bmatrix} = \begin{bmatrix} \cos\theta_{\mathbf{k}} & \sin\theta_{\mathbf{k}}\, e^{i\phi_{\mathbf{k}}} \\ -\sin\theta_{\mathbf{k}}\, e^{-i\phi_{\mathbf{k}}} & \cos\theta_{\mathbf{k}} \end{bmatrix} \begin{bmatrix} |\mathbf{k}\uparrow\rangle \\ |\mathbf{k}\downarrow\rangle \end{bmatrix} , \tag{2.2}$$

where

$$\begin{aligned} \cos^2\theta_{\mathbf{k}} &= \frac{1}{2}\left(1 + \frac{v_z k_z + \Lambda_z}{\sqrt{\sum_{i=x,y,z}(v_i k_i/m + \Lambda_i)^2}}\right) , \\ \tan\phi_{\mathbf{k}} &= -\frac{v_y k_y + \Lambda_y}{v_x k_x + \Lambda_x} \,. \end{aligned}$$

2.1.1 Equal Weight Rashba-Dresselhaus SOC

For concreteness, we now apply this general formalism to the experimentally realized system whose single-particle Hamiltonian takes the following form:

$$\begin{aligned} H_0 &= \sum_\sigma \int d\mathbf{r} \Psi_\sigma^\dagger(\mathbf{r}) \left(\frac{\hbar^2 \mathbf{k}^2}{2m} + \alpha\delta \right) \Psi_\sigma(\mathbf{r}) \\ &+ \int d\mathbf{r} \left(\frac{\Omega}{2} e^{2i\hbar k_r z} \Psi_\uparrow^\dagger(\mathbf{r}) \Psi_\downarrow(\mathbf{r}) + h.c. \right) . \end{aligned} \tag{2.3}$$

Here Ψ_σ and $\Psi_\sigma^\dagger$ are field operators for hyperfine spin states σ, and $\alpha = \pm 1$ for $\sigma = \uparrow, \downarrow$ respectively. Ω is the two-photon Raman coupling strength and k_r the recoil momentum of the Raman beams which is taken to be along the z-axis. Finally δ represents the two-photon detuning. To get rid of the exponential terms, we introduce a local gauge transformation:

$$\tilde{\psi}_\uparrow(\mathbf{r}) = e^{-ik_r z} \Psi_\uparrow(\mathbf{r}) , \quad \tilde{\psi}_\downarrow(\mathbf{r}) = e^{ik_r z} \Psi_\downarrow(\mathbf{r}) . \tag{2.4}$$

Defining the spinor $\tilde{\boldsymbol{\psi}} = (\tilde{\psi}_\uparrow,\ \tilde{\psi}_\downarrow)^T$, we can recast H_0 as

$$H_0 = \int d\mathbf{r}\, \tilde{\boldsymbol{\psi}}^\dagger(\mathbf{r})\, \mathcal{H}_0\, \tilde{\boldsymbol{\psi}}(\mathbf{r}) , \tag{2.5}$$

$$\mathcal{H}_0 = \frac{\hbar^2 \mathbf{k}^2}{2m} + \frac{\hbar^2 k_r}{m} k_z \sigma_z + \frac{\Omega}{2} \sigma_x + \delta \sigma_z , \tag{2.6}$$

where we have neglected a constant energy shift $E_r = \hbar^2 k_r^2/(2m)$ (the recoil energy) in $\mathcal{H}_0$. One can immediately see that $\mathcal{H}_0$ above takes the form of Eq. (2.1) with $\mathbf{v} = (0,\ 0,\ \hbar^2 k_r/m)$ and $\mathbf{\Lambda} = (\Omega/2,\ 0,\ \delta)$.

The single-particle ground state occurs in the lower helicity branch, and is given by $|\mathbf{k}_{\min} -\rangle$ at momentum $\mathbf{k}_{\min} = (0,\ 0,\ k_0)$ with energy

$$E_{\min} = \frac{\hbar^2 k_0^2}{2m} - \sqrt{h^2 + (\lambda k_0 + \delta)^2} , \tag{2.7}$$

where for notational simplicity we have defined $h \equiv \Omega/2$ and $\lambda \equiv \hbar^2 k_r/m$. From $\partial E_{\min}/\partial k_0 = 0$, we obtain

$$k_0 = \frac{\lambda k_0 + \delta}{\sqrt{h^2 + (\lambda k_0 + \delta)^2}}\, k_r \,. \tag{2.8}$$

for $\delta \neq 0$. When $\delta = 0$, it is easy to show that the ground state is doubly degenerate with minima $k_0 = \pm\frac{1}{\lambda}\sqrt{(\frac{\lambda^2 m}{\hbar^2})^2 - h^2}$ when $h < \frac{\lambda^2 m}{\hbar^2}$ or has single minimum at $k_0 = 0$ when $h > \frac{\lambda^2 m}{\hbar^2}$.

It is important to remember that $\mathbf{k}_{\min}$ is not the *mechanical* momentum of the particle. Measured in the lab frame, the mechanical momentum of the particle prepared in this ground state can be calculated as

$$\mathbf{K}_0 = (\mathbf{k}_{\min} + k_r\hat{z})\sin^2\theta_{\mathbf{k}_{\min}} + (\mathbf{k}_{\min} - k_r\hat{z})\cos^2\theta_{\mathbf{k}_{\min}}\,, \tag{2.9}$$

To show that $\mathbf{K}_0 = 0$, we need to "undo" the local gauge transformation, from spinor $\tilde{\boldsymbol{\psi}}$ to $\tilde{\Psi}$.

First, we notice that the ground state minimum stays in the lower helicity branch, which is a superposition of up and down components,

$$\begin{aligned} |\mathbf{k}-\rangle &= -\sin\theta_{\mathbf{k}}|\mathbf{k}\uparrow\rangle + \cos\theta_{\mathbf{k}}|\mathbf{k}\downarrow\rangle & (2.10)\\ &= -\sin\theta_{\mathbf{k}} c^\dagger_{\mathbf{k}\uparrow}|0\rangle + \cos\theta_{\mathbf{k}} c^\dagger_{\mathbf{k}\downarrow}|0\rangle & (2.11)\end{aligned}$$

and the minimum occurs at $\mathbf{k}_{\min} = (0, 0, k_0)$ where ($\hbar = m = 1$)

$$k_0 = \frac{\lambda(\lambda k_0 + \delta)}{\sqrt{h^2 + (\lambda k_0 + \delta)^2}} \tag{2.12}$$

While, from bare spin basis (atomic pseudospin basis) to the model Hamiltonian's basis, spinors are related by

$$\begin{aligned} \Psi_\uparrow(\mathbf{r}) &= e^{+ik_r z}\tilde{\boldsymbol{\psi}}_\uparrow(\mathbf{r}) & (2.13)\\ \Psi_\downarrow(\mathbf{r}) &= e^{-ik_r z}\tilde{\boldsymbol{\psi}}_\downarrow(\mathbf{r}) & (2.14)\end{aligned}$$

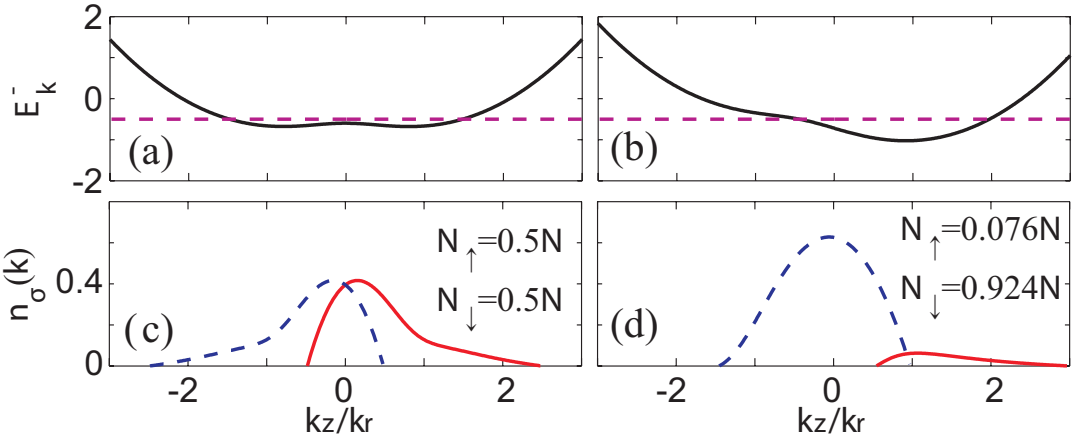

Figure 2.1 : (a) and (b) Single-particle dispersion in the lower helicity branch. The horizontal dashed lines represent the chemical potential of the Fermi sea. (c) and (d) Momentum distribution along the z-axis for the non-interacting Fermi gas represented by (a) and (b), respectively. The relative population of the two spin components are listed in the plot, blue dashed line for spin-down atoms and red thick line for spin-up atoms. For the left column [(a), (c)] we have $\delta = 0$ and $h = 0.6E_r$; for the right column [(b), (d)] we have $\delta = 0.4E_r$ and $h = 0.6E_r$.

For the ground state with quasimomentum $\mathbf{k}_{\min}$, the momentum in the lab frame is

$$
\begin{aligned}
P_0^z &= |\sin\theta_{\mathbf{k}_{\min}}|^2(k_0+k_r) + |\cos\theta_{\mathbf{k}_{\min}}|^2(k_0-k_r) && (2.15)\\
&= \frac{1}{2}\left(1-\frac{\lambda k_x+\delta}{\sqrt{h^2+(\lambda k_x+\delta)^2}}\right)(k_0+k_r) && (2.16)\\
&+ \frac{1}{2}\left(1+\frac{\lambda k_x+\delta}{\sqrt{h^2+(\lambda k_x+\delta)^2}}\right)(k_0-k_r)\\
&= k_0 - \frac{(\lambda k_0+\delta)k_r}{\sqrt{h^2+(\lambda k_0+\delta)^2}} = k_0 - \frac{k_r}{\lambda}k_0 = 0
\end{aligned}
$$

where in the last line, Eq. (2.12) and $k_r = \lambda$ in the dimensionless unit are used.

So far, we have shown that particle in the ground state has exactly zero mechanical momentum in the lab frame, even though its canonical momentum k_0 depend explicitly on the strengths of the SOC λ, and the Zeeman fields h and δ.

2.1.2 Non-interacting Fermi Sea

Next we consider a filled Fermi sea at zero temperature. Following the discussion of section 2.1.1, instead of taking $\mathbf{k} = \mathbf{k}_{\min}$ as in Eq. (2.9), we need to sum over all the momentum under the Fermi surface. Here again one can show analytically that the total momentum of the Fermi gas is zero in the lab frame as the following.

For a given chemical potential μ, Fermi surface is defined by the following equation (we take $\hbar = m = 1$)

$$\frac{k_z^2 + k_\perp^2}{2} - \sqrt{h^2 + (\lambda k_z + \delta)^2} = \mu \,, \tag{2.17}$$

where we have assumed that μ lies below the bottom of the upper helicity branch and the Fermi surface is simply connected, as illustrated in Fig. 2.1. The total mechanical momentum in the lab frame is obtained by integrating over the three-dimensional volume of Fermi sea:

$$\begin{aligned}
K^z_{\rm lab} &= \sum_{\mathbf{k}} \left[|\sin\theta_{\mathbf{k}}|^2 (k_z + k_r) + |\cos\theta_{\mathbf{k}}|^2 (k_z - k_r) \right] \\
&= \frac{V}{(2\pi)^3} \int_{k_1}^{k_2} dk_z \left[k_z - \frac{(\lambda k_z + \delta) k_r}{\sqrt{h^2 + (\lambda k_z + \delta)^2}} \right] \times \left(\mu - \frac{1}{2} k_z^2 + \sqrt{h^2 + (\lambda k_z + \delta)^2} \right) \\
&= \frac{V}{8(2\pi)^3} \left(k_2^4 - k_1^4 + 8\delta\lambda(k_1 - k_2) - 4(\mu + \lambda^2)(k_2^2 - k_1^2) \right) \\
&= 0 \,,
\end{aligned}$$

where $k_{1,2}$ are the intersections of the Fermi level with the lower helicity branch on the z-axis and are simply the roots of Eq. (2.17) after taking $k_\perp = 0$. Similarly,

$$\begin{aligned}
K^x_{\rm lab} &= \sum_{\mathbf{k}} \left[|\sin\theta_{\mathbf{k}}|^2 k_x + |\cos\theta_{\mathbf{k}}|^2 k_x \right] = 0 \,, \\
K^y_{\rm lab} &= \sum_{\mathbf{k}} \left[|\sin\theta_{\mathbf{k}}|^2 k_y + |\cos\theta_{\mathbf{k}}|^2 k_y \right] = 0 \,.
\end{aligned}$$

The single-particle energy dispersion and momentum distributions of two examples of non-interacting Fermi sea (one for $\delta = 0$ and the other $\delta \neq 0$) are illustrated in

Fig. 2.1(a)-(d).

2.2 Dimer Bound State with Finite Center-of-Mass Momentum

Next we consider the attractive s-wave contact interaction between un-like spins which, in terms of the creation and annihilation operators for the original spin states, is represented by

$$\mathcal{H}_{\rm int} = \frac{g}{V}\sum_{\mathbf{k}\mathbf{k}'\mathbf{q}} c^{\dagger}_{\mathbf{q/2}+\mathbf{k}\uparrow} c^{\dagger}_{\mathbf{q/2}-\mathbf{k}\downarrow} c_{\mathbf{q/2}-\mathbf{k}'\downarrow} c_{\mathbf{q/2}+\mathbf{k}'\uparrow}\,, \tag{2.18}$$

where g is the bare coupling strength to be renormalized using the s-wave scattering length a_s. A general two-body wave function describing a dimer state with a definite center-mass momentum $\mathbf{q}$ can be written as [53]:

$$|\Psi\rangle_{\mathbf{q}} = \sum_{\mathbf{k},\sigma,\sigma'} \psi_{\sigma\sigma'}(\mathbf{k})\, c^{\dagger}_{\frac{\mathbf{q}}{2}+\mathbf{k}\sigma} c^{\dagger}_{\frac{\mathbf{q}}{2}-\mathbf{k}\sigma'} |0\rangle\,. \tag{2.19}$$

Inserting this wave function into the Schrödinger equation

$$\big(\mathcal{H}_0 + \mathcal{H}_{\rm int}\big)|\Psi\rangle_{\mathbf{q}} = E_{\mathbf{q}}|\Psi\rangle_{\mathbf{q}}\,, \tag{2.20}$$

and after some lengthy algebra, we arrive at four coupled algebraic equations for the coefficients $\psi_{\sigma\sigma'}(\mathbf{k})$. Self-consistency requires that the energy of the dimer state, $E_{\mathbf{q}}$, satisfies the following equation:

$$\frac{m}{4\pi\hbar^2 a_s} = \frac{1}{V}\sum_{\mathbf{k}}\left[\left(\mathcal{E}_{\mathbf{k},\mathbf{q}} - \frac{4\mathcal{E}^2_{\mathbf{k},\mathbf{q}}(\mathbf{v}\cdot\mathbf{k})^2 - 4\left[\sum_{i=x,y,z} v_i k_i (v_i q_i + 2\Lambda_i)\right]^2}{\mathcal{E}_{\mathbf{k},\mathbf{q}}\left(\mathcal{E}^2_{\mathbf{k},\mathbf{q}} - \sum_{i=x,y,z}(v_i q_i + 2\Lambda_i)^2\right)}\right)^{-1} + \frac{1}{2\epsilon_{\mathbf{k}}}\right], \tag{2.21}$$

where $\mathcal{E}_{\mathbf{k},\mathbf{q}} \equiv E_{\mathbf{q}} - \epsilon_{\frac{\mathbf{q}}{2}+\mathbf{k}} - \epsilon_{\frac{\mathbf{q}}{2}-\mathbf{k}}$, and the interaction has been regularized as $1/g = m/(4\pi\hbar^2 a_s) - 1/V\sum_{\mathbf{k}} 1/(2\epsilon_{\mathbf{k}})$. The explicit forms of $\psi_{\sigma\sigma'}(\mathbf{k})$ can also be found, which we list in the following.

We start from the Schrödinger equation, i.e., Eq. (2.20). Using the form of the Hamiltonian given in Eqs. (2.1) and (2.18), and that for the state vector $|\Psi\rangle_{\mathbf{q}}$ in Eq. (2.19), we can obtain four coupled equations for the coefficients $\psi_{\sigma\sigma'}$ that characterize the state $|\Psi\rangle_{\mathbf{q}}$. Let us introduce the singlet wave function $\psi_s(\mathbf{k}) = \frac{1}{\sqrt{2}}[\psi_{\uparrow\downarrow}(\mathbf{k}) - \psi_{\downarrow\uparrow}(\mathbf{k})]$ and the triplet wavefunctions $\psi_t(\mathbf{k}) = \frac{1}{\sqrt{2}}[\psi_{\uparrow\downarrow}(\mathbf{k}) + \psi_{\downarrow\uparrow}(\mathbf{k})]$, $\psi_u = \frac{1}{\sqrt{2}}(\psi_{\uparrow\uparrow}(\mathbf{k}) + \psi_{\downarrow\downarrow}(\mathbf{k}))$, $\psi_v = \frac{1}{\sqrt{2}}(\psi_{\uparrow\uparrow}(\mathbf{k}) - \psi_{\downarrow\downarrow}(\mathbf{k}))$. The four equations for $\psi_{\sigma\sigma'}$ can be recast into the following form:

$$\mathcal{E}_{\mathbf{k},\mathbf{q}}\,\psi_s = \frac{2g}{V}{\sum_{\mathbf{k}'}}'\psi_s(\mathbf{k}') + 2v_z k_z\psi_t - 2v_x k_x\psi_v - 2v_y i k_y\psi_u\,, \tag{2.22}$$

$$\mathbf{M}\begin{pmatrix}\psi_t\\ \psi_u\\ \psi_v\end{pmatrix} = \begin{pmatrix}2v_z k_z\\ 2iv_y k_y\\ -2v_x k_x\end{pmatrix}\psi_s\,, \tag{2.23}$$

where where $\mathcal{E}_{\mathbf{k},\mathbf{q}} = E_{\mathbf{q}} - \epsilon_{\frac{\mathbf{q}}{2}+\mathbf{k}} - \epsilon_{\frac{\mathbf{q}}{2}-\mathbf{k}}$, and $\sum_{\mathbf{k}}'$ denotes summation over positive momentum k_z, and the matrix $\mathbf{M}$ is given by

$$\mathbf{M} = \begin{pmatrix}\mathcal{E}_{\mathbf{k},\mathbf{q}} & -(v_x q_x + 2\Lambda_x) & -i(v_y q_y + 2\Lambda_y)\\ -(v_x q_x + 2\Lambda_x) & \mathcal{E}_{\mathbf{k},\mathbf{q}} & -(v_z q_z + 2\Lambda_z)\\ i(v_y q_y + 2\Lambda_y) & -(v_z q_z + 2\Lambda_z) & \mathcal{E}_{\mathbf{k},\mathbf{q}}\end{pmatrix}.$$

Denoting

$$M \equiv \det(\mathbf{M}) = \mathcal{E}_{\mathbf{k},\mathbf{q}}\left[\mathcal{E}^2_{\mathbf{k},\mathbf{q}} - \sum_{i=1}^{3}(v_i q_i + 2\Lambda_i)^2\right],$$

and using Cramer's rule in linear algebra, we can express triplet components in terms

of $\psi_s(\mathbf{k})$ as

$$\psi_t(\mathbf{k}) = \frac{2\psi_s(\mathbf{k})}{M}\begin{vmatrix} v_z k_z & -(v_x q_x + 2\Lambda_x) & -i(v_y q_y + 2\Lambda_y) \\ iv_y k_y & \mathcal{E}_{\mathbf{k},\mathbf{q}} & -(v_z q_z + 2\Lambda_z) \\ -v_x k_x & -(v_z q_z + 2\Lambda_z) & \mathcal{E}_{\mathbf{k},\mathbf{q}} \end{vmatrix},$$

$$\psi_u(\mathbf{k}) = \frac{2\psi_s(\mathbf{k})}{M}\begin{vmatrix} \mathcal{E}_{\mathbf{k},\mathbf{q}} & v_z k_z & -i(v_y q_y + 2\Lambda_y) \\ -(v_x q_x + 2\Lambda_x) & iv_y k_y & -(v_z q_z + 2\Lambda_z) \\ i(v_y q_y + 2\Lambda_y) & -v_x k_x & \mathcal{E}_{\mathbf{k},\mathbf{q}} \end{vmatrix},$$

$$\psi_v(\mathbf{k}) = \frac{2\psi_s(\mathbf{k})}{M}\begin{vmatrix} \mathcal{E}_{\mathbf{k},\mathbf{q}} & -(v_x q_x + 2\Lambda_x) & v_z k_z \\ -(v_x q_x + 2\Lambda_x) & \mathcal{E}_{\mathbf{k},\mathbf{q}} & iv_y k_y \\ i(v_y q_y + 2\Lambda_y) & -(v_z q_z + 2\Lambda_z) & -v_x k_x \end{vmatrix}.$$

After inserting expressions of $\psi_t(\mathbf{k})$, $\psi_u(\mathbf{k})$ and $\psi_v(\mathbf{k})$ into Eq. (A.9), and integrating both sides over momentum and dividing by the constant $\frac{g}{V}\sum_{\mathbf{k}}\psi_s(\mathbf{k})$, we finally reach Eq. (2.21). The unnormalized singlet wavefunction is determined from Eq. (A.9) as

$$\psi_s(\mathbf{k}) = \left[\mathcal{E}_{\mathbf{k},\mathbf{q}} - \frac{4\mathcal{E}_{\mathbf{k},\mathbf{q}}^2(\mathbf{v}\cdot\mathbf{k})^2 - 4\left(\sum_{i=x,y,z} v_i k_i (v_i q_i + 2\Lambda_i)\right)^2}{\mathcal{E}_{\mathbf{k},\mathbf{q}}\left(\mathcal{E}_{\mathbf{k},\mathbf{q}}^2 - \sum_{i=x,y,z}(v_i q_i + 2\Lambda_i)^2\right)}\right]^{-1}, \tag{2.24}$$

and the triplet wavefunctions are obtained accordingly.

Now we are in a position to discuss the two-body results when interaction is included. First, note that the two-body interaction Hamiltonian takes the form of Eq. (2.18) after we define the momentum space operators via $\tilde{\psi}_\sigma = \sum_{\mathbf{k}} e^{i\mathbf{k}\cdot\mathbf{r}} c_{\mathbf{k}\sigma}/\sqrt{V}$, and is obviously invariant under the transformation (2.4).

Second, following the general formalism, for a given set of parameters h, δ and a_s, we can obtain numerically the eigen-energy of the dimer state $E_{\mathbf{q}}$ as a function of $\mathbf{q}$. The momentum $\mathbf{q}_0$ at which $E_{\mathbf{q}}$ reaches the minimum labels the ground dimer state.

The binding energy is defined as

$$\epsilon_b = 2E_{\min} - E_{\mathbf{q}_0} \,. \tag{2.25}$$

Only when $\epsilon_b > 0$, can we consider the dimer as a truly two-body bound state. Otherwise, its energy lies in the single-particle continuum. Figure 2.2(a) shows ϵ_b decreases with increasing h and δ. Beyond a critical boundary value, the binding energy becomes negative and no stable bound state can be found. For this system, a two-body bound state only occurs on the BEC side of a Feshbach resonance with $a_s > 0$ [54]. More importantly, $\mathbf{q}_0 = q_0\hat{z}$ will be *non-zero* and along the z-axis as long as both h and δ are finite. Figure 2.2(b) displays q_0 as functions of h and δ. We note that $\mathbf{q}_0$ is an even function of h, and an odd function of δ. In the following, we prove that for a given nonzero h, q_0 deviates from zero for arbitrarily small δ.

2.2.1 Proof of nonzero $\mathbf{q}_0$ induced by Zeeman field

Following the discussion in section 2.1.1, for the equal-weight Rashba-Dresselhaus SOC, by taking $\mathbf{v} = (0,\ 0,\ \lambda)$ and $\mathbf{\Lambda} = (h,\ 0,\ \delta)$, and considering the possibility of a bound state with momentum $\mathbf{q_0} = q_0\hat{z}$, the bound state energy E_{q_0} satisfies:

$$\frac{m}{4\pi\hbar^2 a_{\rm s}} = \frac{1}{V}\sum_{\mathbf{k}} \left\{ \left[\mathcal{E}_{\mathbf{k},\mathbf{q}} - \frac{4\lambda^2 k_z^2}{\mathcal{E}_{\mathbf{k},\mathbf{q}}} \frac{\mathcal{E}^2_{\mathbf{k},\mathbf{q}} - (\lambda q + 2\delta)^2}{\mathcal{E}^2_{\mathbf{k},\mathbf{q}} - 4h^2 - (\lambda q + 2\delta)^2} \right]^{-1} + \frac{1}{2\epsilon_{\mathbf{k}}} \right\} , \tag{2.26}$$

where $\mathcal{E}_{\mathbf{k},\mathbf{q}} = E_q - \epsilon_{\frac{\mathbf{q}}{2}+\mathbf{k}} - \epsilon_{\frac{\mathbf{q}}{2}-\mathbf{k}} = E_q - (\frac{q^2}{4} + k_\perp^2 + k_z^2)$. As a first step, we show that the ground state occurs at $q_0 = 0$ when $\delta = 0$. To this end, we need to prove that $dE_q/dq|_{q_0=0} = 0$. To show this, we take derivative with respect to q on both sides of Eq. (2.26) and take $q_0 = 0$, which yields

$$0 = \left.\frac{dE_q}{dq}\right|_{q_0=0} \sum_{\mathbf{k}} \mathcal{A}(\mathbf{k}) \,, \tag{2.27}$$

$$\mathcal{A}(\mathbf{k}) = \frac{[(k^2 - E_0)^2 - 4h^2)]^2 + 4\lambda^2 k_z^2[(k^2 - E_0)^2 + 4h^2]}{(k^2 - E_0)^2[(k^2 - E_0)^2 - 4h^2 - 4\lambda^2 k_z^2]^2} \,. \tag{2.28}$$

Since the momentum integral in Eq. (2.27) is finite as the integrand $\mathcal{A}(\mathbf{k})$ is non-negative, we must have $dE_q/dq|_{q_0=0} = 0$, indicating that the ground state indeed has exactly zero momentum.

Next, we turn to a finite but small δ. We perform a similar calculation as above and expand all terms to first order in δ. This leads to

$$0 = \left.\frac{dE_q}{dq}\right|_{q_0=0} \sum_{\mathbf{k}} \mathcal{A}(\mathbf{k}) + \delta \sum_{\mathbf{k}} \mathcal{B}(\mathbf{k}) \,, \tag{2.29}$$

$$\mathcal{B}(\mathbf{k}) = \frac{64\lambda^3 h^2 k_z^2}{(k^2 - E_0)^3[(k^2 - E_0)^2 - 4h^2 - 4\lambda^2 k_z^2]^2} \,. \tag{2.30}$$

For a bound state, we have $E_0 < 0$, hence $\mathcal{B}(\mathbf{k})$ is also non-negative. Consequently, we conclude from Eq. (2.29) that $dE_q/dq|_{q_0=0} \propto \delta$. Therefore we have proved that for any finite δ, the ground dimer state cannot have zero momentum.

For the two-body wave function given in Eq. (2.19), the momentum distribution of the hyperfine spin states in the lab frame is given by:

$$\begin{aligned} n_\uparrow(\mathbf{k} + k_r\hat{z}) &= \langle c^\dagger_{\mathbf{k}\uparrow} c_{\mathbf{k}\uparrow} \rangle \\ &= |\psi_{\uparrow\downarrow}(\mathbf{k} - \mathbf{q}/2)|^2 + |\psi_{\uparrow\uparrow}(\mathbf{k} - \mathbf{q}/2)|^2 \,, \end{aligned} \tag{2.31}$$

$$\begin{aligned} n_\downarrow(\mathbf{k} - k_r\hat{z}) &= \langle c^\dagger_{\mathbf{k}\downarrow} c_{\mathbf{k}\downarrow} \rangle \\ &= |\psi_{\downarrow\uparrow}(\mathbf{k} - \mathbf{q}/2)|^2 + |\psi_{\downarrow\downarrow}(\mathbf{k} - \mathbf{q}/2)|^2 \,. \end{aligned} \tag{2.32}$$

Both of these distribution functions will be symmetric along the x- and y-axis, which yields the average momentum along these two axis $P^\sigma_{x,y} = \int d\mathbf{k}\, k_{x,y} n_\sigma(\mathbf{k}) = 0$. By contrast, $n_\sigma(\mathbf{k})$ will be in general asymmetric along the z-axis which results in finite values of $P^\sigma_z = \int d\mathbf{k}\, k_z n_\sigma(\mathbf{k})$. The total momentum can be shown as

$$\begin{aligned} \mathbf{K}_{\text{lab}} &= \sum_{\mathbf{k}} [\mathbf{k}\,(n_\uparrow(\mathbf{k}) + n_\downarrow(\mathbf{k}))] \\ &= \mathbf{q} + (N_\uparrow - N_\downarrow) k_r \hat{z} \,, \end{aligned} \tag{2.33}$$

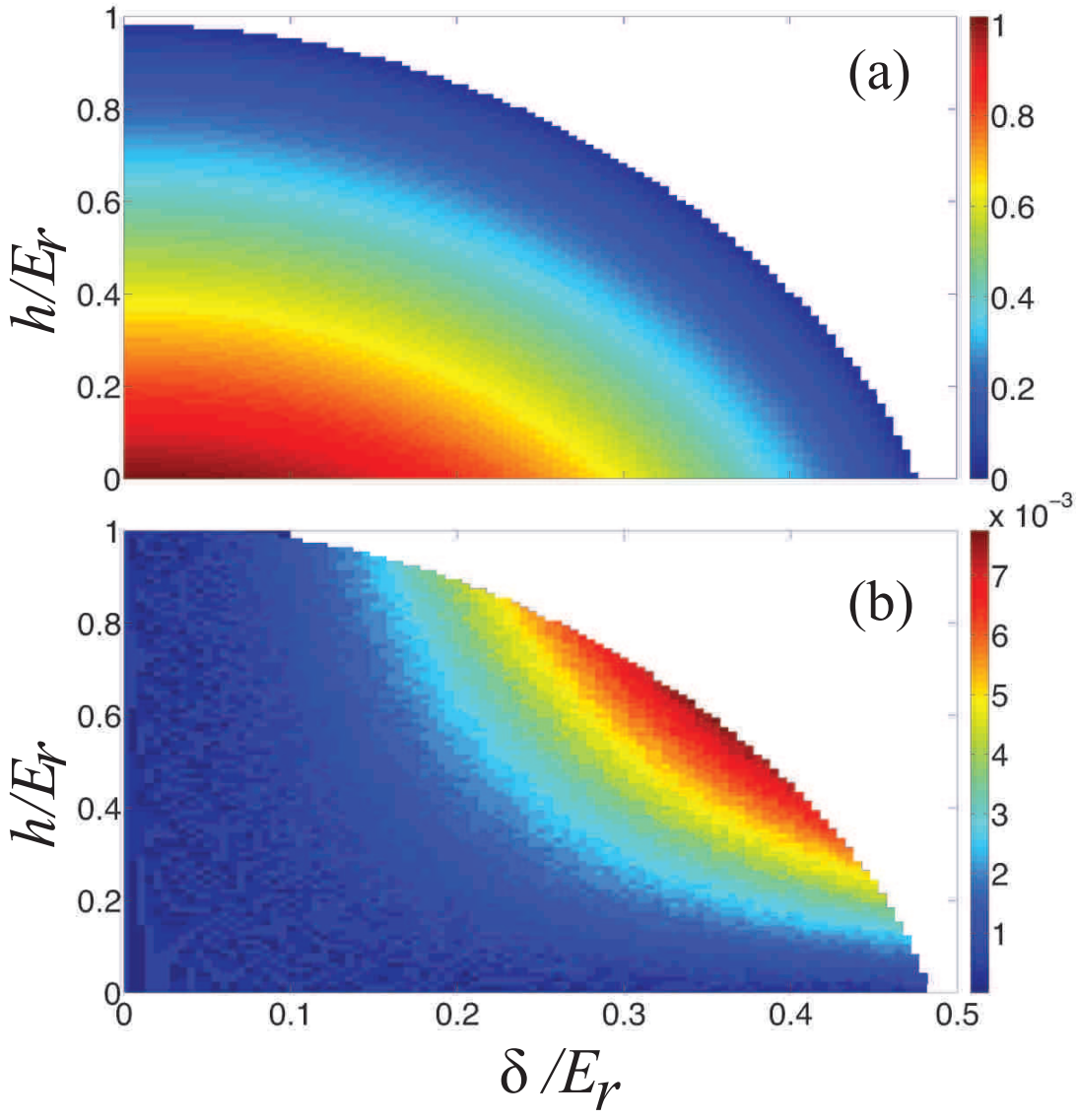

Figure 2.2 : Binding energy ϵ_b (in units of E_r) (a) and the magnitude of the momentum q_0 (in units of k_r) (b) of the dimer bound state, as functions of Zeeman field strengths δ and h. The white region is where no bound states can be found. The scattering length is given by $1/(k_r a_s) = 1$.

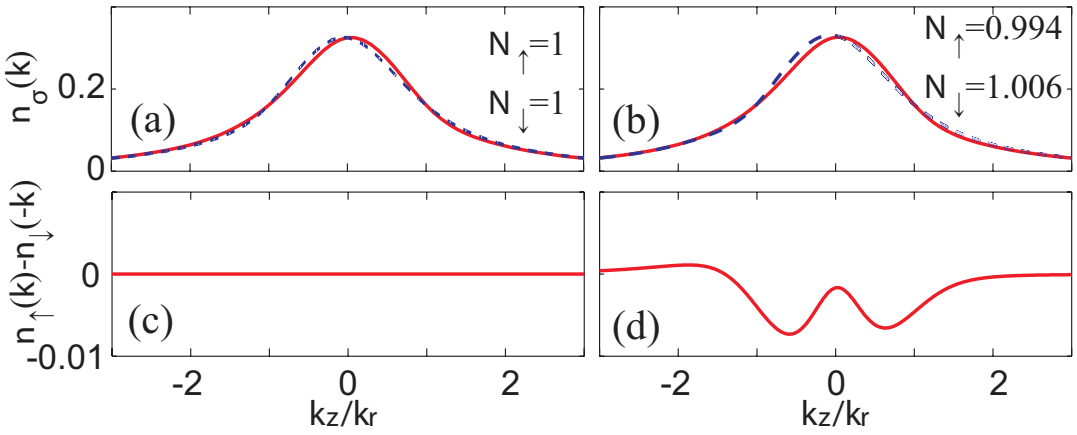

Figure 2.3 : (a) and (b) Momentum distribution along the z-axis of the dimer bound state, discussed in section 2.2. (c) and (d) Difference between $n_\uparrow(k_z)$ and $n_\downarrow(-k_z)$ for the cases shown in (a) and (b), respectively. For the left column [(a), (c)] we have $\delta = 0$ and $h = 0.6E_r$; for the right column [(b), (d)] we have $\delta = 0.4E_r$ and $h = 0.6E_r$. For the interacting case [(a)-(d)], the interaction strength is given by $1/(k_r a_s) = 1$.

where $N_\sigma = \int d\mathbf{k}\, n_\sigma(\mathbf{k})$ is the population in spin-σ and satisfy the obvious constraint $N_\uparrow + N_\downarrow = 2$. In Fig. 2.3(a) and (b), we illustrate how $n_\sigma(k_z) = \int dk_x \int dk_y\, n_\sigma(\mathbf{k})$ changes without and with detuning δ. To see it more clearly, we plot the difference between $n_\uparrow(k_z)$ and $n_\downarrow(-k_z)$ in Fig. 2.3(c) and (d). Notice that it is the SOC that breaks spatial reflectional symmetry such that $n_\sigma(\mathbf{k}) \neq n_\sigma(-\mathbf{k})$ with $\sigma = \uparrow, \downarrow$. However, for $\delta = 0$, one still has the symmetry $n_\uparrow(\mathbf{k}) = n_\downarrow(-\mathbf{k})$ as measured in the experiment of Ref. [55]; with finite δ, this symmetry between $n_\uparrow(\mathbf{k})$ and $n_\downarrow(-\mathbf{k})$ is further broken.

Note that for either $h = 0$ or $\delta = 0$, we obtain $q_0 = 0$ and $N_\uparrow = N_\downarrow = 1$. In either of these cases, both $P_z^\uparrow$ and $P_z^\downarrow$ will be finite, but they have equal magnitude and opposite sign and hence the total momentum of the dimer $P_z = 0$. When both h and δ are non-zero, we obtain finite q_0 and moreover $N_\uparrow \neq N_\downarrow$. Our numerical calculation shows that, under such circumstances, $P_z \approx 2q_0$.

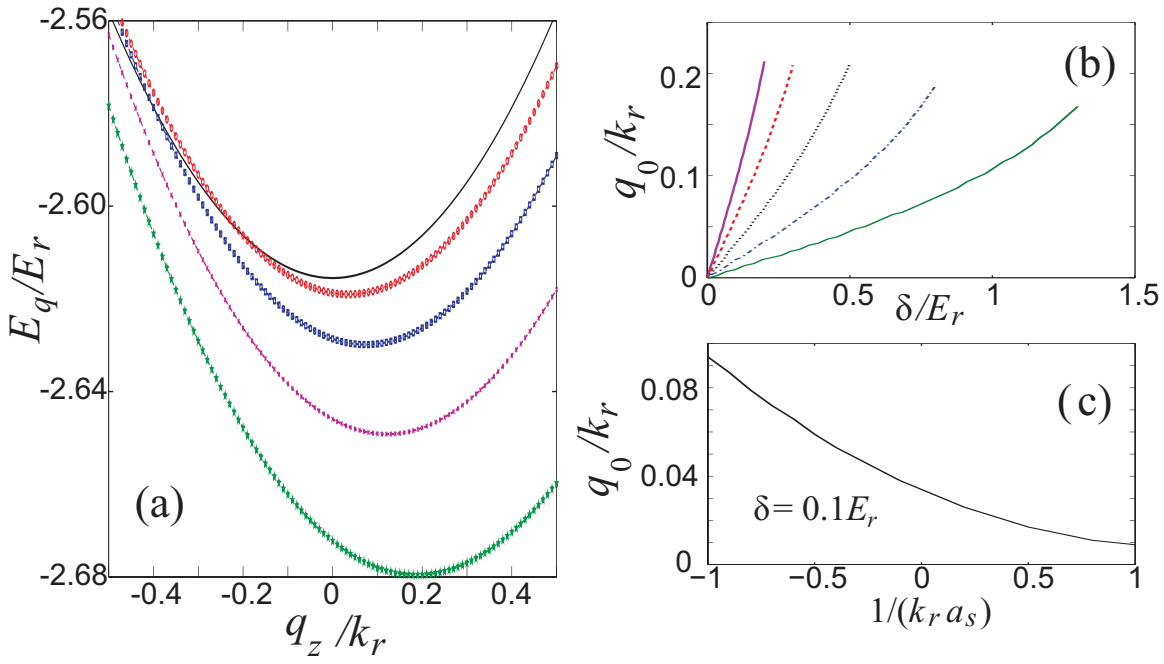

Figure 2.4 : (a) For spherical SOC, bound state energy E_q as a function of q (momentum along the z-axis) for different values of Zeeman field strength, from top to bottom $\delta/E_r = 0, 0.2, 0.4, 0.6, 0.8$ and $1/(k_r a_s) = 1/2$ for all curves. (b) Ground state momentum q_0 as a function of δ at different values of scattering length. From left to right, the curves correspond to $1/(k_r a_s) = -1$, $-1/2$, 0, $1/2$, and 1, respectively. (c) q_0 as a function of $1/(k_r a_s)$ at $\delta/E_r = 0.1$.

This situation, combined with the results for the non-interacting system, leads to the following peculiar phenomenon: In the absence of two-body interaction, the system possesses zero total momentum; when the interaction is turned on, the system picks up a finite total momentum even though the interaction Hamiltonian (2.18) seems to be momentum-conserving. This peculiarity is indeed a salient feature of the SOC. Since the linear momentum of the atom is intimately coupled to its pseudo-spin, as the interaction induces the redistribution of atomic population (i.e., change the value of σ_z) as shown in Fig. 2.1(d) and Fig. 2.3(b), it also modifies the total momentum of the system. This phenomenon can be regarded as a manifestation of the broken Galilean invariance, which is also responsible for other unusual behaviors such as the deviation of dipole oscillation frequency in a harmonically trapped system [56, 57], and the ambiguity in defining Landau critical velocity in spin-orbit coupled condensates [58].

The momentum of each spin species can be readily measured in experiment using the time-of-flight technique. This has actually been performed in a non-interacting SOC Fermi gas [55]. However, our calculation shows that q_0 is only on the order 1% of recoil momentum for the equal Rashba-Dresselhaus SOC (see Fig. 2.2) which is the only type of SOC realized so far.

The magnitude of q_0, however, can be greatly enhanced under other SOC schemes. As an example, we consider the spherical SOC coupling scheme that is recently proposed [59, 60]. For this case, the SOC strength $v_x = v_y = v_z = v$. We take the spin-orbit coupling strength $v = \hbar^2 k_r/m$ to be the same as in the previous case. Due to the isotropic nature of the SOC term, the direction of the Zeeman field is irrelevant. We choose it to be along the z-axis, i.e., $\mathbf{\Lambda} = (0,\, 0,\, \delta)$, which, as we shall show, leads to a dimer state with finite moment $q_0\hat{z}$ along the z-axis. Fig. 2.4(a) demonstrates

that, with increasing δ, the minimum of of the bound state energy E_q deviates away from zero to some finite value. Compared to the former equal Rashba-Dresselhaus SOC case, an essential difference here is that a two-body bound state can be realized even when $a_s < 0$ [61]. Fig. 2.4(b) and (c) show how q_0 varies as functions of δ and a_s. As one can see, as long as δ is non-zero, the dimer ground state possesses finite momentum. Furthermore, The magnitude of q_0 can reach as high as $0.2k_r$. Such a large value should be easily detected in experiment.

For a Zeeman field along the z-axis, we have $\mathbf{q}_0 = q_{2\mathrm{b}}\hat{z}$. Following the above-mentioned protocol, we summarize the "phase diagram" of $q_{2\mathrm{b}}$ as a function of the SO coupling strength and the Zeeman field strength h in Fig. 2.5. As one would expect, the Zeeman field tends to destroy the two-body bound state; whereas SO coupling enhances its formation. The competition between these two outlines the critical boundary value, beyond which ϵ_b becomes negative and no stable bound state can be found. With increasing h, the minimum of $E_{\mathbf{q}}$ deviates further away from zero momentum to some finite value. As long as Zeeman field is *non-zero*, the lowest-energy bound state would occur at *finite* center-of-mass momentum $q_{2\mathrm{b}}$. Our calculation shows that the magnitude of $q_{2\mathrm{b}}$ can be as high as $0.2k_F$.

Finally, for the sake of completeness, we comment on the case of Rashba SOC with $\mathbf{v} = (v_x, v_y, 0)$ and $v_x = v_y = \hbar^2 k_r/m$. In this case, when an in-plane Zeeman field (i.e., with a component in the x-y plane) is present, the resulting dimer bound state will again have finite momentum. A plot similar to Fig. 2.4 can be obtained. Our calculation shows that the maximum q_0 can be reached is about $0.05k_r$.

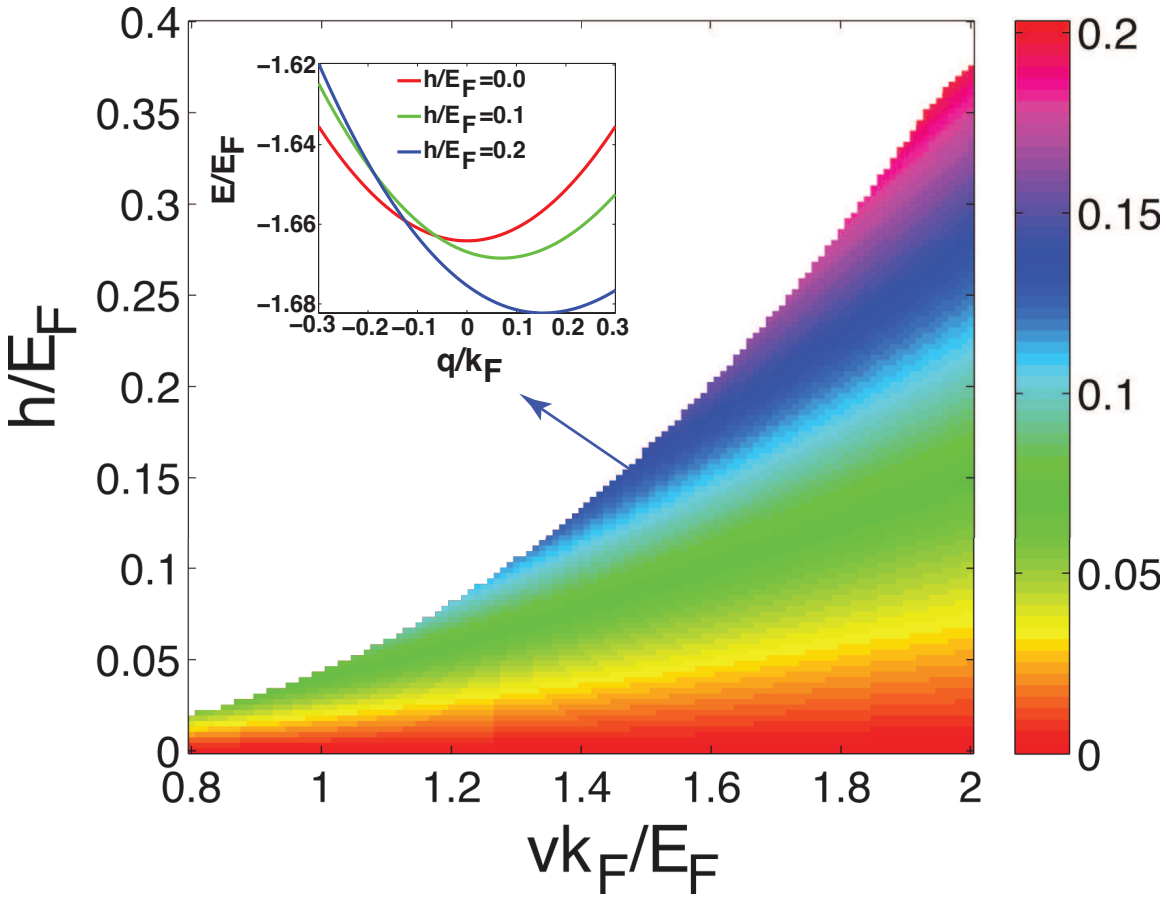

Figure 2.5 : Finite momentum dimer bound state solution for 3DSOC. The coloring shows the magnitude of q_{2b}, varying with the SO coupling strength v and the Zeeman field strength h; the inset shows bound state energy $E_{\mathbf{q}}$ as a function of q/k_F (along the z-axis) for different h, from top to bottom $h/E_F = 0, 0.1, 0.2$. We fix scattering length as $1/(k_F a_s) = -1$

2.3 Summary

In summary, we have studied a single-particle Hamiltonian for a non-interacting homogeneous Fermi gas in three dimensions, subjected to synthetic spin-orbit coupling. We have shown that (a) a single particle in the ground state has exactly zero mechanical momentum in the lab frame, even though its canonical momentum k_0 depends explicitly on the strengths of the SOC λ, and the Zeeman fields h and δ. (b) The total mechanical momentum for the non-interacting Fermi Sea adds up to exactly zero as well. (c) Two fermions, via s-wave scattering, may form a dimer bound state with *finite* center-of-mass mechanical momentum, under proper configuration of SO coupling and Zeeman field. We attribute this peculiar phenomenon to the broken Galilean invariance induced by the SO coupling and special role played by the Zeeman field. We have directly solved the two-body Schrödinger equation in the general formalism, and considered the momentum distribution in the laboratory frame for the experimentally realized system, where finite but relatively small bound state momentum q_0 is found. Finally, we demonstrate that the recently proposed system with spherical SOC [59,60] can result in dimer bound state with up to 20% of the recoil momentum. Note that, for bosons, previous studies have shown in the presence of SOC, the ground state is either plane wave phase or standing wave phase [62–64]. However, in contrast to our work, such states possess exactly *zero* mechanical momentum.

Motivated by the results from single-particle and two-body physics with synthetic coupling and effective Zeeman field, one is naturally tempted to explore the direct analog for the many-body system. Conceptually, at Fermi surface of equal momentum magnitude, not all fermions can find partners to pair with, which thus leads to exotic finite center-of-mass momentum pairing state.

Chapter 3

Superfluid Pairing and Topological Order

A central theme of fundamental physical science has been the search for building blocks of matter. In the 19th century, material compositions as elements were such an example. In the 20th century, the search for elementary particles dominated the field of high energy physics. However, understanding how atoms and electrons as building blocks were put together and form many different states of quantum materials, such as solids, magnets, superconductors, *etc.*, took tremendous efforts of condensed matter physicists for several decades. The discovery and classification of distinctive phases of matter, in the last century, can be often understood by Landau's approach of the principle of spontaneous symmetry breaking. In other words, quantum states of matter possess different underlying symmetries that are spontaneously broken. For example, translation symmetry is broken for crystalline solids, rotation symmetry is broken for magnets, and gauge symmetry is broken for superconductors, *etc.* Spontaneous symmetry breaking leads to a unique order parameter, which is essential for formulating an effective field theory, the well-celebrated Landau-Ginzburg theory [65].

In particular, the nature and the microscopic origin of fermionic pairing was first elucidated in the pioneering work by Bardeen, Cooper, and Schrieffer, widely known as the BCS theory [66]. The attractive pairwise interaction between electrons with opposite spin, albeit extremely weak, can give rise to an instability in a normal electron gas towards the formation of zero-momentum Cooper pairs near Fermi surface,

and because of pair condensation, ordering of conduction electrons emerge naturally. When subjected to an external Zeeman field, the population balance between electrons with different spins may be broken. As a consequence, not all electrons can find a partner to pair up with. If spin-population imbalance is large enough, the pairing of fermions has to occur at finite center-of-mass momentum with a deformed Fermi surface state [67]. This exotic possibility of inhomogeneous superfluid was first predicted by Fulde and Ferrell (FF) [68], and by Larkin and Ovchinnikov (LO) [69] a little later. FF refers to an order parameter with plane-wave form $\Delta(\mathbf{r}) = \Delta_0 e^{i\mathbf{q}\cdot\mathbf{r}}$, which spontaneously breaks time-reversal symmetry; while LO considers the superfluid with a standing-wave order parameter $\Delta(\mathbf{r}) = \Delta_0 \cos(\mathbf{q}\cdot\mathbf{r})$, which explicitly breaks translational symmetry. Both phases have puzzled the solid-state community for decades in terms of unambiguous experimental evidence to prove their existence. Moreover, the FFLO state is also of interest in quantum chromodynamics at low temperature and high density, where the property of asymptotic freedom may favor color superconductivity [70].

In Section 3.1, we apply the functional path integral treatment of the many-body physics for a Fermi gas subjected to an isotropic three-dimensional SO coupling (3DSOC) and an effective Zeeman field. The generation of such 3DSOC has been recently proposed by optically dressing four internal atomic states with a tetrahedral geometry [59, 60]. This version of the SO coupling is less explored and unfamiliar to the condensed matter community, where 2D Rashba and Dresselhaus SO couplings are studied extensively. One important advantage of 3DSOC over lower-dimensional SO interaction is that it provides the greatest enhancement of fermionic pairing [71]. Furthermore, due to its isotropic nature, mathematical simplicity is ensured. The bound states formed by two fermions subject to SOC have been studied rather inten-

sively [53, 54, 72–76]. However, in previous studies, the interplay between the SOC and the Zeeman field has not been thoroughly investigated. We show in the present work that, in the absence of two-body interaction, such a system exhibits zero total momentum. By contrast, in the presence of attractive s-wave interaction and with a proper combination of the SOC and the Zeeman field, the system may form a dimer bound state with *finite* center-of-mass mechanical momentum. At first sight, this result is very surprising since the s-wave interaction is manifestly momentum-conserving. A closer examination will reveal that this is a natural consequence of the broken Galilean invariance due to the presence of the SOC [56–58]. In principle, this finite-momentum dimer state can be realized in the current experimental system with equal-weight combination of Rashba and Dresselhaus SOC. The momentum of the bound state can be measured through standard time-of-flight techniques. In other words, under arbitrarily weak Zeeman field, zero-momentum dimer state and conventional BCS superfluid phase are no longer stable. For a many-body system, the FF state is inherently robust, and ultimately connects to the normal phase in a smooth manner as the Zeeman field strength is increased. Moreover, this type of exotic superfluid has a different origin in comparison with the previously studied FFLO state. In the absence of the SO coupling, individual particle number with different spins is conserved, hence the imbalance induced finite-momentum pairing has parity symmetry between $\mathbf{q}$ and $-\mathbf{q}$, which should be called LO phase by definition; on the other hand, in the presence of the SO coupling, the Zeeman field breaks time-reversal symmetry explicitly and cause the single-particle dispersion to be asymmetric, which underlines the idea of finite-momentum dimer bound states [71] and the FF pairing instability. The center-of-mass momentum of the Cooper pair can be as large as the Fermi momentum. This result should be very encouraging for future experimental

exploration.

The above understanding of phases and phase transitions are governed by Landau's symmetry breaking theory, where different phases are associated with different symmetries and characterized by different order parameters. This approach was widely accepted and believed to give a universal description of the quantum state of matter.

It was only until the discovery of the quantum Hall (QH) state [77], that a new framework of theoretical description was invented. The QH state does not spontaneously break any symmetry as other ground states do, but rather is topologically distinct from the rest. Fundamental properties such as the quantized value of the Hall conductance and the number of gapless modes are independent of material details [78, 79] and remain unchanged by smooth deformations of the material parameters, unless a quantum phase transition occurs.

The theory and experimental realization of topological insulators (TI) is an emerging field that led to numerous discoveries in material physics and future applications of quantum computation. More specifically, TI is insulating in the bulk whose bulk energy gap separates the highest occupied electronic band from the lowest empty band, but the unidirectional flow of electric current is dissipationless which is due to gapless edge states that are protected by time-reversal symmetry. These protected gapless edge states are known as Majorana fermions – exotic quantum particles that act as their own antiparticles and obey non-abelian braiding statistics. Their realizations are believed to lie at the heart of future technologies such as fault-tolerant quantum computers. Roughly speaking, Majorana fermions constitute "half" of an ordinary Dirac fermion, in the sense that two real Majorana fermions γ_1 and γ_2 - which can be separated in arbitrary distance - mathematically define a complex

fermion operator $c = \gamma_1 + i\gamma_2$ [80]. The exchange statistics of Majorana fermions is exotic. Unlike conventional bosons and fermions, braiding Majorana fermions around one another in a 2^N-dimensional Hilbert space (spanned by $2N$ well-separated Majorana fermions) produces non-Abelian unitary transformations in the Hilbert space. Quantum information can then be non-locally encoded in the Hilbert space by such braiding operators and be immune to decoherence, which is ideal for the purpose of quantum computation [81].

In the Section 3.2, we will consider this kind of quantum state characterization using topological orders, which is completely beyond the symmetry breaking paradigm.

3.1 Mean Field Many-Body Physics with Pairing Instability

Motivated by the two-body results, one naturally attempts to explore the direct analog for the many-body system, which we study in this section.

We start by formulating the Hamiltonian for a non-interacting homogeneous spin-1/2 Fermi gas in 3D using field theories:

$$\mathcal{H}_0 = \int d\mathbf{r}\, \psi^\dagger(\mathbf{r})\{\xi_{\mathbf{k}} + \sum_{i=x,y,z} (\lambda_i k_i + \Lambda_i)\, \sigma_i\}\psi(\mathbf{r}) \tag{3.1}$$

where $\xi_{\mathbf{k}} = \hbar^2\hat{\mathbf{k}}^2/(2m) - \mu$ and $\psi = [\psi_\uparrow(\mathbf{r}), \psi_\downarrow(\mathbf{r})]^T$ is the fermionic annihilation field operator. We have defined the general form of SO coupling strength vector $\lambda = (\lambda_x, \lambda_y, \lambda_z)$ as in previous sections, and the Zeeman field vector $\mathbf{\Lambda} = (\Lambda_x, \Lambda_y, \Lambda_z)$. $\boldsymbol{\sigma} = (\sigma_x, \sigma_y, \sigma_z)$ are Pauli matrices acting on the atomic (pseudo-)spin degrees of freedom. This description is a general model valid for various SO coupling schemes. The single-particle spectrum is given by $E^\gamma(\mathbf{k}) = \frac{\hbar^2\mathbf{k}^2}{2m} + \gamma\sqrt{\sum_i(\lambda_i k_i + \Lambda_i)^2}$ with $\gamma = \pm 1$ denoting the two helicity branches. In this section, we will focus on the 3DSOC [59, 60] with $\lambda_x = \lambda_y = \lambda_z = \lambda$. For this case, due to the isotropic nature

of the SO coupling term, the direction of the Zeeman field is irrelevant and we shall choose it to be along the x-axis, and hence $\mathbf{\Lambda} = (h,\, 0,\, 0)$.

It is important to note that the Zeeman field induces an asymmetry in the single-particle dispersion relation. To illustrate this, we consider a filled Fermi sea with simple topology (cf. [82]) at zero temperature. In Fig. 3.1, we plot the Fermi surface without and with Zeeman field. In the absence of the Zeeman field, the Fermi surfaces for both helicity branches are represented by spheres centered at zero momentum, as shown in Fig. 3.1(a). When we turn on the Zeeman field, both Fermi surfaces are distorted and no longer possess reflection symmetry about the $k_x = 0$ plane, as can be clearly seen in Fig. 3.1(b). From this perspective, the ground state of the single particle Hamiltonian is associated with nonzero total momentum along the k_x-axis.

However, we emphasize here that the nonzero total momentum refers to the canonical momentum after gauge transformation, which is different from the experimentally measurable mechanical momentum in the lab frame. The latter, for both the single-particle ground state and the non-interacting Fermi sea, as we have discussed in the Section 2.1.1, is exactly zero.

Next we consider the attractive s-wave contact interaction between un-like spins which, in terms of the creation and annihilation field operators for the original spin states, is represented by

$$\mathcal{H}_{\text{int}} = U_0 \int d\mathbf{r}\, \psi_{\uparrow}^{\dagger}(\mathbf{r})\psi_{\downarrow}^{\dagger}(\mathbf{r})\psi_{\downarrow}(\mathbf{r})\psi_{\uparrow}(\mathbf{r}) \tag{3.2}$$

where U_0 is the bare coupling strength to be renormalized using the s-wave scattering length a_s. In this work, we constrain our attention to the experimentally exploited broad Feshbach resonances, which is well captured by the single-channel Hamiltonian prescribed above.

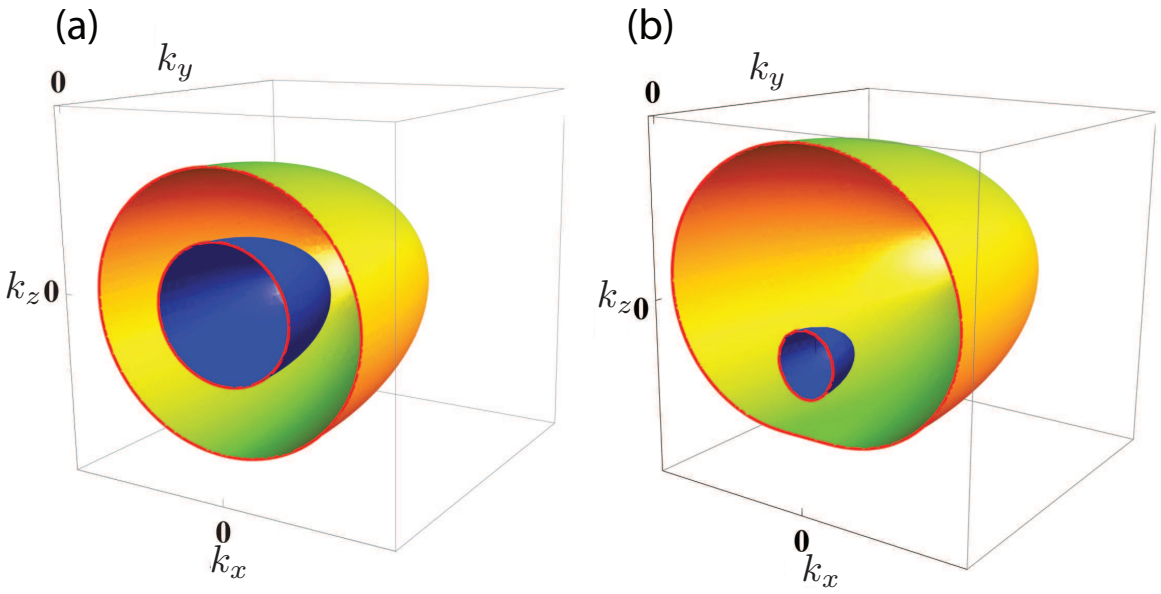

Figure 3.1 : (a) Fermi surfaces (a cut in the $k_y = 0$ plane) in the absence of the Zeeman field. The two concentric Fermi surfaces are spherically symmetric. The inner blue sphere represents the Fermi surface of the + helicity branch, while the outer yellow sphere of the − helicity branch. (b) Fermi surfaces in the presence of the Zeeman field along the x-axis: both Fermi surfaces are deformed in such a way that the cylindrical symmetry about the k_x-axis is still preserved, but the reflection symmetry about the $k_x = 0$ plane is broken.

Here, we outline the functional path integral technique [83–85] and start from the partition function $\mathcal{Z} = \int \mathcal{D}[\psi(\mathbf{r},\tau),\bar{\psi}(\mathbf{r},\tau)] \exp\left\{-S\left[\psi(\mathbf{r},\tau),\bar{\psi}(\mathbf{r},\tau)\right]\right\}$ where the action

$$S\left[\psi,\bar{\psi}\right] = \int_0^\beta d\tau \left[\int d\mathbf{r} \sum_\sigma \bar{\psi}_\sigma(\mathbf{r},\tau)\,\partial_\tau \psi_\sigma(\mathbf{r},\tau) + \mathcal{H}\left(\psi,\bar{\psi}\right)\right] \tag{3.3}$$

is written as an integral over imaginary time τ. Here $\beta = 1/(k_B T)$ is the inverse temperature and $\mathcal{H}\left(\psi,\bar{\psi}\right)$ is obtained by replacing field operators $\psi^\dagger$ and ψ with grassmann variables $\bar{\psi}$ and ψ, respectively. We can integrate out the quartic interaction term using the Hubbard-Stratonovich transformation [85], from which the pairing field $\Delta(\mathbf{r},\tau)$ is defined.

If we assume the mean-field order parameter to be of FF-type $\Delta = \Delta_0 e^{i\mathbf{q}\cdot\mathbf{r}}$, and further integrate out the fermionic fields, we arrive at an effective action as

$$S_{\text{eff}} = \int_0^\beta d\tau \int d\mathbf{r}(-\frac{|\Delta|^2}{U_0}) - \frac{1}{2}\mathrm{Tr}\log[-\mathcal{G}_\Delta^{-1}] + \beta \sum_{\mathbf{k}} \frac{\xi_{\mathbf{k}+\mathbf{q}/2} + \xi_{-\mathbf{k}+\mathbf{q}/2}}{2}, \tag{3.4}$$

$$\mathcal{G}_\Delta^{-1}(\mathbf{k}, i\omega_m) = \begin{bmatrix} i\omega_m - \xi_{\mathbf{k}+\mathbf{q}/2} - f_+ & i\Delta_0\hat{\sigma}_y \\ -i\Delta_0\hat{\sigma}_y & i\omega_m + \xi_{\mathbf{k}-\mathbf{q}/2} - f_- \end{bmatrix} \tag{3.5}$$

where $f_\pm = \sum_i \left(\lambda_i(k_i \pm \frac{q_i}{2}) \pm \Lambda_i\right)\sigma_i$. In the second term of Eq. (3.4), the trace is to be taken over the Nambu spinor space $\Phi(\mathbf{r},\tau) \equiv [\psi_\uparrow, \psi_\downarrow, \bar{\psi}_\uparrow, \bar{\psi}_\downarrow]^T$, the real coordinate space and imaginary time. The last term in Eq. (3.4) comes from interchanging fermionic fields $\bar{\psi}_\uparrow$ and $\bar{\psi}_\downarrow$with $\psi_\uparrow$ and $\psi_\downarrow$ and the corresponding equal-time limiting procedure [85]. From Eq. (3.4), we can further sum over Matsubara frequencies to arrive at the grand thermodynamic potential:

$$\begin{aligned} \frac{\Omega}{V} &= -\frac{1}{\beta}\ln\mathcal{Z} = -\frac{|\Delta|^2 m}{4\pi\hbar^2 a_s} + \frac{1}{V}\sum_{\mathbf{k}} \left[\frac{\xi_{\mathbf{k}+\mathbf{q}/2} + \xi_{-\mathbf{k}+\mathbf{q}/2}}{2} - \frac{1}{4}\sum_{\alpha=1}^{4} |E_{\mathbf{k}}^\alpha| \right. \\ &\left. + \frac{|\Delta|^2}{2\epsilon_{\mathbf{k}}} - \frac{1}{2\beta}\sum_{\alpha=1}^{4} \ln\left(1 + \exp(-\beta|E_{\mathbf{k}}^\alpha|)\right)\right] \end{aligned} \tag{3.6}$$

where we have regularized the bare interaction strength U_0 in terms of the s-wave scattering length a_s by $\frac{1}{U_0} = \frac{m}{4\pi\hbar^2 a_s} - \frac{1}{V}\sum_{\mathbf{k}} \frac{1}{2\epsilon_{\mathbf{k}}}$. $E^{\alpha}_{\mathbf{k}}$ ($\alpha = 1, 2, 3, 4$) are the quasi-particle energy dispersion, which are just the four eigenvalues obtained by solving $\det[\mathcal{G}^{-1}_{\Delta}(\mathbf{k}, E^{\alpha}_{\mathbf{k}})] = 0$. In our case, $E^{\alpha}_{\mathbf{k}}$ are too complicated to be presented here.

We take a canonical ensemble approach by considering a homogeneous system with fixed particle number N and volume λ, and hence the density $n = N/V = k_F^3/(3\pi^2)$. The important quantity that determines the mean field phase diagram shall be the free energy, also known as the Landau potential, defined as $F = \Omega + \mu N$. At zero temperature, it coincides with the ground state energy. For a given set of parameters (including SO coupling strength λ, Zeeman field strength h, interaction parameter $1/(k_F a_s)$, and temperature T), order parameter Δ, chemical potential μ, and the FF momentum $\mathbf{q} = q_{\mathrm{FF}}\,\hat{x}$ should be determined self-consistently by stationary conditions

$$\frac{\partial F}{\partial \Delta} = 0, \quad \frac{\partial F}{\partial \mu} = 0, \quad \frac{\partial F}{\partial q} = 0. \tag{3.7}$$

We shall explicitly consider three types of phase: normal gas ($\Delta = 0$, $q = 0$), BCS state ($\Delta \neq 0$, $q = 0$), and FF state ($\Delta \neq 0$, $q_{\mathrm{FF}} \neq 0$).

3.1.1 Zero-temperature phase diagram on the BCS side

We shall first focus on a relatively weak-interacting regime on the BCS side of the crossover and take $1/(k_F a_s) = -1$. In this regime, we can easily justify the mean-field treatment at both zero and finite temperature, and furthermore the SO coupling effect would be more pronounced [53, 73, 86, 87].

To get some insight first, in Fig. 3.2, we plot the free energy as a function of h for a given SO coupling strength $\lambda = E_F/k_F$. (We choose this relatively large SO strength, to avoid possible complications, e.g. Sarma phase [88], phase separation [89] etc.) It

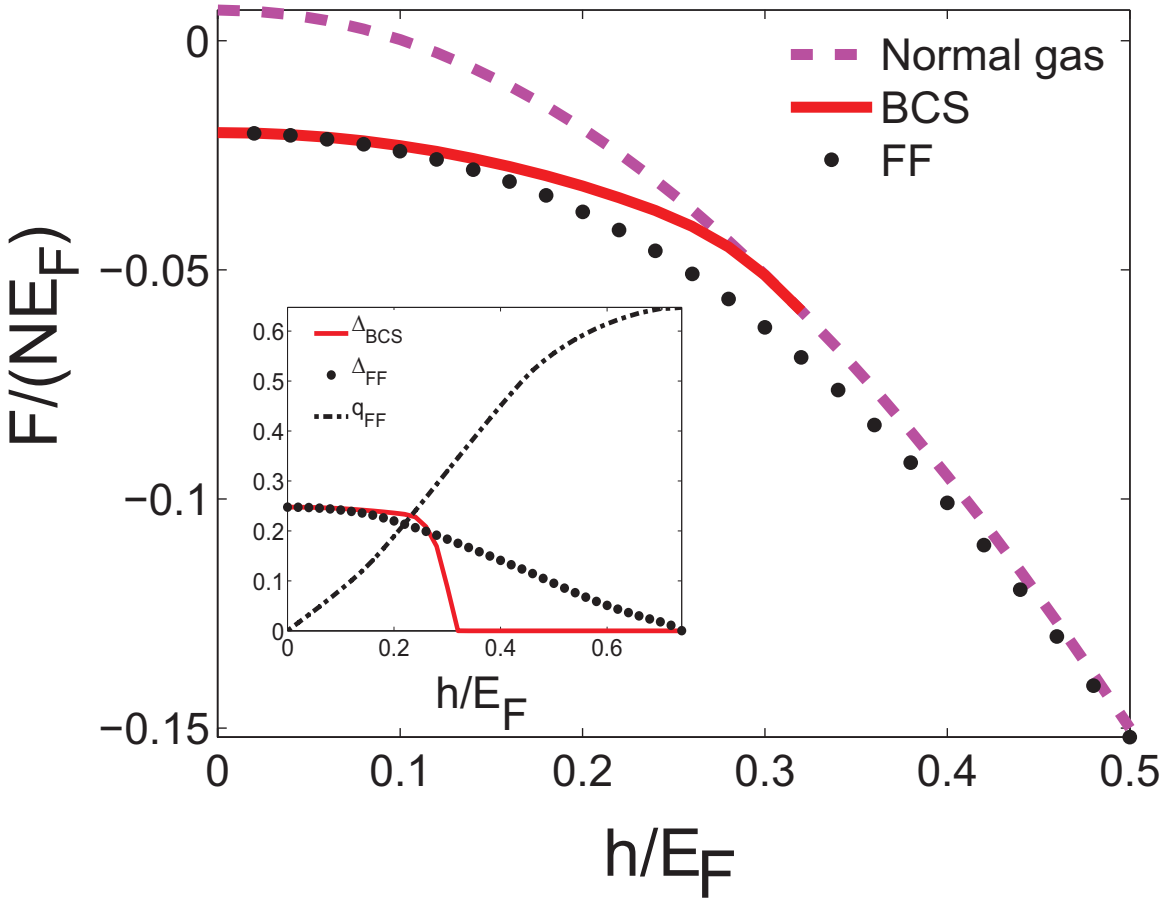

Figure 3.2 : Zero temperature free energy as a function of h for fixed SO coupling strength $\lambda = E_F/k_F$ and interaction strength $1/k_F a_s = -1$. FF superfluid phase is favored throughout the plotted parameter space. In the inset, we plot the BCS order parameter $\Delta_{\rm BCS}$, the FF order parameter $\Delta_{\rm FF}$ (both in units of E_F), and the FF momentum $q_{\rm FF}$ (in units of k_F) as functions of h. Note that we have explicitly excluded the consideration of the so-called LO phase, because of the fact that h has explicitly broken the symmetry in momentum space. One particular direction of quasi-momentum is always favored for a given h value. Consequently, LO phase is guaranteed to give rise to higher free energy state.

is very remarkable to notice that the FF state is energetically favored for arbitrarily small h. For instance, at $h = 0.02E_F$, the gain of energy over the BCS pairing phase is $\Delta F = F_{\rm BCS} - F_{\rm FF} \approx 4.54588 \times 10^{-5} N E_F$. However, this energy gain quickly increases as h is increased. For example, at $h = 0.28E_F$, we have $\Delta F = 1.13728 \times 10^{-2} N E_F$ which is more than two orders of magnitude larger and represents a very large energy value on the BCS side of Feshbach resonance. Once again, the idea of favoring the FF phase is backed by the picture of the Fermi surface deformation (cf. Fig. 3.1) and the two-body bound state solutions [Eq. (2.26) and Fig. 2.5]. When we further increase h, the BCS superfluid is taken over by normal phase as the BCS order parameter drops to zero rather sharply (see the inset of Fig. 3.2); on the other hand, the FF state connects to normal phase very smoothly at a much larger value of h.

The FF state here has different origin with the conventional FFLO states in the absence of the SO coupling [90–92], in which case, for a given interaction strength and with increasing population imbalance (i.e., Zeeman field), one would expect that competitions among various quantum phases (BCS, Sarma, FFLO, and normal phases) could lead to both first- and second-order phase transitions. By contrast in the presence of SO coupling, especially 3DSOC, the FF state dominates almost the entire phase diagram, as we map out in the λ-h plane Fig. 3.3(a). The BCS phase only exists on the axis (i.e., in the absence of either the Zeeman field or the SO coupling). The normal phase and the FF phase are connected by a smooth boundary, which we identify by setting a threshold value of energy difference $|F_{\rm FF} - F_{\rm normal}| \approx 10^{-5} N E_F$. Note that close to the boundary, $\Delta_{\rm FF}$ also becomes exceedingly small. For illustration purposes, we schematically added two small regions near $\lambda = 0$, the LO (green) and the phase separation (blue) regions, in the phase diagram. The boundaries of these two phases in the absence of the SO coupling (i.e., at $\lambda = 0$), which are well studied,

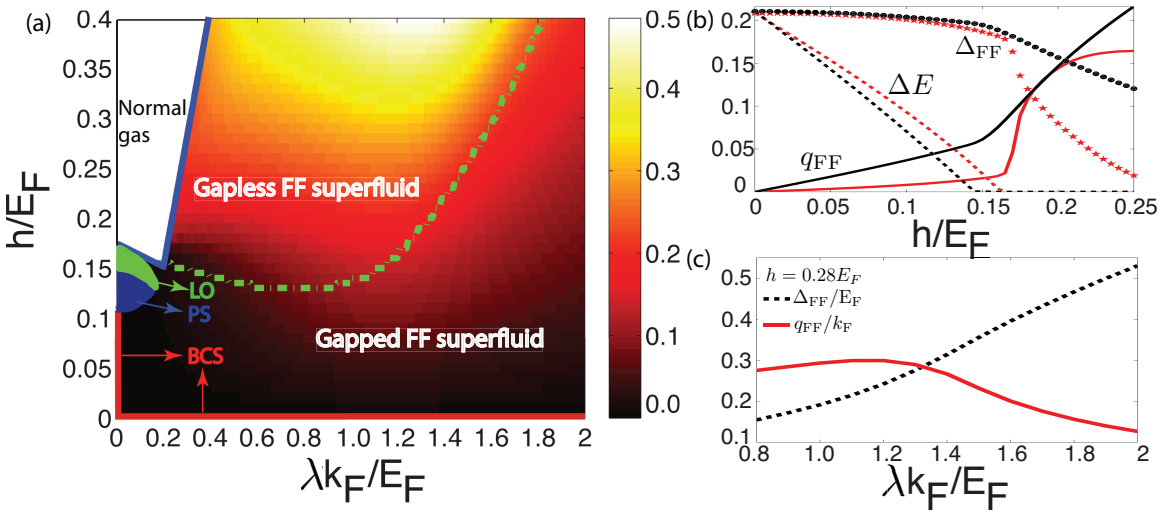

Figure 3.3 : (a) Zero-temperature phase diagram at $1/k_F a_s = -1$ in the parameter space spanned by h and λ. The FF phase is divided into gapped and gapless regions by the green dashed line. The BCS state only exists strictly on the axis marked by two red straight lines. The two blue lines indicate the smooth boundary between the FF state and the normal phase. Within the FF phase, the color scale indicates the momentum $q_{\rm FF}$. LO and phase separation (PS) regions are added schematically for illustration purpose. (b) Single-particle excitation gap ΔE, FF order parameter $\Delta_{\rm FF}$ and momentum $q_{\rm FF}$ as functions of h. The SO coupling strengths are $\lambda = 0.2E_F/k_F$ (red curves) and $0.5E_F/k_F$ (black curves). (c) $\Delta_{\rm FF}$ and $q_{\rm FF}$ as functions of λ for $h = 0.28E_F$. In all plots, the energy is in units of E_F, and the momentum in units of k_F.

are obtained from previous results [88,89,93]. It has been shown that, with increasing SO coupling strength, both these phases are suppressed rather rapidly [93].

Furthermore, in Fig. 3.3(a), the FF phase is divided into the gapped and the gapless regions by examining the single-particle excitation gap $\Delta E = \min\{|E^{\alpha}_{\mathbf{k}}|\}$, where $E^{\alpha}_{\mathbf{k}}$ are quasi-particle dispersions introduced in Eq. (3.6). As shown in Fig. 3.3(b), ΔE decreases monotonically as a function of h and drops to zero at some critical value of h_c which depends on the SO coupling strength λ. The critical value h_c is represented by the green dashed line in Fig. 3.3(a). At h_c, both $q_{\rm FF}$ and $\Delta_{\rm FF}$ exhibit kinks for relatively small SO coupling strength. These kinks get washed out quickly with increasing λ (see, for instance, the inset of Fig. 3.2). On the other hand, in the limit of $\lambda = 0$, these kinks become true jumps signaling the first-order phase transition between the BCS phase and the FF phase region. In Fig. 3.3(c), we plot $q_{\rm FF}$ and $\Delta_{\rm FF}$ as functions of λ for a fixed h. We note that even though $\Delta_{\rm FF}$ increases monotonically as λ, the FF momentum $q_{\rm FF}$ shows non-monotonic behavior: it first increases and then decreases as λ is increased from zero.

It is instructive to make comparisons between the two-body results and the many-body results. To this end, we consider a cloud of degenerate Fermi gas typically realized in experiment, with density $n = 10^{12}\text{cm}^{-3}$ which defines k_F and E_F. We compare the two-body dimer momentum $q_{\rm 2b}$ with the many-body FF pairing momentum $q_{\rm FF}$ in Fig. 3.4 at two different values of SO coupling strengths. Note that the range of h values for which the two-body bound state exists is much smaller than that for the existence of the FF state. For example, at $\lambda = 1.3E_F/k_F$, two-body bound states only exist for $h < 0.1E_F$; while the FF state extends all the way up to about $h \approx E_F$. As such, the largest $q_{\rm FF}$ that can be achieved is much larger than the largest $q_{\rm 2b}$. In the region where both two-body bound state and the FF state exist, $q_{\rm FF}$ and $q_{\rm 2b}$ are

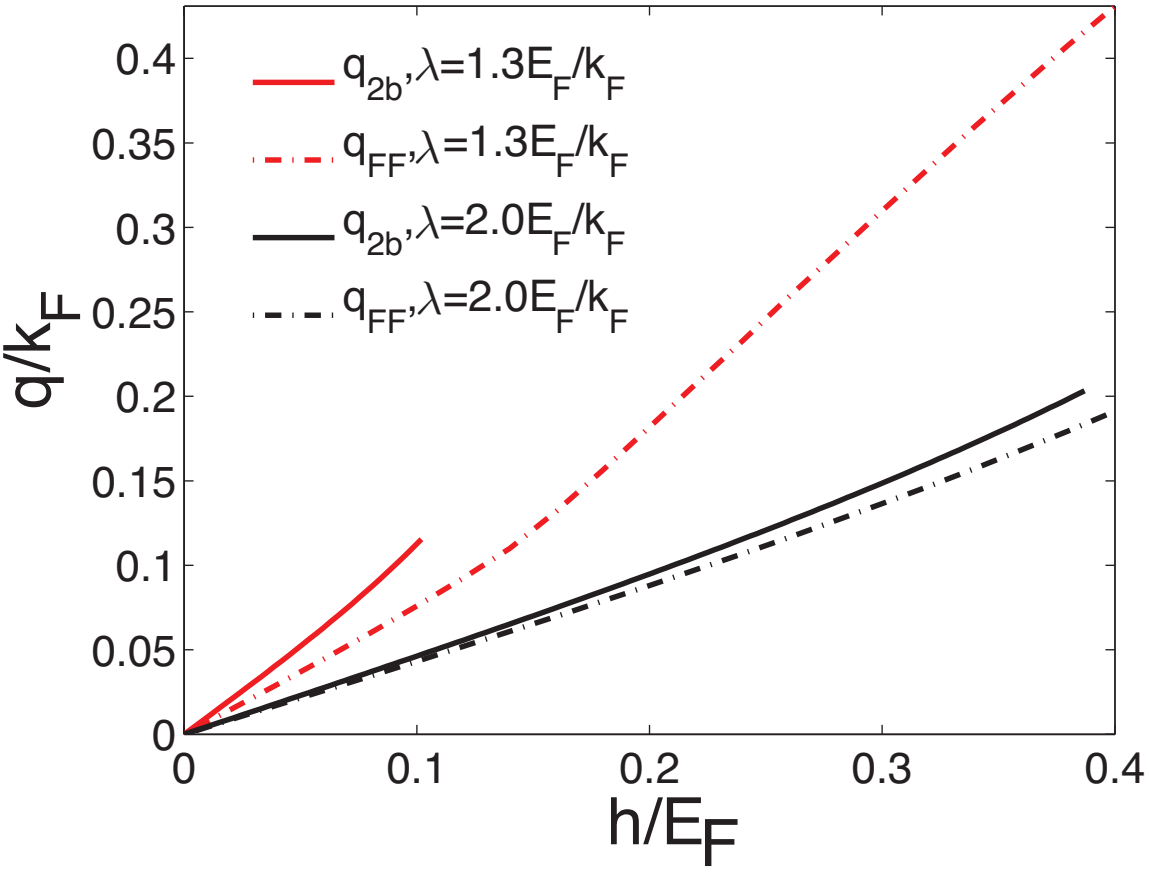

Figure 3.4 : Momentum comparison of the FF state and two-body bound state at $1/k_F a_s = -1$.

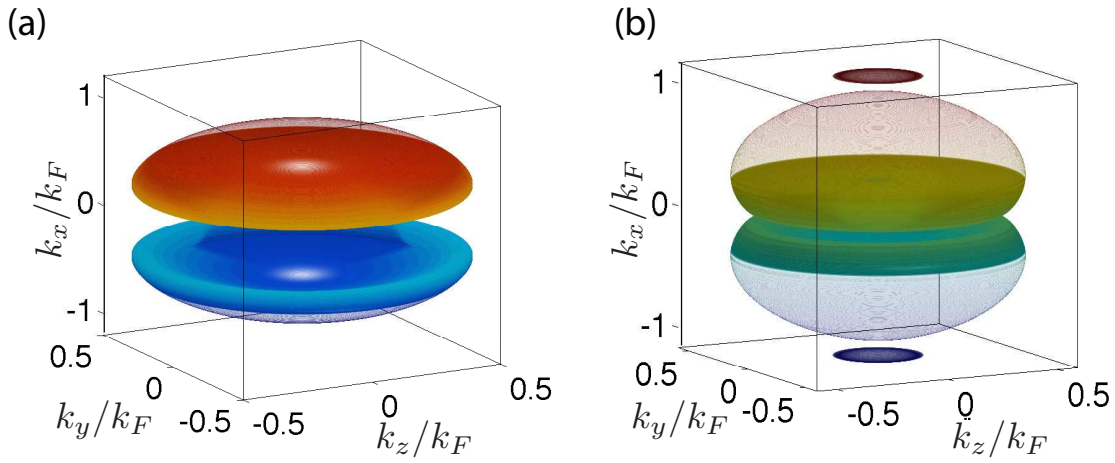

Figure 3.5 : Nodal Fermi surface plots in momentum space. The closed surfaces are formed by momentum values at which the excitation gap ΔE vanishes. Both figures have the same interaction parameter $1/k_F a_s = -1$ as in phase diagram Fig. 3.2 and coupling strength $\lambda = 0.5E_F/k_F$, while $h = 0.2E_F$ for (a) and $h = 0.35E_F$ for (b).

comparable, with the latter somewhat larger. The difference between them, however, becomes smaller as the SO coupling strength increases, indicating that at large SO coupling strength, the many-body properties of the system are also dominated by the two-body physics.

Before ending this subsection, we want to remark on the gapless FF state. For Zeeman field strength above the critical value h_c, one or more quasi-particle energy $E^{\alpha}_{\mathbf{k}}$ will vanish at certain values of momentum $\mathbf{k}$. Such momenta form closed surfaces (nodal Fermi surface) in momentum space with cylindrical symmetry around the k_x-axis and reflection symmetry about the $k_x = 0$ plane. Hence such nodal Fermi surfaces always appear in pairs and may be measured using the technique of momentum-resolved radio-frequency spectroscopy. Two examples are illustrated in Fig. 3.5.

3.1.2 Effects of interaction

So far we have focused on the zero-temperature phase diagram of a weakly-interacting system. Now we briefly discuss the effects of interaction in this subsection and those of finite temperature in the next. In Fig. 3.6(a) and (b), we present two zero-temperature phase diagrams in the h-λ plane for $1/k_F a_s = -2$ and 0, respectively. They are qualitatively similar to the one presented in Fig. 3.3(a) for $1/k_F a_s = -1$. As we move from the BCS limit towards unitarity, the region of normal phase shrinks and the FF superfluid remains dominant. Furthermore, the region for gapped FF phase increases quickly. At unitarity, the whole parameter space presented in Fig. 3.6(b) are occupied by the gapped FF phase. On the other hand, for fixed h and λ, the FF momentum $q_{\rm FF}$ quickly decreases as we go from the BCS side to the BEC side, as shown in Fig. 3.6(c). This result is consistent with the one obtained from the two-body study [71, 94].

3.1.3 Effects of temperature

Finally, we consider the effects of finite temperature. In Fig. 3.7(a), we plot the phase diagram in the parameter space spanned by h and T by taking $1/(k_F a_s) = -1$ and $\lambda = E_F/k_F$. The FF superfluid phase dominates at small h and low T. There is a second order transition towards the normal phase as h and/or T increases. The BCS phase again only lives on the $h = 0$ axis. In Fig. 3.7(b), we compare the free energies for all three phases at $T = 0.1T_F$ and clearly show that the FF phase possesses the lowest free energy at any finite values of h as long as h is below a threshold at which the system turns normal.

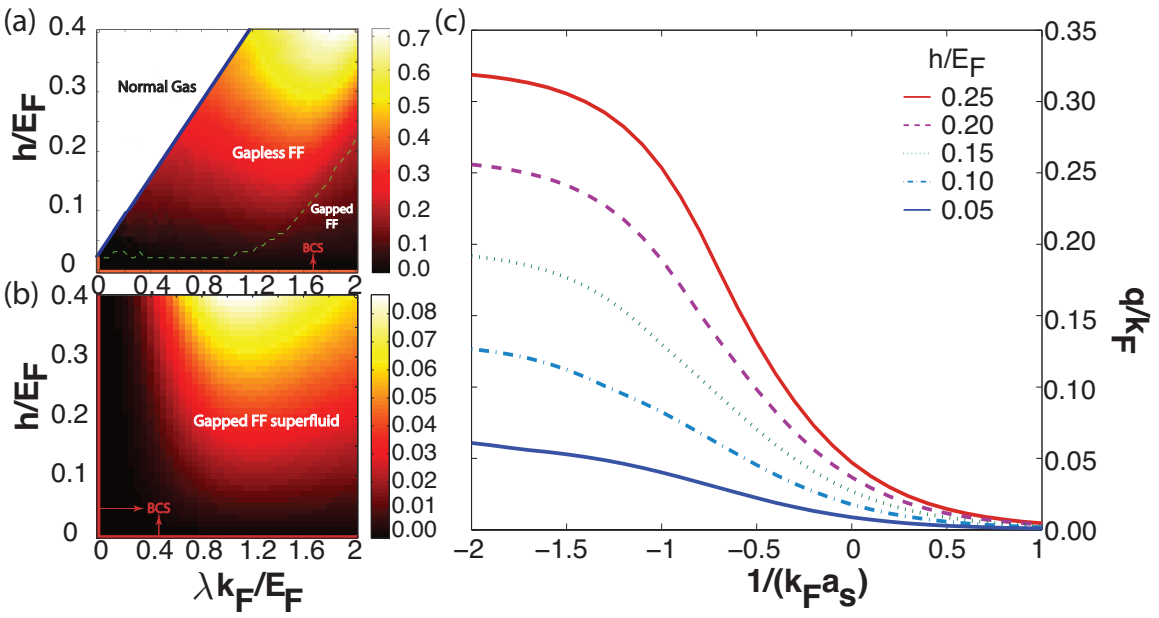

Figure 3.6 : Zero temperature phase diagram with interaction strength $1/k_F a_s = -2$ and $1/k_F a_s = 0$ for (a) and (b), respectively. The color scale represents $q_{\rm FF}/k_F$. (c) FF superfluid momentum $q_{\rm FF}$ as a function of the interaction strength. For curves from top to bottom, $h/E_F = 0.25,\ 0.2,\ 0.15,\ 0.1,\ 0.05$, and the SO coupling strength is fixed to be $\lambda = E_F/k_F$.

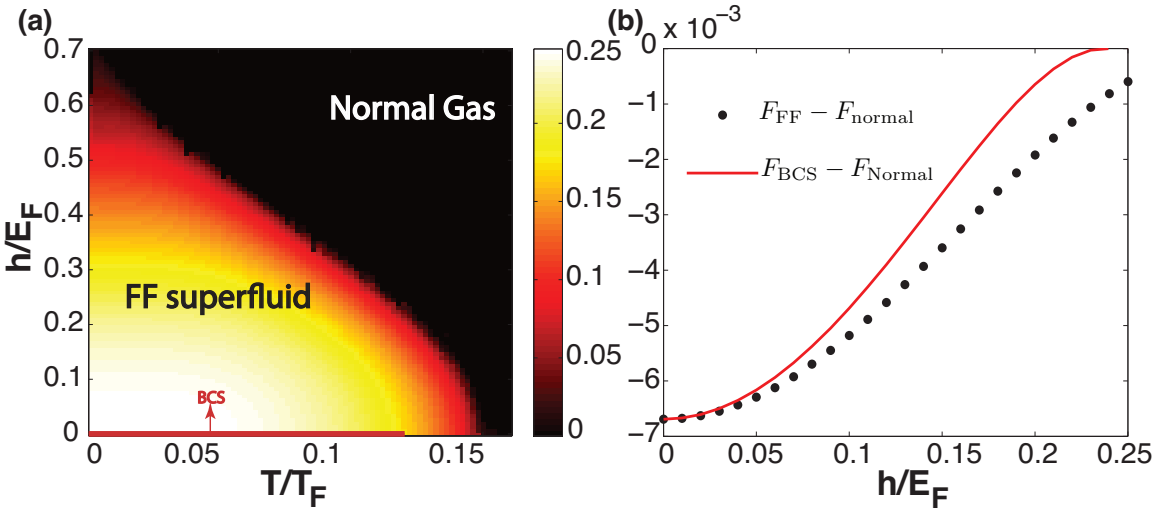

Figure 3.7 : (a) Finite temperature phase diagram at $1/k_F a_s = -1$ and $\lambda = E_F/k_F$. The color scale indicates the FF order parameter $\Delta_{\rm FF}$. (b) The free energy difference between the two superfluid phases (BCS and FF) and the normal phase at temperature $T = 0.1T_F$. The FF phase always has lowest free energy.

3.2 Gapless Topological FF Superfluids

In this Section, we study the topological classification of superfluid states whose symmetry classification properties have been discussed thoroughly in Section 3.1. We found that the gapless regime can be further categorized into topologically non-trivial phase and topologically trivial state. We note that the topologically non-trivial state discussed here is novel in the sense that it is different from other typical topological states that are protected by a non-zero gap energy in the bulk spectrum.

In Section 3.1, we introduced the functional path integral approach based on quantum field theory, and applied the formalism to tackle quantum many-body problems. It is a useful tool to derive systematic approximation schemes, such as introducing Gaussian fluctuations as second order expansion of the mean field operator or computing the effective inter-atomic interaction in terms of ladder diagrams, and often

leads to a much simpler derivation of some exact relations, such as relating two-body T-matrix and many-body T-matrix exactly. It is, however, fully equivalent to the operator formulation using second quantization in quantum mechanics. For our purpose in this Section, we use operator formalism to first of all reproduce the BdG Hamiltonian and introduce the Bogoliubov quasi-particles wavefunctions, which make it easier to compute quantities that are constructed by Bogoliubov quasi-particle wavefunctions, such as bulk topological number, or perform a basis expansion based on boundary conditions by taking into account of geometric properties. In this way, we can better understand the underlying topological properties and study in details the bulk-edge correspondences.

3.2.1 Mean-field Model Hamiltonian and Bogoliubov Theory

To start off, we focus on a 3D spin-orbit coupled two-component Fermi gas with an isotropic spin-orbit coupling $\lambda_{SO}(\hat{\mathbf{k}}) = \lambda(\hat{k}_x\sigma_x + \hat{k}_y\sigma_y + \hat{k}_z\sigma_z)$ subject to an in-plane Zeeman field $h\sigma_x$ [95–97], which can be described by the model Hamiltonian,

$$\mathcal{H} = \int d\mathbf{r} \left[\sum_{\sigma\sigma'} \psi_\sigma^\dagger(\mathbf{r}) H_0^{\sigma\sigma'} \psi_{\sigma'}(\mathbf{r}) + \mathcal{V}_{int} \right], \tag{3.8}$$

where $\psi_\sigma^\dagger(\mathbf{r})$ (ψ_σ) is the field operator for creating (annihilating) an atom with pseudo-spin state $\sigma \in (\uparrow, \downarrow)$ at position $\mathbf{r}$, $H_0 = -\hbar^2\nabla^2/(2m) - \mu + V_{SO}(\hat{\mathbf{k}}) + h\sigma_x$ is the single-particle Hamiltonian with the atomic mass m and chemical potential μ, $\hat{k}_{i=(x,y,z)} = -i\partial_i$ is the momentum operator and $\sigma_{x,y,z}$ are the Pauli matrices. $\mathcal{V}_{int} = U_0\psi_\uparrow^\dagger(\mathbf{r})\psi_\downarrow^\dagger(\mathbf{r})\psi_\downarrow(\mathbf{r})\psi_\uparrow(\mathbf{r})$ describes a pairwise attractive contact interaction of strength $U_0 < 0$, where $U_0^{-1} = m/(4\pi\hbar^2 a_s) - V^{-1}\sum_{\mathbf{k}} m/(\hbar^2\mathbf{k}^2)$ can be expressed in terms of the s-wave scattering length a_s. At the mean-field level, the model Hamiltonian can be solved by taking an order parameter $\Delta(\mathbf{r}) = -U_0\langle\psi_\downarrow(\mathbf{r})\psi_\uparrow(\mathbf{r})\rangle$ and linearizing the interaction Hamiltonian $\mathcal{V}_{int} \simeq -[\Delta(\mathbf{r})\psi_\uparrow^\dagger(\mathbf{r})\psi_\downarrow^\dagger(\mathbf{r}) + \text{H.c.}] - |\Delta(\mathbf{r})|^2/U_0$.

In the presence of an in-plane Zeeman field $h\sigma_x$, it is now widely understood that Cooper pairs acquire a finite centre-of-mass momentum $\mathbf{Q} = q\mathbf{e}_x$ along the x-direction, i.e., $\Delta(\mathbf{r}) = \Delta e^{iqx}$ [95, 98–101]. By using the Nambu spinor $\Phi(\mathbf{r}) \equiv [\psi_\uparrow e^{+iqx/2}, \psi_\downarrow e^{+iqx/2}, \psi_\uparrow^\dagger e^{-iqx/2}, \psi_\downarrow^\dagger e^{-iqx/2}]^T$ to gauge out the momentum related phase in the order parameter, the mean-field model Hamiltonian can be solved by diagonalizing the following Bogoliubov-de Gennes (BdG) Hamiltonian

$$\mathcal{H}_{BdG}(\hat{\mathbf{k}}) \equiv \begin{bmatrix} H_0\left(\frac{\mathbf{Q}}{2} + \hat{\mathbf{k}}\right) & -i\Delta\sigma_y \\ i\Delta\sigma_y & -H_0^*\left(\frac{\mathbf{Q}}{2} - \hat{\mathbf{k}}\right) \end{bmatrix}, \tag{3.9}$$

i.e., $\mathcal{H}_{BdG}\Phi^\nu_{\mathbf{k}\eta}(\mathbf{r}) = E_{\eta\nu}(\mathbf{k})\Phi^\nu_{\mathbf{k}\eta}(\mathbf{r})$, which gives rise to the wavefunction of Bogoliubov quasiparticles, $\Phi^\nu_{\mathbf{k}\eta}(\mathbf{r}) = 1/\sqrt{V}e^{i\mathbf{k}\cdot\mathbf{r}}[u^\nu_{\eta\uparrow}, u^\nu_{\eta\downarrow}, v^\nu_{\eta\uparrow}, v^\nu_{\eta\downarrow}]^T$, and the energy $E_{\eta\nu}(\mathbf{k})$. We obtain four quasi-particle energy dispersions, indexed by $\nu \in (+,-)$ for the particle $(+)$ or hole $(-)$ branch, and $\eta \in$(1,2) for the upper (1) or lower (2) helicity band split by spin-orbit coupling and Zeeman field.

Taking the mean-field approximation for the pairing interaction term, the model Hamiltonian of the Fermi system can be rewritten into a compact form,

$$\mathcal{H} = (1/2)\int d\mathbf{r}\Phi^\dagger(\mathbf{r})\mathcal{H}_{BdG}(\hat{\mathbf{k}})\Phi(\mathbf{r}) - V\Delta^2/U_0 + \sum_{\mathbf{k}}(\xi_{\mathbf{k}+\mathbf{Q}/2} + \xi_{\mathbf{k}-\mathbf{Q}/2})/2$$

where the explicit form of $\mathcal{H}_{BdG}(\hat{\mathbf{k}})$ in Eq. (3.9) is given by

$$\begin{bmatrix} \hat{\xi}_{\mathbf{k}+} + \lambda\hat{k}_z & \Lambda^\dagger_{\mathbf{k}+} & 0 & -\Delta \\ \Lambda_{\mathbf{k}+} & \hat{\xi}_{\mathbf{k}+} - \lambda\hat{k}_z & \Delta & 0 \\ 0 & \Delta & -\hat{\xi}_{\mathbf{k}-} + \lambda\hat{k}_z & \Lambda_{\mathbf{k}-} \\ -\Delta & 0 & \Lambda^\dagger_{\mathbf{k}-} & -\hat{\xi}_{\mathbf{k}-} - \lambda\hat{k}_z \end{bmatrix} \tag{3.10}$$

with $\hat{\xi}_{\mathbf{k}\pm} \equiv \hbar^2(\hat{\mathbf{k}}\pm\mathbf{Q}/2)^2/(2m) - \mu$ and $\Lambda_{\mathbf{k}\pm} \equiv \lambda(\hat{k}_x \pm q/2 + i\hat{k}_y) \pm h$. For a homogeneous Fermi gas with open boundary condition, the BdG Hamiltonian can be diagonalized

by replacing the momentum operators $\hat{k}_i$ $(i = x, y, z)$ by the corresponding c-numbers k_i. Thus, we obtain the energy spectrum of Bogoliubov quasiparticles $E_{\eta\nu}(\mathbf{k})$, where $\nu \in (+, -)$ denotes the particle or hole branch and $\eta \in$(1,2) stands for the upper or lower helicity band. The mean-field thermodynamic potential $\Omega_{\rm mf}$ at the temperature T can be written down straightforwardly,

$$\begin{aligned}\frac{\Omega_{\rm mf}}{V} &= \frac{1}{2V}\sum_{\mathbf{k}}\left[\xi_{\mathbf{k}+\mathbf{Q}/2}+\xi_{\mathbf{k}-\mathbf{Q}/2}-\sum_{\eta=1,2}E_{\eta+}(\mathbf{k})\right] \\ &\quad -\frac{\Delta^2}{U_0}-\frac{k_BT}{V}\sum_{\mathbf{k}\eta=1,2}\ln\left[1+e^{-E_{\eta+}(\mathbf{k})/k_BT}\right], \end{aligned} \tag{3.11}$$

where the last term is the standard expression of thermodynamic potential for non-interacting Bogoliubov quasiparticles. Due to the inherent particle-hole symmetry in the Nambu spinor representation, the summation over the quasiparticle energy has been restricted to the particle branch, to avoid double counting. For a given set of parameters (i.e., the temperature T, s-wave scattering length a_s etc.), different mean-field phases can be determined using the self-consistent stationary conditions: $\partial\Omega_{\rm mf}/\partial\Delta = 0$, $\partial\Omega_{\rm mf}/\partial q = 0$, as well as the conservation of total atom number, $n = -(1/V)\partial\Omega/\partial\mu$, where n is the number density. At a given temperature, the ground state has the lowest free energy $F = \Omega + \mu N$. For simplicity, we only report the results at zero temperature.

3.2.2 Topological Nodal Fulde-Ferrell superfluids

First, we report the phase diagram Fig. 3.8 where an in-plane Zeeman field will drive the Fermi system from a gapped FF superfluid to a gapless phase (labeled as "nodal FF") [95]. Remarkably, at sufficiently large values it will also lead to a gapless topologically non-trivial state ("topological nodal FF"). The evolution of the energy spectrum at a typical spin-orbit coupling strength $\lambda = E_F/k_F$ as a result of the

increasing in-plane Zeeman field is presented in Fig. 3.9.

Physically, the transition to a gapless phase can be well characterized by a global energy gap $E_g = \min E_{2+}(\mathbf{k})$, which is the half of the energy difference between the minimum energy of the particle branch and the maximum of the hole branch due to the particle-hole symmetry $E_{2+}(\mathbf{k}) = -E_{2-}(-\mathbf{k})$. Hence, $E_g \leq 0$ and $E_g > 0$ characterize a gapless and gapped state, respectively. The topological phase transition, on the contrary, is related to the change of the topology of the Fermi surfaces. It is well known that such a change must be accompanied with the close and re-open of an energy gap at some specific points in momentum space [102, 103]. In our continuum case of a homogeneous Fermi gas, this occurs precisely at the origin $\mathbf{k} = \mathbf{0}$ (see Fig. 3.9b). Therefore, naively the topological transition can be determined from the condition $E_{2+}(\mathbf{k} = \mathbf{0}) = 0$ or more explicitly,

$$h_{c2} = \sqrt{\left(\mu - \frac{\hbar^2 q^2}{8m}\right)^2 + \Delta^2} - \frac{\lambda q}{2}. \tag{3.12}$$

In the absence of a FF pairing momentum ($q = 0$), the above condition reduces to the well-known criterion $h_c = \sqrt{\mu^2 + \Delta^2}$ for the appearance of a SLTD topological superfluid *, when an out-of-plane Zeeman field is applied [104, 105]. It is interesting that the gapless transition always occurs before the topological transition, as a result of $E_g \leq E_{2+}(\mathbf{k} = \mathbf{0})$. Thus, bulk-gapped topological FF superfluids, if exist, must appear at very high in-plane Zeeman field. As a superfluid analogue of strong 3D topological insulators [102, 103], they are anticipated to have the unique feature of a single Dirac cone for the energy dispersion of the Majorana edge states. Unfortunately, in the parameter space that we considered, we do not find their existence.

* The most efficient scheme to create topological superfluids is based on the model proposed by Sau, Lutchyn, Tewari and Das Sarma (SLTD) in 2010 [104, 105].

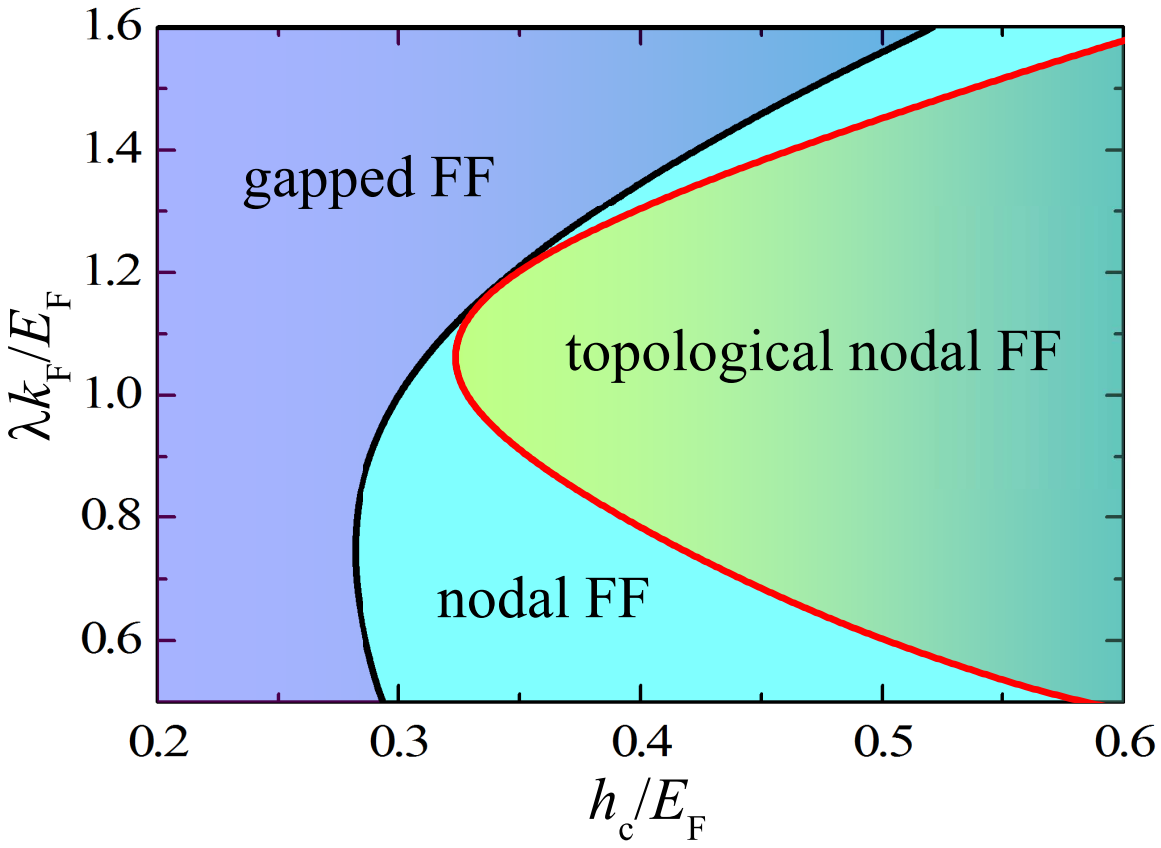

Figure 3.8 : Zero temperature phase diagram of the FF superfluid at the interaction parameter $1/(k_F a_s) = -0.5$. With increasing in-plane Zeeman field, the Fermi cloud changes from a gapped FF superfluid to a gapless FF superfluid, and finally turns into a gapless topological superfluid. In our numerical calculations, using the number density n we have set the Fermi wavevector $k_F = (3\pi^2 n)^{1/3}$ and Fermi energy $E_F = \hbar^2 k_F^2/(2m)$ as the units for wavevector and energy, respectively. Unless specifically noted, we shall focus on the attractive interaction regime with a dimensionless interaction parameter $1/(k_F a_s) = -0.5$ and at zero temperature $T = 0$, for which our mean-field treatment could be well justified.

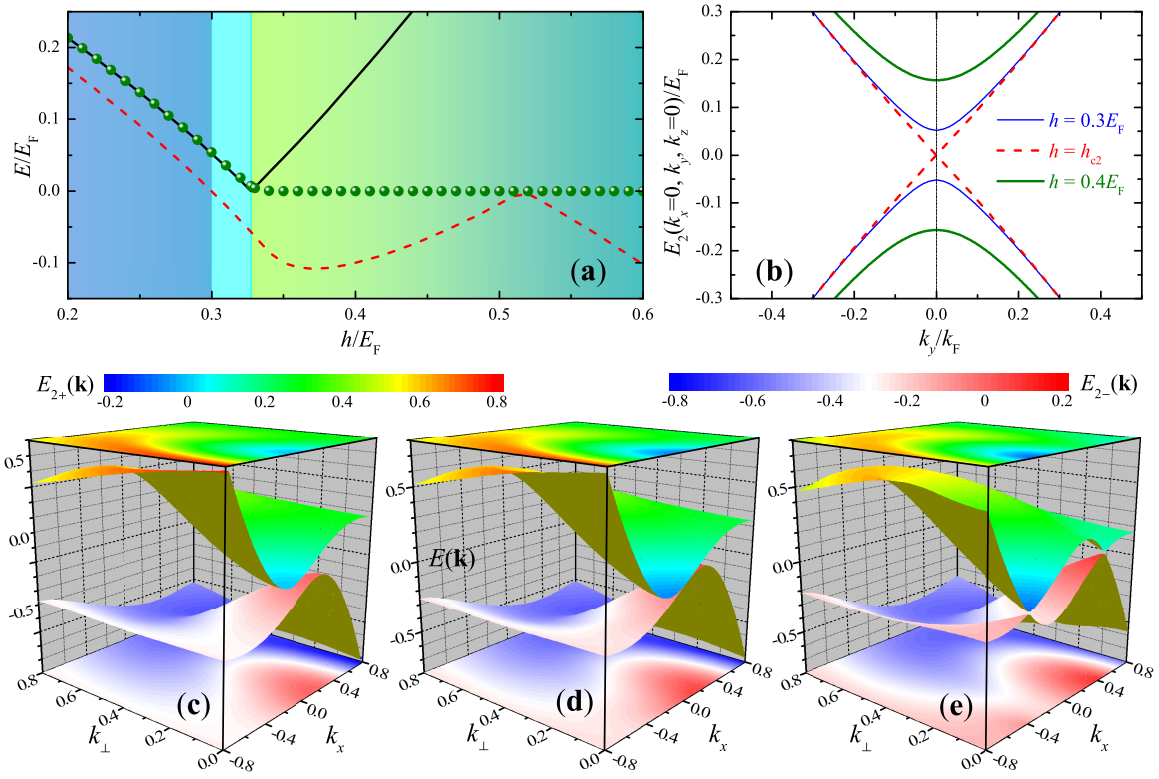

Figure 3.9 : The evolution of the energy gap and of the topology of the Fermi surfaces at $\lambda = E_F/k_F$ with increasing the in-plane Zeeman field. (a) The global energy gap $E_g = \min E_{2+}(\mathbf{k})$ (red dashed line), the energy gap at $\mathbf{k} = 0$ (black solid line), and the minimum energy of the surface states at $k_x = 0$ and $k_z = 0$ (green solid circles) when open boundary is imposed along the y-direction. (b) The energy dispersion $E_{2\pm}(k_y)$ at $k_x = 0$ and $k_z = 0$. (c), (d) and (e) The 3D full plot of the energy dispersion $E_{2\pm}(k_x, k_\perp = \sqrt{k_y^2 + k_z^2})$ at $h_{c1} \simeq 0.3E_F$ (c), $h_{c2} \simeq 0.327E_F$ (d) and $h = 0.4E_F$ (e).

At the coupling strength $\lambda = E_F/k_F$, the gapless transition and topological transition occur at $h_{c1} \simeq 0.3E_F$ and $h_{c2} \simeq 0.327E_F$, respectively, as can be seen from Fig. 3.9a, where E_g (red dashed line) and $E_{2+}(\mathbf{k} = \mathbf{0})$ (black solid line) become zero as the in-plane Zeeman field increases. When $h > h_{c1}$, nodal points which satisfy $E_{2\pm}(\mathbf{k}) = 0$ develop and form two closed surfaces in momentum space [95]. When the in-plane field further increases, passing through the threshold h_{c2} for the topological transition (see Fig. 3.9d), the energy dispersion of the particle- and hole-branches touches at two specific points ($\pm k_W$,0,0), as shown in Fig. 3.9e. Around these points, the dispersion of Bogoliubov quasiparticles in the bulk acquires a linear structure and thereby form a Dirac cone. This is precisely the energy dispersion for massless Weyl fermions [106–108]. In this sense, the gapless topological FF superfluid predicted in this work provides a new avenue for the observation of Weyl fermions around the Weyl nodes ($\pm k_W$,0,0). Indeed, Weyl fermions have recently been discussed in the context of 3D gapped topological superfluids [109, 110].

In our case, the appearance of the Weyl nodes and of the topological order is closely related. Due to the asymmetry in the k_x axis, only one of the Weyl nodes is occupied. Thus, we may characterize the topological order of the gapless FF superfluid by using the topological invariant of Weyl fermions [103, 111]:

$$N_W = \int \frac{d^3\mathbf{k}}{24\pi^2}\epsilon^{\mu\nu\rho}\mathrm{Tr}\left[Q_{\mathbf{k}}^{\dagger}\partial_\mu Q_{\mathbf{k}} Q_{\mathbf{k}}^{\dagger}\partial_\nu Q_{\mathbf{k}} Q_{\mathbf{k}}^{\dagger}\partial_\rho Q_{\mathbf{k}}\right], \tag{3.13}$$

where $Q_{\mathbf{k}}$ is the unitary matrix determined by the BdG Hamiltonian, $\mu, \nu, \rho = (k_x, k_y, k_z)$ and the domain of the integration includes the isolated, occupied Weyl node. The gapless topological FF superfluid is uniquely characterized a nonzero topological invariant $N_W \neq 0$.

3.2.3 Majorana Surface States

Cylindrical hard-wall confinement

To further demonstrate the topological nature of the gapless FF superfluid, we calculate the energy dispersion in the presence of open boundary by imposing cylindrical hard wall confinement perpendicular to the y-z plane. There is a pair of zero-energy Majorana fermion state on the boundary of $r = L$, which is the direct signature of a topologically non-trivial state. The existence of Majorana fermions is reported in Fig. 3.9a by green solid circles. They immediately appear after the change in the topology of the Fermi surfaces.

We now discuss in more detail the Majorana surface states, whose dispersion is shown in Fig. 3.10. Because the boundary we impose has rotational symmetry in the y-z plane and translation symmetry along x-direction, states with different integer orbital angular momentum m and continuous linear momentum k_x are decoupled, where we can perform Bessel function basis expansion.

First, in order to determine the Majorana surface states in the topologically non-trivial phase, we impose a cylindrical hard wall potential, for example, perpendicular to the y-z plane, so that any single-particle wavefunction must vanish identically at the boundary $r = L$. We assume that the radius is sufficiently large so that we can use the solution of a uniform pairing gap. Accordingly, in the BdG Hamiltonian Eq. (3.10), we replace the momentum operator k_y and k_z by its corresponding derivatives in cylindrical coordinates where longitudinal axis is chosen along x-direction. It can

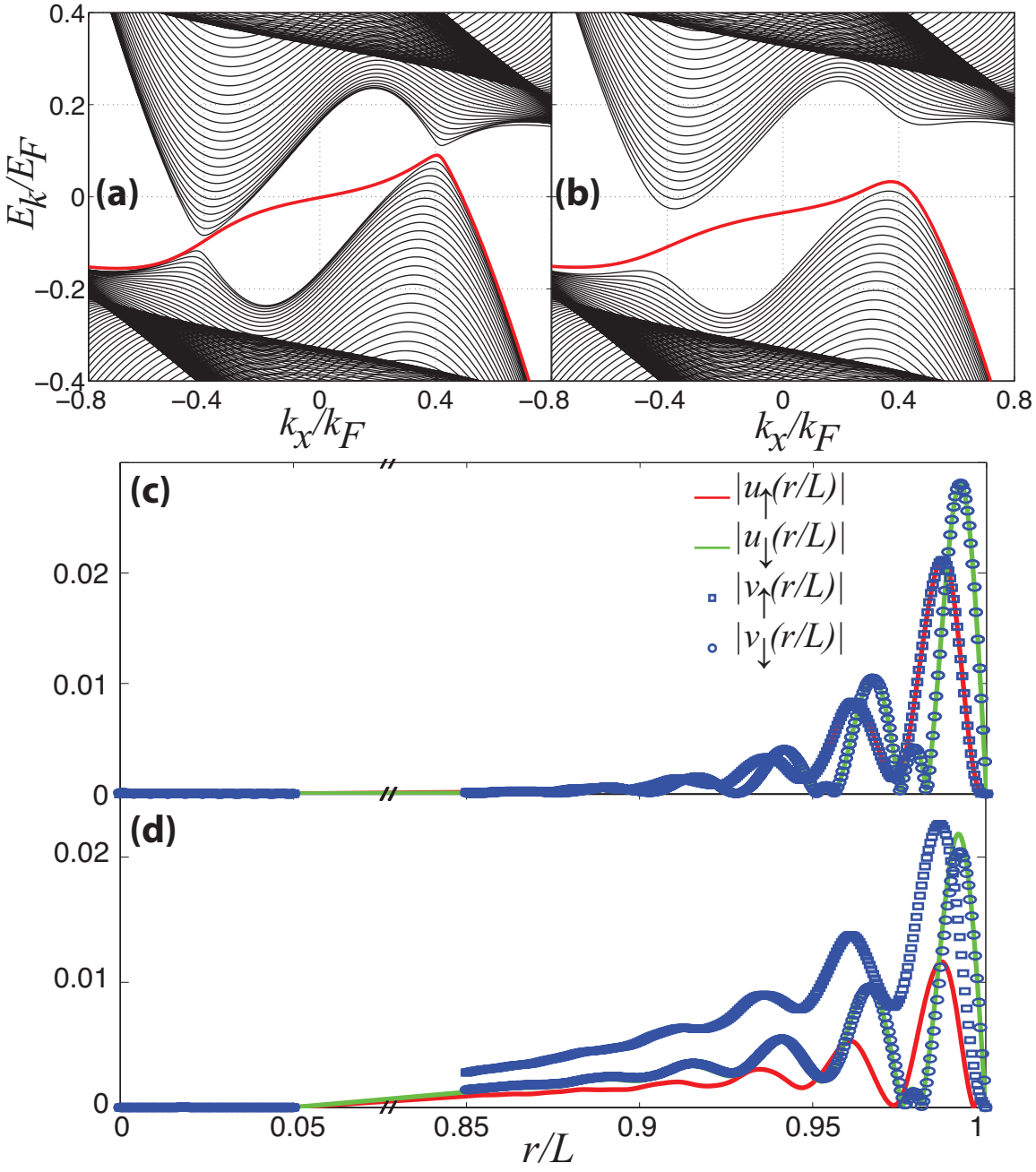

Figure 3.10 : Majorana surface states arising from the hard wall confinement perpendicular to the y-z plane. (a) and (b) The full energy spectrum $E_{k_z}^{(m)}$ along the k_x axis for $m = 0$ and $m = 10$, respectively. The surface states at the two boundaries are highlighted by red solid circles and blue empty squares, respectively. (c) and (d) The wavefunction of the zero-energy Majorana fermions at finite k_x values, satisfying the symmetry $u_\sigma(y) = e^{i\vartheta}v_\sigma^*(y)$, where ϑ is a constant phase factor and $\sigma =\uparrow,\downarrow$. In numerical calculations, we have set the length of the confinement $L = 200k_F^{-1}$. Other parameters are $\lambda = E_F/k_F$ and $h = 0.4E_F$.

be diagonalized by using the following ansatz for the Bogoliubov wavefunctions,

$$\begin{pmatrix} u_\uparrow(\mathbf{r}) \\ u_\downarrow(\mathbf{r}) \\ v_\uparrow(\mathbf{r}) \\ v_\downarrow(\mathbf{r}) \end{pmatrix} = \frac{e^{im\theta}}{\sqrt{2\pi}} \sum_{n=1}^{N_{\max}} \begin{pmatrix} \frac{J_m(\kappa_n^{(m)}\frac{r}{L})}{\sqrt{\mathcal{N}_n^{(m)}}} u_{n\uparrow} \\ \frac{J_{m+1}(\kappa_n^{(m+1)}\frac{r}{L})e^{i\theta}}{\sqrt{\mathcal{N}_n^{(m+1)}}} u_{n\downarrow} \\ \frac{J_{m+1}(\kappa_n^{(m+1)}\frac{r}{L})e^{i\theta}}{\sqrt{\mathcal{N}_n^{(m+1)}}} v_{n\uparrow} \\ \frac{J_m(\kappa_n^{(m)}\frac{r}{L})}{\sqrt{\mathcal{N}_n^{(m)}}} v_{n\downarrow} \end{pmatrix} e^{ik_x x} \tag{3.14}$$

where $\kappa_n^{(m)}$ is the nth positive root of Bessel function of the first kind $J_m(\rho)$ with $m \geq 0$. For states with $m < 0$, we have instead $J_{-m}(\rho) = (-1)^m J_m(\rho)$. Orthogonal condition is given by $\int_0^L J_m(\kappa_n^{(m)}\frac{r}{L}) J_m(\kappa_l^{(m)}\frac{r}{L}) r dr = 0$ where integer $n \neq l$ and normalization reads as $\mathcal{N}_n^{(m)} = \int_0^L J_m(\kappa_n^{(m)}\frac{r}{L}) J_m(\kappa_n^{(m)}\frac{r}{L}) r dr = \frac{1}{2}L^2 \left(J_{m+1}(\kappa_n^{(m)})\right)^2$. Inserting this ansatz into the BdG equation, we convert the BdG Hamiltonian into a $4N_{\max}$ by $4N_{\max}$ Hermitian matrix,

$$\mathcal{H}_{11n}^{(m)} u_n - iv \sum_{l=1}^{N_{\max}} \mathcal{W}_{ln}^{(m)} \alpha_l - \Delta v_n = E_{k_x}^{(m)} u_n \tag{3.15}$$

$$iv \sum_{l=1}^{N_{\max}} \mathcal{W}_{nl}^{(m)} u_l + \mathcal{H}_{22n}^{(m)} \alpha_n + \Delta \beta_n = E_{k_x}^{(m)} \alpha_n \tag{3.16}$$

$$\Delta \alpha_n + \mathcal{H}_{33n}^{(m)} \beta_n + iv \sum_{l=1}^{N_{\max}} \mathcal{W}_{nl}^{(m)} v_l = E_{k_x}^{(m)} \beta_n \tag{3.17}$$

$$-\Delta u_n - iv \sum_{l=1}^{N_{\max}} \mathcal{W}_{ln}^{(m)} \beta_l + \mathcal{H}_{44n}^{(m)} v_n = E_{k_x}^{(m)} v_n \tag{3.18}$$

where all the matrix elements have been analytically worked out (not shown here). The diagonalization directly gives rise to the energies and wavefunctions of the Majorana surface states.

In Fig. 3.10a and b, we plot the full energy spectrum along k_x axis for $m = 0$ and $m = 10$. Majorana zero energy mode can be identified by the energy crossing of surface state contribution, at which points quasi-particle wave-functions become localized at the edge, as shown in Fig. 3.10c and d. Although in comparison, edge

state wave-function is more localized for smaller m values. For even larger orbital angular momentum value around $m \simeq 20$ surface state smoothly connects to the Weyl node located approximately at $k_W \simeq 0.4k_F$ in the bulk. Furthermore, it is straightforward to make use of particle-hole symmetry of the BdG equation to prove, for every zero energy state with $m \geq 0$ and $k_x > 0$, there is a corresponding zero energy state at $-m-1$ and $-k_x$. As there are no net atomic currents at equilibrium, the two counter-propagating chiral surfaces states compensate each other. This is a unique feature of novel gapless topological FF superfluid in our work.

It is worth noting that the 3D gapless topological FF superfluid can not be viewed as a stack of 2D topological superfluids along a specific direction (i.e., z-axis), unlike the standard 3D topological superfluids known so far. For the latter, the Majorana surface states of the 3D system can be understood as the edge states of the 2D system on the surfaces which are parallel to the z-axis and therefore have a flat dispersion that does not depend on k_z [109]. This is analogous to the trivial or weak 3D topological insulators [102,103]. In our case, due to the existence of spin-orbit coupling in all three spatial directions, the dispersion of the Majorana surface states is no longer flat. In this respect, the gapless topological FF superfluid is better regarded as the superfluid analogue of a strong topological insulator [102, 103], although the surface states may not have a Dirac-cone-like dispersion due to the gapless bulk. In consistent with this classification, there is only one pair of zero-energy Majorana fermions localized on each surface, respectively. In Fig. 3.10 (c) and (d), we examine the wave function of Majorana fermions. It satisfies the desired symmetry $u_\sigma(r) = e^{i\vartheta}v^*_\sigma(r)$ for each spin component $\sigma =\uparrow,\downarrow$, up to an unimportant constant phase ϑ [112].

Hard-wall confinement along the y direction

We may also consider imposing hard-wall confinement along a specific direction, for example adding two walls perpendicular to the y axis at $y = 0, L$. In this case, unidirectional Majorana surfaces states propagate in the same direction on opposite boundaries at $y = 0$ and $y = L$, respectively. Any single-particle wavefunction must vanish identically at the boundary $y = 0$ or $y = L$. We assume that the length L is sufficiently large so we use the solution of a uniform pairing gap. Accordingly, in the BdG Hamiltonian Eq. (3.10), we replace the momentum operator k_y with $-i\partial_y$. It can be diagonalized by using the following ansatz for the Bogoliubov wavefunctions,

$$u_\sigma(y) = \sum_{n=1}^{N_{\max}} u_{n\sigma}\psi_n(y), \tag{3.19}$$

$$v_\sigma(y) = \sum_{n=1}^{N_{\max}} v_{n\sigma}\psi_n(y), \tag{3.20}$$

where $\psi_n(y) = \sqrt{2/L}\sin[n\pi y/L]$ is the eigenfunction of the hard wall potential with eigenvalue $\epsilon_n = \hbar^2 n^2\pi^2/(2mL^2)$. Inserting this ansatz into the BdG equation, we convert the BdG Hamiltonian into a $4N_{\max}$ by $4N_{\max}$ symmetric matrix, whose diagonalization directly leads to the energies and wavefunctions of the Majorana surface states.

With this hard wall confinement, the dispersion of Majorana surface states is shown in Fig. 3.11. In momentum space, k_x and k_z are still good quantum numbers, so we actually plot $\min E_{2+}(k_x, k_z)$ and $\max E_{2-}(k_x, k_z)$. There are two sheets in the energy dispersion (Fig. 3.11a), corresponding to the surface states localized at the boundary $y = 0$ and $y = L$, respectively. Remarkably, these two sheets cross at the line $k_z = 0$, indicating that along this line the two branches of surface states are unidirected, that is, propagating in the same direction on opposite boundaries.

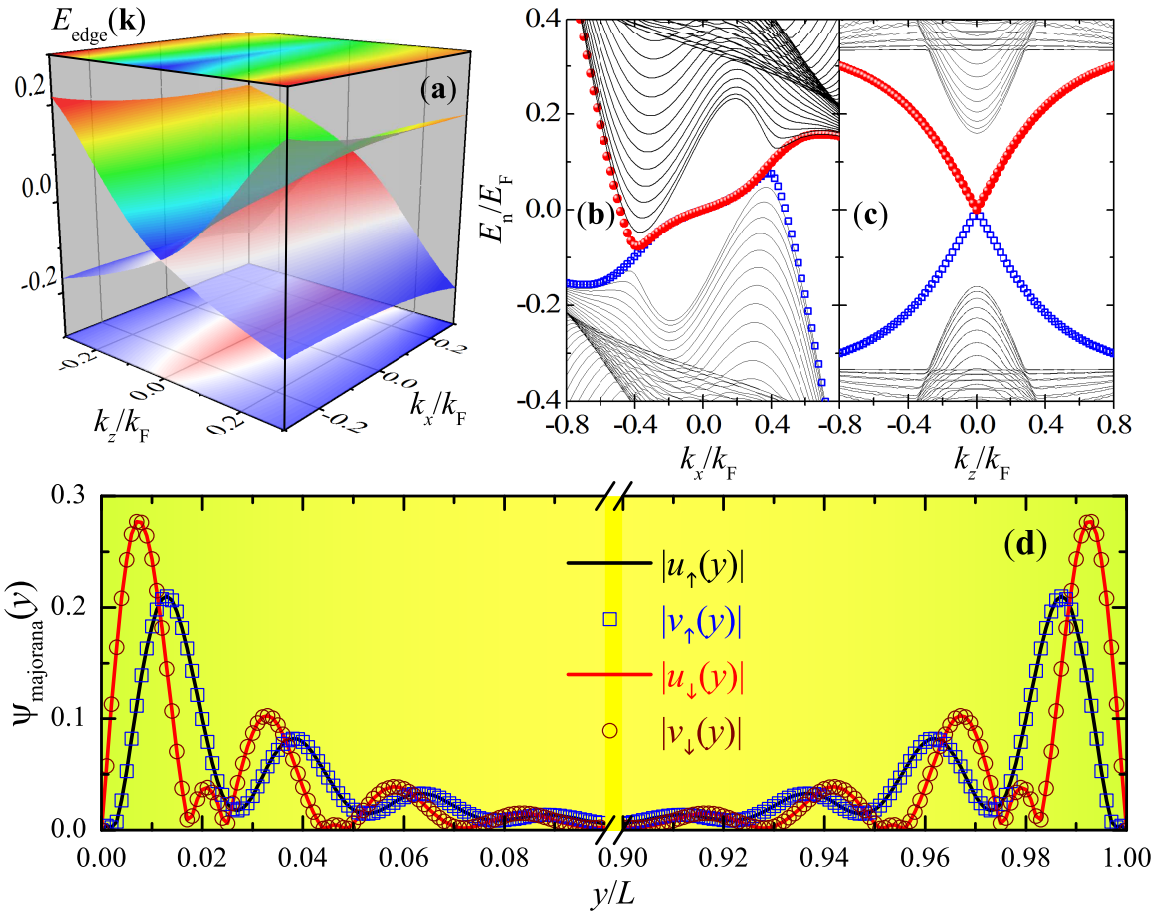

Figure 3.11 : Majorana surface states arising from the hard wall confinement along the y-direction. (a) The surface state dispersion forms two sheets which crosses at the line $k_z = 0$. (b) and (c) The full energy spectrum $E_{2\pm}(k_x, k_z)$ along the k_z or k_x axis, respectively. The surface states at the two boundaries are highlighted by red solid circles and blue empty squares, respectively. (d) The wavefunction of the zero-energy Majorana fermions at $k_x = 0$ and $k_z = 0$. In numerical calculations, we have set the length of the confinement $L = 200k_F^{-1}$. Other parameters are $\lambda = E_F/k_F$ and $h = 0.4E_F$ as in Fig. 3.10.

This is highlighted in Fig. 3.11b, from which we also identify that the unidirected Majorana surface states smoothly connect the two Weyl nodes ($\pm k_W$,0,0) in the bulk, where $k_W \simeq 0.4k_F$. Recall that at equilibrium there are no net atomic currents. As in the cylinderically symmetric case, the current due to these co-propagating surface states on opposite boundaries therefore must be compensated by the current induced by some extra counter-propagating modes in the bulk. This can only happen in systems with a gapless bulk. We note that, the unidirected Majorana surface states only occur along the line $k_z = 0$. Actually, if we make a cut on the two sheets along other directions, for example, along the line $k_x = 0$, it is easy to see that the Majorana surface states become counter-propagating (see Fig. 3.11c for the dispersion as a function of k_z), resembling the surface states in the standard gapped topological superfluid. This follows the fact that at $k_x = 0$ our topological FF superfluid is actually gapped in the bulk. By comparing the two limiting cases shown in Figs. 3.11b and 3.11c, it is clear that the unidirected surface states discussed in our work is a unique feature of novel gapless topological FF superfluid.

3.3 Summary

In Summary, in Section 3.1, we have studied a 3D spin-orbit coupled Fermi gas subjected to an effective Zeeman field. Based on the picture of Fermi surface deformation, the two-body calculations, and the mean-field many-body results, we conclude that the BCS state with zero-momentum Cooper pairs is not stable against Fulde-Ferrell superfluid pairing at any finite Zeeman field strength. We have found that the FF phase is robust against interaction and finite temperature, and the corresponding center-of-mass momentum of the Cooper pair can be comparable to the Fermi momentum. The finite-momentum dimer state in the two-body situation and the FF

state in the many-body setting both originate from the asymmetric momentum distribution as a consequence of the interplay between spin-orbit coupling and the Zeeman field. This asymmetry also determines the direction of the momentum for the dimer state or the Cooper pairs. The FF state in the present work is not exactly the same as the FF or FFLO state in the context of a spin-imbalanced Fermi gas without spin-orbit coupling. In the latter case, the direction of the momentum of the Cooper pairs is determined through the mechanism of spontaneous symmetry breaking. For a similar reason, we only considered FF state in our work, not the FFLO state. The FFLO state requires the Cooper pairs to possess two momenta with equal magnitude but opposite directions. However, in our case, the asymmetric momentum distribution uniquely picks one particular momentum rather than an opposite pair.

In Section 3.2, we propose a new mechanism to create topologically non-trivial states by using an in-plane Zeeman field only. Novel gapless topological superfluids with inhomogeneous Fulde-Ferrell pairing orders parameter can be realized using three-dimensional spin-orbit coupled s-wave superfluids, where the finite momentum pairing and topological order are both driven by the in-plane Zeeman field. They feature unidirected Majorana surface modes and a pair of zero-energy Majorana fermions at the edges, which are quite different from the standard gapped topological superfluids that are known to date. These new features will greatly enrich our understanding of topological quantum matters, in both solid-state and cold-atom systems.

So far in this dissertation, we have discussed *stationary* ground state properties, for single-particle state, two-body states, mean field many-body phases characterized by spontaneous symmetry breaking and topological orders. In the next Chapter, we explore the interesting far out-of-equilibrium physics for a particular physical realization of non-integrable quantum dynamical system.

Chapter 4

Quench Dynamics

Beyond investigating topological properties of stationary ground states, out-of-equilibrium quantum physics is also extremely interesting yet challenging to explore. Quantum statistical mechanics provides a general framework under which the characterization of equilibrium states of many-body systems is well established. To describe systems slightly perturbed out of equilibrium, the linear response theory turns out to be extremely successful. Much is less known, however, on the quantum coherent dynamics of a system far-from-equilibrium. A main reason for that can be ascribed to the fact that such dynamics is generally difficult to access in experiments due to unavoidable relaxation and dissipation from interactions with the environment. However, the dynamics of quantum systems far-from-equilibrium is of great interest from a fundamental viewpoint because it can provide us with the properties of the system beyond the ground state, for instance, excitations, thermalization, (dynamical) phase transitions and related universalities [113–118]; see more details in a recent Review [119]. In this regard, ultracold atom systems provide a new platform for the exploration of intriguing far-from-equilibrium *coherent* dynamics [116, 120, 121]. This is made possible by the precise control of key parameters in cold atomic systems as well as the ideal isolation from environment [122].

For these reasons, the coherent dynamics of the s-wave Bardeen-Cooper-Schrieffer (BCS) superfluid has been intensively studied over the past decade [123–130]. In these theoretical studies, via the so-called Anderson's pseudospin representation, the BCS

model can be *exactly* mapped into a classical spin model, which is proven to be integrable and can be solved exactly using the auxiliary Lax vector method [131,132]. It has been shown that the quench dynamics of the system depends strongly on both the initial and the final values of the quench parameter, which is often chosen to be the interaction strength. In general, three different phases can be identified according to the long-time asymptotic behavior of the order parameter: the undamped oscillation phase (synchronization phase), the damped oscillation phase, and the over-damped phase. Integrability of the Hamiltonian is essential to understand these results. The p-wave superfluid has the same mathematical structure as the s-wave superfluid, thus similar phases are observed in a recent study [133, 134]. As the p-wave superfluid supports topological phases, a quenched p-wave superfluid is found to support dynamical topological phases within certain parameter regimes. However, a Fermi gas with p-wave interactions, realized by tuning the system close to a p-wave Feshbach resonance, suffers from strong incoherent losses due to inelastic collisions [135]. On the other hand, one may realize cold atomic systems with effective p-wave interactions. Such candidates include ultracold polar molecules with long-range dipolar interaction [136] and spin-1/2 Fermi gases subject to synthetic partial waves [137]. Both of these systems are being intensively investigated in cold atom research.

As quantum simulators of real world materials, the spin-orbit coupled degenerate Fermi gas provides a new platform to realize topological superfluids and related topological excitations. In this Chapter, we study the quench dynamics and topological edge states in a spin-orbit (SO) coupled superfluid Fermi gas in two dimension (2D), motivated by the very recent realization of SO coupling in ultracold atoms [138–143]. The ground state of this system can be topologically nontrivial in some parameter regimes [144–160]. This is because the SO coupling, Zeeman field and s-wave inter-

action together can lead to effective p-wave pairing. This system possesses several control parameters that can be readily tuned in experiments, which makes it ideal to study the far-from-equilibrium *coherent* dynamics and related topological phase transitions. However, the simultaneous presence of the SO coupling and the Zeeman field breaks the integrability of this model [161], and changes the system from a single-band to a two-band structure. It is therefore natural to ask the fundamental question: "What types of post-quench dynamical phases will this system exhibit, and how do these dynamical phases differ from the ones supported by the integrable models?" In our study, we choose the Zeeman field as the quench parameter for the reasons to be discussed below. It is quite surprising that all the phases supported by the integrable model still exist in our non-integrable system, although there exists unique topological features in our system. We provide a complete phase diagram and investigate each phases in details. We also show how dynamical topological phases, which can support topologically protected edge states, emerge in this model.

4.1 Novel Topological Superfluids

4.1.1 Model Hamiltonian

To make progress, as an example, we consider a 2D system of uniform SO coupled degenerate Fermi gas with s-wave interaction confined in the xy-plane, whose Hamiltonian is written as $\mathcal{H} = \mathcal{H}_0 + \mathcal{V}$, where ($\hbar = 1$)

$$\begin{aligned} \mathcal{H}_0 &= \sum_{\mathbf{k},s,s'} c^\dagger_{\mathbf{k}s} \left[\xi_{\mathbf{k}} + \alpha(k_y\sigma_x - k_x\sigma_y) + h\sigma_z\right]_{ss'} c_{\mathbf{k}s'}, \\ \mathcal{V} &= g \sum_{\mathbf{k},\mathbf{k}',\mathbf{q}} c^\dagger_{\mathbf{k}+\mathbf{q}\uparrow} c^\dagger_{\mathbf{k}'-\mathbf{q}\downarrow} c_{\mathbf{k}'\downarrow} c_{\mathbf{k}\uparrow}, \end{aligned} \tag{4.1}$$

where $s, s' = \uparrow, \downarrow$ label the pseudospins represented by two atomic hyperfine states, $\mathbf{k}$ is the momentum operator, $\xi_{\mathbf{k}} = \epsilon_{\mathbf{k}} - \mu$, where $\epsilon_{\mathbf{k}} = \mathbf{k}^2/2m$ denotes kinetic energy

and μ is the chemical potential, α is the Rashba SO coupling strength, $\sigma_{x,y,z}$ are the Pauli matrices, h is the Zeeman field along the z-axis, $c_{\mathbf{k}s}$ is the annihilation operator which annihilates a fermion with momentum $\mathbf{k}$ and spin s, and g represents the inter-species s-wave interaction strength. Notice that the 2D system is created from the three dimensional system by applying a strong confinement along the z-axis, thus g in principle can be controlled by both confinement and Feshbach resonance. This 2D degenerate Fermi gas has been realized in recent experiments [162–165].

We consider the quench dynamics of the Fermi gas at the mean field level, thus the potential defect production, i.e., the so-called Kibble-Zurek mechanism, after the quench is not considered. Imagine that we prepare the initial system in the ground state with Zeeman field h_i. At time $t = 0^+$, we suddenly change the Zeeman field from h_i to some final value h_f. This scheme should be in stark contrast to previous literatures, in which the interaction strength g generally serves as the quench parameter [123–130, 133, 134]. We choose the Zeeman field as our quench parameter for the following reasons. (1) As we shall show in the discussion of the ground state properties of this system, the Zeeman field directly determines the topological structure of the ground state. (2) In SO coupled quantum gases, the laser intensity and/or detuning serve as the effective Zeeman field, and these parameters can be changed in a very short time scale, satisfying the criterion for a sudden quench. By contrast, a change of the interaction strength is achieved by tuning the magnetic field, via a Feshbach resonance, which usually cannot be done very rapidly. (3) Moreover, changing the effective Zeeman field in SO coupled quantum gases has already been demonstrated in recent experiments [138–142], in which both the magnitude and the sign of the Zeeman field can be changed.

The superfluid order parameter is defined as $\Delta = g\Sigma_{\mathbf{k}}\langle c_{-\mathbf{k}\downarrow}c_{\mathbf{k}\uparrow}\rangle$ and the interaction

term can be rewritten as $\mathcal{V} \to \Delta^* c_{-\mathbf{k}\downarrow} c_{\mathbf{k}\uparrow} + \Delta c^\dagger_{\mathbf{k}\uparrow} c^\dagger_{-\mathbf{k}\downarrow} - |\Delta|^2/g$. Therefore, under the Numbu spinor basis $\Psi_{\mathbf{k}} = (c_{\mathbf{k}\uparrow}, c_{\mathbf{k}\downarrow}, -c^\dagger_{-\mathbf{k}\downarrow}, c^\dagger_{-\mathbf{k}\uparrow})^T$, the total Hamiltonian becomes $\mathcal{H} = \Sigma_{\mathbf{k}} \Psi^\dagger_{\mathbf{k}} \mathcal{M}_{\mathbf{k}} \Psi_{\mathbf{k}} - |\Delta|^2/g$, where the Bogoliubov-de Gennes (BdG) operator reads as [144, 145]

$$\mathcal{M}_{\mathbf{k}} = \frac{1}{2} \begin{pmatrix} H_0(\mathbf{k}) & \Delta \\ \Delta^* & -\sigma_y H_0^*(-\mathbf{k}) \sigma_y \end{pmatrix}. \tag{4.2}$$

Assuming $f_{\mathbf{k}\pm} = (u_{\mathbf{k}\pm}, v_{\mathbf{k}\pm}, p_{\mathbf{k}\pm}, q_{\mathbf{k}\pm})^T$ are the two energy levels of $\mathcal{M}_{\mathbf{k}}$ with positive eigenvalues, the initial value of chemical potential and order parameter are determined by minimizing the thermodynamical potential [144–147, 150–158], which is equivalent to solving the gap equation

$$\sum_{\mathbf{k}} \left[\frac{1}{2\epsilon_{\mathbf{k}} + E_b} - \sum_{s=\pm} \frac{E_0 + s h^2}{4 E_0 E^+_{\mathbf{k}s}} \right] = 0, \tag{4.3}$$

and number equation

$$n = \sum_{\mathbf{k}} \left[1 - \sum_{s=\pm} \frac{\xi_{\mathbf{k}}}{2} \frac{E_0 + s(h^2 + \alpha^2 k^2)}{E_0 E^+_{\mathbf{k}s}} \right], \tag{4.4}$$

where $E^\eta_{\mathbf{k}\pm} = \eta \sqrt{\xi^2_{\mathbf{k}} + \alpha^2 k^2 + h^2 + |\Delta|^2 \pm 2E_0}$ are the excitation energies, with $\eta = \pm$ correspond to the particle and hole branches respectively and $E_0 = \sqrt{h^2(\xi^2_{\mathbf{k}} + |\Delta|^2) + \alpha^2 k^2 \xi^2_{\mathbf{k}}}$. Here the bare interaction strength g should be regularized by $1/g = -\sum_{\mathbf{k}} 1/(2\epsilon_{\mathbf{k}} + E_b)$ [145]. As a result, in the following, the interaction strength is quantitatively defined by the binding energy $E_b \in [0, \infty)$. Throughout our numerical calculations, the energy unit is chosen as the Fermi energy $E_F = k_F^2/2m$, where $k_F = \sqrt{2\pi n}$ is the Fermi wavenumber for a non-interacting Fermi gas without SO coupling and Zeeman field in 2D. We only consider the physics at zero temperature. Throughout this work, we choose the binding energy $E_b = 0.2E_F$, and the corresponding scattering length $k_F a_{2\mathrm{D}} = \sqrt{2E_F/E_b} \simeq 3.1623$ and $\ln(k_F a_{2\mathrm{D}}) \simeq 1.1513$, which is around the BEC-BCS crossover regime. Since $k_F a_{2\mathrm{D}} > 1$, the superfluid is composed of weakly bound

Cooper pairs. For a typical Fermi gas of ^{6}Li, $k_F \sim 1/\mu$m, $E_F \sim 1$kHz , and the relevant time scale discussed in this work is $1/E_F \sim 1$ms . The long time collective oscillations of degenerate Fermi gas that much longer than this relevant time scale has been demonstrated in experiments [166, 167].

4.1.2 Vanishing energy gap of the ground state phases

Before we turn to the discussion of the quench dynamics, let us first briefly outline the ground state properties of the system. The most salient feature of the system is a topological phase transition induced by the Zeeman field [144–147,150–158]. Without loss of generality, we assume that $h \geq 0$, in which case, the spin-up atoms (spin-down atoms) represent the minority (majority) species. It is well known that the topology of the superfluid is encoded in the topological index W [144–147], which corresponds to the topological state with $W = 1$ if $h > \sqrt{\mu^2 + \Delta^2}$, while $h < \sqrt{\mu^2 + \Delta^2}$ yields $W = 0$ and the state is non-topological. In Fig. 4.1(a), we show how μ, Δ and the single-particle excitation gap E_0 at zero momentum change as a function of the Zeeman field h. At the critical point, $h_c = \sqrt{\mu^2 + \Delta^2}$, the excitation gap E_0 vanishes, indicating a topological phase transition. This feature is also essential for the realization of the long-time far-from-equilibrium *coherent* evolution.

4.1.3 Spin textures in momentum space

To see this phase transition more clearly, we also examine the momentum space spin texture. The spin vector is defined as $\mathbf{S}(\mathbf{k}) = (c^\dagger_{\mathbf{k}\uparrow}, c^\dagger_{\mathbf{k}\downarrow})\boldsymbol{\sigma}\,(c_{\mathbf{k}\uparrow}, c_{\mathbf{k}\downarrow})^T$, with the corresponding ground state expectation value given by $\langle S_x(\mathbf{k})\rangle = 2\sum_{\eta=\pm} \Re[p^*_{\mathbf{k}\eta} q_{\mathbf{k}\eta}]$, $\langle S_y(\mathbf{k})\rangle = 2\sum_{\eta=\pm} \Im[p^*_{\mathbf{k}\eta} q_{\mathbf{k}\eta}]$, and $\langle S_z(\mathbf{k})\rangle = \sum_{\eta=\pm}(|q_{\mathbf{k}\eta}|^2 - |p_{\mathbf{k}\eta}|^2)$. As shown in Fig. 4.1(b), we find that $\langle S_z(0)\rangle$, the spin component along the z-axis (which is just the

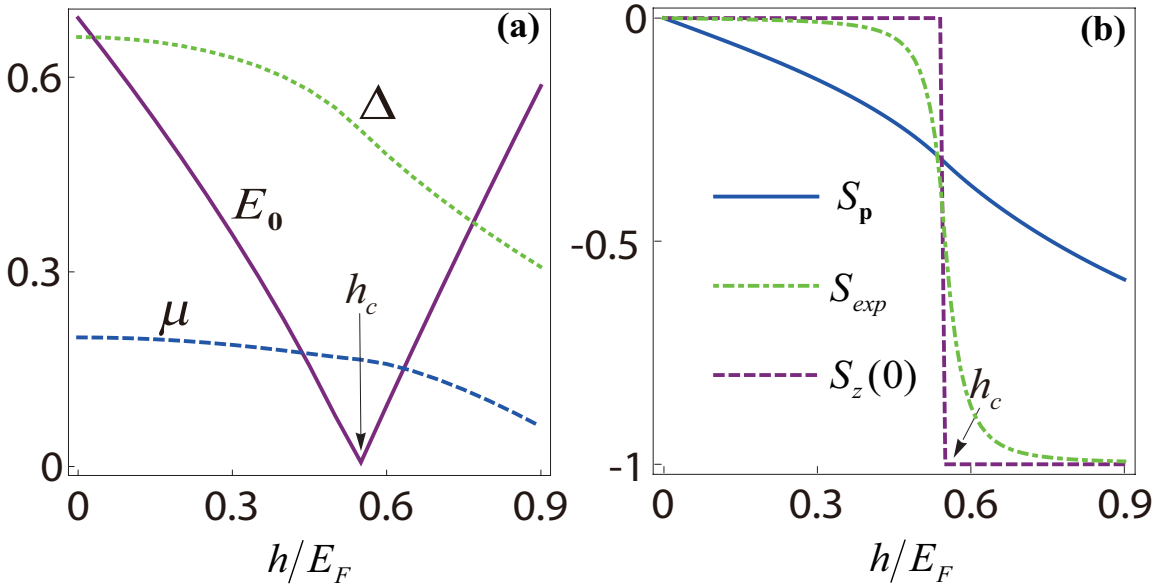

Figure 4.1 : Topological phase transition in spin-orbit coupled superfluids. (a) Plot of E_0 (energy gap at zero momentum), Δ, and μ as functions of h. The arrow marks the critical Zeeman field $h_c \sim 0.545E_F$. The topological phase transition is characterized by the topology of the ground state instead of symmetry because no spontaneous symmetry breaking takes place across the phase transition point. (b) Plot of the total spin polarization $S_{\rm p}$ and zero momentum spin population $S_z(0)$ as a function of Zeeman field. $S_{\rm p}$ is a smooth function of h, whereas $S_z(0)$ jumps at h_c due to band inversion transition. $S_{\rm exp}$ is the spin population averaged over a region in momentum space (see text), which mimics the possible finite momentum resolution in realistic experiments. Throughout this paper if not specified otherwise we take $E_b = 0.2E_F$ and $\alpha k_F = 1.2E_F$.

population difference between the two spin species) at $\mathbf{k} = 0$, jumps discontinuously when the Zeeman field crosses the critical value h_c, while the total spin polarization which is defined as $S_{\rm p} = (n_\uparrow - n_\downarrow)/n$, changes smoothly with respect to h. We emphasize that the jump of $S_z(0)$ across the topological boundary is still visible if we take the finite momentum resolution into account, as will be the case in realistic experiments; see curve $S_{\rm exp} = \int d\mathbf{k}\, S_z(\mathbf{k}) / \int d\mathbf{k}\, n(\mathbf{k})$ in Fig. 4.1 (b), where $n(\mathbf{k})$ is the total density at momentum $\mathbf{k}$ and the integral is performed in a circular area in momentum space centered at $\mathbf{k} = \mathbf{0}$ with a radius of $0.1k_F$. In fact, as shown below, the jump of $\langle S_z(0)\rangle$ just implies a change of topology of the spin texture.

The Hamiltonian at $\mathbf{k} = 0$ can be reduced to

$$\mathcal{M}_{\mathbf{k}=\mathbf{0}} = \begin{pmatrix} -\mu + h & 0 & \Delta & 0 \\ 0 & -\mu - h & 0 & \Delta \\ \Delta^* & 0 & \mu + h & 0 \\ 0 & \Delta^* & 0 & \mu - h \end{pmatrix}. \tag{4.5}$$

We first consider the spin texture in the stationary condition. If $|h| < \sqrt{\mu^2 + \Delta^2}$, the two eigenvectors with positive eigenvalues are $f_{0,+} = (\frac{-\mu+\lambda}{\sqrt{\Delta^2+(\mu-\lambda)^2}}, 0, \frac{\Delta}{\sqrt{\Delta^2+(\mu-\lambda)^2}}, 0)^T$ and $f_{0,-} = (0, \frac{-\mu+\lambda}{\sqrt{\Delta^2+(\mu-\lambda)^2}}, 0, \frac{\Delta}{\sqrt{\Delta^2+(\mu-\lambda)^2}})^T$ respectively, where $\lambda = \sqrt{\mu^2 + \Delta^2}$. Then, from the expression of $\langle S_z(\mathbf{k})\rangle$ in the main text, we can directly get that $\langle S_z(0)\rangle = 0$ and $Q = 0$, which means the system has topologically trivial spin texture. In contrast, if $|h| > \sqrt{\mu^2 + \Delta^2}$, the two eigenvectors will become $f_{0,+} = (\frac{-\mu+\lambda}{\sqrt{\Delta^2+(\mu-\lambda)^2}}, 0, \frac{\Delta}{\sqrt{\Delta^2+(\mu-\lambda)^2}}, 0)^T$ and $f_{0,-} = (\frac{-\mu-\lambda}{\sqrt{\Delta^2+(\mu+\lambda)^2}}, 0, \frac{\Delta}{\sqrt{\Delta^2+(\mu+\lambda)^2}}, 0)^T$ respectively. So, in this region, we will have $\langle S_z(0)\rangle = -1$ and $Q = -1$, which means the system has a topologically nontrivial spin texture. We see that the sudden changes of $S_z(0)$ is due to the band inversion transition across the critical point.

Typical spin textures for $h < h_c$ and $h > h_c$ are plotted in Fig. 4.2(a) and (b), re-

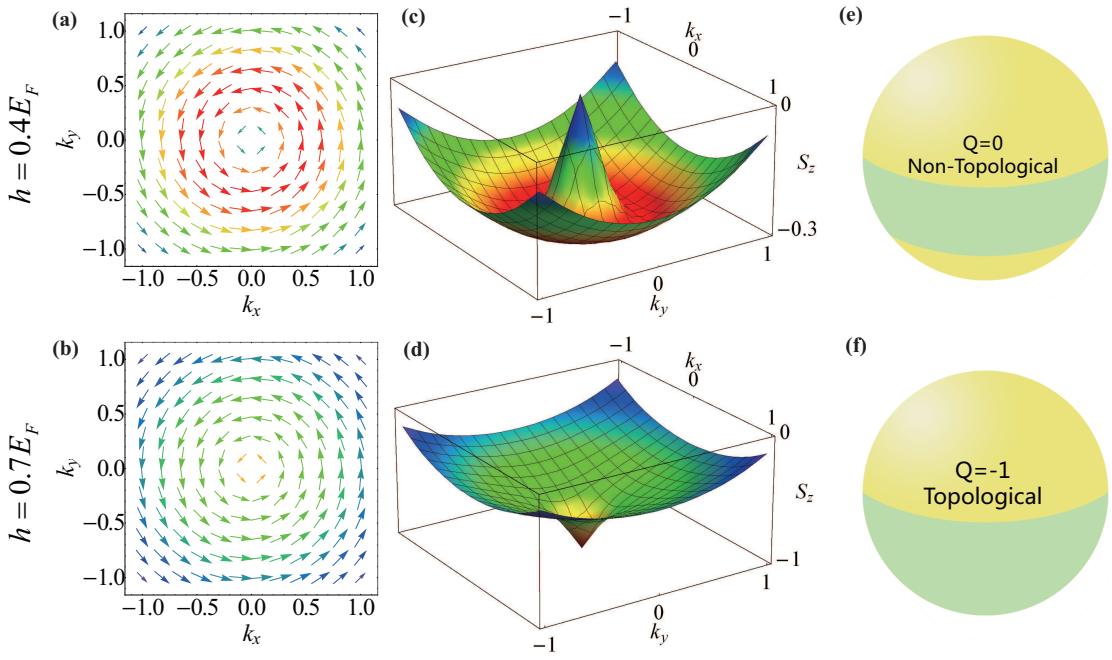

Figure 4.2 : Topological properties of the spin texture. (a), (b) Spin texture for the normalized spin vector $\mathbf{s}$ (Skyrmion) of the ground state of a non-topological state ($h = 0.4E_F$) and a topological state ($h = 0.7E_F$), respectively. For the parameter we used, $h_c \sim 0.545E_F$, see also Fig. 4.1 (a). The corresponding z-component of the spin vector, $S_z(\mathbf{k})$, are plotted in (c) and (d). (e) and (f) represent schematic plot of the mapping from the 2D momentum space onto a unit sphere for non-topological phase and topological phase, respectively. The darker green region represents the area swept out by the spin vector when the momentum $\mathbf{k}$ varies from 0 to ∞.

spectively. The topology of the system can be characterized by the Skyrmion number defined as

$$Q = \int \frac{d^2\mathbf{k}}{2\pi} \left[\mathbf{s} \cdot (\partial_{k_x} \mathbf{s} \times \partial_{k_y} \mathbf{s}) \right], \tag{4.6}$$

where $\mathbf{s}(\mathbf{k}) = \langle \mathbf{S}(\mathbf{k}) \rangle / |\langle \mathbf{S}(\mathbf{k}) \rangle|$ is the normalized spin vector, which maps the 2D momentum space to a unit sphere S^2. In this sense, Q is nothing but the number of times the spin vector wraps around the south hemisphere. Note that for momenta with fixed magnitude $|\mathbf{k}|$, s_x and s_y always sweep out a circle parallel to the equator. In the topologically trivial regime, we always have $s_z(0) = 0$, see Fig. 4.2(c). Hence as $|\mathbf{k}|$ increases from zero, $\mathbf{s}$ begins at the equator, descends toward the south pole and then returns to the equator as $|\mathbf{k}| \to \infty$. Thus in this regime, $\mathbf{s}(\mathbf{k})$ initially sweeps out the darker green region in the southern hemisphere of Fig. 4.2(e), but then unsweeps the same area, resulting in a vanishing winding number $Q = 0$. In contrast, in the topologically nontrivial regime, we have $s_z(0) = -1$, see Fig. 4.2(d). Hence as $|\mathbf{k}|$ increases from zero to infinity, the spin vector covers the entire southern hemisphere exactly once, as shown schematically in Fig. 4.2(f), which leads to a nontrivial winding number $Q = -1$. The sudden change of spin polarization is due to band inversion transition across the critical point.

It is worth pointing out that, for any quench, we always have $\frac{\partial}{\partial t}\langle S_z(0,t) \rangle = 0$, regardless of the initial and final values of h. When $\mathbf{k} = 0$, we have $i\partial_t q_\pm = \Delta^* v_\pm - h q_\pm$ and $i\partial_t p_\pm = \Delta^* u_\pm + h q_\pm$. Substituting these equations into $\dot{S}_z(t) = \sum_{\eta=\pm} \dot{q}_\eta^* q_\eta + q_\eta^* \dot{q}_\eta - \dot{p}_\eta^* p_\eta + p_\eta^* \dot{p}_\eta$, we immediately find that $\dot{S}_z(t) = 0$. Thus we have the important conclusion that $\langle S_z(0,t) \rangle = \langle S_z(0,0) \rangle$, which means Q remains unchanged over time. We need to emphasize that this spin texture is totally different from the pseudospin texture discussed in Ref. [133]. The *true* spin texture discussed in this work can be directly probed in experiments from the time-of-flight imaging [141,168,169] in which

$Q(t) = Q(0)$ can be directly verified.

Therefore, Q is unchanged over time after the quench. We can see that, the Q and W are equivalent at equilibrium, but their dynamics after a sudden quench are different. As shown below, W, which describes the topology of the full spectrum of the Hamiltonian, will evolve in time, while Q, which reflects the topological nature of the the state itself, will not. A similar conclusion is found in the study of the quenched p-wave superfluid [133, 134]. We emphasize that the momentum space spin texture studied here can be measured in cold atom experiments using the standard time-of-flight technique [141, 168, 169].

4.2 Quench Dynamics

4.2.1 Time-dependent Bogoliubov-de Gennes equation

The coherent dynamics of this model cannot be exactly solved due to the lack of any nontrivial symmetry [161], thus it should be computed numerically.

The initial value of $\mu(0)$ and $\Delta(0)$ can be directly determined by solving the gap equation and number equation self-consistently, with which the initial wavefunction at $t = 0^-$ is constructed. Then we take the initial values as $\Delta(0)$ and $\mu(0)$ and plug them back into

$$\begin{pmatrix} \xi_{\mathbf{k}} + h & \lambda(k_x - ik_y) & 0 & -\Delta(0) \\ \lambda(k_x + ik_y) & \xi_{\mathbf{k}} - h & \Delta(0) & 0 \\ 0 & \Delta(0) & -(\xi_{\mathbf{k}} + h) & \lambda(k_x + ik_y) \\ -\Delta(0) & 0 & \lambda(k_x - ik_y) & -(\xi_{\mathbf{k}} - h) \end{pmatrix} \begin{pmatrix} u^\eta_{\mathbf{k}}(0) \\ \alpha^\eta_{\mathbf{k}}(0) \\ \beta^\eta_{\mathbf{k}}(0) \\ v^\eta_{\mathbf{k}}(0) \end{pmatrix} = E^\eta_{\mathbf{k}} \begin{pmatrix} u^\eta_{\mathbf{k}}(0) \\ \alpha^\eta_{\mathbf{k}}(0) \\ \beta^\eta_{\mathbf{k}}(0) \\ v^\eta_{\mathbf{k}}(0) \end{pmatrix} \tag{4.7}$$

and straightforwardly diagonalize it for given momentum $\mathbf{k}$ and obtain wave-functions of $u^\eta_{\mathbf{k}}$, $\alpha^\eta_{\mathbf{k}}$, $\beta^\eta_{\mathbf{k}}$, $v^\eta_{\mathbf{k}}$ and eigenenergy $E^\eta_{\mathbf{k}}$.

In this case, the topological phase can be realized when [144, 145],

$$h^2 > \mu^2 + \Delta^2. \tag{4.8}$$

However, this phase can only be realized in the BEC-BCS crossover regime. A simple but intuitive argument is that, in both the BEC and BCS limit, $\mu^2 \gg \Delta^2$, thus in these two limits, $|h| \gg |\Delta|$, and the pairing can be easily destroyed by the Pauli depairing effect. As a result, the topological phase can only be realized in a small parameter window near the strong coupling regime. In the following, we choose the Zeeman field as the quench parameter instead of others, because it is the most easily controllable parameter in the current experiments [138–143]. Eq. (4.8).

Immediately after the quench of the Zeeman field, as a reasonable but general assumption, the system's wavefunction takes the BCS form

$$|\Psi(t)\rangle = \prod_{\mathbf{k},\pm} f^{\dagger}_{\mathbf{k}\pm}\Psi_{\mathbf{k}}|0\rangle, \tag{4.9}$$

where the dynamics of the vectors $f_{\mathbf{k}\pm}(t)$ are determined by the following time-dependent BdG equation

$$i\frac{\partial}{\partial t}f_{\mathbf{k}\pm} = \mathcal{M}_{\mathbf{k}}f_{\mathbf{k}\pm}. \tag{4.10}$$

Here $\mathcal{M}_{\mathbf{k}}$ is the time-dependent BdG Hamiltonian in which $\Delta(t)$ now evolves in time after the quench. In fact Eq. (4.10) is equivalent to

$$i\partial_t|\Psi(t)\rangle = H|\Psi(t)\rangle. \tag{4.11}$$

The above semiclassical equation can be derived from $\delta_{\Psi^*}\mathcal{L} = 0$, with $\mathcal{L} = \langle\Psi|i\partial_t - H|\Psi\rangle$.

As a technical note, we rewrite Eq. 4.10 in more details here. With the initial

values (as benchmarks), we quench value of h and evolve the functions according to

$$\begin{pmatrix} \xi_{\mathbf{k}}+h & \lambda(k_x-ik_y) & 0 & -\Delta(t) \\ \lambda(k_x+ik_y) & \xi_{\mathbf{k}}-h & \Delta(t) & 0 \\ 0 & \Delta^*(t) & -(\xi_{\mathbf{k}}+h) & \lambda(k_x+ik_y) \\ -\Delta^*(t) & 0 & \lambda(k_x-ik_y) & -(\xi_{\mathbf{k}}-h) \end{pmatrix} \begin{pmatrix} u^\eta_{\mathbf{k}}(t) \\ \alpha^\eta_{\mathbf{k}}(t) \\ \beta^\eta_{\mathbf{k}}(t) \\ v^\eta_{\mathbf{k}}(t) \end{pmatrix} = i\frac{\partial}{\partial t} \begin{pmatrix} u^\eta_{\mathbf{k}}(t) \\ \alpha^\eta_{\mathbf{k}}(t) \\ \beta^\eta_{\mathbf{k}}(t) \\ v^\eta_{\mathbf{k}}(t) \end{pmatrix} \tag{4.12}$$

where

$$\Delta(t) = -\frac{U_0}{2}\frac{1}{V}\sum_{\eta=1}^{4}\sum_{\mathbf{k}}\left[u^\eta_{\mathbf{k}}(t)v^{\eta*}_{\mathbf{k}}(t)f(E^\eta_{\mathbf{k}}(t=0)) + \alpha^\eta_{\mathbf{k}}(t)\beta^{\eta*}_{\mathbf{k}}(t)f(-E^\eta_{\mathbf{k}}(t=0))\right] \tag{4.13}$$

where we need to use renormalization $1/U_0 = m/(4\pi\hbar^2 a_s) - \sum_{\mathbf{k}} 1/2\epsilon_{\mathbf{k}}$.

For two dimensional system, the renormalization is given by

$$\begin{aligned} \frac{1}{U_0} &= -\frac{2\pi}{(2\pi)^2}\int_0^{k_c} kdk\frac{1}{E_b+2\epsilon_k} && (4.14)\\ &= -\frac{1}{2\pi}\frac{1}{4}\log(2k^2+E_b)|_0^{k_c} && (4.15)\\ &= -\frac{1}{8\pi}\log(1+\frac{2k_c^2}{E_b}) && (4.16) \end{aligned}$$

where I have used $\frac{1}{V}\sum_{\mathbf{k}} = \frac{1}{(2\pi)^2}\int_0^{k_c} kdk\int_0^{2\pi} d\theta$ and as for BdG matrix elements, $k_x = k\cos\theta$, $k_y = k\sin\theta$.

As a result of particle-hole symmetry, integration in $\Delta(t)$ can be reduced to radial direction only, since the relative phase between k_x and k_y would not matter.

$$\Delta(t) = -\frac{1}{2U_0}\frac{1}{V}\sum_{\eta=1}^{4}\frac{1}{2\pi}\int_0^{k_c} kdk\left[u^\eta_{\mathbf{k}}(t)v^{\eta*}_{\mathbf{k}}(t)f(E^\eta_{\mathbf{k}}(t=0)) + \alpha^\eta_{\mathbf{k}}(t)\beta^{\eta*}_{\mathbf{k}}(t)f(-E^\eta_{\mathbf{k}}(t=0))\right] \tag{4.17}$$

To get accurate time-dependent results, the momentum integral meshgrid number is expected to be above 2000 points, and time step shall be around 0.0005.

4.2.2 Phase diagram of the quench dynamics

We now turn to our discussion on the quench dynamics. As in Refs. [133, 134], we capture the dynamics using a phase diagram presented in Fig. 4.3. The phase diagram contains three different dynamical phases (which should not be confused with the equilibrium phases of a many-body system), identified by the distinct long-time asymptotic behavior of the order parameter in the parameter space spanned by the initial and final values of the Zeeman field h_i and h_f. The three phases are labeled as phase I, II and III in Fig. 4.3.

In phase I (the undamped oscillation phase), the magnitude of the order parameter oscillates periodically without damping, although the wavefunction does not recover itself periodically. Away from the phase boundaries, the oscillation amplitude can be as large as a significant fraction of E_F (see Fig. 4.4 below). $|\Delta(t)|$ shows persistent oscillations, which is from the collisionless coherent dynamics. The dark blue dashed line separates phase I into non-topological Floquet state denoted as $\mathrm{NTS_{Floquet}}$ and topological Floquet state labeled as $\mathrm{TS_{Floquet}}$.

In phase II (the damped oscillation), the order parameter exhibits damped oscillation with a power-law decay to a finite value. $|\Delta(t)| \to \Delta_\infty$, a nonzero constant value, which serves as the basic parameter to determine the long-time asymptotic behavior. The orange dashed lines are the non-equilibrium extension of the topological phase transition at $h = h_c$, which separates phase II into two parts, NTS and TS accordingly. Inside NTS (TS) region, the energy spectrum of quasi-stationary Hamiltonian is trivial (nontrivial) without (with) topologically protected edge modes. $W = 0$ or 1 marks the topological index at $t = +\infty$.

In phase III (the overdamped phase), the order parameter decays to zero exponentially. We also show that within phase I and II, there exists dynamical topological

regimes where topological edge states emerge in the asymptotic limit. $|\Delta(t)| \to 0$ due to strong dephasing from the out-of-phase collisions. We need to emphasize that the transition between various phases is smooth. However, these different phases are well distinguished not very close to the boundaries (distance $> 0.1\ E_F$). All other parameters are identical to Fig. 4.1. We have repeated the same calculation for several different values of SO coupling strengths and found no qualitative differences.

Next, we shall discuss the properties of each phase in more details.

4.2.3 Phase I

In Fig. 4.4 we plot the dynamics of the magnitude of the order parameter for a typical point in phase I (point A in Fig. 4.3), from which we find that $|\Delta(t)|$ oscillates asymptotically as [124]

$$|\Delta(t)| = \Delta_+ \mathrm{dn}[\Delta_+(t - \tau_0/2), \kappa], \quad \kappa = 1 - \Delta_-^2/\Delta_+^2, \tag{4.18}$$

where $\mathrm{dn}[u, k]$ is the periodic Jacobi elliptic function, and Δ_+ and Δ_- are the maximum and minimum value of $|\Delta(t)|$, respectively. This expression was first derived by Barankov *et al.* for the weakly-interacting conventional BCS superfluid [124]. The fitted result using this empirical formula are presented in Fig. 4.4 as dashed line, which fits the numerical results surprisingly well. This phase can be understood from the picture of synchronization effect. In the integrable models [124, 128, 134], the Hamiltonian is mapped into a classical spin model parameterized by $\mathbf{k}$ and the spin dynamics can be described as a precession around an effective Zeeman field, which is constructed by order parameter and the kinetic energy. For a large order parameter such that the contribution from the kinetic energy is small, the effective Zeeman field is essentially the same for different Cooper pairs and as a result, all Cooper pairs precess with roughly the same frequency and phase coherence is therefore maintained.

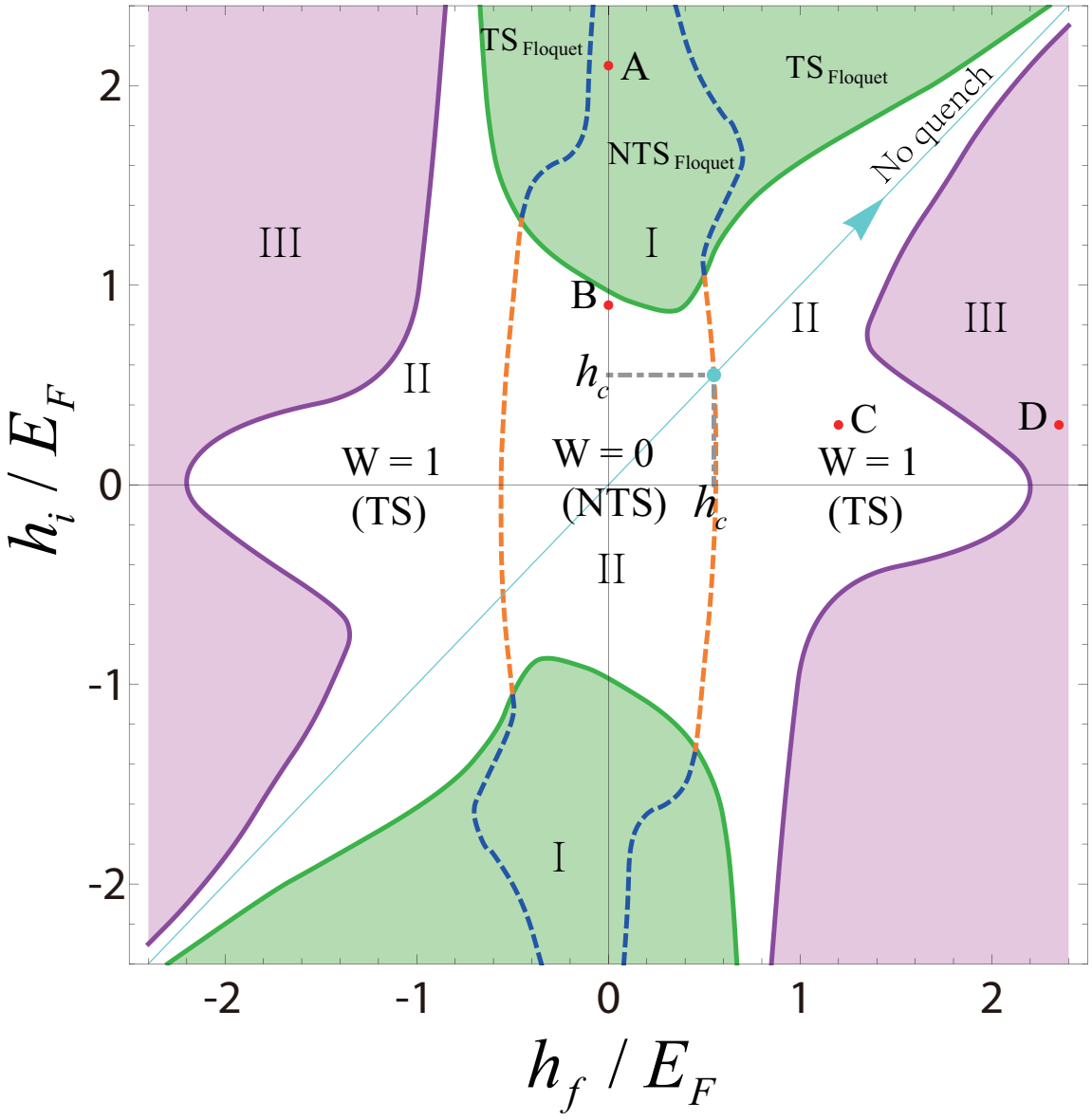

Figure 4.3 : Phase diagram of the quenched spin-orbit coupled superfluid condensate. The different phases in this figure are obtained by the long-time asymptotic behavior of the order parameter upon the quench of the Zeeman field from initial value h_i to final value h_f. The diagonal light blue line, with $h_i = h_f$, is the case without quench, thus the quantum state is unchanged. h_c marks the quantum critical point separating the topological superfluid and non-topological superfluid in the equilibrium ground state, which is determined by $h_c^2 = \Delta^2 + \mu^2$. Three different dynamical phases observed in this system are labeled with I, II, and III by green, white and purple shaded areas, respectively.

Here we reinterpret the synchronization effect as a consequence of the condensate formed by Bose condensed Cooper pairs. The condensate ensure phase coherence of the constituent Cooper pairs. This reinterpretation is fully consistent with the spin precession picture, however it now becomes clear that the synchronization effect does not rely on whether the system is integrable or not. To substantiate this reinterpretation, we first notice that the Phase I region occurs in the parameter space where $|h_f| < |h_i|$, for which shortly after the quench the order parameter is increased (see Fig. 4.4). Second, we artificially include a finite temperature T in the post-quench dynamical evoltion. For small T, the behavior of the order parameter remains essentially the same as the zero-temperature result. For large T, however, the order parameter no longer exhibits undamped oscillation, but rather decays to a constant. For the parameters used in Fig 4.4, this occurs when $T \geqslant 0.2E_F$. Such a behavior can be easily undersood as a sufficiently large T destroys the condensate and hence phase coherence between different Cooper pairs is lost.

To gain more insights into this persistent oscillating behavior, it is helpful to investigate the spin population dynamics. We found that, as shown in the inset of Fig. 4.4, the persistent oscillation of the order parameter is not accompanied by a similar oscillation in the spin population. In fact, after the quench S_{p} exhibits damped oscillation and quickly reaches a steady-state value. Recently, the dynamics of the spin polarization after quench in a Fermi gas above the critical temperature has been measured in experiments [140]. The decay of the spin polarization can be attributed to the interband Rabi oscillation, in which, different momentum state has slightly different Rabi frequency, such that destructive interference gives rise to the damping phenomenon.

Equation (4.18) provides an empirical formula for the asymptotic dynamics of the

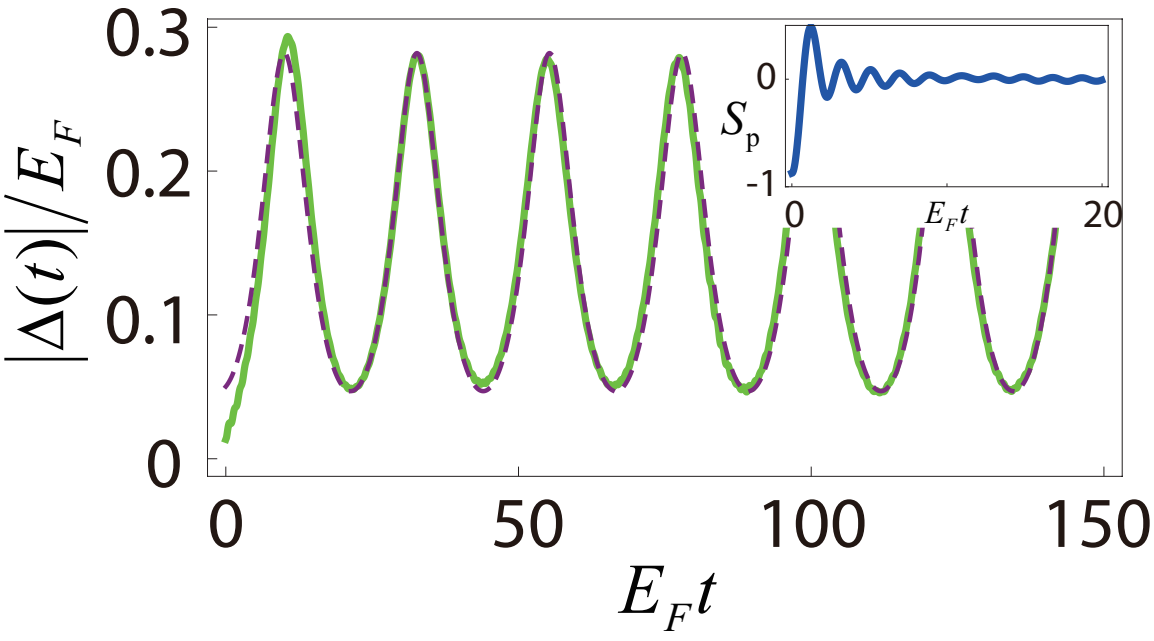

Figure 4.4 : Dynamics of order parameter and spin polarization in phase I. We plot the result for point A $(h_i = 2.1, h_f = 0)E_F$ in Fig. 4.3 with green solid line. The purple dashed line is the best fit using Eq. (4.18) with fitted parameter $\Delta_+ = 0.282E_F$, $\Delta_- = 0.047E_F$. Inset shows the dynamics of spin polarization after quench, which quickly approaches a constant at the time scale of few $1/E_F$.

$|\Delta(t)|$. The order parameter itself behaves like $\Delta(t) = |\Delta(t)|e^{-i2\mu_\infty t+i\varphi(t)}$ [133, 134], where $\varphi(t)$ (modulo 2π) is also a periodic function with commensurate period to $|\Delta(t)|$. The phase factor's linear piece in time, $-2\mu_\infty t$, can be gauged out by a unitary transformation [134]. After the gauge transformation, we obtain a BdG Hamiltonian $\tilde{\mathcal{M}}_{\mathbf{k}}(t)$ that is periodic in time. For such a periodic system, we may invoke the Floquet theorem to examine its Floquet spectrum.

For a general periodically driven Hamiltonian $\hat{H}_{\mathbf{k}}(t)$ with period T, that is, $\hat{H}_{\mathbf{k}}(t) = \hat{H}_{\mathbf{k}}(t+T)$, we invoke the Floquet theorem to examine its Floquet spectrum. We can define the Floquet wavefunction as $|\varphi_{\mathbf{k}}(t)\rangle = e^{-i\varepsilon_{\mathbf{k}}t}|\Psi_{\mathbf{k}}(t)\rangle$, where ε is the quasiparticle spectrum and $|\Psi_{\mathbf{k}}(t)\rangle = |\Psi_{\mathbf{k}}(t+T)\rangle$, i.e., the wavefunction in the time-domain is also a periodic function. We are able to expand $|\Psi_{\mathbf{k}}(t)\rangle = \sum_n \Psi_{n,\mathbf{k}} e^{in2\pi t/T}$. Then we can map the time-dependent model to the time-independent model $\mathcal{H}_{4(2N+1)\times 4(2N+1)}\Psi_{\mathbf{k}} = \varepsilon\Psi_{\mathbf{k}}$, where $\Psi_{\mathbf{k}} = (\Psi_{-N,\mathbf{k}}, \Psi_{-N+1,\mathbf{k}}, \cdots, \Psi_{N-1,\mathbf{k}}, \Psi_{N,\mathbf{k}})^T$ with N being a truncation of frequencies. This model has particle-hole symmetry defined as $\Sigma = \mathbb{I}_{2N+1} \otimes \sigma_x K$ with K being the conjugate operator and $\mathbb{I}_{2N+1}$ being an identity matrix. In our two dimensional model, this equivalent model belongs to topological D class with index $\mathbb{Z}$.

To determine whether the system is topological in the Floquet sense, we calculate the spectrum $\varepsilon_{\mathbf{k}\pm}$ in a strip by adding a hard-wall boundary condition in the x-direction. In the long-time limit, the order parameter in phase I approaches $\Delta(t) = |\Delta_\infty(t)|e^{-2i\mu_\infty t+i\varphi(t)}$, where $|\Delta_\infty(t)|$ is periodic in time, e.g. see Fig. 4.4. We make a gauge transformation, similar to that in Eq. (4.28), by identifying μ_∞ as the effective chemical potential, and we obtain $\tilde{\mathcal{M}}_{\mathbf{k}}(t)$ from Eq. (4.2) by replacing μ with μ_∞ and Δ with $|\Delta(t)|e^{i\varphi(t)}$. Obviously, $\tilde{\mathcal{M}}_{\mathbf{k}}(t) = \tilde{\mathcal{M}}_{\mathbf{k}}(t+T)$, where T is the period determined by both $|\Delta(t)|$ and $\varphi(t)$. Now we assume the eigenvectors of the above

effective Hamiltonian to be $\tilde{f}_{\mathbf{k}\pm}(t) = \Phi_{\mathbf{k}\pm}(t)e^{-i\varepsilon_{\mathbf{k}\pm}t}$, where $\Phi_{\mathbf{k}\pm}(t+T) = \Phi_{\mathbf{k}\pm}(t)$. Then we have

$$\left(\tilde{\mathcal{M}}_{\mathbf{k}}(t) - i\partial_t\right)\Phi_{\mathbf{k}\pm}(t) = \varepsilon_{\mathbf{k}\pm}\Phi_{\mathbf{k}\pm}(t), \tag{4.19}$$

where $\varepsilon_{\mathbf{k}\pm}$ is the quasiparticle dispersion. Similar to the discussion of dynamical edge state in the previous section, we impose a hard wall boundary condition along x direction with length L. We expand the wavefunction in the following way,

$$\Phi_{\mathbf{k}\pm} = \mathcal{A}\sum_{n=1}^{N_{\max}}\sum_{m=-M_{\max}}^{M_{\max}}\sin(\frac{n\pi x}{L})e^{\frac{2im\pi t}{T}}\begin{pmatrix}\tilde{u}_{nm}^{\pm}\\ \tilde{v}_{nm}^{\pm}\\ \tilde{p}_{nm}^{\pm}\\ \tilde{q}_{nm}^{\pm}\end{pmatrix}, \tag{4.20}$$

where $N_{\max}$ and $M_{\max}$ are basis cutoff for the spatial and temporal expansion and $\mathcal{A} = (2/LT)^{1/2}$. Then Eq. (4.19) can be recast into a sparse self-adjoint complex matrix form of size $(4N_{\max} \times (2M_{\max}+1)) \times (4N_{\max} \times (2M_{\max}+1))$. The direct diagonalization of this matrix gives rise to Floquet spectrum. In practice, since we are only concerned with the eigenenergies close to zero, we could utilize the shift and invert spectral transformation and compute only a portion of eigenenergies using the ARPACK library routines. For instance, we choose cutoffs as $N_{\max} = 200$ and $M_{\max} = 15$ and only compute 500 eigenvalues around zero-energy out of total 24800 ones for a given k_y. The results are presented in Fig. 4.5. The robustness of these protected edge states are also examined by slightly changing the model parameters, in which we find that the linear dispersions of these edge states are unchanged.

Two examples of the spectrum are plotted in Fig. 4.5. In the example shown in Fig. 4.5(a), the spectrum is gapped, corresponding to a topologically trivial Floquet state. By contrast, the spectrum shown in Fig. 4.5(b), exhibits gapless modes at $k_y = 0$. An enlarged view of these modes are presented in Fig. 4.5(c). Note that

due to the finite-size effect, the energies of these gapless modes are not exactly zero, but on the order of $10^{-3}E_F$ and are well separated from the rest of the spectrum. In Fig. 4.5(d), we show the evolution of the wavefunctions of one pair of the gapless modes over one oscillation period. As one can see, the gapless modes are well localized at the boundaries. Furthermore, we have verified that their wavefunctions satisfy the requirement for Majorana modes. Hence these gapless excitations represent the Majorana edge modes and the system can therefore be characterized as a topological Floquet state. We have also verified that the edge states with the same chirality are localized at the same boundary. Thus no direct coupling is allowed between them due to particle-hole symmetry.

The intrinsic particle-hole symmetry ensures that the zero energy states are Majorana fermions at $k_y = 0$ in a strip along y direction. The wavefunction of these Majorana fermions can be constructed using $\psi = \psi_i \pm \Sigma\psi_i$, where ψ_i is the quasiparticle wavefunctions with energy approach zero. We can observe: (1) The edge states have well-defined chirality which are defined as $\Sigma\psi = \pm\psi$; (2) These edge modes are well-localized at the boundaries when the strip width is much larger than the coherent length; (3) All the edge states with the same chirality are localized at the same boundary; (4) For a general random potential $\mathcal{V}$, the matrix elements $\langle\psi_i|\mathcal{V}|\psi_j\rangle \equiv 0$ when ψ_i and ψ_j have the same chirality. Thus these zero energy states are robust against perturbations and the Majorana edge states can always be observed in the topological phase regime. We have numerically verified this point by slightly varying the parameters of the Hamiltonian and we find that the edge modes will not be gapped out without closing the quasiparticle energy gap at zero momentum.

This explains the robustness of the edge modes from a perturbative viewpoint, even though there can exist multiple edge modes near the same boundary. We note

that the number of the edge modes depends on the parameter set. For the example shown in Fig. 4.5(b), there are 7 pair of edge modes. In the phase diagram of Fig. 4.3, inside phase I, the two dark blue dashed lines characterize the topological boundaries, which separate the non-topological states denoted by $\mathrm{NTS_{Floquet}}$ from the topological states denoted by $\mathrm{TS_{Floquet}}$.

As a technical note, we document more details following Eq. 4.20. After phase fixing, the Hamiltonian is periodic in time with period T. According to the Floquet theorem, we have $\begin{pmatrix} U(y,t) \\ A(y,t) \\ B(y,t) \\ V(y,t) \end{pmatrix} = \begin{pmatrix} u(y,t)e^{-i\varepsilon t} \\ \alpha(y,t)e^{-i\varepsilon t} \\ \beta(y,t)e^{+i\varepsilon t} \\ v(y,t)e^{+i\varepsilon t} \end{pmatrix}$ where $|\Phi(t)\rangle \equiv \begin{pmatrix} u(y,t) \\ \alpha(y,t) \\ \beta(y,t) \\ v(y,t) \end{pmatrix}$ and $|\Phi(t+T)\rangle = |\Phi(t)\rangle$. This is because we need to respect the particle-hole symmetry- Then we write $H(t)|\psi(t)\rangle = i\partial_t|\psi(t)\rangle$ as

$$\begin{pmatrix} H-i\partial_t & \Lambda & & -\Delta \\ \Lambda^\dagger & H-i\partial_t & \Delta & \\ & \Delta^* & H+i\partial_t & \Lambda^\dagger \\ -\Delta^* & & \Lambda & H+i\partial_t \end{pmatrix} \begin{pmatrix} u(y,t) \\ \alpha(y,t) \\ \beta(y,t) \\ v(y,t) \end{pmatrix} = i\hbar\frac{\partial}{\partial t} \begin{pmatrix} u(y,t) \\ \alpha(y,t) \\ \beta(y,t) \\ v(y,t) \end{pmatrix} \tag{4.21}$$

We expand the wavefunction in both position and time as (assuming hard wall boundary condition along y direction)

$$|\Phi(t)\rangle \equiv \begin{pmatrix} u(y,t) \\ \alpha(y,t) \\ \beta(y,t) \\ v(y,t) \end{pmatrix} = \sum_{p=-P_{max}}^{P_{max}} \sum_{n=1}^{N_{max}} \sqrt{\frac{2}{L}} \sin(\frac{n\pi y}{L}) \frac{1}{\sqrt{T}} \exp(+i\frac{2p\pi t}{T}) \begin{pmatrix} u_{np} \\ \alpha_{np} \\ \beta_{np} \\ v_{np} \end{pmatrix} \tag{4.22}$$

where $N_{max} = 200$ and $P_{max} = 10$ are good cutoffs. The Hamiltonian can be recast into a self-adjoint matrix form of size $(N_{max} \times (2P_{max}+1)) \times (N_{max} \times (2P_{max}+1))$,

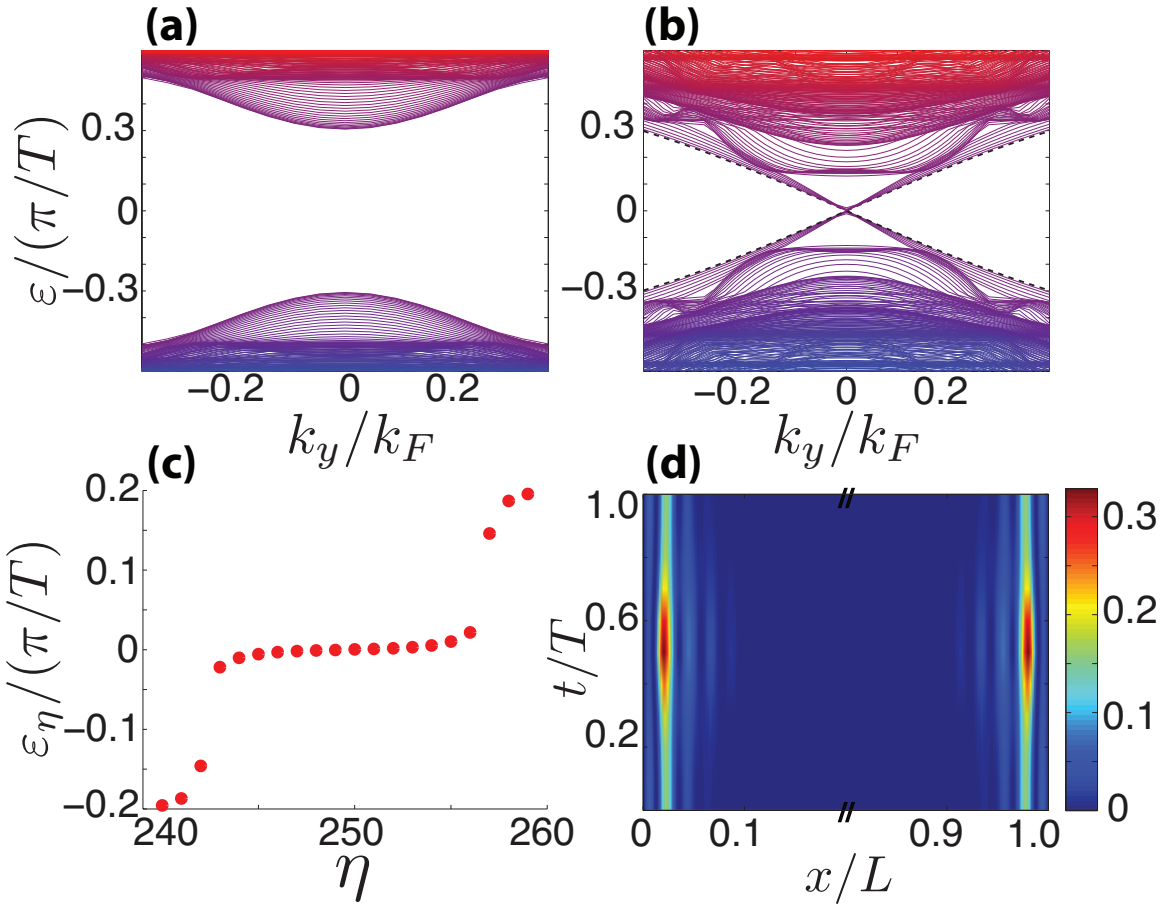

Figure 4.5 : Dynamical Floquet state in a strip for phase I. Imposing a strip geometry, we find the quasiparticle spectrum is trivial (gapped) in (a) $(h_i = 1.5, h_f = 0.3)E_F$ and topologically nontrivial (gapless) in (b) $(h_i = 2.1, h_f = 0.9)E_F$. Seven pairs of edge states with linear dispersion at small $\mathbf{k}$ have been identified in (b), which is a direct manifestation of bulk topology based on bulk-edge correspondence. (c) An enlarged view of the low-lying quasiparticle spectrum at $k_y = 0$. Here n is the index for quasiparticle states. (d) Evolution of the wavefunction for one pair of edge states (the two symbols shown in purple in (c), $n = 249$ and $n = 250$) in one full period. Here we only plot the $|u|^2$ component of the wavefunction, and the other components show a similar behavior, i.e., they are also well localized near the boundary.

we have

$$\begin{aligned}
\left(k_x^2-\mu_\infty+h+(\frac{m\pi}{L})^2+\frac{2p\pi}{T}\right)u_{mp}+\lambda k_x\alpha_{mp}-\sum_{n\neq m}\Lambda_{mn}\alpha_{np}-\sum_q\Gamma^{(1)}_{pq}v_{mq} &= Eu_{mp}\\
\lambda k_x u_{mp}+\sum_{n\neq m}\Lambda_{mn}u_{np}+\left(k_x^2-\mu_\infty-h+(\frac{m\pi}{L})^2+\frac{2p\pi}{T}\right)\alpha_{mp}+\sum_q\Gamma^{(1)}_{pq}\beta_{mq} &= E\alpha_{mp}\\
\sum_q\Gamma^{(2)}_{pq}\alpha_{mq}-\left(k_x^2-\mu_\infty+h+(\frac{m\pi}{L})^2+\frac{2p\pi}{T}\right)\beta_{mp}+\lambda k_x v_{mp}+\sum_{n\neq m}\Lambda_{mn}v_{np} &= E\beta_{mp}\\
-\sum_q\Gamma^{(2)}_{pq}u_{mq}+\lambda k_x\beta_{mp}-\sum_{n\neq m}\Lambda_{mn}\beta_{np}-\left(k_x^2-\mu_\infty-h+(\frac{m\pi}{L})^2+\frac{2p\pi}{T}\right)v_{mp} &= Ev_{mp}
\end{aligned}$$

where,

$$\Gamma^{(1)}_{pq} = \int_0^T\frac{dt}{T}|\Delta_\infty(t)|\exp\left(+i\frac{2\pi}{T}(q-p)t+i\phi(t)\right) \tag{4.23}$$

$$\Gamma^{(2)}_{pq} = \int_0^T\frac{dt}{T}|\Delta_\infty(t)|\exp\left(-i\frac{2\pi}{T}(q-p)t-i\phi(t)\right) \tag{4.24}$$

$$\Lambda_{mn} = \frac{2\lambda mn}{L}\frac{(1-(-1)^{m+n})}{(m^2-n^2)} \tag{4.25}$$

The self-adjoinct property of the matrix can be easily checked by noting $\Lambda_{mn}=-\Lambda_{nm}$ and $\Gamma^{(1)*}_{pq}=\Gamma^{(2)}_{qp}$. Instead of performing serials of exponential matrix multiplication, we construct the matrix once and diagonalize it directly to examine Floquet spectrum within the range of $[-\frac{\pi}{T},\frac{\pi}{T}]$. However, the price to pay is that the matrix size becomes very large, with $S_{max}\times S_{max}$ where $S_{max}=(2P_{max}+1)4N_{max}$. Of note is that the matrix is not only Hermitian but also sparse, and the degree of denseness can be calculated by first calculating the number of nonzero entries $(2P_{max}+1)(4N_{max}+4N_{max}+4(4N_{max}\times 4N_{max}))+2P_{max}(2P_{max}+1)4N_{max}=8N_{max}(2P_{max}+1)(1+8N_{max}+P_{max})$and the ratio of nonzero entries to the total matrix elements is $\frac{8N_{max}+P_{max}+1}{2N_{max}(2P_{max}+1)}$.

4.2.4 Phase II

In this damped phase, the magnitude of the order parameter undergoes damped oscillation and tends to a finite equilibrium value. Two examples (corresponding to

points B and C in Fig. 4.3) are shown in Fig. 4.6. Here the magnitude of the order parameter can be described by the following power-law decay function [123, 125, 126, 128]

$$|\Delta(t)| = \Delta_\infty + \frac{A}{t^\nu}\cos(2E_{\rm g}^\infty t + \theta), \tag{4.26}$$

where Δ_∞ is the magnitude of the order parameter in the asymptotic limit, which in general does not equal to the order parameter Δ_f determined by the Zeeman field h_f at equilibrium. $E_{\rm g}^\infty$ is the minimal band gap of the effective Hamiltonian at $t \to \infty$. It should be pointed out that, unlike the conventional BCS model, $E_{\rm g}^\infty$ does not in general equal to Δ_∞ in the current model, due to the presence of the SO coupling and the Zeeman field. The second term on the r.h.s. of Eq. (4.26) gives rise to the decay of the order parameter. The exponent ν, characterizing the power-law decay, is not a universal constant in this model. This is in distinct contrast to the conventional BCS model, where $\nu = 1/2$ [123, 126, 128] in the BCS limit, and $\nu = 3/2$ [125] in the Bose-Einstein Condensation (BEC) limit.

In this phase, the order parameter behaves as $\Delta(t) = \Delta_\infty e^{-i2\mu_\infty t}$ in the asymptotic limit [133, 134]. Again we can gauge out the phase factor linear in time and treat μ_∞ as an effective chemical potential [134]. We can therefore construct a time-independent BdG Hamiltonian by replacing the chemical potential and order parameter in Eq. (4.2) with μ_∞ and Δ_∞, respectively. This is still a dynamical phase because $\mu_\infty \neq \mu_f$, and $\Delta_\infty \neq \Delta_f$, where Δ_f and μ_f are equilibrium order parameter and chemical potential with Zeeman field h_f. For example, for point B, we have $\Delta_f = 0.662E_F$ and $\mu_f = 0.199E_F$, whereas numerically we obtain $\Delta_\infty \approx 0.456E_F$ and $\mu_\infty \approx -0.019E_F$. Given the asymptotic time-independent BdG Hamiltonian, the region of the dynamical topological phase can be determined by the condition

$$h_f^2 > |\Delta_\infty|^2 + \mu_\infty^2, \tag{4.27}$$

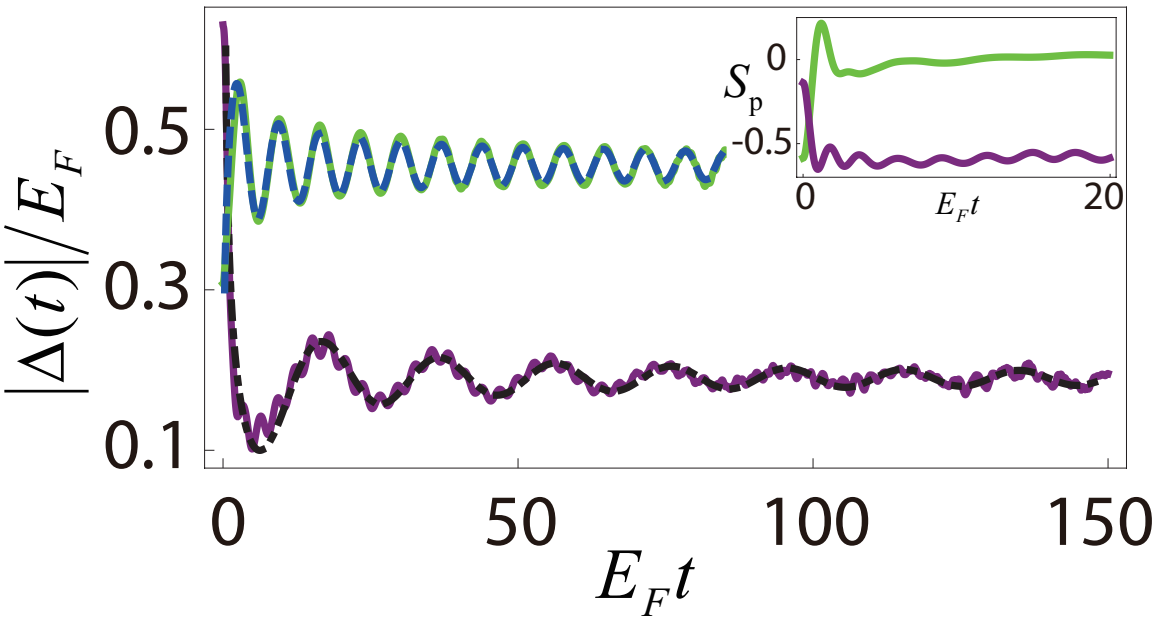

Figure 4.6 : Dynamics of order parameter and spin texture in phase II. Green line represents dynamics for point B ($h_i = 0.9, h_f = 0)E_F$ and the purple line is the result for point C ($h_i = 0.3, h_f = 1.2)E_F$ in Fig. 4.3, and dashed lines represent the fitted curve using Eq. (4.26). For point B (blue dashed line), $\Delta_\infty = 0.455E_F$, $E_g^\infty = 0.456E_F$, $A = -0.16E_F^{1+\nu}$, $\theta = \pi/4$, and $\nu = 1/2$ while for point C (black dot-dashed line), $\Delta_\infty = 0.19E_F$, $E_g^\infty = 0.16E_F$, $A = 0.2E_F^{1+\nu}$, $\theta = \pi/4$ and $\nu = 3/4$. Inset shows the corresponding dynamics of the spin polarization, with green line for point B and red line for point C.

with a topological index $W = 1$, otherwise we have a non-topological dynamical phase with $W = 0$. In the following we will show that dynamical edge state can indeed be observed in the topological regime.

In this regime, the magnitude of the order parameter will gradually approach a constant, while its phase factor oscillates periodically, i.e., $\Delta(t) \to \Delta_\infty e^{-i\mu_\infty t}$ up to a trivial constant, which is the only time-dependent parameter in the BdG Eq. (4.10). This oscillating phase can be gauged out by defining

$$f_{\mathbf{k}\pm} = (\tilde{u}_{\mathbf{k}\pm}e^{-i\mu_\infty t}, \tilde{v}_{\mathbf{k}\pm}e^{-i\mu_\infty t}, \tilde{p}_{\mathbf{k}\pm}e^{+i\mu_\infty t}, \tilde{q}_{\mathbf{k}\pm}e^{+i\mu_\infty t})^T e^{-iE_{\mathbf{k},\pm}t},$$

where $\tilde{f}_{\mathbf{k}\pm} = (\tilde{u}_{\mathbf{k}\pm}, \tilde{v}_{\mathbf{k}\pm}, \tilde{p}_{\mathbf{k}\pm}, \tilde{q}_{\mathbf{k}\pm})^T$. Inserting this wavefunction to Eq. (4.10), we find that

$$\tilde{\mathcal{M}}_{\mathbf{k}}\tilde{f}_{\mathbf{k}\pm} = E_{\mathbf{k},\pm}\tilde{f}_{\mathbf{k}\pm}, \tag{4.28}$$

where $\tilde{\mathcal{M}}_{\mathbf{k}}$ is identical to Eq. (4.2) except that $\mu = \mu_\infty$ and $\Delta = \Delta_\infty$. We immediately see that μ_∞ is the effective chemical potential of the model in the quasi-equilibrium condition. Note that this phase is still dynamical phase because the $\mu_\infty \neq \mu_f$ and $\Delta_\infty \neq \Delta_f$, where μ_f and Δ_f are equilibrium chemical potential and order parameter with Zeeman field h_f; see our numerical results in the main text. We did not observe the abrupt change of order parameter in all our calculations [170].

This model can support dynamical edge state in the topological regime defined by Eq. (4.27). Similar to the analysis in Ref. [144], we can prove exactly that the bulk system is always fully gapped except at the critical point of h_c for $\mathbf{k} = 0$. Thus the closing and reopening of the gap provides important indications for topological phase transition. To see the topological phase transition more clearly, we consider a strip superfluids with length L by imposing hard wall boundary at the x direction. To this end, we replace $k_x \to -i\partial_x$, while k_y remains as a good quantum number. Along the

x direction, we construct the wavefunction using plane wave basis [171]

$$\begin{pmatrix} \tilde{u}(x) \\ \tilde{v}(x) \\ \tilde{p}(x) \\ \tilde{q}(x) \end{pmatrix} = \sum_{n=1}^{N_{\max}} \sqrt{\frac{2}{L}} \sin\left(\frac{n\pi x}{L}\right) \begin{pmatrix} \tilde{u}_n \\ \tilde{v}_n \\ \tilde{p}_n \\ \tilde{q}_n \end{pmatrix}, \tag{4.29}$$

where $N_{\max}$ is the basis cutoff. Upon inserting this ansatz into Eq. (4.28), we can convert the matrix $\tilde{\mathcal{M}}_{\mathbf{k}}$ into a $4N_{\max}$ by $4N_{\max}$ matrix, whose diagonalization directly leads to the protected modes of dynamical edge state dictated by nontrivial topological invariants. Empirically, we found $N_{\max} = 200$ is a good basis cutoff for a long strip with $L = 200k_F^{-1}$. The numerical results are presented in Fig. 4.7.

We have also calculated the Chern number $\mathcal{C} = \frac{i}{2\pi}\sum_{n<0}\int dk_x dk_y \varepsilon^{ab}\langle\partial_{k_a}\psi_{n\mathbf{k}}|\partial_{k_b}\psi_{n\mathbf{k}}\rangle$ of the system, where $n < 0$ means that we sum over all occupied bands of effective time-independent Hamiltonian [see Eq. (4.28)]. We find that $\mathcal{C} = 1$ (0) in the topological (non-topological) regime defined above.

As a technical note, we write out the computation of Chern number in more details here. Berry curvature for hole branch is defined by $\Gamma^{\nu=-} \equiv \gamma_1^{\nu=-} + \gamma_2^{\nu=-}$,

$$\begin{aligned}
\gamma_\eta^\nu &= i(\langle\partial_{k_x}\Phi_\eta^\nu|\partial_{k_y}\Phi_\eta^\nu\rangle - k_x \longleftrightarrow k_y) \\
&= -2\Im\langle\frac{\partial\Psi_\eta^\nu}{\partial k_x}|\frac{\partial\Psi_\eta^\nu}{\partial k_y}\rangle \\
&= -2\Im\left[\begin{pmatrix} \frac{\partial u_{\mathbf{k}}}{\partial k_x} & \frac{\partial\alpha_{\mathbf{k}}}{\partial k_x} & \frac{\partial\beta_{\mathbf{k}}}{\partial k_x} & \frac{\partial v_{\mathbf{k}}}{\partial k_x} \end{pmatrix}^* \cdot \begin{pmatrix} \frac{\partial u_{\mathbf{k}}}{\partial k_y} \\ \frac{\partial\alpha_{\mathbf{k}}}{\partial k_y} \\ \frac{\partial\beta_{\mathbf{k}}}{\partial k_y} \\ \frac{\partial v_{\mathbf{k}}}{\partial k_y} \end{pmatrix}\right]_\eta^\nu \\
&= -2\Im\left(\frac{\partial u_{\mathbf{k}}^*}{\partial k_x}\frac{\partial u_{\mathbf{k}}}{\partial k_y} + \frac{\partial\alpha_{\mathbf{k}}^*}{\partial k_x}\frac{\partial\alpha_{\mathbf{k}}}{\partial k_y} + \frac{\partial\beta_{\mathbf{k}}^*}{\partial k_x}\frac{\partial\beta_{\mathbf{k}}}{\partial k_y} + \frac{\partial v_{\mathbf{k}}^*}{\partial k_x}\frac{\partial v_{\mathbf{k}}}{\partial k_y}\right)_\eta^\nu
\end{aligned}$$

Chern number is defined as

$$C^{\nu=-} = \frac{1}{2\pi}\int d^2\mathbf{k}\sum_{\eta=1,2}\gamma_\eta^{\nu=-} \tag{4.30}$$

where the summation runs over the two occupied quasi-hole bands. The equivalent definition for Berry curvature is

$$\begin{aligned}\gamma_\eta^{\nu=-} &= i\sum_{\nu'\neq\nu}\sum_{\eta'=1,2}\frac{\langle\nu\eta|\partial_{k_x}H_{BdG}|\nu'\eta'\rangle\langle\nu'\eta'|\partial_{k_y}H_{BdG}|\nu\eta\rangle - (k_x\leftrightarrow k_y)}{(E_{\mathbf{k}}^{\nu\eta}-E_{\mathbf{k}}^{\nu'\eta'})^2}\\ &= -2\sum_{\nu'\neq\nu}\sum_{\eta'=1,2}\Im\frac{\langle\nu\eta|\partial_{k_x}H_{BdG}|\nu'\eta'\rangle\langle\nu'\eta'|\partial_{k_y}H_{BdG}|\nu\eta\rangle}{(E_{\mathbf{k}}^{\nu\eta}-E_{\mathbf{k}}^{\nu'\eta'})^2}\end{aligned}$$

Derivatives for Hamiltonian is straightforward,

$$\frac{\partial}{\partial k_x}\begin{pmatrix}\xi_{\mathbf{k}}+h & \lambda(k_x-ik_y) & 0 & -\Delta(t)\\ \lambda(k_x+ik_y) & \xi_{\mathbf{k}}-h & \Delta(t) & 0\\ 0 & \Delta^*(t) & -(\xi_{\mathbf{k}}+h) & \lambda(k_x+ik_y)\\ -\Delta^*(t) & 0 & \lambda(k_x-ik_y) & -(\xi_{\mathbf{k}}-h)\end{pmatrix} = \begin{pmatrix}2k_x & \lambda & 0 & 0\\ \lambda & 2k_x & 0 & 0\\ 0 & 0 & -2k_x & \lambda\\ 0 & 0 & \lambda & -2k_x\end{pmatrix}$$

$$\frac{\partial}{\partial k_y}\begin{pmatrix}\xi_{\mathbf{k}}+h & \lambda(k_x-ik_y) & 0 & -\Delta(t)\\ \lambda(k_x+ik_y) & \xi_{\mathbf{k}}-h & \Delta(t) & 0\\ 0 & \Delta^*(t) & -(\xi_{\mathbf{k}}+h) & \lambda(k_x+ik_y)\\ -\Delta^*(t) & 0 & \lambda(k_x-ik_y) & -(\xi_{\mathbf{k}}-h)\end{pmatrix} = \begin{pmatrix}2k_y & -i\lambda & 0 & 0\\ i\lambda & 2k_y & 0 & 0\\ 0 & 0 & -2k_y & i\lambda\\ 0 & 0 & -i\lambda & -2k_y\end{pmatrix}$$

where I have chosen $\hbar = 2m = 1$. Then, we have a simplified notation

$$\begin{aligned}\gamma_\eta^{\nu=-} &= -2\sum_{\nu'\neq\nu}\sum_{\eta'=1,2}\Im\frac{\langle\nu\eta|h_x|\nu'\eta'\rangle\langle\nu'\eta'|h_y|\nu\eta\rangle}{(E_{\mathbf{k}}^{\nu\eta}-E_{\mathbf{k}}^{\nu'\eta'})^2}\\ &= -2\sum_{\nu'\neq\nu}\sum_{\eta'=1,2}\Im\Big\{\frac{1}{(E_{\mathbf{k}}^{\nu\eta}-E_{\mathbf{k}}^{\nu'\eta'})^2}\begin{pmatrix}u & \alpha & \beta & v\end{pmatrix}^*\times\begin{pmatrix}2k_xu'+\lambda\alpha'\\ \lambda u'+2k_x\alpha'\\ -2k_x\beta'+\lambda v'\\ \lambda\beta'-2k_xv'\end{pmatrix}\end{aligned}$$

$$\cdot \quad \begin{pmatrix} u' & \alpha' & \beta' & v' \end{pmatrix}^* \times \begin{pmatrix} 2k_y u - i\lambda\alpha \\ i\lambda u + 2k_y\alpha \\ -2k_y\beta + i\lambda v \\ -i\lambda\beta - 2k_y v \end{pmatrix} \Bigg\}$$

$$= -2\sum_{\nu'\neq\nu}\sum_{\eta'=1,2} \Im\left\{\frac{1}{(E_{\mathbf{k}}^{\nu\eta} - E_{\mathbf{k}}^{\nu'\eta'})^2}\Xi_1\cdot\Xi_2\right\}$$

where

$$\Xi_1 = (2k_x u'u^* + \lambda\alpha' u^* + \lambda u'\alpha^* + 2k_x\alpha'\alpha^* - 2k_x\beta'\beta^* + \lambda v'\beta^* + \lambda\beta' v^* - 2k_x v' v^*)$$

$$\Xi_2 = (2k_y u'^* u - i\lambda u'^*\alpha + i\lambda\alpha'^* u + 2k_y\alpha'^*\alpha - 2k_y\beta'^*\beta + i\lambda\beta'^* v - i\lambda v'^*\beta - 2k_y v'^* v)$$

And therefore,

$$C^{\nu=-} = \frac{-2}{2\pi}\int dk_x \int dk_y \sum_{\nu'\neq\nu}\sum_{\eta=1,2}\sum_{\eta'=1,2} \Im\left\{\frac{1}{(E_{\mathbf{k}}^{\nu\eta} - E_{\mathbf{k}}^{\nu'\eta'})^2}\Xi_1\cdot\Xi_2\right\} \quad (4.31)$$

$$= \frac{-2}{2\pi}\int dk_x \int dk_y \sum_{\eta=1,2}\sum_{\eta'=1,2} \Im\left\{\frac{1}{(E_{\mathbf{k}}^{-\eta} - E_{\mathbf{k}}^{+\eta'})^2}\Xi_1\cdot\Xi_2\right\} \quad (4.32)$$

In practice, we observe the curvature as a function of momentum k_x and k_y are rotationally symmetric. Therefore, we can have

$$C^{\nu=-} = -\frac{4}{\pi}\int_0^{k_c} dk_x \int_0^{k_c} dk_y \sum_{\eta=1,2}\sum_{\eta'=1,2} \Im\left\{\frac{1}{(E_{\mathbf{k}}^{-\eta} - E_{\mathbf{k}}^{+\eta'})^2}\Xi_1\cdot\Xi_2\right\} \quad (4.33)$$

where k_c is the momentum cutoff introduced numerically, and integration mesh only requires 100 grids, which can already give rise to very accurate results of Chern number! Numerically, I have checked $\gamma_\eta^{\nu=-}(k_x, k_y)$ is rotationally symmetric. As a result, we may further reduce the momentum integration to the radial direction, as the following,

$$C^{\nu=-} = -2\int_0^{k_c} kdk \sum_{\eta=1,2}\sum_{\eta'=1,2} \Im\left\{\frac{1}{(E_k^{-\eta} - E_k^{+\eta'})^2}\Xi_1\cdot\Xi_2\right\} \quad (4.34)$$

where

$$\Xi_1 = (2ku'u^* + \lambda\alpha'u^* + \lambda u'\alpha^* + 2k\alpha'\alpha^* - 2k\beta'\beta^* + \lambda v'\beta^* + \lambda\beta' v^* - 2kv'v^*)$$

$$\Xi_2 = (2ku'^* u - i\lambda u'^*\alpha + i\lambda\alpha'^* u + 2k\alpha'^*\alpha - 2k\beta'^*\beta + i\lambda\beta'^* v - i\lambda v'^*\beta - 2kv'^* v)$$

where we may empirically choose $k_c \sim 10k_F$ and grids around 500 points.

Note that in the calculation, we need to update $E^{\nu\eta}_{\mathbf{k}}(t)$ at each time step in the following way,

$$E^{\nu\eta}_{\mathbf{k}}(t) = \begin{pmatrix} u^\eta_{\mathbf{k}}(t) & \alpha^\eta_{\mathbf{k}}(t) & \beta^\eta_{\mathbf{k}}(t) & v^\eta_{\mathbf{k}}(t) \end{pmatrix}^* \times \begin{pmatrix} \xi_{\mathbf{k}} + h & \lambda(k_x - ik_y) & 0 & -\Delta(t) \\ \lambda(k_x + ik_y) & \xi_{\mathbf{k}} - h & \Delta(t) & 0 \\ 0 & \Delta^*(t) & -(\xi_{\mathbf{k}} + h) & \lambda(k_x + ik_y) \\ -\Delta^*(t) & 0 & \lambda(k_x - ik_y) & -(\xi_{\mathbf{k}} - h) \end{pmatrix} \times \begin{pmatrix} u^\eta_{\mathbf{k}}(t) \\ \alpha^\eta_{\mathbf{k}}(t) \\ \beta^\eta_{\mathbf{k}}(t) \\ v^\eta_{\mathbf{k}}(t) \end{pmatrix}$$

The topological nature of the system can also be manifested by examining the existence of the Majorana edge modes. To this end, we obtain the BdG spectrum by adding a hard-wall boundary along the x-direction. Examples are shown in Fig. 4.7. We show the energy gap at zero momentum at $t = \infty$, $E_0^\infty = |h_f - \sqrt{\mu_\infty^2 + |\Delta_\infty|^2}|$, as a function of the final Zeeman field h_f in Fig. 4.7(a) for fixed initial Zeeman field. The closing and reopening of the energy gap E_0^∞ signals the dynamical topological phase transition. Indeed, we show that zero-energy dynamical edge state can be observed in the topological regime, see Fig. 4.7(d), where the bulk spectrum is gapped and the edge state is gapless.

4.2.5 Phase III

In phase III, the order parameter quickly decays to zero (see Fig. 4.8) according to $\Delta(t) \sim \exp(-t/T^*)$, where $T^* \sim 1/\Delta$, the decay time, is equal to the order parameter

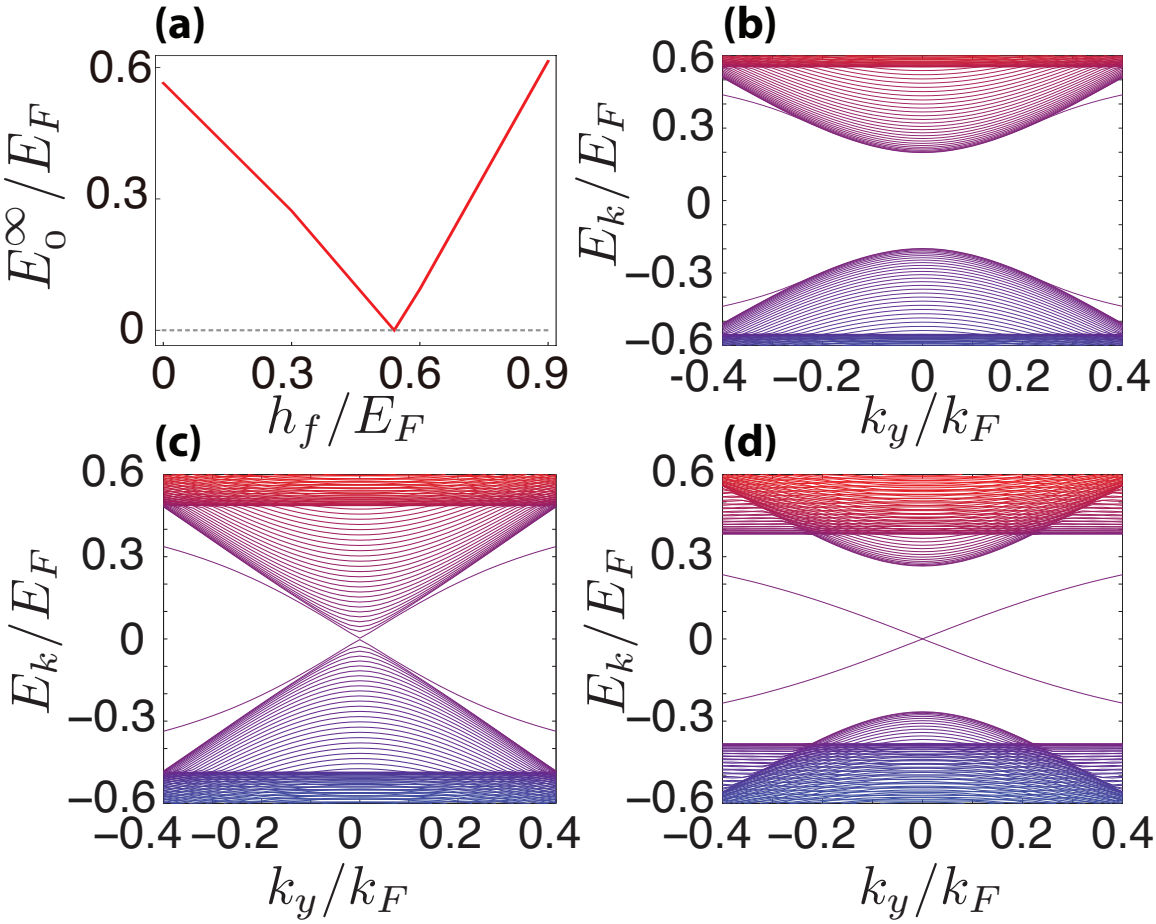

Figure 4.7 : Dynamical edge state in a strip for phase II. (a) Energy gap at $\mathbf{k} = 0$, $E_0^\infty = |h_f - \sqrt{|\Delta_\infty|^2 + \mu_\infty^2}|$, as a function of final Zeeman field. The closing and reopening of energy gap E_0^∞ signals a transition from a trivial phase ($W = 0$) to topological phase $W = 1$ at $h_c = 0.53E_F$. In this plot $h_i = 0.6E_F$ is used, and all the other parameters are identical to that in Fig. 4.1. (b) - (d) show the band structure in a strip geometry with hard wall boundary condition. Robust edge states with linear dispersion can be observed in the topological phase regime. The final Zeeman field from (b) to (d) are $0.4E_F$, $0.55E_F$, and $0.7E_F$, respectively.

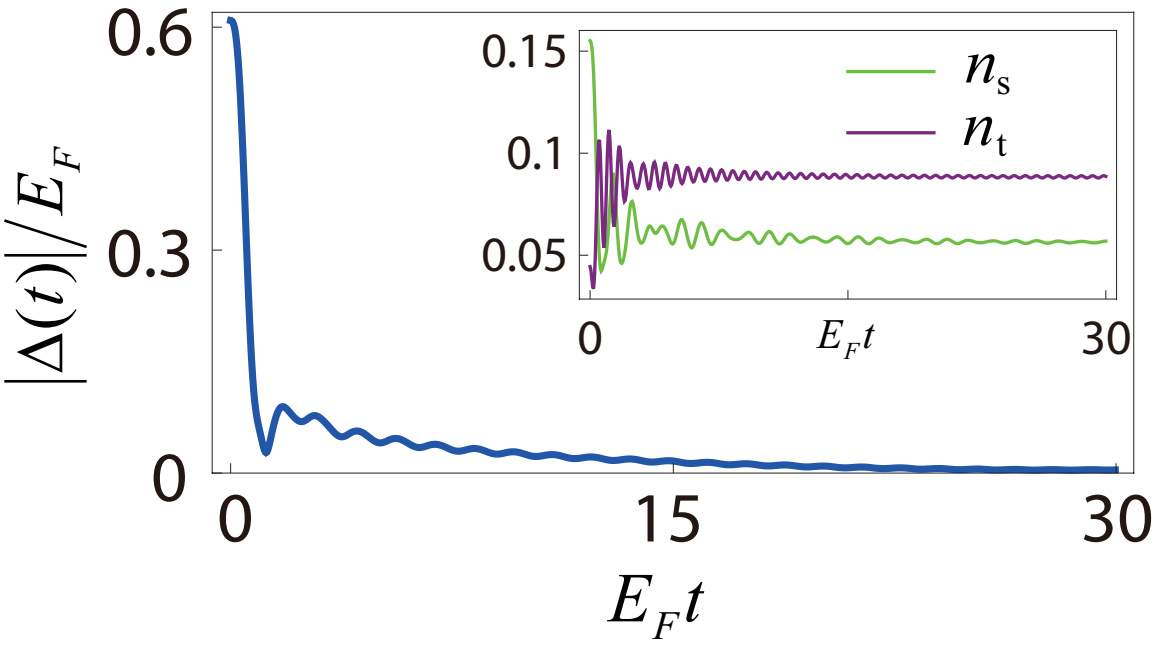

Figure 4.8 : Dynamics of order parameter and condensate fraction in phase III. We plot the result for point D $(h_i = 0.3, h_f = 2.4)E_F$ in Fig. 4.3. Inset shows the dynamics of condensate fraction of singlet pairing n_s (green) and triplet pairing n_t (purple), which remains finite values although $|\Delta(t)|$ approaches zero in the long-time limit.

dynamical time. However, we need to emphasize that a vanishing order parameter does not mean that the system has become a normal gas. We demonstrate this by showing the dynamics of both the singlet and the triplet condensate fraction, defined as $n_s = \sum_{\mathbf{k}} |\langle c_{\mathbf{k}\uparrow} c_{-\mathbf{k}\downarrow}\rangle|^2/n$ and $n_t = \sum_{\mathbf{k}} |\langle c_{\mathbf{k}\uparrow} c_{-\mathbf{k}\uparrow}\rangle|^2/n$.

Recall Bogoliubov transformation,

$$\psi_\sigma(\mathbf{x}) = \frac{1}{V}\sum_{\mathbf{k}} \Big[u_{\mathbf{k}\sigma}(\mathbf{x},t) c_{\mathbf{k}\sigma} + v^*_{\mathbf{k}\bar{\sigma}}(\mathbf{x},t) c^\dagger_{\mathbf{k}\bar{\sigma}} + \alpha_{\mathbf{k}\bar{\sigma}}(\mathbf{x},t) c_{\mathbf{k}\bar{\sigma}} + \beta^*_{\mathbf{k}\sigma}(\mathbf{x},t) c^\dagger_{\mathbf{k}\sigma} \Big] \tag{4.35}$$

where $\sigma = \uparrow, \downarrow$ and correspondingly $\bar{\sigma} = \downarrow, \uparrow$. For the homogeneous system we study here, we use plane-wave as the basis and wavefunctions take the following form,

$$\begin{pmatrix} u_{\mathbf{k}}(\mathbf{x}) \\ \alpha_{\mathbf{k}}(\mathbf{x}) \\ \beta_{\mathbf{k}}(\mathbf{x}) \\ v_{\mathbf{k}}(\mathbf{x}) \end{pmatrix} = \begin{pmatrix} u_{\mathbf{k}} e^{+iqz/2} \\ \alpha_{\mathbf{k}} e^{+iqz/2} \\ \beta_{\mathbf{k}} e^{-iqz/2} \\ v_{\mathbf{k}} e^{-iqz/2} \end{pmatrix} e^{i\mathbf{k}\cdot\mathbf{x}} \tag{4.36}$$

We further have

$$\begin{aligned}
\psi_\sigma(\mathbf{k}') &= \int e^{-i\mathbf{k}'\cdot\mathbf{x}} d\mathbf{x} \frac{1}{V}\sum_{\mathbf{k}} \Big[u_{\mathbf{k}\sigma}(\mathbf{x},t) c_{\mathbf{k}\sigma} + v^*_{\mathbf{k}\bar{\sigma}}(\mathbf{x},t) c^\dagger_{\mathbf{k}\bar{\sigma}} + \alpha_{\mathbf{k}\bar{\sigma}}(\mathbf{x},t) c_{\mathbf{k}\bar{\sigma}} + \beta^*_{\mathbf{k}\sigma}(\mathbf{x},t) c^\dagger_{\mathbf{k}\sigma} \Big] \\
&= \int e^{-i\mathbf{k}'\cdot\mathbf{x}} d\mathbf{x} d\mathbf{k} \Big[u_{\mathbf{k}\sigma} e^{iqz/2} e^{i\mathbf{k}\cdot\mathbf{x}} c_{\mathbf{k}\sigma} + v^*_{\mathbf{k}\bar{\sigma}} e^{iqz/2} e^{-i\mathbf{k}\cdot\mathbf{x}} c^\dagger_{\mathbf{k}\bar{\sigma}} \\
&+ \alpha_{\mathbf{k}\bar{\sigma}} e^{iqz/2} e^{i\mathbf{k}\cdot\mathbf{x}} c_{\mathbf{k}\bar{\sigma}} + \beta^*_{\mathbf{k}\sigma} e^{iqz/2} e^{-i\mathbf{k}\cdot\mathbf{x}} c^\dagger_{\mathbf{k}\sigma} \Big] \\
&= \int d\mathbf{k} \Big[u_{\mathbf{k}\sigma} c_{\mathbf{k}\sigma} \delta(k + q/2 - k') + v^*_{\mathbf{k}\bar{\sigma}} c^\dagger_{\mathbf{k}\bar{\sigma}} \delta(q/2 - k - k') \\
&+ \alpha_{\mathbf{k}\bar{\sigma}} c_{\mathbf{k}\bar{\sigma}} \delta(k + q/2 - k') + \beta^*_{\mathbf{k}\sigma} c^\dagger_{\mathbf{k}\sigma} \delta(q/2 - k - k') \Big] \\
&= u_{-\mathbf{q}/2+\mathbf{k}'\sigma} c_{-\mathbf{q}/2+\mathbf{k}'\sigma} + v^*_{\mathbf{q}/2-\mathbf{k}'\bar{\sigma}} c^\dagger_{\mathbf{q}/2-\mathbf{k}'\bar{\sigma}} + \alpha_{-\mathbf{q}/2+\mathbf{k}'\bar{\sigma}} c_{-\mathbf{q}/2+\mathbf{k}'\bar{\sigma}} + \beta^*_{\mathbf{q}/2-\mathbf{k}'\sigma} c^\dagger_{\mathbf{q}/2-\mathbf{k}'\sigma}
\end{aligned}$$

Then, we should have

$$\begin{aligned}
N_0 &= \int d\mathbf{k}|\langle\Big(u_{-\mathbf{q}/2+\mathbf{k}\uparrow}c_{-\mathbf{q}/2+\mathbf{k}\uparrow}+v^*_{\mathbf{q}/2-\mathbf{k}\downarrow}c^\dagger_{\mathbf{q}/2-\mathbf{k}\downarrow}+\alpha_{-\mathbf{q}/2+\mathbf{k}\downarrow}c_{-\mathbf{q}/2+\mathbf{k}\downarrow}+\beta^*_{\mathbf{q}/2-\mathbf{k}\uparrow}c^\dagger_{\mathbf{q}/2-\mathbf{k}\uparrow}\Big)\\
&\times \Big(u_{-\mathbf{q}/2-\mathbf{k}\downarrow}c_{-\mathbf{q}/2-\mathbf{k}\downarrow}+v^*_{\mathbf{q}/2+\mathbf{k}\uparrow}c^\dagger_{\mathbf{q}/2+\mathbf{k}\uparrow}+\alpha_{-\mathbf{q}/2-\mathbf{k}\uparrow}c_{-\mathbf{q}/2-\mathbf{k}\uparrow}+\beta^*_{\mathbf{q}/2+\mathbf{k}\downarrow}c^\dagger_{\mathbf{q}/2+\mathbf{k}\downarrow}\Big)\rangle|^2\\
&= \int d\mathbf{k}|u_{-\mathbf{q}/2+\mathbf{k}\uparrow}v^*_{\mathbf{q}/2+\mathbf{k}\uparrow}\langle c_{-\mathbf{q}/2+\mathbf{k}\uparrow}c^\dagger_{\mathbf{q}/2+\mathbf{k}\uparrow}\rangle+v^*_{\mathbf{q}/2-\mathbf{k}\downarrow}u_{-\mathbf{q}/2-\mathbf{k}\downarrow}\langle c^\dagger_{\mathbf{q}/2-\mathbf{k}\downarrow}c_{-\mathbf{q}/2-\mathbf{k}\downarrow}\rangle\\
&+ \alpha_{-\mathbf{q}/2+\mathbf{k}\downarrow}\beta^*_{\mathbf{q}/2+\mathbf{k}\downarrow}\langle c_{-\mathbf{q}/2+\mathbf{k}\downarrow}c^\dagger_{\mathbf{q}/2+\mathbf{k}\downarrow}\rangle+\beta^*_{\mathbf{q}/2-\mathbf{k}\uparrow}\alpha_{-\mathbf{q}/2-\mathbf{k}\uparrow}\langle c^\dagger_{\mathbf{q}/2-\mathbf{k}\uparrow}c_{-\mathbf{q}/2-\mathbf{k}\uparrow}\rangle|^2
\end{aligned}$$

If we consider zero in-plane Zeeman field, we set $\mathbf{q}=0$. Then, we have

$$N_0=\int d\mathbf{k}|u_{\mathbf{k}\uparrow}v^*_{\mathbf{k}\uparrow}\langle c_{\mathbf{k}\uparrow}c^\dagger_{\mathbf{k}\uparrow}\rangle+v^*_{-\mathbf{k}\downarrow}u_{-\mathbf{k}\downarrow}\langle c^\dagger_{-\mathbf{k}\downarrow}c_{-\mathbf{k}\downarrow}\rangle+\alpha_{\mathbf{k}\downarrow}\beta^*_{\mathbf{k}\downarrow}\langle c_{\mathbf{k}\downarrow}c^\dagger_{\mathbf{k}\downarrow}\rangle+\beta^*_{-\mathbf{k}\uparrow}\alpha_{-\mathbf{k}\uparrow}\langle c^\dagger_{-\mathbf{k}\uparrow}c_{-\mathbf{k}\uparrow}\rangle|^2$$

Due to redundancy in BdG construction and particle-symmetry, we further have

$$N_0 = \frac{1}{4}\frac{1}{V}\sum_{\mathbf{k}}|u_{\mathbf{k}}v^*_{\mathbf{k}}f(E_{\mathbf{k}})+\alpha_{\mathbf{k}}\beta^*_{\mathbf{k}}f(-E_{\mathbf{k}})|^2 \tag{4.37}$$

$$= \frac{1}{4}\frac{1}{V}\sum_{\mathbf{k}}\left|\sum_{\eta=1}^{4}u^\eta_{\mathbf{k}}(t)v^{\eta*}_{\mathbf{k}}(t)f(E^\eta_{\mathbf{k}}(t=0))+\alpha^\eta_{\mathbf{k}}(t)\beta^{\eta*}_{\mathbf{k}}(t)f(-E^\eta_{\mathbf{k}}(t=0))\right|^2 \tag{4.38}$$

which we could have obtained in a much simpler way, by doing analogy with Δ.

Similarly, we have triplet condensate fraction,

$$\begin{aligned}
N_1 &= \int d\mathbf{k}|\langle\Big(u_{-\mathbf{q}/2+\mathbf{k}\uparrow}c_{-\mathbf{q}/2+\mathbf{k}\uparrow}+v^*_{\mathbf{q}/2-\mathbf{k}\downarrow}c^\dagger_{\mathbf{q}/2-\mathbf{k}\downarrow}+\alpha_{-\mathbf{q}/2+\mathbf{k}\downarrow}c_{-\mathbf{q}/2+\mathbf{k}\downarrow}+\beta^*_{\mathbf{q}/2-\mathbf{k}\uparrow}c^\dagger_{\mathbf{q}/2-\mathbf{k}\uparrow}\Big)\\
&\times \Big(u_{-\mathbf{q}/2-\mathbf{k}\uparrow}c_{-\mathbf{q}/2-\mathbf{k}\uparrow}+v^*_{\mathbf{q}/2+\mathbf{k}\downarrow}c^\dagger_{\mathbf{q}/2+\mathbf{k}\downarrow}+\alpha_{-\mathbf{q}/2-\mathbf{k}\downarrow}c_{-\mathbf{q}/2-\mathbf{k}\downarrow}+\beta^*_{\mathbf{q}/2+\mathbf{k}\uparrow}c^\dagger_{\mathbf{q}/2+\mathbf{k}\uparrow}\Big)\rangle|^2\\
&= \int d\mathbf{k}|u_{-\mathbf{q}/2+\mathbf{k}\uparrow}\beta^*_{\mathbf{q}/2+\mathbf{k}\uparrow}\langle c_{-\mathbf{q}/2+\mathbf{k}\uparrow}c^\dagger_{\mathbf{q}/2+\mathbf{k}\uparrow}\rangle+v^*_{\mathbf{q}/2-\mathbf{k}\downarrow}\alpha_{-\mathbf{q}/2-\mathbf{k}\downarrow}\langle c^\dagger_{\mathbf{q}/2-\mathbf{k}\downarrow}c_{-\mathbf{q}/2-\mathbf{k}\downarrow}\rangle \tag{4.39}\\
&+ \alpha_{-\mathbf{q}/2+\mathbf{k}\downarrow}v^*_{\mathbf{q}/2+\mathbf{k}\downarrow}\langle c_{-\mathbf{q}/2+\mathbf{k}\downarrow}c^\dagger_{\mathbf{q}/2+\mathbf{k}\downarrow}\rangle+\beta^*_{\mathbf{q}/2-\mathbf{k}\uparrow}u_{-\mathbf{q}/2-\mathbf{k}\uparrow}\langle c^\dagger_{\mathbf{q}/2-\mathbf{k}\uparrow}c_{-\mathbf{q}/2-\mathbf{k}\uparrow}\rangle|^2 \tag{4.40}
\end{aligned}$$

Setting $\mathbf{q}=0$ and using the redundancy reduction, we have

$$N_1 = \frac{1}{4}\frac{1}{V}\sum_{\mathbf{k}}|u_{\mathbf{k}}\beta^*_{\mathbf{k}}f(E_{\mathbf{k}})+\alpha_{\mathbf{k}}v^*_{\mathbf{k}}f(-E_{\mathbf{k}})|^2 \tag{4.41}$$

$$= \frac{1}{4}\frac{1}{V}\sum_{\mathbf{k}}\left|\sum_{\eta=1}^{4}u^\eta_{\mathbf{k}}(t)\beta^{\eta*}_{\mathbf{k}}(t)f(E^\eta_{\mathbf{k}}(t=0))+\alpha^\eta_{\mathbf{k}}(t)v^{\eta*}_{\mathbf{k}}(t)f(-E^\eta_{\mathbf{k}}(t=0))\right|^2 \tag{4.42}$$

As shown in Fig. 4.8), one can see that in the long-time limit, the condensate fraction remains non-zero even though the order parameter vanishes. Non-zero condensate fraction means that the system still contains nontrivial pairings. However, the pairing field for different momenta oscillates at different frequencies, which leads to dephasing and hence a vanishing order parameter.

4.3 Summary

In this chapter, we have demonstrated that dynamical topological phases can be realized in an SO coupled degenerate Fermi gas by quenching the Zeeman field. The Zeeman field directly determines the topological properties of the ground state, which is completely characterized by the zero-momentum spin polarization $S_z(0)$, a quantity that is directly measurable in cold atom experiments using the standard time-of-flight technique. We have further mapped out the post-quench phase diagram according to the asymptotic behavior of the order parameter. In the undamped phase, the persistent oscillation of the order parameter may support a topological Floquet state with multiple edge states. In the damped phase, the magnitude of the order parameter gradually approaches a constant via a power-law decay, and this phase contains a dynamical topological portion in certain parameter regions. One pair of edge modes can be observed in this case. In the overdamped phase, the order parameter quickly decays to zero exponentially while the condensate fraction remains finite.

The presence of the SO coupling and the Zeeman field breaks the integrability of our model. However, the same types of post-quench dynamical phases observed in our model are also present in integrable models studied previously. This raises the important question on the relationship between integrability and the long-time asymptotic post-quench behavior of the superfluid/superconducting system. This

issue has been intensively investigated in other models regarding relaxation, thermalization and phase transitions [114,119], in which integrability plays the most essential role therein. Our work here shows that this is a rather subtle question and further studies are needed to provide a definitive answer.

We finally comment on the feasibility of observing the exotic dynamical topological phases unveiled in this chapter. The dynamics of the superfluids are mainly determined by two characteristic time scales, that is, the energy relaxation time $\tau_\epsilon \sim E_F/E_{\rm g}^2$, where $E_{\rm g}$ is the energy gap of the superfluids before quench, and the order parameter dynamical time $\tau_\Delta \sim 1/\Delta$. As we have already mentioned, the quench of the effective Zeeman field in SO coupled Fermi gases can be achieved at a time scale much smaller than $1/E_F$ [142]. The far-from-equilibrium *coherent* evolution can be realized when $\tau_\epsilon > t \geq \tau_\Delta$ [124,128]. The ultracold Fermi gas provides a natural system to explore the physics in the far-from-equilibrium condition at a time scale of $1/E_F$. In the BCS limit $\Delta = \sqrt{2E_F E_b}$ approaches zero. Thus $E_{\rm g} = \Delta \ll E_F$ ($\mu > 0$ in the BCS limit), and we immediately have $\tau_\epsilon \gg \tau_\Delta$ (Using point A in Fig. 4.3 as an example, we have $\Delta \sim 0.013E_F$, $\mu \sim 0.7E_F$, $E_{\rm g} \sim 0.009E_F$, thus $\tau_\Delta \sim 70/E_F$ and $\tau_\epsilon \sim 10^4/E_F \sim 160\tau_\Delta$). In our system, the SO coupling and the Zeeman field can greatly change the band structure of the superfluids. For example, the energy gap is no longer determined solely by the order parameter and chemical potential, but instead, it is a very complicated function of all parameters. At the boundary of topological phase transition, we have $E_{\rm g} = E_0 = 0$. In the vicinity of this boundary, $\tau_\epsilon \sim E_F/(h - \sqrt{\Delta^2 + \mu^2})^2$, we naturally expect that $\tau_\epsilon \gg \tau_\Delta$. We should emphasize that this condition, which can only be realized in the BCS limit in a conventional s-wave superfluid, can now be realized very easily in a SO coupled model in the strong coupling regime because of the different parameter dependence

for these two time scales. Meanwhile, the temperature effect is also a critical issue in ultracold atomic system. In the BCS limit, we expect $T_c = \frac{2E_F e^\gamma}{\pi}\sqrt{E_b/2E_F} \sim \frac{1}{2}\Delta$ for a conventional superfluid [172], where $\gamma \simeq 0.577$ is the Euler's constant. The required temperature is thus very low in order to observe the coherent dynamics of superfluids, which poses a great challenge to the experiments [162–165]. This dilemma can be resolved in our model because of the dramatic change in band structure caused by the SO coupling and the Zeeman field. In the strong coupling regime, we expect the relevant temperature to be determined by the Kosterlitz-Thouless transition temperature $T_{\rm KT} \sim 0.1E_F$ [145, 172], which is experimentally accessible within current technology [162–165]. In fact, the temperature effect may become important only when $T \gg \Delta$, in which case the pairing may be destroyed. We have verified that the persistent oscillations in phase I regime can still be observed if we add a small finite temperature T in the time-dependent BdG equation. For instance, for the parameter set used in Fig. 4.4, oscillations can be observed up to $T \approx 0.2E_F$. For these reasons, we expect that the relevant dynamics of the order parameter and associated *dynamical* topological phase transitions in phase I and phase II regimes can be realized using realistic cold atom setup at the currently achievable temperatures.

So far, from Chapter 2 to 4, we have considered spin-orbit interaction created by two-photon Raman process stimulated by coherent laser beams. This means the laser field serves as semi-classical field, well described by coherent state. Atoms flip spins by absorbing or emitting photon and exchanging momentum due to conservation law. To consider atoms' back-kick onto photon field simultaneously in this process, we turn next to our proposal of putting atoms in the cavity field, and realize the dynamical coupling between spin, orbit, and quantized light field. New and interesting non-trivial physics are expected from the synthesis of cavity QED and spin-orbit coupling.

Chapter 5

Light Field Induced Dynamical Spin-Orbit Coupling

When an atom interacts with a quantized light field supported by an optical cavity, the atom and the light field mutually affect each other. A self-consistent solution for the light field and the atom is thus required. This has been a major theme in cavity quantum electrodynamics (CQED) [173]. In traditional CQED settings, only the internal dynamics of the atom is relevant: the cavity photons induce quantum transitions among different atomic internal states, and the atom affects the cavity field by emitting/absorbing cavity photons. The link between Cavity photon and Atomic internal states in Fig. 5.1 illustrates the relationship between the cavity and the atom. In recent years, ultracold atoms have been put inside optical cavities and in such a situation, one can no longer neglect the center-of-mass (COM) motion of the atom. Emitting or absorbing even a single photon can significantly change the motional states of the atom. This situation is represented by the link between cavity photon and atomic external states in Fig. 5.1. In fact, the mutual influence of the cavity field and the atomic COM motion can be put into the broader context of optomechanics. Here the atoms can be regarded as a mechanical system whose dynamics is controlled by, and in the same time provides a back-action to, the cavity field. A variety of phenomena in this "ultracold atom + cavity" system, which is an example of an optomechanical system, has been explored experimentally [174–180] and theoretically [181, 182].

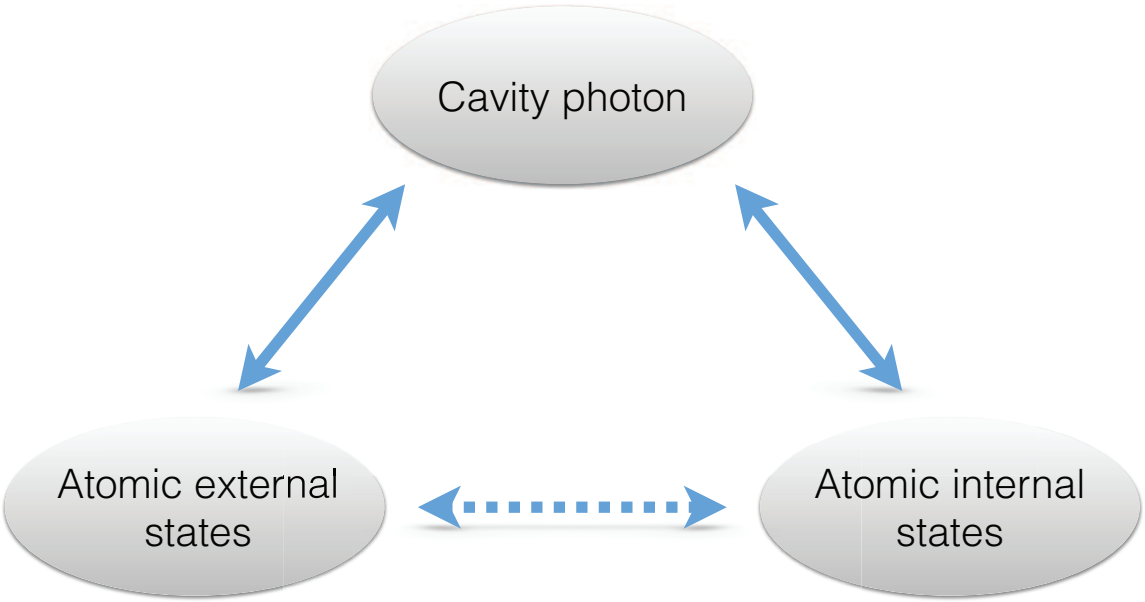

Figure 5.1 : A new frontier in both CQED and cold atoms research, in which one needs to take into account the interplay among the cavity photons, the atomic external states, and also the atomic internal degrees of freedom.

Another recent breakthrough in cold atom research is the realization of spin-orbit coupling (SOC) in ultracold atoms, in both bosonic [183] and fermionic systems [55, 184]. Realization of SOC in cold atoms involves a two-photon Raman transition between two hyperfine ground states as schematically shown in Fig. 5.2(b). The Raman-induced transition between the two atomic levels and the associated momentum transfer due to photon recoil give rise to an effective coupling between the COM motion and the internal states of the atom. Due to its non-Abelian nature, SOC not only significantly affects the physics of a single atom, but, perhaps more importantly, also profoundly changes the properties of a many-body system. It is an essential ingredient underlying such diverse phenomena as topological superconductors/insulators, Majorana and Weyl fermions, quantum spin-Hall effects, etc.

In the experiments of spin-orbit coupled quantum gases, the Raman beams that generate the SOC are provided by two classical laser fields, which are not affected by the atoms. Here we consider a situation where one of the Raman beams is replaced by a quantized light field supported by an optical cavity, as schematically shown in Fig. 5.2(a). In this scheme, akin to other "ultracold atom + cavity" systems, there will be a back-action from the atom to the light. Therefore the SOC in the atom is generated by a quantized light field which itself is affected by the atomic dynamics. In this sense, the cavity-assisted SOC becomes *dynamic* [185]. In other words, the same cavity photon can affect both the internal states (via inducing a transition between different states of the atom) and the external COM motion (via photon recoil) of the atom. As a result, it naturally induces an effective coupling between the two atomic degrees of freedom, as is represented by the dashed link between Atomic external states and Atomic internal states in Fig. 5.1. Furthermore, in previous experimental studies of cold-atom based cavity optomechanical systems [174–180], only the COM

motion of the atom is included. The inclusion of the internal spin degrees of freedom and the resulting SOC opens up a new avenue of research in cavity optomechanical systems. We will show that this dynamic SOC dramatically modifies the atomic dispersion relation, dynamical instabilities, vanishing atom-photon entanglement at large atomic momentum tail and re-entrant superadiant phase in the thermodynamic limit.

5.1 Back-action From Atom(s) to Photon Field

We consider a single atom (or, a non-interacting Bose-Einstein condensate) with two relevant internal states (denoted as $|\uparrow\rangle$ and $|\downarrow\rangle$) confined inside a unidirectional optical ring cavity, depicted schematically in Fig. 5.2. The cavity is pumped by a coherent laser field with frequency ω_p and pumping rate ε_p. It supports a single mode traveling wave and has an intrinsic angular frequency ω_c. An additional coherent laser beam with frequency ω_R shines on the atom, which together with the cavity field provides the Raman transition between $|\uparrow\rangle$ and $|\downarrow\rangle$ states. During the Raman transition, a recoil momentum of $\pm 2\hbar q_r \hat{z}$ is transferred to the atom. We treat the leakage of cavity photon phenomenologically by introducing a cavity decay rate κ. The model Hamiltonian is thus written as (we take $\hbar = 1$),

$$\begin{aligned} H &= \sum_{\sigma} \int d\mathbf{r} \left[\Psi_{\sigma}^{\dagger}(\mathbf{r}) \left(\frac{\hat{\mathbf{k}}^2}{2m} + \epsilon_{\sigma}^{0} \right) \Psi_{\sigma}(\mathbf{r}) \right] \\ &+ \frac{\Omega}{2} \int d\mathbf{r}\, e^{+2iq_r z} \Psi_{\uparrow}^{\dagger}(\mathbf{r}) \Psi_{\downarrow}(\mathbf{r}) \tilde{c} e^{+i\omega_R t} \\ &+ \frac{\Omega}{2} \int d\mathbf{r}\, e^{-2iq_r z} \tilde{c}^{\dagger} \Psi_{\downarrow}^{\dagger}(\mathbf{r}) \Psi_{\uparrow}(\mathbf{r}) e^{-i\omega_R t} \\ &+ i\varepsilon_p (\tilde{c}^{\dagger} e^{-i\omega_p t} - \tilde{c} e^{+i\omega_p t}) + \omega_c \tilde{c}^{\dagger} \tilde{c} - i\kappa \tilde{c}^{\dagger} \tilde{c}, \end{aligned} \tag{5.1}$$

where $\Psi_{\sigma}(\mathbf{r})$ ($\sigma = \uparrow, \downarrow$) is the atomic annihilation operator, ϵ_{σ}^{0} is the corresponding bare atomic energy, and $\tilde{c}$ represents the photon annihilation operator. Ω describes

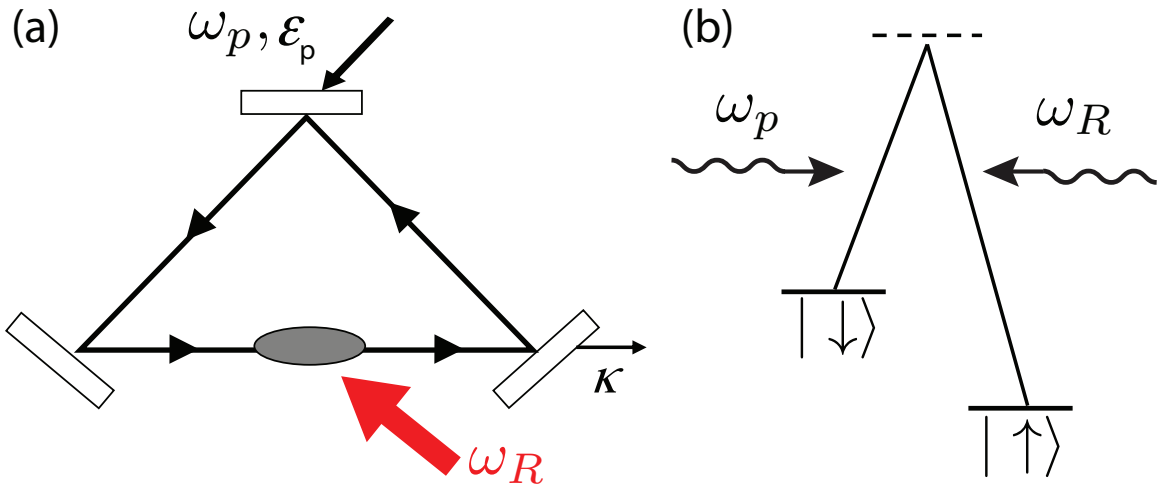

Figure 5.2 : (a) Schematic diagram of the cavity-assisted spin-orbit coupled system; (b) Level diagram of atom photon/light field interaction.

the atom-photon coupling strength. However, the true Raman coupling strength also includes the cavity photon amplitude of $\tilde{c}$ or $\tilde{c}^\dagger$ which is coupled to the atomic operators. It is this coupling that renders the resulting SOC *dynamic*.

It is convenient to work work in a frame rotating at pump laser frequency ω_p by transforming the photon operator to $c = \tilde{c}e^{i\omega_p t}$. This is equivalent to performing an unitary transformation $U = e^{+i\omega_p \tilde{c}^\dagger \tilde{c} t}$ to the Hamiltonian (5.1), by $H' = UHU^{-1} + i\frac{dU}{dt}U^{-1}$. From H', we perform another unitary transformation $\tilde{U} = e^{i\delta_R t(\Psi_\uparrow^\dagger \Psi_\uparrow - \Psi_\downarrow^\dagger \Psi_\downarrow)/2}$, with $\delta_R = \omega_p - \omega_R$, to obtain the Hamiltonian H''. Finally, after a gauge transformation to atomic operators $\psi_\uparrow = \Psi_\uparrow e^{-iq_r z}$ and $\psi_\downarrow = \Psi_\downarrow e^{+iq_r z}$, we arrive at the following effective Hamiltonian $\mathcal{H}_{\text{eff}}$:

$$\begin{aligned}
\mathcal{H}_{\text{eff}} &= \sum_\sigma \int d\mathbf{r} \left[\psi_\sigma^\dagger(\mathbf{r}) \left(\frac{\hat{\mathbf{k}}^2 + 2\alpha q_r k_z}{2m} + \alpha\tilde{\delta} \right) \psi_\sigma(\mathbf{r}) \right] \\
&+ \frac{\Omega}{2} \int d\mathbf{r} \left[\psi_\uparrow^\dagger(\mathbf{r})\psi_\downarrow(\mathbf{r})c + c^\dagger \psi_\downarrow^\dagger(\mathbf{r})\psi_\uparrow(\mathbf{r}) \right] \\
&+ i\varepsilon_p(c^\dagger - c) - \delta_c c^\dagger c - i\kappa c^\dagger c, \qquad (5.2)
\end{aligned}$$

where $\tilde{\delta} = \delta_R/2 + (\epsilon_\uparrow^0 - \epsilon_\downarrow^0)$ represents the two-photon Raman detuning; $\delta_c = \omega_p - \omega_c$ is the cavity-pump detuning, and $\alpha = \pm 1$ for $\sigma = \uparrow, \downarrow$, respectively.

The resulting effective Hamiltonian $\mathcal{H}_{\text{eff}}$ in Eq. (5.21) has Raman coupling term fundamentally different from experimentally realized ones (cf [55, 183, 184] for instance). The amplitude of Raman coupling in Eq. 5.21 is not only related to Ω, but also determined by photon field operator in rotating frame. It is indeed in this sense the generation of cavity-assisted dynamical SOC is *novel*.

5.2 Mean Field Theory

From the Hamiltonian (5.21), one can easily obtain the following equations of motion (EOM):

$$i\frac{d}{dt}c = i\varepsilon_p - (\delta_c + i\kappa)c + \frac{\Omega}{2}\int d\mathbf{r}\psi_\downarrow^\dagger(\mathbf{r})\psi_\uparrow(\mathbf{r}), \tag{5.3}$$

$$i\frac{\partial}{\partial t}\psi(\mathbf{r}) = \begin{pmatrix} \frac{\hat{\mathbf{k}}^2 + 2q_r k_z}{2m} + \tilde{\delta} & \frac{\Omega}{2}c \\ \frac{\Omega}{2}c^\dagger & \frac{\hat{\mathbf{k}}^2 - 2q_r k_z}{2m} - \tilde{\delta} \end{pmatrix} \psi(\mathbf{r}), \tag{5.4}$$

where $\psi(\mathbf{r}) \equiv [\psi_\uparrow(\mathbf{r}), \psi_\downarrow(\mathbf{r})]^T$. To proceed further, we adopt a mean-field approximation by replacing the operators by their respective expectation values: $c \to \langle c \rangle$, $\psi_\sigma(\mathbf{r}) \to \langle \psi_\sigma(\mathbf{r}) \rangle \equiv \varphi_\sigma(\mathbf{r})$, which is valid for small quantum fluctuations of both operators c and $\psi_\sigma(\mathbf{r})$. Assuming a homogeneous atomic density distribution, we take the plane-wave ansatz for the atomic modes $\varphi_\sigma(\mathbf{r}) = e^{i\mathbf{k}\cdot\mathbf{r}}\varphi_\sigma$ with the normalization condition $|\varphi_\uparrow|^2 + |\varphi_\downarrow|^2 = 1$. The steady-state solution for the photon field is given by

$$\langle c \rangle = \frac{\varepsilon_p - \frac{i}{2}\Omega\varphi_\downarrow^*\varphi_\uparrow}{\kappa - i\delta_c}. \tag{5.5}$$

Substituting Eq. (5.5) into Eq. (5.4), we have

$$i\dot{\varphi}_\uparrow = \left(\frac{\mathbf{k}^2}{2m} + q_r k_z + \tilde{\delta}\right)\varphi_\uparrow + \frac{\Omega}{2}\frac{\varepsilon_p - \frac{i\Omega}{2}\varphi_\downarrow^*\varphi_\uparrow}{\kappa - i\delta_c}\varphi_\downarrow\,, \tag{5.6}$$

$$i\dot{\varphi}_\downarrow = \left(\frac{\mathbf{k}^2}{2m} - q_r k_z - \tilde{\delta}\right)\varphi_\downarrow + \frac{\Omega}{2}\frac{\varepsilon_p + \frac{i\Omega}{2}\varphi_\uparrow^*\varphi_\downarrow}{\kappa + i\delta_c}\varphi_\uparrow\,. \tag{5.7}$$

For a given atomic quasi-momentum $\mathbf{k}$, we define energy levels as the solution of the time-independent version of Eqs. (5.6) and (5.7), obtained by replacing $i(\partial/\partial t)$ with the eigenenergy $\epsilon(\mathbf{k})$. After some calculation, we find that $\epsilon(\mathbf{k})$ obeys a quartic equation:

$$4\epsilon^4 + B\epsilon^3 + C\epsilon^2 + D\epsilon + E = 0\,, \tag{5.8}$$

where

$$\begin{aligned}
B &= -(8k_z^2 + 2w)\\
C &= 6k_z^4 + 3k_z^2 w - 4(q_r k_z + \delta)^2 + |v|^2 - 4|u|^2\\
D &= -2k_z^6 - \frac{3}{2}wk_z^4 + 4k_z^2(q_r k_z + \tilde{\delta})^2 - |v|^2 k_z^2 + 2w(q_r k_z + \tilde{\delta})^2\\
E &= (\frac{k_z^4}{4} - (q_r k_z + \tilde{\delta})^2)(k_z^4 + |v|^2 + wk_z^2) - |u|^2 k_z^4
\end{aligned}$$

This quartic equation can be solved analytically, but the expressions are cumbersome. We plot the typical behavior of the dispersion relation $\epsilon(k_z)$ vs k_z for $\tilde{\delta} = 0$ in Fig. 5.3. Note that we always take $k_x = k_y = 0$, as the SOC only occurs along the z-axis. A maximum of four real roots are allowed by Eq. (5.8). As we will show, in such regimes, a loop structure develops in the dispersion curve.

As shown in Fig. 5.3, for $\delta_c = 0$ (i.e., the pump field is resonant with the cavity), we always have two dispersion branches. The two branches are gapped when the atom-photon coupling strength Ω is small and touch each other at $k_z = 0$ when Ω exceeds a critical value. For $\delta_c \neq 0$, we again have two gapped branches at small Ω.

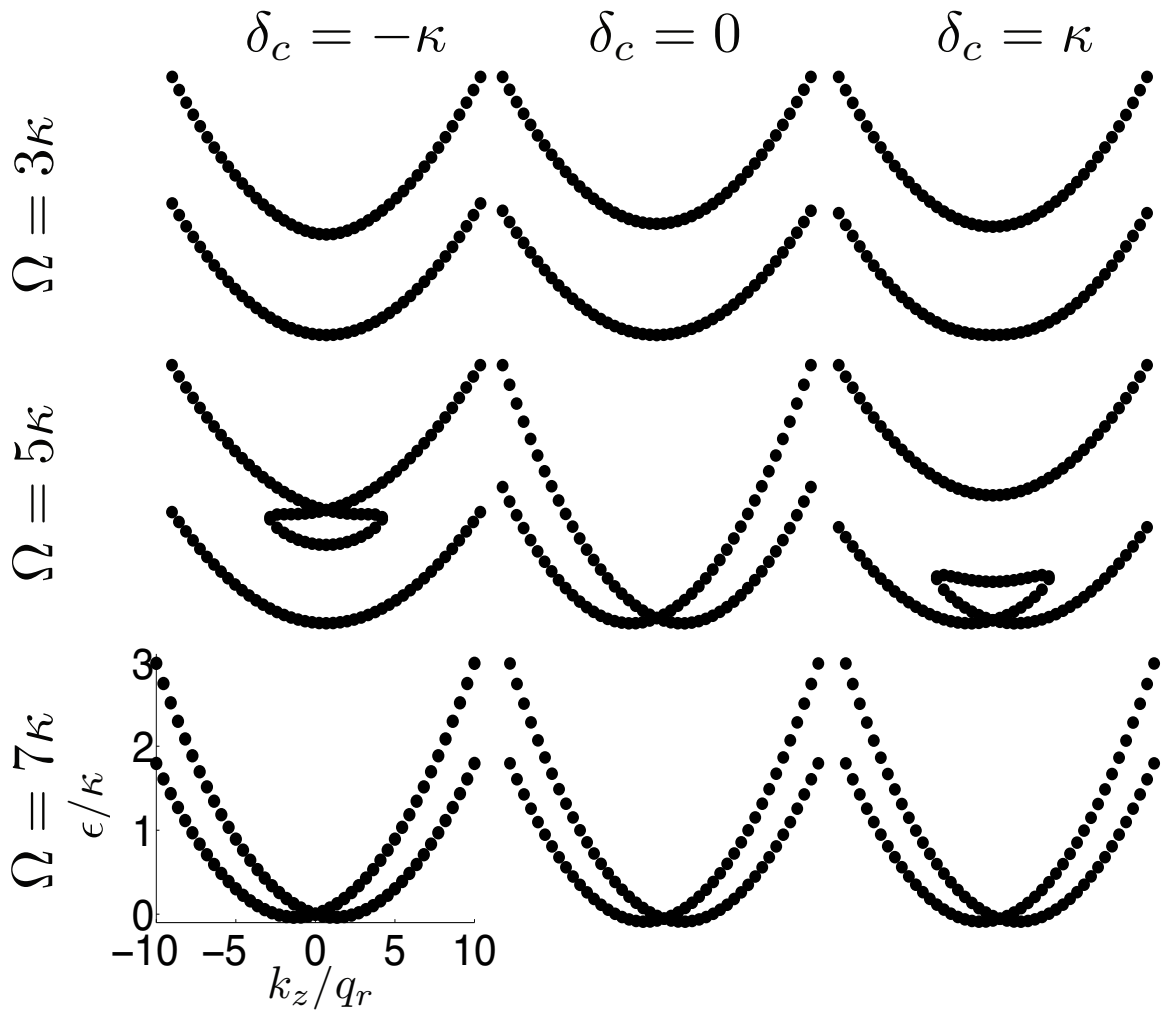

Figure 5.3 : Eigenenergy ϵ as a function of quasi-momentum. We set $\tilde{\delta} = 0$ and $\varepsilon_p = \kappa$. For nonzero δ_c, a loop structure forms when $\Omega_c^{(1)} < \Omega < \Omega_c^{(2)}$. For $\delta_c = \pm\kappa$, $\Omega_c^{(1)} = 4\varepsilon_p$ and $\Omega_c^{(2)} = 4\sqrt{2}\varepsilon_p$. Throughout our calcultion, we take κ and $\sqrt{2m\kappa}$ to be the units for energy and momentum, respectively. A typical value for κ is $2\pi \times 1$ MHz, and we choose $q_r = 0.22$ in our units.

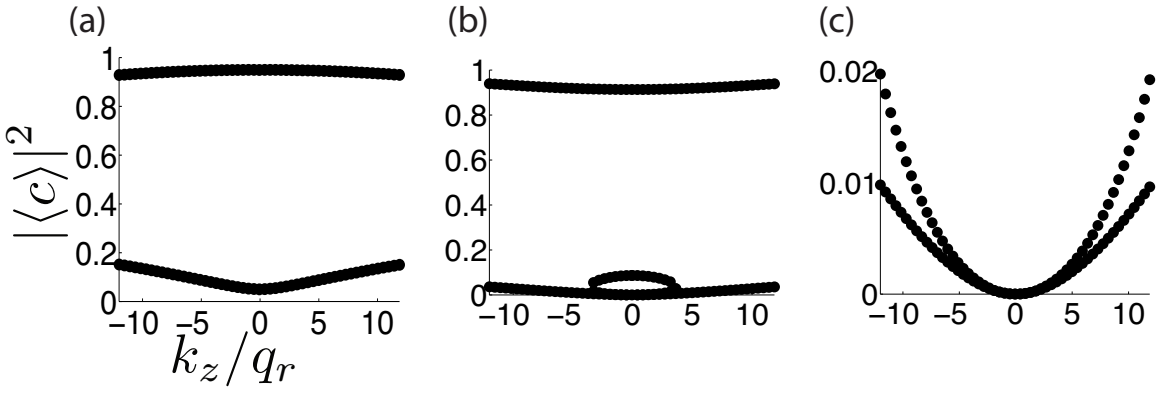

Figure 5.4 : Photon number distribution as a function of atom's quasi-momentum. The parameters are the same as in the right column of Fig. 5.3, where $\delta_c = \kappa$, $\varepsilon_p = \kappa$, and $\Omega/\kappa = 3$, 5, and 7 from (a) to (c).

As Ω is increased beyond a critical value, a loop appears near $k_z = 0$ in either the upper or the lower branch depending on the sign of δ_c. The loop increases in size as Ω increases and finally touches the other branch and dissolves when Ω reaches a second critical value. Note that such a dispersion relation is markedly different from that without the cavity, in which case one always obtains two gapped branches. The dispersion curves for finite $\tilde{\delta}$ are qualitatively similar, but in that case the curves are no longer symmetric about $k_z = 0$ and the loop emerges at finite k_z (see Fig. 5.7 below).

The photon number distributions corresponding to the right column of Fig. 5.3 are plotted in Fig. 5.4. As seen in Fig. 5.4(c), for sufficiently large Ω, the cavity photon number decreases dramatically. Correspondingly, the effective Raman coupling becomes negligibly small, and the atomic dispersion curve becomes quadratic as in the absence of laser fields (see the bottom row of Fig. 5.3). This is analogous to the photon blockade phenomenon [186] in which the strong atom-photon coupling keeps pump photons from entering the cavity.

We can gain some insights about the general structure of the dispersion curve, and particularly the appearance and disappearance of the loop, by examining the quartic equation (5.8) for $k_z = 0$ and $\tilde{\delta} = 0$. Under these conditions, Eq. (5.8) is simplified to:

$$\epsilon^2(4\epsilon^2 - 2w\epsilon + |v|^2 - 4|u|^2) = 0\,, \tag{5.9}$$

with the constraint that the root $\epsilon = 0$ is only valid for $\Omega \geq 4\epsilon_p$. Here the coefficients $w = v + v^* = 2(\frac{\Omega}{2})^2 \frac{\delta_c}{\kappa^2+\delta_c^2}$, $u = \frac{\Omega}{2}\frac{\varepsilon_p}{\kappa - i\delta_c}$ and $v = \frac{\Omega}{2}\frac{-\frac{i}{2}\Omega}{\kappa - i\delta_c}$. Simple analysis shows that there are three regimes. First, when $\Omega < 4\varepsilon_p \equiv \Omega_c^{(1)}$, Eq. (5.9) has two real roots, one positive and one negative. This corresponds to the two gapped branches for small Ω in the top row of Fig. 5.3. Second, when $\Omega_c^{(1)} \leq \Omega \leq 4\varepsilon_p\sqrt{1 + (\delta_c/\kappa)^2} \equiv \Omega_c^{(2)}$, Eq. (5.9) has four real roots — two degenerate roots at $\epsilon = 0$ and two additional roots with the same sign. This corresponds to the looped regime in the middle row of Fig. 5.3. Finally when $\Omega > \Omega_c^{(2)}$, only the two degenerate roots at $\epsilon = 0$ exist, which correspond to the gapless regime represented by the bottom row in Fig. 5.3. Note that for $\delta_c = 0$, we have $\Omega_c^{(1)} = \Omega_c^{(2)} = 4\epsilon_p$, and the loop never develops.

In the case of vanishing two-photon detuning (i.e., $\delta = 0$), simple analysis shows that there should be a total of four regimes, as shown in Fig. 5.5(a). In region I, the two dispersion branches are gapped, and the lower branch has a double degenerate minima, as shown in Fig. 5.5(b1). This dispersion curve structure is very similar to the case when both Raman beams are provided by classical coherent laser fields (we shall refer to this as the "classical case") and the Raman coupling strength is small. In region II, as shown in Fig. 5.5(b2), the two dispersion branches are still gapped, but the lower branch has a single minimum. This is similar to the classical case with a large Raman coupling strength. Regions III and IV do not have analogs in the classical case. Region III features a loop structure, as shown in Fig. 5.5(b3), whereas

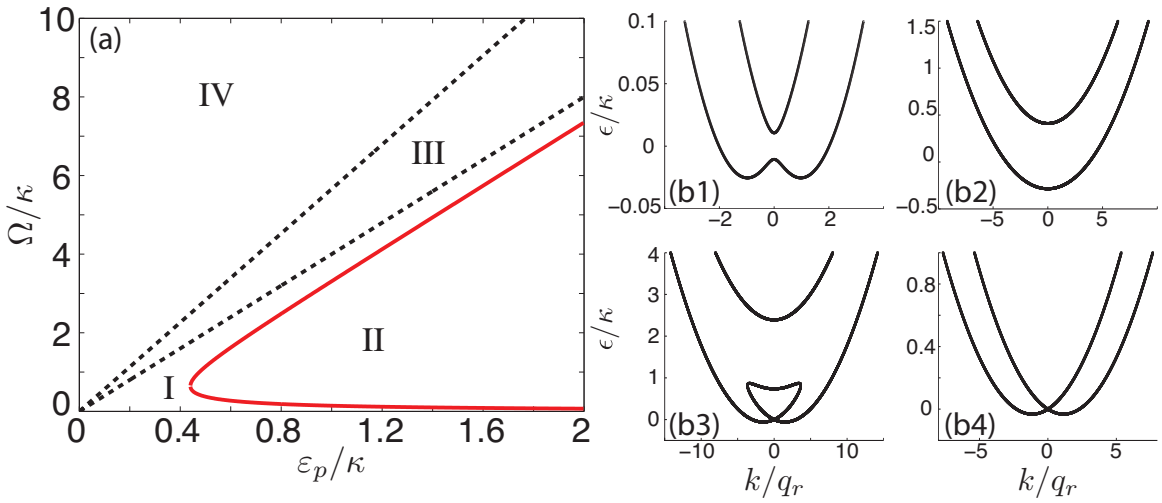

Figure 5.5 : Single particle eigen-energy spectrum "phase diagram". The dispersion curve is generally catagorized by four regions, represented from I to IV in (a). From (b1) to (b4), we fix $\varepsilon_p = \kappa$. In region I, the dispersion has double minima as shown in (b1) with $\Omega = 0.03\kappa$; region II is enclosed by the red solid curve in (a) and we show the typical point in (b2) ($\Omega = \kappa$) where only a single minimum exisits in the lower helicity branch; region III is enclosed by the black dashed lines in (a) and it is a region where loop structure emerges, as in (b3) with $\Omega = 5\kappa$; finally, in region IV we recover the double minimum dispersion although it's different from region I by closing the gap at $k = 0$, as in (b4) with $\Omega = 8\kappa$. Throughout the paper we fix $\delta_c = \kappa$ and $\delta = 0$, and adopt a dimensionless unit system with $\hbar = m = \kappa = 1$. A typical value for κ is $2\pi \times 1$ MHz, and we choose $q_r = 0.22$ in our dimensionless units (based on a realistic experimental parameter estimate).

in Region IV, the loop dissolves but the two dispersion branches becomes gapless at $k = 0$, as shown in Fig. 5.5(b4). In the looped region, the quartic equation (5.8) yields four real roots. It can be shown that this requires the coupling strength Ω to satisfy

$$\Omega_c^{(1)} \equiv 4\varepsilon_p \leq \Omega \leq 4\varepsilon_p\sqrt{1+(\delta_c/\kappa)^2} \equiv \Omega_c^{(2)} .$$

The two dashed lines in Fig. 5.5(a) represent the two critical values $\Omega_c^{(1)}$ and $\Omega_c^{(2)}$, respectively.

It is instructive to examine how the effective Raman coupling strength Ω_{eff} behaves as a function of Ω. In Fig. 5.6(a), we plot $|\Omega_{\text{eff}}|$ for the lowest dispersion branch as a function of Ω for different k values. Note that $|\Omega_{\text{eff}}|^2 = \Omega^2 n_{\text{photon}}$ where $n_{\text{photon}} = |c|^2$ is the steady-state cavity photon number. A few remarks can be made based on this plot. First, the fact that Ω_{eff} is different for different k clearly shows the influence of the atomic COM motion on both the atomic internal dynamics and the cavity photon number. Second, $|\Omega_{\text{eff}}|$ is not a monotonous function of Ω. For given k, $|\Omega_{\text{eff}}|$ increases with Ω linearly for small Ω. This can be intuitively understood as follows. At such weak atom-photon coupling, the back-action from the atom to the cavity photon is negligible. The number of cavity photons n_{photon} is roughly given by $n_{\text{photon}} \approx n_0 = \left|\frac{\varepsilon_p}{\kappa - i\delta_c}\right|^2 = \frac{\varepsilon_p^2}{\kappa^2+\delta_c^2}$, where n_0 is the number of cavity photons when the atom is absent. As a result, we have $|\Omega_{\text{eff}}| \approx \Omega\sqrt{n_0}$ which is independent of the atomic quasi-momentum k. On the other limit, when Ω is very large, the strong atom-cavity coupling strength significantly detunes the cavity away from resonance and the cavity photon number n_{photon}, and hence $|\Omega_{\text{eff}}|$, decreases as a function of Ω. Such a non-monotonous behavior of Ω_{eff} is a unique feature of the cavity system and a direct manifestation of the non-linearity of the system arising from the back-action of the atom on the cavity photon.

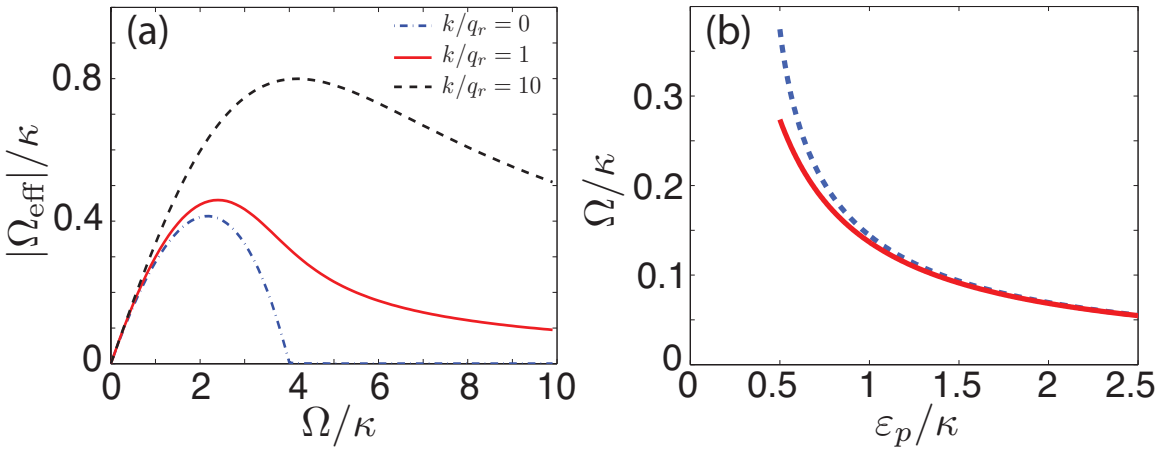

Figure 5.6 : (a) Effective Raman coupling $|\Omega_{\rm eff}|$ is plotted as a function of atom-photon coupling strength Ω for different k values, $0, q_r, 10q_r$ for blue dash-dot, red solid and black dashed lines. We observe that $|\Omega_{\rm eff}|$ does not monotonically increases with Ω but rather peaks at an intermediate value, then approaches zero in the large Ω limit. Figure (b) shows a comparison between critical boundary of region I and II (red solid curve) and the analytical result (blue dashed line) given in Eq. (5.10). At large ε_p limit, the two results match asymptotically well.

From the above analysis, it should also become clear that when the effect of the back-action is weak (which occurs when Ω is small and/or ε_p is large), we should recover the properties of the classical case. In particular, in the classical case, the lower dispersion branch change from two degenerate minima to a single minimum when the Raman coupling strength exceeds a critical value. Using our notation, this occurs when $|\Omega_{\rm eff}|$ exceeds the critical value $4E_r$ where $E_r = q_r^2/(2m)$ is the photon recoil energy. For weak atom-cavity coupling, $|\Omega_{\rm eff}| = \Omega\sqrt{n_0} = \Omega\frac{\varepsilon_p}{\sqrt{\kappa^2+\delta_c^2}}$. Hence the critical value of Ω is given by

$$\Omega = 4E_r\frac{\sqrt{\kappa^2+\delta_c^2}}{\varepsilon_p}\,. \tag{5.10}$$

In Fig. 5.6(b), we plot this critical value (blue dashed line) as a function of cavity pump rate ε_p and compare it with the numerically determined lower boundary (red solid line) between region I and II of Fig. 5.5(a). The two curves overlap with each

other when ε_p increases. Therefore, as we have expected, in the limit of weak atom-cavity coupling and strong cavity pumping, we fully recover the classical case where the SOC is induced by two classical laser beams.

The emergence of the loop structure is a distinctive nonlinear feature of the system. We remark that similar loop structures or the associated hysteretic phenomena have been found in other nonlinear systems. For Bose-Einstein condensates (BEC) in optical lattices, periodic potential favors Bloch wave solutions whereas density-density interaction prefers quadratic dispersion. Usually upon reaching a critical value, where nonlinearity wins over external potential term, swallowtail in the energy dispersion emerges from the tip. This leads to the understanding of nonlinear Landau-Zener tunneling of BEC between two Bloch bands [187], where nonzero transition probability occurs even in the adiabatic limit, known as the hysteresis effect [188]. The swallowtail also helped to explain the breakdown of superfluidity when BEC flows through optical lattices [189]. For the loop region, there are multiple solutions for the wave-functions within one band and they cause dynamical instability that destroys the superflow of BEC [190]. In other nonlinear systems, e.g. superfluid Fermi gas in optical lattices [191], cavity-induced feedback system [192], affirmative evidences of band structure loop have also been found. The nonlinearity may originate from the mean-field density-density interaction [193] or from the cavity-induced feedback between atoms and photons [194]. The case studied here corresponds to the latter situation. However, in previous studies of "ultracold atom + cavity" systems [194], the interaction between the cavity photons and atoms is dispersive, and so it does not induce SOC directly. As we will show below, the system studied here possesses very different dynamical and stability properties.

Stability and Dynamical Analysis — Nonlinear systems usually possess intriguing

stability properties. To examine the stability of the eigenstates obtained above, we introduce conjugate variables $p = |\varphi_\downarrow|^2 - |\varphi_\uparrow|^2$ and $\theta = \text{angle}(\varphi_\downarrow) - \text{angle}(\varphi_\uparrow)$, which correspond to the spin magnetization and the relative phase between the two atomic spin states. The EOM for p and θ can be easily derived from Eqs. (5.6) and (5.7) as,

$$\dot{p} = \frac{\Omega^2\kappa}{\kappa^2+\delta_c^2}\frac{1-p^2}{4}\left(1-\frac{4\varepsilon_p(\kappa\sin\theta+\delta_c\cos\theta)}{\Omega\kappa\sqrt{1-p^2}}\right), \tag{5.11}$$

$$\dot{\theta} = 2(k_r k_z+\tilde{\delta}) + \frac{\kappa\varepsilon_p\cos\theta-\delta_c\varepsilon_p\sin\theta}{\kappa^2+\delta_c^2}\frac{\Omega p}{\sqrt{1-p^2}} + \left(\frac{\Omega}{2}\right)^2\frac{\delta_c}{\kappa^2+\delta_c^2}p\,, \tag{5.12}$$

from which we can readily obtain the fixed points (p^*,θ^*) by setting $\dot{p}=\dot{\theta}=0$, we obtain fixed points equations,

$$\sqrt{1-p^{*2}} = \frac{4\varepsilon_p}{\Omega\kappa}(\kappa\sin\theta^*+\delta_c\cos\theta^*)\,, \tag{5.13}$$

$$\left(\frac{\Omega}{2}\right)^2\left(\frac{\kappa}{\kappa^2+\delta_c^2}\frac{\kappa\cos\theta^*-\delta_c\sin\theta^*}{\kappa\sin\theta^*+\delta_c\cos\theta^*}+\frac{\delta_c}{\kappa^2+\delta_c^2}\right)p^* +2(q_r k_z+\tilde{\delta})=0\,, \tag{5.14}$$

. The solutions are identical to eigenstates obtained in terms of $\varphi_\uparrow$ and $\varphi_\downarrow$. To check the stability, we linearize the equations around the fixed points by taking $p=p^*+\delta p$, $\theta=\theta^*+\delta\theta$, and arrive at

$$\frac{d}{dt}\begin{pmatrix}\delta p\\ \delta\theta\end{pmatrix} = \begin{pmatrix}f_1 & f_2\\ g_1 & g_2\end{pmatrix}\begin{pmatrix}\delta p\\ \delta\theta\end{pmatrix} \equiv \mathcal{M}\begin{pmatrix}\delta p\\ \delta\theta\end{pmatrix}, \tag{5.15}$$

where matrix elements of $\mathcal{M}$ are given by

$$f_1 = -\frac{p^*\kappa\Omega^2}{2(\kappa^2+\delta_c^2)} + \frac{p^*\varepsilon_p\Omega(\delta_c\cos\theta^*+\kappa\sin\theta^*)}{(\kappa^2+\delta_c^2)\sqrt{1-p^{*2}}} \tag{5.16}$$

$$f_2 = \frac{\sqrt{1-p^{*2}}}{1+\delta_c^2}\varepsilon_p\Omega(\delta_c\sin\theta^*-\kappa\cos\theta^*) \tag{5.17}$$

$$g_1 = \frac{\Omega}{4(\kappa^2+\delta_c^2)}(\delta_c\Omega + \frac{4\varepsilon_p(\kappa\cos\theta^* - \delta_c\sin\theta^*)}{(1-p^{*2})^{3/2}}) \quad (5.18)$$

$$g_2 = -\frac{p^*\varepsilon_p\Omega}{\sqrt{1-p^{*2}}(\delta_c^2+\kappa^2)}(\delta_c\cos\theta^* + \kappa\sin\theta^*) \quad (5.19)$$

If any of the eigenvalues of $\mathcal{M}$ has a positive real part, the fluctuation terms δp and $\delta\theta$ grow exponentially in time and therefore the system is dynamically unstable [195]. For unstable states, we denote the largest real part as γ, which can be regarded as the decay rate of the unstable states.

A typical result of the stability analysis is shown in Fig. 5.7, where we plot the dispersion curves and indicate the stability of the states using colored triangles. One can observe: (1) in the regime without the loop, one branch is stable and the other branch is unstable; (2) in the regime with the loop, there may exist one or two stable branches and correspondingly three or two unstable branches. This means that the cavity feedback completely alters the system's stability. Nevertheless, for a relatively large cavity pumping rate as shown in Fig. 5.7(a)-(c), γ is small and the unstable branches are more robust compared with the case represented in Fig. 5.7 (d)-(f) where a smaller ε_p is used. This can be understood as follows: as the cavity pump rate ε_p is increased, the cavity photon number increases and the back-action from the atom to the photon becomes less important. Therefore we expect (and have confirmed from our calculation) that in the strong pump limit, the cavity system would not be very different from the conventional system without a cavity [55, 183, 184].

A direct way to detect dynamical instability experimentally in this system is to count the sudden change in the cavity photon number. As an example, we consider the following situation. We start from a stable eigenstate represented in Fig. 5.7(a). From $t = 0$ to $4000/\kappa$, the two-photon detuning $\tilde{\delta}$ is changed linearly from 0.05κ to -0.05κ and remains fixed at -0.05κ afterwards. We plot the evolution of the

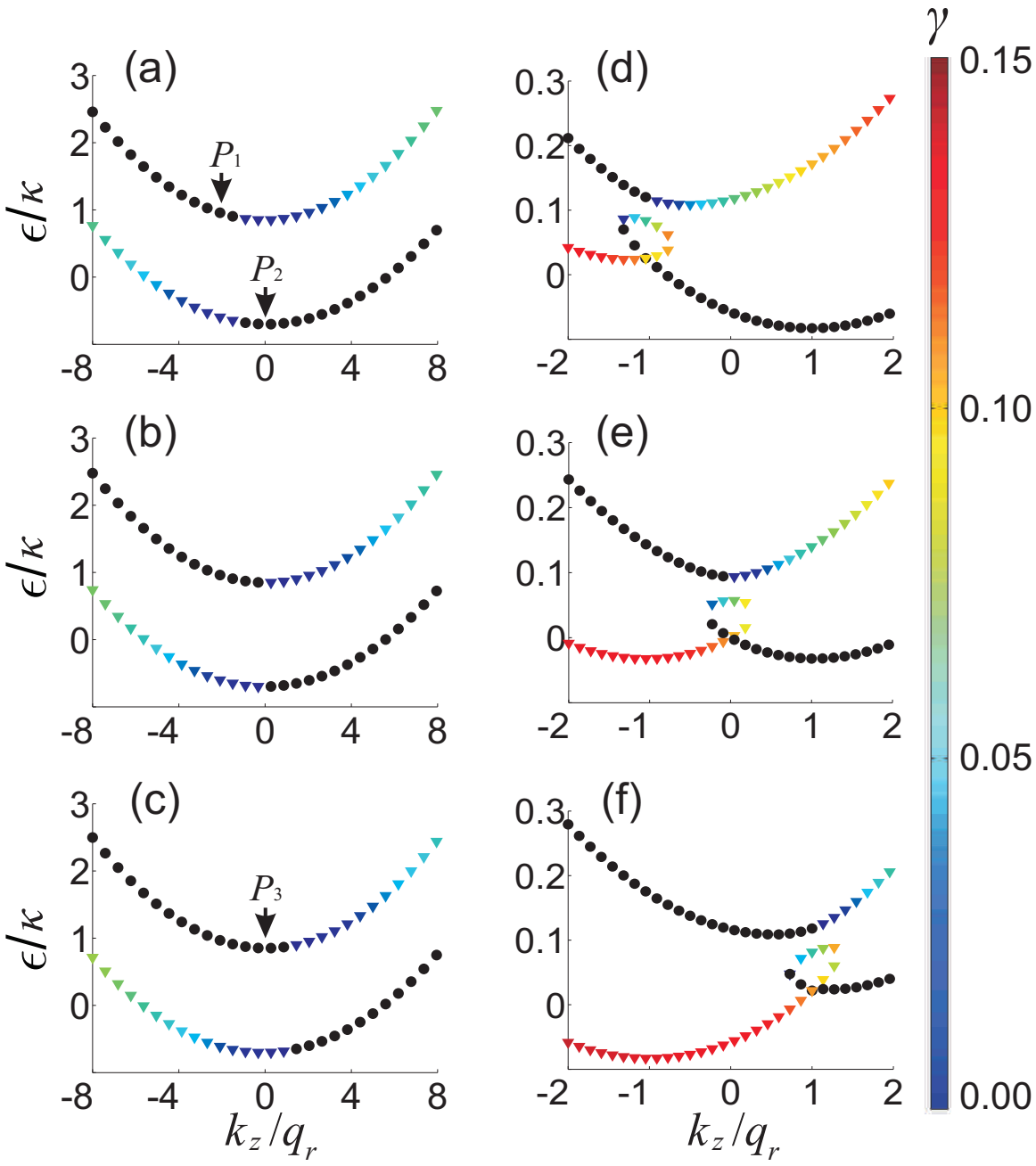

Figure 5.7 : Stability analysis of the dispersion curve. Colored triangles represent dynamically unstable states and black solid dots represent dynamically stable ones. The colorbar represents γ, the decay rate of the unstable states. In all figures, $\Omega = 1.1\kappa$ and $\delta_c = \kappa$. From (a) to (c) $\varepsilon_p = 2\kappa$ and $\tilde{\delta} = 0.05$, 0, and -0.05κ; from (d) to (f) $\varepsilon_p = 0.2\kappa$, and $\tilde{\delta} = 0.05$, 0, -0.05κ.

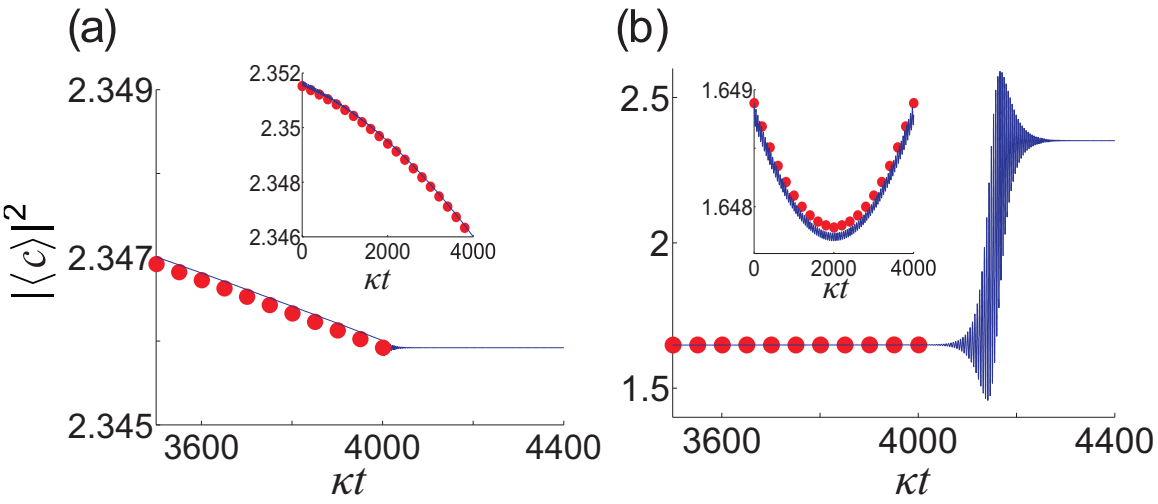

Figure 5.8 : Evolution of photon number. The initial states are prepared using the same set of parameters as in Fig. 5.7(a). In (a), we start from point P_1 with $k_z = -2q_r$ and in (b) we start from point P_2 with $k_z = 0$, both indicated in Fig. 5.7(a). From $t = 0$ to $4000/\kappa$, $\tilde{\delta}$ is linearly tuned from 0.05κ to -0.05κ and remains fixed afterwards. Red solid dots represent the photon number corresponding to the instantaneous eigenstate, while blue solid lines represent the dynamical evolution according to Eqs. (5.3) and (5.4) after mean-field approximation.

photon number in Fig. 5.8. In Fig. 5.8(a) we start from the state referred to as P_1 in Fig. 5.7(a). During the whole evolution, the photon number follows the corresponding value of the instantaneous eigenstate as the system remains dynamically stable. In Fig. 5.8(b) we start from the state referred to as P_2 in Fig. 5.7(a). During the linear ramp of $\tilde{\delta}$, the photon number follows the corresponding values of the instantaneous eigenstate. However, at the end of the ramp, the system evolves into a dynamically unstable state. The dynamical instability sets in some time after the end of the ramp and the photon number jumps to a different value after a short transient time. The final state matches the stable state P_3 with the same atomic quasi-momentum as indicated in Fig. 5.7(c) (note that the quasi-momentum does not change during the time evolution).

5.3 Density Matrix Approach

The mean-field treatment relies on two implicit assumptions: (1) the atom-photon correlation is negligible, and (2) the photon field can be well approximated by a coherent state. In order to examine the validity of these assumption, and hence the validity of the mean-field approximation, we now turn to a full quantum treatment based on the Master equation:

$$\dot{\rho} = \frac{1}{i\hbar}[\mathcal{H}_{\text{eff}}, \rho] + \mathcal{L}[\rho]\,. \tag{5.20}$$

Here ρ is the total density operator of the coupled atom-cavity system, the effective Hamiltonian $\mathcal{H}_{\text{eff}}$ is given by,

$$\begin{aligned}\mathcal{H}_{\text{eff}} &= \sum_{\sigma=\uparrow,\downarrow}\int dz\left[\hat{\psi}^{\dagger}_{\sigma}(z)\left(\frac{k^2+2\alpha_\sigma q_r k}{2m}+\alpha_\sigma\delta\right)\hat{\psi}_\sigma(z)\right]+\frac{\Omega}{2}\int dz\left[\hat{\psi}^{\dagger}_{\uparrow}(z)\hat{\psi}_{\downarrow}(z)\hat{c}+h.c.\right]\\ &+ i\varepsilon_p(\hat{c}^{\dagger}-\hat{c})-\delta_c\hat{c}^{\dagger}\hat{c}\,.\end{aligned} \tag{5.21}$$

The dissipation arising from cavity decay is modeled by the Liouvillean term in the standard form of Lindblad super-operator [196, 197],

$$\mathcal{L}[\rho] = \kappa(2c\rho\hat{c}^{\dagger}-\hat{c}^{\dagger}\hat{c}\rho-\rho\hat{c}^{\dagger}\hat{c})\,. \tag{5.22}$$

Again, due to spatial homogeneity, we decouple momentum eigenstates by taking the plane-wave ansatz for the atomic modes as $\hat{\psi}_\sigma(z) = e^{ikz}\hat{\psi}_\sigma$. As there is no coupling between atomic operators with different k, we can work in the subspace for a fixed value of k. Here we explicitly write the commutator in Eq. (5.20), for a given atomic quasi-momentum k, as,

$$\begin{aligned}[\mathcal{H}_{\text{eff}}(k),\rho] &= \left(\frac{k^2}{2m}+\frac{q_r k}{m}+\delta\right)\left(\hat{\psi}^{\dagger}_{\uparrow}\hat{\psi}_{\uparrow}\rho-\rho\hat{\psi}^{\dagger}_{\uparrow}\hat{\psi}_{\uparrow}\right)+\left(\frac{k^2}{2m}-\frac{q_r k}{m}-\delta\right)\left(\hat{\psi}^{\dagger}_{\downarrow}\hat{\psi}_{\downarrow}\rho-\rho\hat{\psi}^{\dagger}_{\downarrow}\hat{\psi}_{\downarrow}\right)\\ &+\frac{\Omega}{2}\left(\hat{\psi}^{\dagger}_{\uparrow}\hat{\psi}_{\downarrow}\hat{c}\rho+\hat{c}^{\dagger}\hat{\psi}^{\dagger}_{\downarrow}\hat{\psi}_{\uparrow}\rho-\rho\hat{\psi}^{\dagger}_{\uparrow}\hat{\psi}_{\downarrow}c-\rho\hat{c}^{\dagger}\hat{\psi}^{\dagger}_{\downarrow}\hat{\psi}_{\uparrow}\right)\\ &+i\varepsilon_p\left(\hat{c}^{\dagger}\rho-\hat{c}\rho-\rho\hat{c}^{\dagger}+\rho\hat{c}\right)-\delta_c\left(\hat{c}^{\dagger}\hat{c}\rho-\rho\hat{c}^{\dagger}\hat{c}\right)\,.\end{aligned} \tag{5.23}$$

Note that if the photon recoil $q_r = 0$, which occurs when the cavity mode and the external laser beams are co-propagating, the COM kinetic energy terms $k^2/(2m)$ can be gauged away after a simple gauge transformation. Our model is then reduced to the J-C model and the atomic COM motion does not play a role. To solve the Master equation (5.20), we choose our basis states as direct product states of photon Fock state $|n\rangle$ and atomic internal state $|\sigma =\uparrow,\downarrow\rangle$: $|n;\sigma\rangle \equiv |n\rangle \otimes |\sigma\rangle$, where non-negative integer n denotes cavity photon number. Our goal is to calculate the entire matrix elements of the density operator under this set of basis states, denoted by $\langle m;\sigma|\rho|n;\sigma'\rangle \equiv \rho_{mn}^{\sigma\sigma'}$. We found the governing equation for the matrix element can be written as,

$$\begin{aligned}
\frac{d}{dt}\rho_{mn}^{\sigma\sigma'} &= -i\left(\frac{k^2}{2m}+\frac{q_r k}{m}+\delta\right)\left(\delta_{\sigma\uparrow}-\delta_{\sigma'\uparrow}\right)\rho_{mn}^{\sigma\sigma'} - i\left(\frac{k^2}{2m}-\frac{q_r k}{m}-\delta\right)\left(\delta_{\sigma\downarrow}-\delta_{\sigma'\downarrow}\right)\rho_{mn}^{\sigma\sigma'} \\
&+ \frac{\Omega}{2i}(\delta_{\sigma\uparrow}\sqrt{m+1}\rho_{m+1n}^{\bar{\sigma}\sigma'} + \delta_{\sigma\downarrow}\sqrt{m}\rho_{m-1n}^{\bar{\sigma}\sigma'} - \delta_{\sigma'\uparrow}\sqrt{n+1}\rho_{mn+1}^{\sigma\bar{\sigma'}} - \delta_{\sigma'\downarrow}\sqrt{n}\rho_{mn-1}^{\sigma\bar{\sigma'}}) \\
&+ \varepsilon_p\left(\sqrt{m}\rho_{m-1n}^{\sigma\sigma'} - \sqrt{m+1}\rho_{m+1n}^{\sigma\sigma'} + \sqrt{n}\rho_{mn-1}^{\sigma\sigma'} - \sqrt{n+1}\rho_{mn+1}^{\sigma\sigma'}\right) \\
&+ i\delta_c\left(m-n\right)\rho_{mn}^{\sigma\sigma'} + \kappa\left(2\sqrt{m+1}\sqrt{n+1}\rho_{m+1n+1}^{\sigma\sigma'} - (m+n)\rho_{mn}^{\sigma\sigma'}\right), \qquad (5.24)
\end{aligned}$$

where $\bar{\sigma}$ represents the flip-spin value, i.e. $\bar{\uparrow} =\downarrow$ and $\bar{\downarrow} =\uparrow$.

With Eq. (5.24), we can study the dynamical evolution of the density operator ρ for a given initial state. Obviously, we need to introduce a sufficiently large photon number cutoff. Once we obtain the density operator, all relevant physical quantities can be readily calculated. An example is given in Fig. 5.9, where we show the time evolution of the cavity photon number $n = \mathrm{Tr}[\rho\hat{n}] = \mathrm{Tr}[\rho\hat{c}^\dagger\hat{c}]$ for the initial state $|0;\uparrow\rangle$. The three different curves in Fig. 5.9 correspond to different atomic quasi-momentum k.

As evidenced in Fig. 5.9, due to the presence of cavity decay, a steady state will eventually be reached. Let us now focus on the properties of the steady state. The

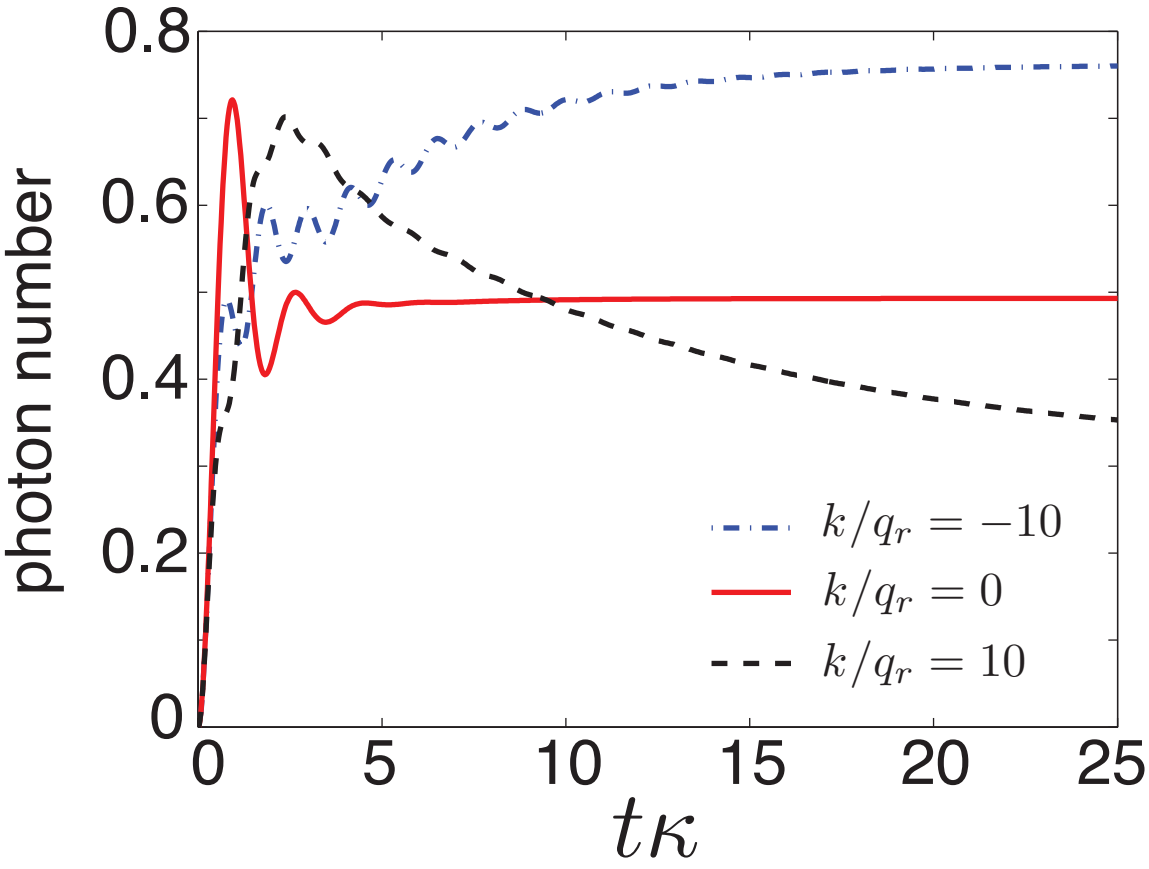

Figure 5.9 : Time evolution of cavity photon number. The initial state is given by $|0;\uparrow\rangle$ and we consider the same parameter as in Fig. 5.10(a) with $k/q_r = -10$, 0, 10. The steady-state values, obtained in the long time limit as shown here, correspond to red dashed lines at corresponding k values in Fig. 5.10(a).

steady-state density operator matrix elements can be obtained by equating the RHS of Eq. (5.24) to zero. The red dashed lines in Fig. 5.10(a)-(c) represent the steady-state photon number as functions of atomic quasi-momentum k. The horizontal arrows in the plot represent the cavity photon number by setting $q_r = 0$, in which case our model reduces to the J-C model and all physical quantities become k-independent.

To have a better understanding of the photon statistics, we study the steady-state photon number fluctuation. Specifically, we calculate the normalized photon number fluctuation defined as

$$\Delta_n = \frac{\langle (\Delta n)^2 \rangle}{\langle \hat{n} \rangle} = \frac{\langle \hat{n}^2 \rangle - \langle \hat{n} \rangle^2}{\langle n \rangle},$$

where the expectation values of the operators are obtained with the help of the steady-state density operator. For a coherent cavity field, the photon fluctuation is Poissonian and we have $\Delta_n = 1$. The solid curves in Fig. 5.10(d)-(f) represent Δ_n (left vertical axis) as functions of k, and the horizontal arrows pointing to left give the values of Δ_n from the J-C model by setting $q_r = 0$. For the parameters we have used, we note that the J-C model always predicts a super-Poissonian photon statistics, whereas our model gives super-Poissonian photon statistics only for small atomic quasi-momentum, but Poissonian statistics as $k/q_r \to \pm\infty$.

Last but not least, to characterize the correlation between the atom and the cavity field, we investigate the so-called negativity which measures the degree of entanglement for a mixed state system. The negativity is defined as $\mathcal{N}(\rho) = (||\rho^{T_A}||_1 - 1)/2$, where ρ^{T_A} is the partial transpose of the density operator with respect to either the atom subsystem or the cavity subsystem, and $||\rho^{T_A}||_1$ denotes its trace norm with the definition $||\hat{A}||_1 \equiv \mathrm{Tr}[\sqrt{\hat{A}^\dagger \hat{A}}]$. A negativity of zero indicates that the two subsystems (the atom and the cavity, in our case) are not entangled, whereas a positive negativity means that finite degree of entanglement is present. The dashed curves

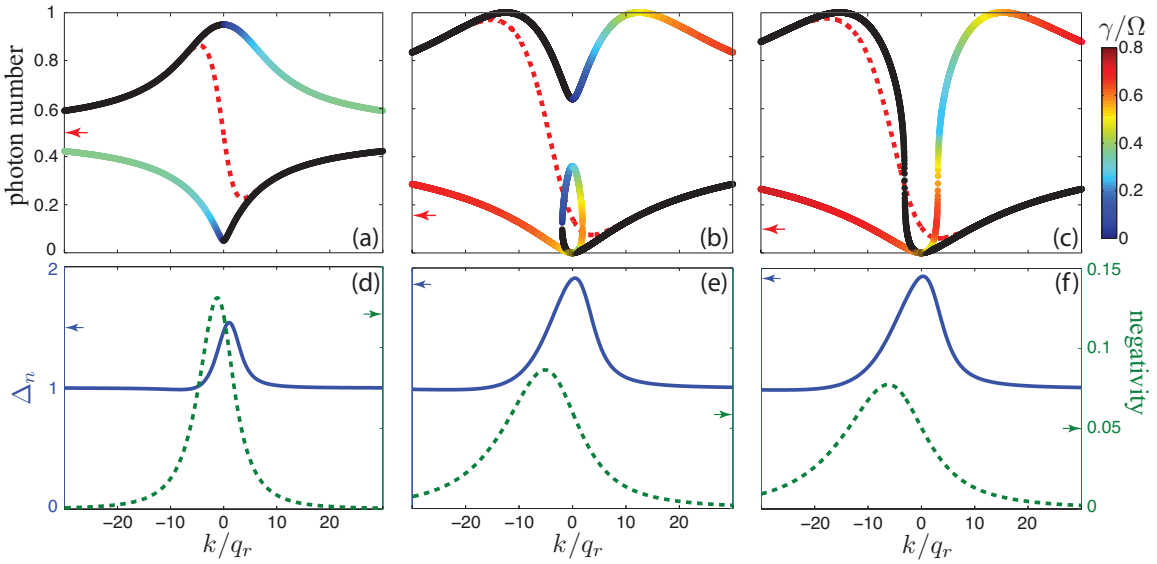

Figure 5.10 : (a)∼(c) Photon number obtained from the mean-field approach (solid curves) and from quantum mechanical Master equation approach (red dashed curves). From (a) to (c), $\Omega = 3\kappa,\ 5.6\kappa,\ 6\kappa$. The color on the solid curves represents the normalized decay rate γ/Ω of unstable mean-field states. The black color represents stable mean-field states. We have used $\varepsilon_p = \kappa$, and other parameters are the same as before. (d)∼(f) Corresponding photon number fluctuation (blue solid curve) and negativity (green dashed line) obtained from the quantum approach. The parameters used here are the same in (a)∼(c), respectively. The horizontal arrows indicate results from the J-C model by taking $q_r = 0$.

in Fig. 5.10(d)-(f) represent the negativity (right vertical axis) in the steady state as functions of k, and the horizontal arrows pointing to right give the values of the negativity from the J-C model by setting $q_r = 0$. One can observe that for the chosen parameters, the J-C model always predicts a finite degree of entanglement between the atom and the cavity field. By contrast, the degree of entanglement in our model weakens when $k/q_r \to \pm\infty$.

In Fig. 5.10(a)-(c), in addition to the steady-state photon number obtained from the quantum treatment (dashed curves), we also plot the photon number $n_{\text{photon}} = |c|^2$ obtained from the mean-field approach (solid curves). In the quantum treatment, the

steady-state density matrix is obtained by solving a set of linear equations. For a given k, the solution is unique. Hence we only get one steady-state photon number for a given atomic quasi-momentum. On the other hand, the mean-field treatment allows multiple steady-state solutions corresponding to different real roots of the quartic equation Eq. (5.8). Hence a single k value is associated with more than one steady-state photon number. However, due to the non-linearity intrinsic in the mean-field method, not all steady-states are dynamically stable. A straightforward stability analysis allows us to quantify the dynamical stability of the mean-field states. The stability information of the mean-field states are encoded as the color value in the solid curves. Those stable states are represented by black color, while any color other than black indicates an unstable state, and the color value represents the decay rate (see the colorbar) of the corresponding state. From Fig. 5.10(a)-(c), we clearly see that at large atomic quasi-momentum $k/q_r \to \pm\infty$, the Master equation result overlaps with the stable mean-field branch; while at small $|k|$, the quantum result deviates significantly away from the mean-field solution.

The agreement for large $|k|$ and the discrepancy at small $|k|$ are both consistent with the results of the negativity and photon number fluctuations as presented in Fig. 5.10(d)-(f): At large $|k|$, the negativity is small (i.e., atom-cavity entanglement is weak) and the photon number fluctuation tends to Poissonian (i.e., the photon field is well approximated by a coherent state), this is exactly the regime where we expect the mean-field approximation is valid. By contrast, for small $|k|$, the quantum calculation indicates that there is non-negligible entanglement between the atom and the cavity field, and the cavity field itself cannot be assumed as a coherent state. Hence the mean-field assumption is no longer valid.

The reason why mean-field approximation only works for large $|k|$ is actually

rather simple. Consider a Raman transition process where the atom jumps from $|\uparrow\rangle$ to $|\downarrow\rangle$. The quasi-momentum k does not change during this process, however the real momentum changes from $k+q_r$ to $k-q_r$. Therefore the effective two-photon Raman detuning is not just 2δ, but $2\delta+2q_rk/m$, where the additional term comes from the difference of the kinetic energies for different pseudo-spin state $|\sigma\rangle$. In other words, the SOC renders the two-photon detuning momentum-dependent. In the examples we presented in this work, we have taken $\delta=0$. Hence the Raman transition is only near-resonant for small $|k|$, and becomes far off-resonant for large $|k|$. Therefore, for large $|k|$, the atom-photon coupling, and hence the atomic back-action to cavity, are weak. This explains why the mean-field assumption becomes valid in this regime.

5.4 Superradiant Phase in Thermodynamic Limit

So far, we have been focusing on the properties of a single atom. In this section, we consider a system where the single mode cavity photon field is coupled to many atoms in the thermodynamic limit. We neglect the bare interactions between atoms. However, as each atom influences the whole photon field which back acts on the other atoms, the photon field induces an effective coupling between atoms. When the atomic COM motion is neglected, our model reduces to the TC model. One of the most well-known many-body effects in this model is the Dicke superradiant phase transition [198–200]. Here we investigate how the COM degree of freedom and the SOC affect the Dicke phase transition.

We consider a canonical ensemble where N atoms inside the cavity are confined within a box with volume V. In the thermodynamic limit, both N and V are taken to be infinity but the number density $\rho=N/V$ is finite. The Hamiltonian of this

system is given by

$$H = \omega_L c^\dagger c + \sum_{j=1}^{N} \hat{h}_j \,, \tag{5.25}$$

with the Hamiltonian for the jth atom

$$\hat{h}_j = \frac{\hat{\mathbf{k}}_j^2}{2m} + \frac{q_r \hat{k}_{zj}}{m}\sigma_z^j + \frac{\omega_0}{2}\sigma_z^j + \frac{\tilde{\Omega}}{2\sqrt{N}}\left(\sigma_j^+ c + \sigma_j^- c^\dagger\right) \,, \tag{5.26}$$

where $\tilde{\Omega} = \sqrt{N}\Omega$ is the rescaled Raman coupling strength, and $\hat{\mathbf{k}}_j$ is the three dimensional quasi-momentum operator for the jth atom.

To investigate the thermodynamic phase transition at temperature T, we take a similar approach as in Ref. [200] in which the Dicke phase transition in the TC model is investigated. The canonical partition function $Z = \mathrm{Tr}\left(e^{-\beta H}\right)$ with $\beta = 1/\left(k_B T\right)$ can be calculated as

$$Z = \frac{V^N}{(2\pi)^{3N}} \int \frac{d^2\alpha}{\pi} \int \left(\prod_{j=1}^{N} d\mathbf{k}_j\right) \sum_{\{\sigma_j\}} \langle\Psi| \, e^{-\beta H} \, |\Psi\rangle \,, \tag{5.27}$$

where we have chosen the states

$$|\Psi\rangle = |\alpha\rangle \prod_{j=1}^{N} |\mathbf{k}_j\rangle \, |\sigma_j\rangle \tag{5.28}$$

as our basis states to evaluate the trace. Here $|\alpha\rangle$ is the photon coherent state, i.e., the eigenstate of photon annihilation operator such that $c|\alpha\rangle = \alpha|\alpha\rangle$, $|\mathbf{k}_j\rangle$ is the momentum eigenstate, and $|\sigma_j\rangle$ is the eigenstate of σ_z^j for the jth atom. By using the condition $N \to \infty$, we obtain

$$\langle\alpha| \, e^{-\beta H} \, |\alpha\rangle = \exp\left[-\beta\left(\omega_L \left|\alpha\right|^2 + \sum_{j=1}^{N} \hat{h}_j^\alpha\right)\right] \,, \tag{5.29}$$

where

$$\hat{h}_j^\alpha = \frac{\hat{\mathbf{k}}_j^2}{2m} + \frac{q_r \hat{k}_{zj}}{m}\sigma_z^j + \frac{\omega_0}{2}\sigma_z^j + \frac{\tilde{\Omega}}{2\sqrt{N}}\left(\sigma_j^+ \alpha + \sigma_j^- \alpha^*\right) \,. \tag{5.30}$$

As the summation over spin and integral over momentum in Eq. (5.27) are independent for different atoms, the partition function can be simplified as

$$Z = \int \frac{d^2\alpha}{\pi} e^{-\beta\omega_L|\alpha|^2} \left[\frac{V}{(2\pi)^3} \int d\mathbf{k} \left(e^{-\beta\epsilon^+} + e^{-\beta\epsilon^-} \right) \right]^N , \tag{5.31}$$

where

$$\epsilon^{\pm} = \frac{\mathbf{k}^2}{2m} \pm \sqrt{\left(\frac{q_r k_z}{m} + \frac{\omega_0}{2} \right)^2 + \left(\frac{\tilde{\Omega}}{2} \right)^2 \frac{|\alpha|^2}{N}} \tag{5.32}$$

are the eigenvalues of $\hat{h}_j^{\alpha}$ in Eq. (5.30). Integrating over the complex angle of α and x, y components of $\mathbf{k}$ in (5.31), and letting $u = \frac{|\alpha|^2}{N}$, we can rewrite the partition function as

$$Z = C_1 \int_0^{\infty} du \exp\left\{ N\left[F(u) \right] \right\} , \tag{5.33}$$

with constant $C_1 = N \left(\frac{mV}{4\pi^2\beta} \right)^N$ and

$$F(u) = -\beta\omega_L u + \log S\left(u\right) , \tag{5.34}$$

$$S\left(u\right) = 2 \int dk_z \exp\left(-\frac{\beta k_z^2}{2m} \right) \cosh \xi\left(k_z, u\right) , \tag{5.35}$$

$$\xi\left(k_z, u\right) = \beta \sqrt{\left(\frac{q_r k_z}{m} + \frac{\omega_0}{2} \right)^2 + \left(\frac{\tilde{\Omega}}{2} \right)^2} \, u \, . \tag{5.36}$$

The Laplace's method [200] is used to deal with the integral over u in Eq. (5.33). For $N \to \infty$, this yields

$$Z = C_2 \max_{u \in [0,\infty)} \exp\left\{ N\left[F(u) \right] \right\} , \tag{5.37}$$

where C_2 is a constant and we denote that the maximum of $F(u)$ is reached at $u = u_0$. We numerically obtain a $u_0 \geqslant 0$ by taking the first and second order derivatives of $F(u)$, and it is straightforward to show that u_0 is actually the normalized photon number

$$u_0 = \frac{\left\langle c^{\dagger} c \right\rangle}{N} , \tag{5.38}$$

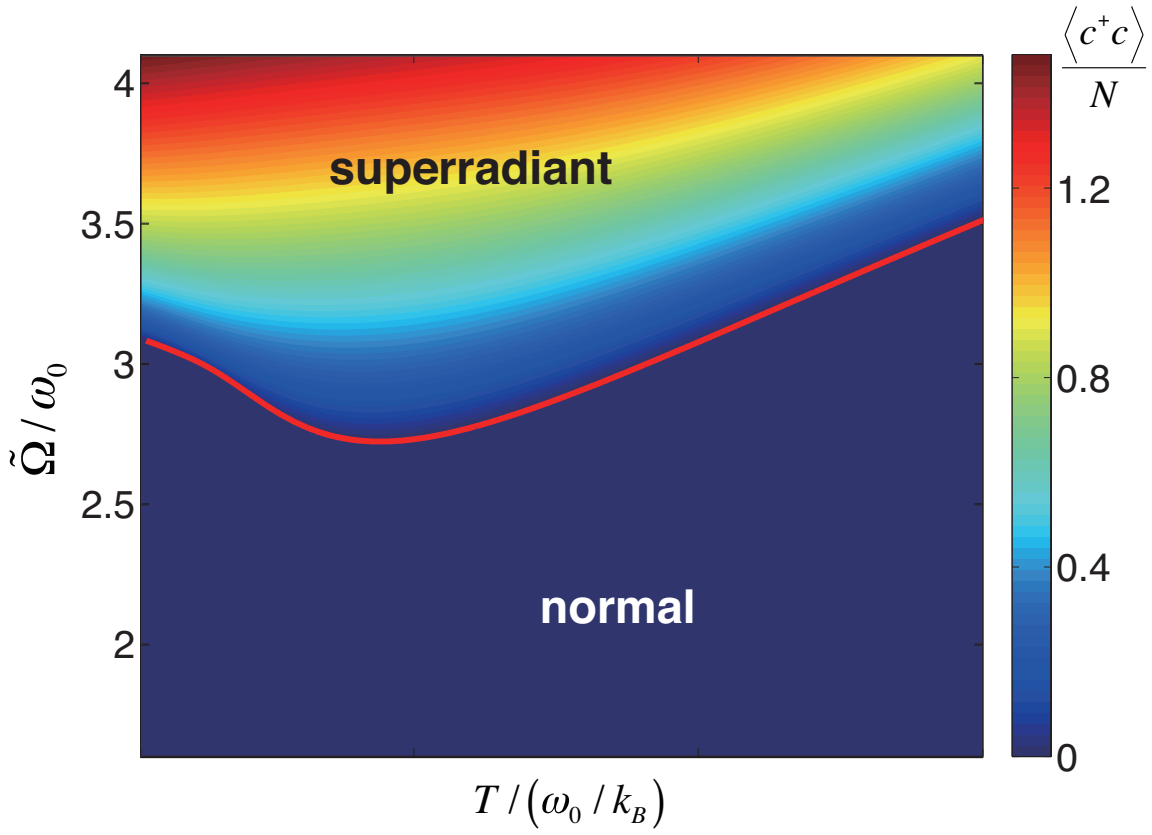

Figure 5.11 : Normalized photon number $\langle c^\dagger c\rangle/N$ as a function of temperature T and effective Raman coupling strength $\widetilde{\Omega}$ with $E_r = 0.5\omega_0$, where $\langle c^\dagger c\rangle$ is the average photon number and N is the atom number. Here $\langle c^\dagger c\rangle/N > 0$ corresponds to the superradiant phase and $\langle c^\dagger c\rangle/N = 0$ corresponds to the normal phase. We take $\omega_L = 0.8\omega_0$ in these figures.

where $\langle c^\dagger c\rangle/N > 0$ corresponds to the superradiant phase with a macroscopic photon excitation appearing in the thermodynamic limit; and $\langle c^\dagger c\rangle/N = 0$ corresponds to the normal phase.

Figure 5.11 shows $\langle c^\dagger c\rangle/N$ as a function of the temperature T and the rescaled Raman coupling strength $\tilde{\Omega}$ with the SOC strength $E_r = 0.5\omega_0$. The red solid line in the figure represents the critical coupling strength $\tilde{\Omega}_c$ (i.e., the phase boundary): Above this line, we have $\langle c^\dagger c\rangle/N > 0$ and the system is in the superradiant phase; and

below this line, $\langle c^\dagger c\rangle/N = 0$ which corresponds to the normal phase. In Fig. 5.12(a), we plot $\tilde{\Omega}_c$ as a function of T for several different values of E_r. As in the previous single-atom case, we recover the usual TC model when $E_r = 0$ (bottom curve in Fig. 5.12(a)). For the TC model, $\tilde{\Omega}_c$ is a monotonically increasing function of T, and $\tilde{\Omega}_c = 2\sqrt{\omega_0\omega_L}$ at $T = 0$. For finite E_r, $\tilde{\Omega}_c$ is larger than the corresponding value in the TC model. In other words, in the presence of the SOC, the regime of normal phase is enlarged, which is consistent with the single-atom property that the SOC enlarges the $n = 0$ regime with no photons. The upward shift of $\tilde{\Omega}_c$ at finite E_r is more pronounced at lower temperature. This may not be surprising as, at lower temperature, the average atomic COM kinetic energy is lower and hence the photon recoil plays a more significant role. This temperature dependent shift leads to another important feature brought by the SOC: $\tilde{\Omega}_c$ is no longer a monotonic function of T, as can be easily seen in Fig. 5.12(a), and reaches the minimum value at a finite temperature.

A consequence of the nonmonotonic behaviour of $\tilde{\Omega}_c$ is that the normal phase may become reentrant as the temperature varies. This is depicted in Fig. 5.12(b), where we plot $\langle c^\dagger c\rangle/N$ as a function of T with $\tilde{\Omega} = 2.9\omega_0$ for $E_r = 0.5\omega_0$ (red solid line) and $E_r = 0$ (blue dashed line). For the TC model ($E_r = 0$), the system is in the superradiant phase at sufficiently low temperature when $\tilde{\Omega} > 2\sqrt{\omega_0\omega_L}$ (as is the case shown in Fig. 5.12(b)) with finite $\langle c^\dagger c\rangle/N$. As temperature increases, $\langle c^\dagger c\rangle/N$ decreases monotonically until it reaches 0 at the critical temperature T_c which is given by

$$\frac{4\omega_0\omega_L}{\tilde{\Omega}^2} = \tanh\left(\frac{\omega_0}{2\omega_L k_B T_c}\right). \tag{5.39}$$

For the example shown in Fig. 5.12(b) with finite E_r, the system is in the normal phase with $\langle c^\dagger c\rangle/N = 0$ at both the low and the high temperature ends, and is in the

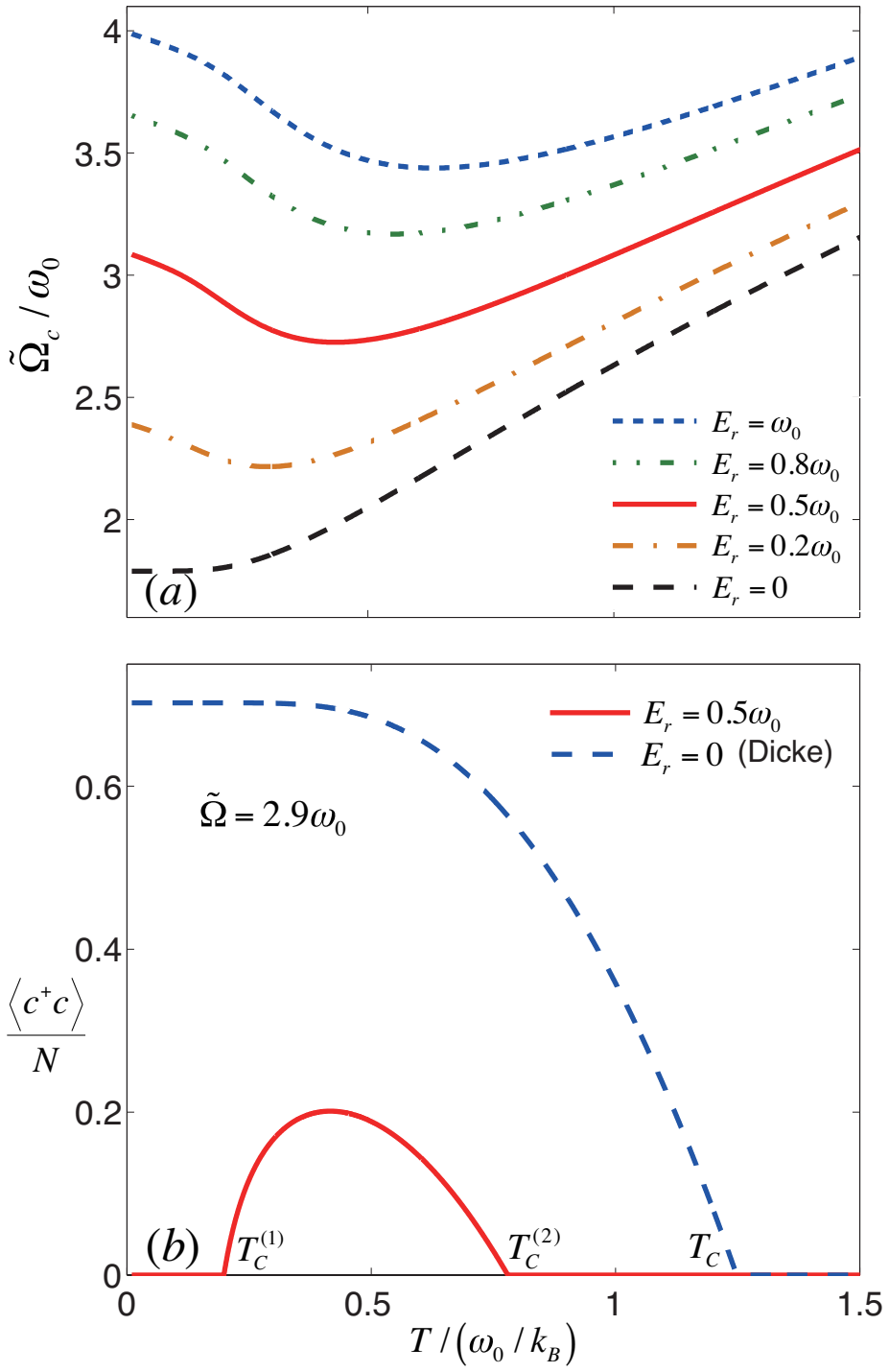

Figure 5.12 : (a) Normal-Superradiant Phase boundary in $T - \widetilde{\Omega}$ plane for $E_r/\omega_0 = 0, 0.2, 0.5, 0.8, 1$. (b) $\langle c^\dagger c \rangle / N$ as a function of T for $\widetilde{\Omega} = 2.9\omega_0$ with $E_r/\omega_0 = 0, 0.5$. We take $\omega_L = 0.8\omega_0$ in these figures.

superradiant phase in an intermediate temperature window between $T_c^{(1)}$ and $T_c^{(2)}$.

A remark is in order. In our derivation of the partition function Z in Eq. (5.27), we have treated the N atoms as distinguishable particles which obey the Boltzmann distribution. In other words, we have ignored the quantum statistics of atoms. This should be a good assumption at high temperature. We may estimate the temperature regime in which this assumption is valid as follows. Let us assume that the atoms are ideal bosons. The critical temperature for the bosons to form a Bose-Einstein condensate is given by

$$T_{\mathrm{BEC}} = 3.31\frac{\hbar^2\rho^{\frac{2}{3}}}{mk_B} \approx 3\times 10^{-4}\left(\frac{\hbar\omega_0}{k_B}\right), \tag{5.40}$$

where we have taken typical values such that the atomic number density $\rho = 10^{13}\mathrm{cm}^{-3}$, m the mass of ^{87}Rb atom, and energy splitting between two ground state hyperfine states $\omega_0 = 2\pi\times 4.81\mathrm{MHz}$. When $T \gg T_{\mathrm{BEC}}$, quantum statistics is not important, and the bosons can in practice be treated as distinguishable particles. As T_{BEC} is very small in our unit system, our results as presented in Fig. 5.11 and Fig. 5.12 should largely remain valid for typical experimental situations. Note that as T_{BEC} is roughly the same as Fermi degenerate temperature, this estimate is also valid for a system of Fermi gas. How to properly incorporate quantum statistics of atoms in the calculation for temperatures within the quantum degenerate regime remains a challenge and will be investigated in the future.

5.5 Summary

In Section 5.2, we have considered a system consisting of a single atom (or a non-interacting condensate) whose two hyperfine spin ground states are Raman coupled by two light fields, one of which is a quantized cavity field. In this setting, the internal and

external degrees of freedom of the atom and the cavity field are dynamically coupled. This coupling leads to a dynamic SOC for the atom. We have calculated the atomic dispersion relation and examined its stability and dynamic properties. In comparison to the static SOC generated by two classical laser beams which are not affected by the atomic dynamics, the cavity feedback dramatically modifies the properties of the system. Besides giving rise to new physics in the study of synthetic SOC in cold atoms, our system also represents a new cold-atom-based cavity optomechanical system. From a practical point of view, all the ingredients proposed in this work have been demonstrated in various labs. Hence our proposal can be readily tested in experiment. In fact, recent work reported in Refs. [176, 177] investigated a BEC inside a ring cavity. A straightforward modification can be used to study the physics predicted in our work. In the future, it will be interesting to extend the study to include inter-atomic interactions and to the case where a system of fermions are Raman coupled via cavity fields. Our current work on the single-particle physics will serve as an important first step towards understanding the many-body properties of the system.

In Section 5.3, we have studied spin-orbit coupled cold atoms inside a ring cavity system, employing both the mean-field theory and the full quantum mechanical Master equation approach. By treating both light and atom on equal footing and seeking the self-consistent solution in both approaches, we have found: (1) cavity-assisted SOC dramatically modifies atomic dispersion relation, (2) intriguing dynamical instabilities exist in the system, (3) atom's back-action onto cavity field also leads to non-trivial atom-photon coupling that is fundamentally different from either the system with classical-laser induced SOC in the absence of the cavity or the J-C model where the atomic COM motion is neglected (i.e., by taking $q_r = 0$). We have also

explored correspondence and discussed the connection between the mean-field and the quantum approaches. The two distinctively different approaches provide us with a deeper understanding and complementary insights into this system. We conclude that the synthesis of cavity QED and SOC is not a trivial combination and interesting new physics emerges in this setting. Our work will serve as the first steps for further exploration. For instance, we have only considered a single-mode plane-wave cavity. What would happen if a more commonly used standing-wave cavity is employed? We have not taken into account the quantum statistics of the atom, nor the interactions between atoms. A theoretical investigation with these factors taken into account will be much more challenging, but perhaps also much more exciting, as this would truly represent a new frontier of research where cavity QED meets many-body physics.

Chapter 6

Summary

In this dissertation, we started from the historical notes of ultra-cold atomic physics, introduced the very recent experimental development in creating light-induced gauge potentials that allow systems of charge-neutral atoms to behave like charged particles in a magnetic field. We theoretically studied novel ground state properties of spin-orbit coupled atomic systems, including single-particle Hamiltonians, a non-interacting Fermi sea, a two-body bound state, and many-body systems at the mean-field level. We found out that spin-orbit coupling makes a dramatic change to the band structure, may favor pairing at finite center-of-mass momentum for two body bound states, and induces a Fulde-Ferrell type of Cooper pairs for many body systems. We noted that beyond symmetry breaking paradigm of characterization of quantum states, topological order is a new and important concept in modern physics. We explored the topological state classification in a gapless Fulde-Ferrell state in our specific realization of the Hamiltonian. Based on the ground state properties and phase transitions, we considered non-equilibrium dynamical response properties for systems undergoing a parameter quench. We discovered our non-integrable quantum system undergoes non-trivial dynamical evolution, depending on a different system parameter (Zeeman field strength in our case) of initial and final values. We mapped out the complete post-quench phase diagram and investigated each phase in great details. We are surprised but delighted to find out how dynamical topological phases which support topologically protected edge states can naturally emerge in this model. We

also comment that the relevant dynamics predicted by our work are within reach of current cold-atom experimental setups. Going beyond a semi-classical description of coherent laser fields, which is used to assist two-photon Raman processes, we propose to put atoms in the cavity field and study the fully dynamical coupling between atom's pseudo-spin, orbital degrees of freedom including center-of-mass/harmonic oscillator state, and quantized light field. We solved the "full" system using semi-classical theory and the full quantum master equation approach. We have shown that rich physics are emergent in this trio system, such as loop structure in energy dispersion relation, dynamical instabilities, vanishing atom-photon entanglement at large atomic momentum tail and re-entrant superadiant phase in the thermodynamic limit. The two distinctively different approaches provide us with a deeper understanding and complementary insights into this system. We conclude that the synthesis of cavity QED and SOC is not a trivial combination and new physics emerges naturally.

In retrospect, we note that ultra-cold atomic systems in the past few decades have demonstrated a wide range of quantum simulation for condensed-matter systems, where many-body effects determine the basic physics of the system: BEC creation [10–12, 201], Feshbach resonances [33], Tonks-Girardeau gases [202, 203], the superfluid to Mott-insulator transition [13], Berezinskii-Kosterlitz-Thouless physics for bosonic systems in two-dimensions [204], the crossover from BEC to BCS superfluid in fermions [205], and synthetic gauge field manipulation for bosons and fermions [25–27, 30–32, 184, 206]. We are truly in an exciting era of fulfilling and surpassing Richard Feynman's vision of building quantum simulators, in order to deepen our understanding of the quantum mechanical nature of the universe. Ultra-cold atomic system provides such a clean and versatile tabletop platform, where theorists and experimentalists meet and collaborate to make significant progresses together.

Chapter 7

Epilogue

Ultra-cold atoms and condensed-matter physics is the study of various collective behavior of infinitely complex assemblies of electrons, nuclei, magnetic moments, spin, atoms, molecules or qubits. The complexity is reflected in the size of the state space, which grows exponentially with the number of particles, reminiscent of the 'curse of dimensionality' commonly encountered in the machine learning and deep learning field of studies. Despite the curse, the machine learning community has developed various techniques to turn it into a blessing. Remarkable progresses have been made, over the last few decades but most prominently within the last ten years, to recognize, classify, interpolate, and characterize complex sets of data. It is one of today's most rapidly growing technical fields, lying at the intersection of computer science, applied statistics, applied mathematics and electrical and computer engineering, and at the core of artificial intelligence and data science. The rapid progresses have been driven by the combination of development of new learning algorithms and theories, new programming frameworks and hardware infrastructures, and the ongoing explosion in the availability of online data and low-cost computations. Not to mention and going into details of how the adoption of machine-learning based solutions have been playing a more and more important role throughout various domain science, technology and commerce, I would like to note that machine learning has been on the frontier of fundamental research in physics, and is being used to solve long outstanding problems in quantum science. Machine learning and in particular, deep

learning approaches have been used to search for exotic particles and improved the search power and precision of high-energy particle colliders [207], an exact mapping between the variational renormalization group and deep learning has been made [208], quantum algorithms for supervised and unsupervised machine learning has been proposed [209,210], machine learning has been used to classify phases of matter with one specific example of classifying phases and phase transitions in the Ising model [211], and solving many-body problems with machine learning based approaches [212–223] (for a more comprehensive and actively updating list of publications combing the fields of physics especially quantum mechanics and machine learning, please see Roger Melko and Miles Stoudenmire's blog page [224]).

Nonetheless, beyond the news headlines, there are serious efforts quietly emerging in the corridors and on the blackboards of academia and industry on this nascent field of quantum machine learning. The field is still in the preliminary stages of defining itself. To some, it is the (obvious) plan to implement machine learning on future quantum hardware, or at least, to explore whether any advantage exists in doing so. However, to others it is using existing machine learning algorithms to attack the myriad of ultra-complex problems encountered on a daily basis by physicists studying quantum systems using conventional computers. Finally, to some it is the opportunity to take strategies developed during years of struggle on these ultra-complex problems, and to use this experience to improve machine learning algorithms for the larger community of data scientists. Whatever it means, it is an exciting time to be involved in quantum machine learning, as we watch the field begins to take shape.

Finally, I would like to mention a few words on how to get started with machine learning based on my own experience from the past one or two years. To be honest, it is actually quite overwhelming to digest all the new progresses within a short period of

time, while still multitasking on one's own research works. Here are my suggestions:

1. Sign up for the free course of Machine Learning taught by Andrew Ng (Associate Professor, Stanford University; Chief Scientist, Baidu; Chairman and Co-founder, Coursera) at coursera.org:

    - Attentively watch the video lectures, take notes and finish the homework coding assignments in Matlab or Octave.
    - This course gives an excellent overview of the Machine Learning in a very compact presentation, and going through the book "An Introduction to Statistical Learning with Applications in R" by Gareth James, Daniela Witten, Trevor Hastie and Robert Tibshirani at the same time should be very helpful in getting the details right. (You don't have to know R scripting language to be able to read and understand this book's materials.)

2. (Optional) Sign up for the Machine Learning Specialization taught by Emily Fox and Carlos Guestrin at coursera.org offered by University of Washington:

    - This course focuses on applied machine learning algorithms and real world datasets exposure experience. Most of data insights are only available from transforming, visualizing, statistically compiling the raw dataset before feeding them as modeling inputs. Python is a great and versatile tool for data manipulations.

3. (Optional) I had an internship experience at Amazon over the summer of 2016. I worked as an applied scientist at the Kindle engineering team in Seattle, WA:

    - My project was to build a customer level response-propensity model for mobile push notifications. I had Kindle app datasets of all customers'

purchase history, last page read information, interaction response for push notifications, etc. The dataset is stored on a Yarn cluster as csv format, with more than 6 billion records (around 10TB).

- The idea was to build a prediction/classification model for future push-notification responses. Intuitively, if the customer was very active using the app and making book purchases, the customer would be very likely to respond to push notifications (such as deals, promotions, or suggested books, etc.) sent out by campaign owners (marketing team at kindle team).
- Working with an experienced applied scientist (Kannan Shah) as my mentor, I learned to aggregate large datasets using Apache Spark in Java, preprocess and convert the datasets into compressed JSON files and store them on AWS S3 service. Besides necessary engineering efforts in coding, we invested our time heavily in feature engineering – a process that involves a combination of science and product sense to define functions that can transform and reveal the structure of datasets. We came up with a sliding-observation time window strategy that identifies the target and takes into account of historical records within a cutoff time window, and carefully avoided data leakage problems.
- At modeling stage, we used logistic regression with L1 and L2 regularization to learn the training data and perform classifications for test data, and studied various metrics to evaluate and improve the model performance.

4. Work on a predictive modeling project from a data competition challenge website, such as kaggle.com:

    - It is relatively easy for anyone to wrangle the dataset in anyway they want

and build a model that learns from the training data and makes some better-than-random prediction for test data. However, it is challenging yet very important for one to make *consistent* improvements in reducing generalization error.

- Kaggle provides such a platform that everyone has access to the same modeling goal, same training/test dataset, with target information hidden from test data. A leaderboard (e.g. 3:7 ratio over random split of test data for public and private leaderboard respectively) helps one to benchmark and compete against others' best predictions.
- The forum of each competition is dedicated to experience sharing, code sharing, and asking questions. The community is flourished by numerous passionate practitioners of data science and machine learning, and many of them have either worked on a lot of past competitions, or they are full-time data scientist or university professors who work on the projects just for fun and learning new things.
- It is best to learn from doing and coding in the vast fields of machine learning applications. Theory and concepts are important but one will typically learn so much clearer and more by actually working on a concrete problem.

5. Deep learning:

    - The field of deep learning has attracted tremendous attention due to its robust neural network learning functionality and some level of automatic discovery of "artificial intelligence".
    - From basic mathematical tools, machine learning concepts to most estab-

lished deep learning algorithms, I would recommend reading the part I and II of the Deep Learning book by Ian Goodfellow and Yoshua Bengio and Aaron Courville, MIT Press *. Part III emphasizes on deep learning research that are more advanced yet speculative, which can be left to be revisited once one feels comfortable with the fundamentals.

- Follow the cs231n course offered by Stanford University and work on projects using deep learning †
- Kaggle has many data challenges that involve primarily deep learning modelings.

* Full HTML format for the web version of the book is available at http://www.deeplearningbook.org

† Familiarize oneself with TensorFlow and try to reproduce the known model performance from some famous benchmark datasets, such as MNIST, ImageNet, PASCAL VOC etc.

Appendix A

Derivations of 2-body Wavefunctions

In Sec. 2.2, we presented the results concerning the attractive s-wave contact interaction between two un-like spins. Solving the two-particle Schrodinger equation is the key process. Here we present more detailed mathematical derivations, especially regarding to the generalized Cooper Equations.

A.1 Generalized Cooper Equation

We start from the explicit form of single particle Hamiltonian

$$H_0 = \frac{\hbar^2}{2m}(k_x^2+k_y^2+k_z^2) + v_1 k_x\sigma_x + v_2 k_y\sigma_y + v_3 k_z\sigma_z + h\sigma_z + \delta\sigma_x + \eta\sigma_y \quad \text{(A.1)}$$

$$\text{(A.2)}$$

and denote the two body wavefunction as

$$|\Psi\rangle_{\mathbf{q}} = \sum_{\mathbf{k}}{}' \left[\psi_{\uparrow\downarrow}(\mathbf{k}) c^\dagger_{\frac{\mathbf{q}}{2}+\mathbf{k}\uparrow} c^\dagger_{\frac{\mathbf{q}}{2}-\mathbf{k}\downarrow} + \psi_{\downarrow\uparrow}(\mathbf{k}) c^\dagger_{\frac{\mathbf{q}}{2}+\mathbf{k}\downarrow} c^\dagger_{\frac{\mathbf{q}}{2}-\mathbf{k}\uparrow} + \psi_{\uparrow\uparrow}(\mathbf{k}) c^\dagger_{\frac{\mathbf{q}}{2}+\mathbf{k}\uparrow} c^\dagger_{\frac{\mathbf{q}}{2}-\mathbf{k}\uparrow} + \psi_{\downarrow\downarrow}(\mathbf{k}) c^\dagger_{\frac{\mathbf{q}}{2}+\mathbf{k}\downarrow} c^\dagger_{\frac{\mathbf{q}}{2}-\mathbf{k}\downarrow}\right] |0\rangle \quad \text{(A.3)}$$

where $\sum'_{\boldsymbol{k}}$ denotes summation over positive momentum $\mathbf{k}$. We solve the two-body Schrodinger equation $\big(\mathcal{H}_0 + \mathcal{H}_{\text{int}}\big)|\Psi\rangle_{\mathbf{q}} = E_{\mathbf{q}}|\Psi\rangle_{\mathbf{q}}$ by denoting $S(p) = \epsilon_p + h + v_3 p_z$ and $T(p) = \epsilon_p - h - v_3 p_z$, $U(p) = v_1 p_x + \delta - i(v_2 p_y + \eta)$, $V(p) = v_1 p_x + \delta + i(v_2 p_y + \eta)$.

Then we have the single particle Hamiltonian as,

$$\begin{aligned} H_0 &= \sum_p S(p)c^\dagger_{p\uparrow}c_{p\uparrow} + T(p)c^\dagger_{p\downarrow}c_{p\downarrow} + U(p)c^\dagger_{p\uparrow}c_{p\downarrow} + V(p)c^\dagger_{p\downarrow}c_{p\uparrow} \\ &= \sum_p \left(S(p)c^\dagger_{p\uparrow} + V(p)c^\dagger_{p\downarrow}\right)c_{p\uparrow} + \left(T(p)c^\dagger_{p\downarrow} + U(p)c^\dagger_{p\uparrow}\right)c_{p\downarrow} \end{aligned}$$

Applying H_0 to $|\Psi\rangle_{\mathbf{q}}$ using above notations, we have

$$\begin{aligned} H_0|\Psi\rangle_{\boldsymbol{q}} &= \sum_{\boldsymbol{k'}} \psi_{\uparrow\downarrow}(\boldsymbol{k'})[S(\frac{q}{2}+k)c^\dagger_{\frac{q}{2}+k\uparrow} + V(\frac{q}{2}+k)c^\dagger_{\frac{q}{2}+k\downarrow}]c^\dagger_{\frac{q}{2}-k\downarrow} \\ &+ \psi_{\downarrow\uparrow}(\boldsymbol{k'})[S(\frac{q}{2}-k)c^\dagger_{\frac{q}{2}-k\uparrow} + V(\frac{q}{2}-k)c^\dagger_{\frac{q}{2}-k\downarrow}]c^\dagger_{\frac{q}{2}+k\downarrow}(-1) \\ &+ \psi_{\uparrow\uparrow}(\boldsymbol{k'})[S(\frac{q}{2}+k)c^\dagger_{\frac{q}{2}+k\uparrow} + V(\frac{q}{2}+k)c^\dagger_{\frac{q}{2}+k\downarrow}]c^\dagger_{\frac{q}{2}-k\uparrow} \\ &+ \psi_{\uparrow\uparrow}(\boldsymbol{k'})[S(\frac{q}{2}-k)c^\dagger_{\frac{q}{2}-k\uparrow} + V(\frac{q}{2}-k)c^\dagger_{\frac{q}{2}-k\downarrow}]c^\dagger_{\frac{q}{2}+k\uparrow}(-1) \\ &+ \psi_{\uparrow\downarrow}(\boldsymbol{k'})[T(\frac{q}{2}-k)c^\dagger_{\frac{q}{2}-k\downarrow} + U(\frac{q}{2}-k)c^\dagger_{\frac{q}{2}-k\uparrow}]c^\dagger_{\frac{q}{2}+k\uparrow}(-1) \\ &+ \psi_{\downarrow\uparrow}(\boldsymbol{k'})[T(\frac{q}{2}+k)c^\dagger_{\frac{q}{2}+k\downarrow} + U(\frac{q}{2}+k)c^\dagger_{\frac{q}{2}+k\uparrow}]c^\dagger_{\frac{q}{2}-k\uparrow} \\ &+ \psi_{\downarrow\downarrow}(\boldsymbol{k'})[T(\frac{q}{2}+k)c^\dagger_{\frac{q}{2}+k\downarrow} + U(\frac{q}{2}+k)c^\dagger_{\frac{q}{2}+k\uparrow}]c^\dagger_{\frac{q}{2}-k\downarrow} \\ &+ \psi_{\downarrow\downarrow}(\boldsymbol{k'})[T(\frac{q}{2}-k)c^\dagger_{\frac{q}{2}-k\downarrow} + U(\frac{q}{2}-k)c^\dagger_{\frac{q}{2}-k\uparrow}]c^\dagger_{\frac{q}{2}+k\downarrow}(-1) \\ &= \sum_{\boldsymbol{k'}} \left[S(\frac{q}{2}+k)\psi_{\uparrow\downarrow} + V(\frac{q}{2}-k)\psi_{\uparrow\uparrow} + T(\frac{q}{2}-k)\psi_{\uparrow\downarrow} + U(\frac{q}{2}+k)\psi_{\downarrow\downarrow}\right] c^\dagger_{\frac{\mathbf{q}}{2}+\mathbf{k}\uparrow}c^\dagger_{\frac{\mathbf{q}}{2}-\mathbf{k}\downarrow} \\ &+ \left[S(\frac{q}{2}-k)\psi_{\downarrow\uparrow} + V(\frac{q}{2}+k)\psi_{\uparrow\uparrow} + T(\frac{q}{2}+k)\psi_{\downarrow\uparrow} + U(\frac{q}{2}-k)\psi_{\downarrow\downarrow}\right] c^\dagger_{\frac{\mathbf{q}}{2}+\mathbf{k}\downarrow}c^\dagger_{\frac{\mathbf{q}}{2}-\mathbf{k}\uparrow} \\ &+ \left[S(\frac{q}{2}+k)\psi_{\uparrow\uparrow} + U(\frac{q}{2}-k)\psi_{\uparrow\downarrow} + S(\frac{q}{2}-k)\psi_{\uparrow\uparrow} + U(\frac{q}{2}+k)\psi_{\downarrow\uparrow}\right] c^\dagger_{\frac{\mathbf{q}}{2}+\mathbf{k}\uparrow}c^\dagger_{\frac{\mathbf{q}}{2}-\mathbf{k}\uparrow} \\ &+ \left[T(\frac{q}{2}+k)\psi_{\downarrow\downarrow} + V(\frac{q}{2}-k)\psi_{\downarrow\uparrow} + T(\frac{q}{2}-k)\psi_{\downarrow\downarrow} + V(\frac{q}{2}+k)\psi_{\uparrow\downarrow}\right] c^\dagger_{\frac{\mathbf{q}}{2}+\mathbf{k}\downarrow}c^\dagger_{\frac{\mathbf{q}}{2}-\mathbf{k}\downarrow} \end{aligned}$$

and applying the interaction Hamiltonian to $|\Psi\rangle_{\mathbf{q}}$ gives us

$$H_{int}|\Psi\rangle_{\boldsymbol{q}} = \frac{g}{V}{\sum_{\mathbf{k'}}}' \left[\psi_{\uparrow\downarrow}(\mathbf{k'}) - \psi_{\downarrow\uparrow}(\mathbf{k'})\right] c^\dagger_{\frac{\mathbf{q}}{2}+\mathbf{k}\uparrow}c^\dagger_{\frac{\mathbf{q}}{2}-\mathbf{k}\downarrow} \tag{A.4}$$

After grouping terms and some simplifications, we obtain four coupled equations as

$$
\begin{aligned}
(\mathcal{E}_{\mathbf{k},\mathbf{q}} - 2v_3k_z)\psi_{\uparrow\downarrow}(\mathbf{k}) &= \frac{g}{V}{\sum_{\mathbf{k}'}}'\Big[\psi_{\uparrow\downarrow}(\mathbf{k}') - \psi_{\downarrow\uparrow}(\mathbf{k}')\Big] + \Big[V(\frac{q}{2}-k)\Big]\psi_{\uparrow\uparrow}(\mathbf{k}) + \Big[U(\frac{q}{2}+k)\Big]\psi_{\downarrow\downarrow}(\mathbf{k}) \\
(\mathcal{E}_{\mathbf{k},\mathbf{q}} + 2v_3k_z)\psi_{\downarrow\uparrow}(\mathbf{k}) &= \frac{g}{V}{\sum_{\mathbf{k}'}}'\Big[\psi_{\downarrow\uparrow}(\mathbf{k}') - \psi_{\uparrow\downarrow}(\mathbf{k}')\Big] + \Big[V(\frac{q}{2}+k)\Big]\psi_{\uparrow\uparrow}(\mathbf{k}) + \Big[U(\frac{q}{2}-k)\Big]\psi_{\downarrow\downarrow}(\mathbf{k}) \\
(\mathcal{E}_{\mathbf{k},\mathbf{q}} - 2h - v_3q_z)\psi_{\uparrow\uparrow}(\mathbf{k}) &= \Big[U(\frac{q}{2}-k)\Big]\psi_{\uparrow\downarrow}(\mathbf{k}) + \Big[U(\frac{q}{2}+k)\Big]\psi_{\downarrow\uparrow}(\mathbf{k}) \\
(\mathcal{E}_{\mathbf{k},\mathbf{q}} + 2h + v_3q_z)\psi_{\downarrow\downarrow}(\mathbf{k}) &= \Big[V(\frac{q}{2}+k)\Big]\psi_{\uparrow\downarrow}(\mathbf{k}) + \Big[V(\frac{q}{2}-k)\Big]\psi_{\downarrow\uparrow}(\mathbf{k})
\end{aligned}
$$

where $\mathcal{E}_{\mathbf{k},\mathbf{q}} = E_{\mathbf{q}} - \epsilon_{\frac{\mathbf{q}}{2}+\mathbf{k}} - \epsilon_{\frac{\mathbf{q}}{2}-\mathbf{k}}$.

Let's introduce $\psi_s(\boldsymbol{k}) = \frac{1}{\sqrt{2}}[\psi_{\uparrow\downarrow}(\boldsymbol{k}) - \psi_{\downarrow\uparrow}(\boldsymbol{k})]$ and $\psi_t(\boldsymbol{k}) = \frac{1}{\sqrt{2}}[\psi_{\uparrow\downarrow}(\boldsymbol{k}) + \psi_{\downarrow\uparrow}(\boldsymbol{k})]$, $\psi_u = \frac{1}{\sqrt{2}}(\psi_{\uparrow\uparrow} + \psi_{\downarrow\downarrow})$, $\psi_v = \frac{1}{\sqrt{2}}(\psi_{\uparrow\uparrow} - \psi_{\downarrow\downarrow})$, and after some adding and subtracting equations, we have

$$
\begin{aligned}
\mathcal{E}_{\mathbf{k},\mathbf{q}}\psi_t \quad -2v_3k_z\psi_s &= (v_1q_x + 2\delta)\psi_u + i(v_2q_y + 2\eta)\psi_v && \text{(A.5)} \\
\mathcal{E}_{\mathbf{k},\mathbf{q}}\psi_s \quad -2v_3k_z\psi_t &= \frac{2g}{V}{\sum_{k'}}'\psi_s - 2v_1k_x\psi_v - 2v_2ik_y\psi_u && \text{(A.6)} \\
\mathcal{E}_{\mathbf{k},\mathbf{q}}\psi_u - (2h + v_3q_z)\psi_v &= (v_1q_x + 2\delta)\psi_t + 2iv_2k_y\psi_s && \text{(A.7)} \\
\mathcal{E}_{\mathbf{k},\mathbf{q}}\psi_v - (2h + v_3q_z)\psi_u &= -2v_1k_x\psi_s - i(v_2q_y + 2\eta)\psi_t && \text{(A.8)}
\end{aligned}
$$

In matrix form, it is written as

$$
\begin{pmatrix}
-2v_3k_z & \mathcal{E}_{\boldsymbol{k},\boldsymbol{q}} & -(v_1q_x + 2\delta) & -i(v_2q_y + 2\eta) \\
\mathcal{E}_{\boldsymbol{k},\boldsymbol{q}} & -2v_3k_z & 2iv_2k_y & 2v_1k_x \\
-2iv_2k_y & -(v_1q_x + 2\delta) & \mathcal{E}_{\boldsymbol{k},\boldsymbol{q}} & -(2h + v_3q_z) \\
2v_1k_x & i(v_2q_y + 2\eta) & -(2h + v_3q_z) & \mathcal{E}_{\boldsymbol{k},\boldsymbol{q}}
\end{pmatrix}
\begin{pmatrix} \psi_s \\ \psi_t \\ \psi_u \\ \psi_v \end{pmatrix}
=
\begin{pmatrix} 0 \\ \frac{g}{V}\sum_{\boldsymbol{k}}\psi_s \\ 0 \\ 0 \end{pmatrix}
$$

Since single particle spectrum $E_{\boldsymbol{k}} = \frac{\hbar^2k^2}{2m} \pm \sqrt{(v_1k_x + \delta)^2 + (v_2k_y + \eta)^2 + (v_3k_z + h)^2}$ has lowest energy at finite $\boldsymbol{k}$ value, we assume the $\boldsymbol{q}$ vector as $\boldsymbol{q} = (q_x, q_y, q_z)$. Then

we have,

$$\begin{pmatrix} \mathcal{E}_{\boldsymbol{k},\boldsymbol{q}} & -(v_1q_x+2\delta) & -i(v_2q_y+2\eta) \\ -(v_1q_x+2\delta) & \mathcal{E}_{\boldsymbol{k},\boldsymbol{q}} & -(2h+v_3q_z) \\ i(v_2q_y+2\eta) & -(2h+v_3q_z) & \mathcal{E}_{\boldsymbol{k},\boldsymbol{q}} \end{pmatrix} \begin{pmatrix} \psi_t \\ \psi_u \\ \psi_v \end{pmatrix} = \begin{pmatrix} 2v_3k_z\psi_s \\ 2iv_2k_y\psi_s \\ -2v_1k_x\psi_s \end{pmatrix}$$

By applying the Cramer's rule in matrix algebra, we have the following relations

$$\begin{aligned} \psi_t &= 2 \begin{vmatrix} v_3k_z & -(v_1q_x+2\delta) & -i(v_2q_y+2\eta) \\ iv_2k_y & \mathcal{E}_{\mathbf{k},\mathbf{q}} & -(v_3q_z+2h) \\ -v_1k_x & -(v_3q_z+2h) & \mathcal{E}_{\mathbf{k},\mathbf{q}} \end{vmatrix} \psi_s/\mathbf{M} \\ \mathcal{E}_{\mathbf{k},\mathbf{q}}\psi_s \quad -2v_3k_z\psi_t &= \frac{2g}{V}{\sum_{k'}}' \psi_s - 2v_1k_x\psi_v - 2v_2ik_y\psi_u \qquad \text{(A.9)} \\ \psi_u &= 2 \begin{vmatrix} \mathcal{E}_{\mathbf{k},\mathbf{q}} & v_3k_z & -i(v_2q_y+2\eta) \\ -(v_1q_x+2\delta) & iv_2k_y & -(v_3q_z+2h) \\ i(v_2q_y+2\eta) & -v_1k_x & \mathcal{E}_{\mathbf{k},\mathbf{q}} \end{vmatrix} \psi_s/\mathbf{M} \\ \psi_v &= 2 \begin{vmatrix} \mathcal{E}_{\mathbf{k},\mathbf{q}} & -(v_1q_x+2\delta) & v_3k_z \\ -(v_1q_x+2\delta) & \mathcal{E}_{\mathbf{k},\mathbf{q}} & iv_2k_y \\ i(v_2q_y+2\eta) & -(v_3q_z+2h) & -v_1k_x \end{vmatrix} \psi_s/\mathbf{M} \end{aligned}$$

where

$$\mathbf{M} = \begin{vmatrix} \mathcal{E}_{\mathbf{k},\mathbf{q}} & -(v_1q_x+2\delta) & -i(v_2q_y+2\eta) \\ -(v_1q_x+2\delta) & \mathcal{E}_{\mathbf{k},\mathbf{q}} & -(v_3q_z+2h) \\ i(v_2q_y+2\eta) & -(v_3q_z+2h) & \mathcal{E}_{\mathbf{k},\mathbf{q}} \end{vmatrix}.$$

Furthermore, the determinant of $\mathbf{M}$ is given by

$$\det(\mathbf{M}) = \mathcal{E}_{\mathbf{k},\mathbf{q}}[\mathcal{E}^2_{\mathbf{k},\mathbf{q}} - (v_1q_x+2\delta)^2 - (v_2q_y+2\eta)^2 - (v_3q_z+2h)^2] \equiv M$$

Then we have the Cooper equation after some algebra,

$$1/g = \frac{1}{V}\sum_k \frac{1}{\mathcal{E}_{\mathbf{k},\mathbf{q}} - 2v_3k_z\frac{2\mathbf{M}_1}{M} + 2v_1k_x\frac{2\mathbf{M}_2}{M} + 2v_2ik_y\frac{2\mathbf{M}_3}{M}}$$

where

$$\mathbf{M}_1 = \begin{vmatrix} v_3k_z & -(v_1q_x+2\delta) & -i(v_2q_y+2\eta) \\ iv_2k_y & \mathcal{E}_{\mathbf{k},\mathbf{q}} & -(v_3q_z+2h) \\ -v_1k_x & -(v_3q_z+2h) & \mathcal{E}_{\mathbf{k},\mathbf{q}} \end{vmatrix},$$

$$\mathbf{M}_2 = \begin{vmatrix} \mathcal{E}_{\mathbf{k},\mathbf{q}} & -(v_1q_x+2\delta) & v_3k_z \\ -(v_1q_x+2\delta) & \mathcal{E}_{\mathbf{k},\mathbf{q}} & iv_2k_y \\ i(v_2q_y+2\eta) & -(v_3q_z+2h) & -v_1k_x \end{vmatrix},$$

$$\mathbf{M}_3 = \begin{vmatrix} \mathcal{E}_{\mathbf{k},\mathbf{q}} & v_3k_z & -i(v_2q_y+2\eta) \\ -(v_1q_x+2\delta) & iv_2k_y & -(v_3q_z+2h) \\ i(v_2q_y+2\eta) & -v_1k_x & \mathcal{E}_{\mathbf{k},\mathbf{q}} \end{vmatrix}$$

Using regularization relation and more compact summation notations, we arrive at the generalized Cooper equation, which is exactly the same as Eq. 2.21,

$$\frac{m}{4\pi\hbar^2 a_s} = \frac{1}{V}\sum_k \left(\frac{1}{\mathcal{E}_{\mathbf{k},\mathbf{q}} - \frac{4\mathcal{E}^2_{\mathbf{k},\mathbf{q}}\sum_{i=1}^3 v_i^2k_i^2 - 4\left[\sum_{i=1}^3 v_ik_i(v_iq_i+2\Lambda_i)\right]^2}{\mathcal{E}_{\mathbf{k},\mathbf{q}}\left(\mathcal{E}^2_{\mathbf{k},\mathbf{q}} - \sum_{i=1}^3 (v_iq_i+2\Lambda_i)^2\right)}} + \frac{1}{2\epsilon_k} \right) \tag{A.10}$$

where $\boldsymbol{v} = (v_1, v_2, v_3)$, $\boldsymbol{q} = (q_1, q_2, q_3)$, $\boldsymbol{\Lambda} = (\delta, \eta, h)$, and singlet wavefunction is determined from Eq. A.9 accordingly. The unnormalized singlet wavefunction is given by

$$\psi_s = \frac{1}{\mathcal{E}_{\mathbf{k},\mathbf{q}} - \frac{4\mathcal{E}^2_{\mathbf{k},\mathbf{q}}\sum_{i=1}^3 v_i^2k_i^2 - 4\left(\sum_{i=1}^3 v_ik_i(v_iq_i+2\Lambda_i)\right)^2}{\mathcal{E}_{\mathbf{k},\mathbf{q}}\left(\mathcal{E}^2_{\mathbf{k},\mathbf{q}} - \sum_{i=1}^3 (v_iq_i+2\Lambda_i)^2\right)}}. \tag{A.11}$$

It is worthy to point out that the exact solution of two-particle Schrodinger equation is equivalent to computing the inverse vertex function using the relation $\mathrm{Re}\left[\Gamma^{-1}_{2\mathrm{b}}\left(\mathbf{q}=0;\omega=E_B\right)=0\right]$. The bonus is that two-particle Schrodinger equation gives singlet and triplet wavefunctions, in addition to binding energy expressions.

A.2 Inverse Vertex Function

In this section, we show that using functional path integral approach, and performing Gaussian fluctuation expansions, we are able to show the finite bound state is also stable beyond mean field assumptions.

We employ the functional path integral method [83, 84] to study the problem and consider the partition function,

$$\mathcal{Z} = \int \mathcal{D}[\psi(\mathbf{r},\tau), \bar{\psi}(\mathbf{r},\tau)] \exp\left\{-S\left[\psi(\mathbf{r},\tau), \bar{\psi}(\mathbf{r},\tau)\right]\right\}, \tag{A.12}$$

where the action

$$S\left[\psi,\bar{\psi}\right] = \int_0^\beta d\tau \left[\int d\mathbf{r} \sum_\sigma \bar{\psi}_\sigma(\mathbf{r},\tau)\,\partial_\tau \psi_\sigma(\mathbf{r},\tau) + \mathcal{H}\left(\psi,\bar{\psi}\right)\right].$$

is written as an integral over imaginary time τ. Here $\beta = 1/(k_B T)$ is the inverse temperature and $\mathcal{H}\left(\psi,\bar{\psi}\right)$ is obtained by replacing the field operators ψ^+ and ψ with the grassmann variables $\bar{\psi}$ and ψ, respectively. We can use the Hubbard-Stratonovich transformation to transform the quartic interaction term into the quadratic form as:

$$e^{-U_0 \int dx d\tau \bar{\psi}_\uparrow \bar{\psi}_\downarrow \psi_\downarrow \psi_\uparrow} = \int \mathcal{D}\left[\Delta,\bar{\Delta}\right] \exp\left\{\int_0^\beta d\tau \int d\mathbf{r} \left[\frac{|\Delta(\mathbf{r},\tau)|^2}{U_0} + \left(\bar{\Delta}\psi_\downarrow\psi_\uparrow + \Delta\bar{\psi}_\uparrow\bar{\psi}_\downarrow\right)\right]\right\}, \tag{A.13}$$

from which the pairing field $\Delta(\mathbf{r},\tau)$ is defined.

Let us now formally introduce the 4-dimensional Nambu spinor $\Phi(\mathbf{r},\tau) \equiv [\psi_\uparrow, \psi_\downarrow, \bar{\psi}_\uparrow, \bar{\psi}_\downarrow]^T$ and rewrite the action as,

$$\mathcal{Z} = \int \mathcal{D}[\Phi,\bar{\Phi};\Delta,\bar{\Delta}] \exp\left\{-\int d\tau \int d\mathbf{r} \int d\tau' \int d\mathbf{r}' \left[-\frac{1}{2}\bar{\Phi}(\mathbf{r},\tau)\mathcal{G}^{-1}\Phi(\mathbf{r}',\tau') - \frac{|\Delta(\mathbf{r},\tau)|^2}{U_0}\delta(\mathbf{r}-\mathbf{r}')\delta(\tau-\tau')\right] - \frac{\beta}{V}\sum_{\mathbf{k}} \xi_{\mathbf{k}}\right\},$$

where V is the quantization volume and $\mathcal{G}$ is the single-particle Green function.

Integrating out the original fermionic fields, we may rewrite the partition function as

$$\mathcal{Z} = \int \mathcal{D}[\Delta, \bar{\Delta}] \, \exp\left\{-S_{\text{eff}}\left[\Delta, \bar{\Delta}\right]\right\} ,$$

where the effective action is given by

$$S_{\text{eff}}\left[\Delta, \bar{\Delta}\right] = \int_0^\beta d\tau \int d\mathbf{r} \left\{-\frac{\left|\Delta\left(\mathbf{r}, \tau\right)\right|^2}{U_0}\right\} - \frac{1}{2}\text{Tr}\ln\left[-\mathcal{G}^{-1}\right] + \frac{\beta}{V}\sum_{\mathbf{k}} \xi_{\mathbf{k}}.$$

where the trace is over all the spin, spatial, and temporal degrees of freedom. To proceed, we restrict ourselves to the Gaussian fluctuation and expand $\Delta\left(\mathbf{r}, \tau\right) = \Delta_0 + \delta\Delta\left(\mathbf{r}, \tau\right)$. The effective action is then decomposed accordingly as $S_{\text{eff}} = S_0 + \Delta S$, where the saddle-point action is

$$S_0 = \int_0^\beta d\tau \int d\mathbf{r} \left(-\frac{\Delta_0^2}{U_0}\right) - \frac{1}{2}\text{Tr}\ln\left[-\mathcal{G}_0^{-1}\right] + \frac{\beta}{V}\sum_{\mathbf{k}} \xi_{\mathbf{k}} \,, \tag{A.14}$$

where $\mathcal{G}_0^{-1}$ has the same form as $\mathcal{G}^{-1}$ with Δ replaced by Δ_0, and, in the momentum space, the fluctuation action takes the form [$k \equiv (\mathbf{k}, i\omega_m)$ and $q \equiv (\mathbf{q}, i\nu_n)$]: $\Delta S = \sum_{\mathbf{q}, i\nu_n}\left[-\frac{1}{U_0}\delta\Delta(q)\delta\bar{\Delta}(q)\right] + \frac{1}{2}\left(\frac{1}{2}\right)\text{Tr}_\sigma \sum_{k,q}\left[\mathcal{G}_0\left(k\right)\Sigma\left(q\right)\mathcal{G}_0\left(k-q\right)\Sigma\left(-q\right)\right]$, where

$$\Sigma\left(q\right) = \begin{bmatrix} 0 & i\delta\Delta\left(q\right)\hat{\sigma}_y \\ -i\delta\bar{\Delta}\left(-q\right)\hat{\sigma}_y & 0 \end{bmatrix}. \tag{A.15}$$

The low-energy effective two-body interaction is characterized by the vertex function, which we derive in this section. We shall consider the normal state where the pairing field vanishes, i.e., $\Delta_0 = 0$, in which case the Green

function reduces to its non-interacting form as $\mathcal{G}_0(k) = \mathrm{Diag}\{\hat{g}_0(k), -\hat{g}_0(-k)\}$. The fluctuation action is given by $\Delta S = \sum_q \left[-\Gamma^{-1}(q)\right] \delta\Delta(q)\delta\bar{\Delta}(q)$, where $\Gamma^{-1}(q)$ is the inverse vertex function.

$$\begin{aligned}\Gamma^{-1}(\boldsymbol{q}, i\nu_n) &= \frac{m}{4\pi\hbar^2 a_s} - \frac{1}{2V}\sum_{\boldsymbol{k}}\left[\frac{1}{i\nu_n - \epsilon_{h,\boldsymbol{q}/2+\boldsymbol{k},+} - \epsilon_{-h,\boldsymbol{q}/2-\boldsymbol{k},+}} + \frac{1}{i\nu_n - \epsilon_{h,\boldsymbol{q}/2+\boldsymbol{k},-} - \epsilon_{-h,\boldsymbol{q}/2-\boldsymbol{k},-}} + \frac{1}{\epsilon_k}\right] \\ &+ \frac{1}{4V}\sum_{\boldsymbol{k}}\left[1 + \frac{(h^2 + hvq_z + v^2(\boldsymbol{q}/2+\boldsymbol{k})\cdot(\boldsymbol{q}/2-\boldsymbol{k}))}{\sqrt{(v(q_z/2+k_z)+h)^2 + v^2(\boldsymbol{q}/2+\boldsymbol{k})_\perp^2}\sqrt{(v(q_z/2-k_z)-h)^2 + v^2(\boldsymbol{q}/2-\boldsymbol{k})_\perp^2}}\right]\bar{C}^{2b}_{res}(\boldsymbol{q}, i\nu_n; \boldsymbol{k})\end{aligned}$$

where

$$\begin{aligned}\bar{C}^{2b}_{res}(\boldsymbol{q}, i\nu_n; \boldsymbol{k}) &= \frac{1}{i\nu_n - \epsilon_{h,\boldsymbol{q}/2+\boldsymbol{k},+} - \epsilon_{-h,\boldsymbol{q}/2-\boldsymbol{k},+}} + \frac{1}{i\nu_n - \epsilon_{h,\boldsymbol{q}/2+\boldsymbol{k},-} - \epsilon_{-h,\boldsymbol{q}/2-\boldsymbol{k},-}} \\ &\quad - \frac{1}{i\nu_n - \epsilon_{h,\boldsymbol{q}/2+\boldsymbol{k},+} - \epsilon_{-h,\boldsymbol{q}/2-\boldsymbol{k},-}} - \frac{1}{i\nu_n - \epsilon_{h,\boldsymbol{q}/2+\boldsymbol{k},-} - \epsilon_{-h,\boldsymbol{q}/2-\boldsymbol{k},+}}\end{aligned}$$

where

$$\epsilon_{h,\boldsymbol{q}/2+\boldsymbol{k},+} = \frac{\hbar^2(\boldsymbol{q}/2+\boldsymbol{k})^2}{2m} + \sqrt{(v(\boldsymbol{q}/2+\boldsymbol{k})_z + h)^2 + v^2(\boldsymbol{q}/2+\boldsymbol{k})_\perp^2} \tag{A.16}$$

$$= \frac{1}{2}\left(\frac{q^2}{4} + k^2 + qk\cos\theta\right) + \sqrt{(q_z/2+k_z+h)^2 + (\boldsymbol{q}/2+\boldsymbol{k})^2 - (q_z/2+k_z)^2} \tag{A.17}$$

$$= \frac{1}{2}\left(\frac{q^2}{4} + k^2 + qk\cos\theta\right) + \sqrt{h^2 + 2(q_z/2+k_z)h + \left(\frac{q^2}{4} + k^2 + qk\cos\theta\right)} \tag{A.18}$$

$$\epsilon_{-h,\boldsymbol{q}/2-\boldsymbol{k},+} = \frac{1}{2}\left(\frac{q^2}{4} + k^2 - qk\cos\theta\right) + \sqrt{h^2 - 2(q_z/2-k_z)h + \left(\frac{q^2}{4} + k^2 - qk\cos\theta\right)} \tag{A.19}$$

$$\epsilon_{h,\boldsymbol{q}/2+\boldsymbol{k},-} = \frac{1}{2}\left(\frac{q^2}{4} + k^2 + qk\cos\theta\right) - \sqrt{h^2 + 2(q_z/2+k_z)h + \left(\frac{q^2}{4} + k^2 + qk\cos\theta\right)} \tag{A.20}$$

$$\epsilon_{-h,\boldsymbol{q}/2-\boldsymbol{k},-} = \frac{1}{2}\left(\frac{q^2}{4} + k^2 - qk\cos\theta\right) - \sqrt{h^2 - 2(q_z/2-k_z)h + \left(\frac{q^2}{4} + k^2 - qk\cos\theta\right)} \tag{A.21}$$

Setting $\Gamma^{-1}(\mathbf{q} = \mathbf{q}_0, i\nu_n = E_B) = 0$ should give us exactly the same form of generalized Cooper equation. However, the algebra is rather involved to show explicitly, and we checked numerically that it is indeed equivalent.

Appendix B

Basis Expansion Method

In this appendix, we supplement results presented in Sec. 3.2 with more mathematical derivations regarding the eigenspectrum with boundary conditions. before using basis expansion method, I tried one whole week of finite-difference method, it turns out the finite-difference method does not have good convergence rate for this system in 1D, where length L is ideally set to infinity, otherwise the finite size effect will kick in where gapless mode will become gapped. Basis expansion method is a method with global function that automatically satisfies boundary condition. Finite difference method gives a local update and builds up a sparse matrix, though Hermitian. Former one has exponential convergence rate, whereas the latter one gives quadratic convergence according to the book "Lecture Notes on Solving Large Scale Eigenvalue Problems" by Prof. Dr. Peter Arbenz D-INFK ETH Zurich (http://people.inf.ethz.ch/arbenz/ewp/Lnotes/lsevp2010.pdf).

We start from Eq. 3.11 and write out explicitly the thermodynamic potential after momentum space integration as,

$$\frac{\Omega}{V} = -\frac{|\Delta|^2}{8\pi a_s} + \frac{1}{V}\sum_{\mathbf{k}}\left[\frac{\xi_{\mathbf{k}+q\mathbf{e}_x/2}+\xi_{-\mathbf{k}+q\mathbf{e}_x/2}}{2} - \frac{1}{4}\sum_{\eta=1}^{4}|E_{\mathbf{k}}^{\eta}| + \frac{|\Delta|^2}{2\epsilon_{\mathbf{k}}} - \frac{1}{2\beta}\sum_{\eta=1}^{4}\ln\left(1+\exp(-\beta|E_{\mathbf{k}}^{\eta}|)\right)\right] \tag{B.1}$$

$$= -\frac{|\Delta|^2}{8\pi a_s} + \frac{1}{(2\pi)^3}\int d^3k\left[k^2+\frac{q^2}{4}-\mu - \frac{1}{4}\sum_{\eta=1}^{4}|E_{\mathbf{k}}^{\eta}| + \frac{|\Delta|^2}{2\epsilon_{\mathbf{k}}} - \frac{1}{2\beta}\sum_{\eta=1}^{4}\ln\left(1+\exp(-\beta|E_{\mathbf{k}}^{\eta}|)\right)\right] \tag{B.2}$$

and $E^{\eta}_{\mathbf{k}}$ are diagonalized for given Δ , q , μ as variational parameters.

For the sake of simplicity in coding, I choose $h\sigma_z$ as the Zeeman field and BdG Hamiltonian is given by

$$H_{BdG} = \begin{pmatrix} \xi_{\mathbf{k}+\frac{q}{2}\mathbf{e}_z} + v_3(k_z+\frac{q}{2}) + h & v_1k_x - iv_2k_y & 0 & -\Delta \\ v_1k_x + iv_2k_y & \xi_{\mathbf{k}+\frac{q}{2}\mathbf{e}_z} - v_3(k_z+\frac{q}{2}) - h & \Delta & 0 \\ 0 & \Delta & -(\xi_{\mathbf{k}-\frac{q}{2}\mathbf{e}_z} - v_3(k_z-\frac{q}{2}) + h) & v_1k_x + iv_2k_y \\ -\Delta & 0 & v_1k_x - iv_2k_y & -(\xi_{\mathbf{k}-\frac{q}{2}\mathbf{e}_z} + v_3(k_z-\frac{q}{2}) - h) \end{pmatrix}$$

where $v_1 = v_2 = v_3 = v$. I put hard wall boundaris along y direction and at $y = 0$ and $y = L$ the wavefunction vanishes.

$$\begin{pmatrix} u(y) \\ \alpha(y) \\ \beta(y) \\ v(y) \end{pmatrix} = \sum_{n=1}^{N_{max}} \sqrt{\frac{2}{L}} \sin(\frac{n\pi y}{L}) \begin{pmatrix} u_n \\ \alpha_n \\ \beta_n \\ v_n \end{pmatrix} \tag{B.3}$$

$N_{max} = 200$ is a good cutoff. To convert the coupled differential equations into matrix equation, we replace ivk_y by $v\partial_y$,

$$\begin{aligned}
\left(k_x^2 + k_z^2 + \frac{q^2}{4} + k_zq + v_3(k_z+\frac{q}{2}) + h - \partial_{yy}\right) u(y) + (vk_x - v\partial_y)\alpha(y) - \Delta v(y) &= Eu(y) \\
(vk_x + v\partial_y)u(y) + \left(k_x^2 + k_z^2 + \frac{q^2}{4} + k_zq - v_3(k_z+\frac{q}{2}) - h - \partial_{yy}\right)\alpha(y) + \Delta\beta(y) &= E\alpha(y) \\
\Delta\alpha(y) - \left(k_x^2 + k_z^2 + \frac{q^2}{4} - k_zq - v_3(k_z-\frac{q}{2}) + h - \partial_{yy}\right)\beta(y) + (vk_x + v\partial_y)v(y) &= E\beta(y) \\
-\Delta u(y) + (vk_x - v\partial_y)\beta(y) - \left(k_x^2 + k_z^2 + \frac{q^2}{4} - k_zq + v_3(k_z-\frac{q}{2}) - h - \partial_{yy}\right)v(y) &= Ev(y)
\end{aligned}$$

Then we plug in expression of the quasiparticle wavefunctions to arrive at,

$$\sum_{n=1}^{N_{max}} \sqrt{\frac{2}{L}} \sin(\frac{n\pi y}{L}) \left(k_x^2 + k_z^2 + \frac{q^2}{4} + k_z q + v_3(k_z + \frac{q}{2}) + h + (\frac{n\pi}{L})^2 \right) u_n + \sum_{n=1}^{N_{max}} \sqrt{\frac{2}{L}} \left(v k_x \sin(\frac{n\pi y}{L}) - v \frac{n\pi}{L} \cos(\frac{n\pi y}{L}) \right) \alpha_n$$

$$-\Delta \sum_{n=1}^{N_{max}} \sqrt{\frac{2}{L}} \sin(\frac{n\pi y}{L}) v_n = E \sum_{n=1}^{N_{max}} \sqrt{\frac{2}{L}} \sin(\frac{n\pi y}{L}) u_n$$

$$\sum_{n=1}^{N_{max}} \sqrt{\frac{2}{L}} \left(v k_x \sin(\frac{n\pi y}{L}) + v \frac{n\pi}{L} \cos(\frac{n\pi y}{L}) \right) u_n + \sum_{n=1}^{N_{max}} \sqrt{\frac{2}{L}} \sin(\frac{n\pi y}{L}) \left(k_x^2 + k_z^2 + \frac{q^2}{4} + k_z q - v_3(k_z + \frac{q}{2}) - h + (\frac{n\pi}{L})^2 \right) \alpha_n$$

$$+\Delta \sum_{n=1}^{N_{max}} \sqrt{\frac{2}{L}} \sin(\frac{n\pi y}{L}) \beta_n = E \sum_{n=1}^{N_{max}} \sqrt{\frac{2}{L}} \sin(\frac{n\pi y}{L}) \alpha_n$$

$$\Delta \sum_{n=1}^{N_{max}} \sqrt{\frac{2}{L}} \sin(\frac{n\pi y}{L}) \alpha_n - \sum_{n=1}^{N_{max}} \sqrt{\frac{2}{L}} \sin(\frac{n\pi y}{L}) \left(k_x^2 + k_z^2 + \frac{q^2}{4} - k_z q - v_3(k_z - \frac{q}{2}) + h + (\frac{n\pi}{L})^2 \right) \beta_n$$

$$+ \sum_{n=1}^{N_{max}} \sqrt{\frac{2}{L}} \left(v k_x \sin(\frac{n\pi y}{L}) + v \frac{n\pi}{L} \cos(\frac{n\pi y}{L}) \right) v_n = E \sum_{n=1}^{N_{max}} \sqrt{\frac{2}{L}} \sin(\frac{n\pi y}{L}) \beta_n$$

$$-\Delta \sum_{n=1}^{N_{max}} \sqrt{\frac{2}{L}} \sin(\frac{n\pi y}{L}) u_n + \sum_{n=1}^{N_{max}} \sqrt{\frac{2}{L}} \left(v k_x \sin(\frac{n\pi y}{L}) - v \frac{n\pi}{L} \cos(\frac{n\pi y}{L}) \right) \beta_n$$

$$- \sum_{n=1}^{N_{max}} \sqrt{\frac{2}{L}} \sin(\frac{n\pi y}{L}) \left(k_x^2 + k_z^2 + \frac{q^2}{4} - k_z q + v_3(k_z - \frac{q}{2}) - h + (\frac{n\pi}{L})^2 \right) v_n = E \sum_{n=1}^{N_{max}} \sqrt{\frac{2}{L}} \sin(\frac{n\pi y}{L}) v_n$$

Using integral relations

$$\frac{2}{L}\int_0^L \sin(\frac{m\pi}{L}y)\sin(\frac{n\pi}{L}y)dy = \delta_{mn} \tag{B.4}$$

$$\frac{2}{L}\int_0^L \sin(\frac{m\pi}{L}y)\cos(\frac{n\pi}{L}y)dy = 0, \quad \text{for } m=n \tag{B.5}$$

$$= \frac{2m(1-(-1)^{m+n})}{(m^2-n^2)\pi}, \quad \text{for } m\neq n \tag{B.6}$$

we have

$$\left(k_x^2+k_z^2+\frac{q^2}{4}+k_zq+v_3(k_z+\frac{q}{2})+h+(\frac{m\pi}{L})^2\right)u_m+vk_x\alpha_m-\sum_{n\neq m}\frac{2vmn}{L}\frac{(1-(-1)^{m+n})}{(m^2-n^2)}\alpha_n-\Delta v_m = Eu_m$$

$$vk_xu_m+\sum_{n\neq m}\frac{2vmn}{L}\frac{(1-(-1)^{m+n})}{(m^2-n^2)}u_n+\left(k_x^2+k_z^2+\frac{q^2}{4}+k_zq-v_3(k_z+\frac{q}{2})-h+(\frac{m\pi}{L})^2\right)\alpha_m+\Delta\beta_m = E\alpha_m$$

$$\Delta\alpha_m-\left(k_x^2+k_z^2+\frac{q^2}{4}-k_zq-v_3(k_z-\frac{q}{2})+h+(\frac{m\pi}{L})^2\right)\beta_m+vk_xv_m+\sum_{n\neq m}\frac{2vmn}{L}\frac{(1-(-1)^{m+n})}{(m^2-n^2)}v_n = E\beta_m$$

$$-\Delta u_m+vk_x\beta_m-\sum_{n\neq m}\frac{2vmn}{L}\frac{(1-(-1)^{m+n})}{(m^2-n^2)}\beta_n-\left(k_x^2+k_z^2+\frac{q^2}{4}-k_zq+v_3(k_z-\frac{q}{2})-h+(\frac{m\pi}{L})^2\right)v_m = Ev_m$$

The matrix for coefficients are real and symmetric, and in the diagonalization routine, only lower left part is referenced. However, the subblock within the SOC term is antisymmetric, or skew symmetric: $A=-A^T$.

For the Hamiltonian in PRA85, 021603(R) by Hui Hu et al, with $\Delta=\Delta e^{-i\theta}$, the reason for relative phase between

wavefunctions is the following:

$$x = r\cos\theta \tag{B.7}$$

$$y = r\sin\theta \tag{B.8}$$

$$\partial_x = \cos\theta\partial_r - \frac{\sin\theta}{r}\partial_\theta \tag{B.9}$$

$$\partial_y = \sin\theta\partial_r + \frac{\cos\theta}{r}\partial_\theta \tag{B.10}$$

$$\nabla^2 = \frac{1}{r}\frac{\partial}{\partial r}(r\frac{\partial}{\partial r}) + \frac{1}{r^2}\frac{\partial^2}{\partial\theta^2} \equiv D_r + \frac{1}{r^2}\frac{\partial^2}{\partial\theta^2} \tag{B.11}$$

Then,

$$V_{SO} = \lambda(k_y + ik_x) = -i\lambda(\partial_y + i\partial_x) = e^{-i\theta}\lambda(\partial_r - \frac{i}{r}\partial_\theta) \tag{B.12}$$

$$V_{SO}^\dagger = \lambda(k_y - ik_x) = -i\lambda(\partial_y - i\partial_x) = -e^{i\theta}\lambda(\partial_r + \frac{i}{r}\partial_\theta) \tag{B.13}$$

From

$$H_{BdG} = \begin{bmatrix} H_\uparrow & V_{so} & 0 & -\Delta \\ V_{so}^\dagger & H_\downarrow & \Delta & 0 \\ 0 & \Delta^* & -H_\uparrow & V^\dagger \\ -\Delta^* & 0 & V_{so} & -H_\downarrow \end{bmatrix} \tag{B.14}$$

we have

$$(H_\uparrow + D_r + \frac{1}{r^2}\frac{\partial^2}{\partial\theta^2})u(\mathbf{r}) + e^{-i\theta}(\partial_r - \frac{i}{r}\partial_\theta)\alpha(\mathbf{r}) - \Delta e^{-i\theta}v(\mathbf{r}) = Eu(\mathbf{r}) \quad \text{(B.15)}$$

$$-e^{i\theta}\lambda(\partial_r + \frac{i}{r}\partial_\theta)u(\mathbf{r}) + (H_\downarrow + D_r + \frac{1}{r^2}\frac{\partial^2}{\partial\theta^2})\alpha(\mathbf{r}) + \Delta e^{-i\theta}\beta(\mathbf{r}) = E\alpha(\mathbf{r}) \quad \text{(B.16)}$$

$$\Delta e^{i\theta}\alpha(\mathbf{r}) + (-H_\uparrow D_r + \frac{1}{r^2}\frac{\partial^2}{\partial\theta^2})\beta(\mathbf{r}) - e^{i\theta}\lambda(\partial_r + \frac{i}{r}\partial_\theta)v(\mathbf{r}) = E\beta(\mathbf{r}) \quad \text{(B.17)}$$

$$-\Delta e^{i\theta}u(\mathbf{r}) + e^{-i\theta}(\partial_r - \frac{i}{r}\partial_\theta)\beta(\mathbf{r}) + (-H_\downarrow + D_r + \frac{1}{r^2}\frac{\partial^2}{\partial\theta^2})v(\mathbf{r}) = Ev(\mathbf{r}) \quad \text{(B.18)}$$

The construction of wavefunctions can be decomposed into different angular momentum m, but we need to pay attention to the relative phase, in order to have an eigenvalue matrix equation:

$$u(\mathbf{r}) = \frac{e^{im\theta}}{\sqrt{2\pi}}u(r)e^{-i\theta} \quad \text{(B.19)}$$

$$\alpha(\mathbf{r}) = \frac{e^{im\theta}}{\sqrt{2\pi}}\alpha(r) \quad \text{(B.20)}$$

$$\beta(\mathbf{r}) = \frac{e^{im\theta}}{\sqrt{2\pi}}\beta(r)e^{+i\theta} \quad \text{(B.21)}$$

$$v(\mathbf{r}) = \frac{e^{im\theta}}{\sqrt{2\pi}}v(r) \quad \text{(B.22)}$$

For cylindrical boundary condition in the plane of x-y with radius $r = L$, we use basis expansion as ($m \geq 0$, integer.),

assuming states with different m are decoupled

$$\begin{pmatrix} u(\mathbf{r}) \\ \alpha(\mathbf{r}) \\ \beta(\mathbf{r}) \\ v(\mathbf{r}) \end{pmatrix} = e^{ik_z z} \sum_{n=1}^{N_{max}} \begin{pmatrix} \frac{u_n}{\sqrt{\mathcal{N}_n^{(m)}}} J_m(\kappa_n^{(m)} \frac{r}{L}) \\ \frac{\alpha_n}{\sqrt{\mathcal{N}_n^{(m+1)}}} J_{m+1}(\kappa_n^{(m+1)} \frac{r}{L}) e^{i\theta} \\ \frac{\beta_n}{\sqrt{\mathcal{N}_n^{(m+1)}}} J_{m+1}(\kappa_n^{(m+1)} \frac{r}{L}) e^{i\theta} \\ \frac{v_n}{\sqrt{\mathcal{N}_n^{(m)}}} J_m(\kappa_n^{(m)} \frac{r}{L}) \end{pmatrix} \frac{e^{im\theta}}{\sqrt{2\pi}} \tag{B.23}$$

where $\kappa_n^{(m)}$ are the nth root of Bessel function J_m. For states with $m < 0$, we have instead $J_{-m}(x) = (-1)^m J_m(x)$, which is NOT linearly independent solution of Bessel equation. States at $r = 0$ should not diverge, the second kind of Bessel function $N_m(x)$ should be discarded.

SOC terms are written as

$$V_{SO} = vk_x - ivk_y = -iv(\partial_x - i\partial_y) = -ve^{-i\theta}(i\partial_r + \frac{1}{r}\partial_\theta) \tag{B.24}$$

$$V_{SO}^\dagger = vk_x + ivk_y = -iv(\partial_x + i\partial_y) = ve^{i\theta}(-i\partial_r + \frac{1}{r}\partial_\theta) \tag{B.25}$$

we have

$$\left(k_z^2+\frac{q^2}{4}+k_zq+v_3(k_z+\frac{q}{2})+h-(\frac{1}{r}\frac{\partial}{\partial r}(r\frac{\partial}{\partial r})+\frac{1}{r^2}\frac{\partial^2}{\partial\theta^2})\right)u(\mathbf{r})-ve^{-i\theta}(i\partial_r+\frac{1}{r}\partial_\theta)\alpha(\mathbf{r})-\Delta v(\mathbf{r}) = Eu(\mathbf{r}) \quad \text{(B.26)}$$

$$ve^{i\theta}(-i\partial_r+\frac{1}{r}\partial_\theta)u(\mathbf{r})+\left(k_z^2+\frac{q^2}{4}+k_zq-v_3(k_z+\frac{q}{2})-h-(\frac{1}{r}\frac{\partial}{\partial r}(r\frac{\partial}{\partial r})+\frac{1}{r^2}\frac{\partial^2}{\partial\theta^2})\right)\alpha(\mathbf{r})+\Delta\beta(\mathbf{r}) = E\alpha(\mathbf{r}) \quad \text{(B.27)}$$

$$\Delta\alpha(\mathbf{r})-\left(k_z^2+\frac{q^2}{4}-k_zq-v_3(k_z-\frac{q}{2})+h-(\frac{1}{r}\frac{\partial}{\partial r}(r\frac{\partial}{\partial r})+\frac{1}{r^2}\frac{\partial^2}{\partial\theta^2})\right)\beta(\mathbf{r})+ve^{i\theta}(-i\partial_r+\frac{1}{r}\partial_\theta)v(\mathbf{r}) = E\beta(\mathbf{r}) \quad \text{(B.28)}$$

$$-\Delta u(\mathbf{r})-ve^{-i\theta}(i\partial_r+\frac{1}{r}\partial_\theta)\beta(\mathbf{r})-\left(k_z^2+\frac{q^2}{4}-k_zq+v_3(k_z-\frac{q}{2})-h-(\frac{1}{r}\frac{\partial}{\partial r}(r\frac{\partial}{\partial r})+\frac{1}{r^2}\frac{\partial^2}{\partial\theta^2})\right)v(\mathbf{r}) = Ev(\mathbf{r}) \quad \text{(B.29)}$$

Normalization of Bessel function is given by

$$\mathcal{N}_n^{(m)}=\int_0^L J_m(\kappa_n^{(m)}\frac{r}{L})J_m(\kappa_n^{(m)}\frac{r}{L})rdr=\frac{1}{2}L^2\left(J_{m+1}(\kappa_n^{(m)})\right)^2 \quad \text{(B.30)}$$

Then Eq. B.23 becomes,

$$\begin{pmatrix} u(\mathbf{r}) \\ \alpha(\mathbf{r}) \\ \beta(\mathbf{r}) \\ v(\mathbf{r}) \end{pmatrix} = e^{ik_zz}\sum_{n=1}^{N_{max}}\frac{\sqrt{2}}{L}\frac{e^{im\theta}}{\sqrt{2\pi}}\begin{pmatrix} \frac{J_m(\kappa_n^{(m)}\frac{r}{L})}{|J_{m+1}(\kappa_n^{(m)})|}u_n \\ \frac{J_{m+1}(\kappa_n^{(m+1)}\frac{r}{L})}{|J_{m+2}(\kappa_n^{(m+1)})|}\alpha_ne^{i\theta} \\ \frac{J_{m+1}(\kappa_n^{(m+1)}\frac{r}{L})}{|J_{m+2}(\kappa_n^{(m+1)})|}\beta_ne^{i\theta} \\ \frac{J_m(\kappa_n^{(m)}\frac{r}{L})}{|J_{m+1}(\kappa_n^{(m)})|}v_n \end{pmatrix} \quad \text{(B.31)}$$

Orthogonal condition for Bessel function,

$$\int_0^L J_m(\kappa_n^{(m)}\frac{r}{L})J_m(\kappa_l^{(m)}\frac{r}{L})rdr=0 \quad \text{(B.32)}$$

for $n \neq l$. Derivative relations for Bessel functions:

$$\frac{\partial}{\partial r} J_0(\kappa_n^{(0)} \frac{r}{L}) = -\frac{\kappa_n^{(0)}}{L} J_1(\kappa_n^{(0)} \frac{r}{L}) \tag{B.33}$$

$$\frac{\partial}{\partial r} J_m(\kappa_n^{(m)} \frac{r}{L}) = \frac{\kappa_n^{(m)}}{2L} \left(J_{m-1}(\kappa_n^{(m)} \frac{r}{L}) - J_{m+1}(\kappa_n^{(m)} \frac{r}{L}) \right), \quad \text{for } m \geq 1 \tag{B.34}$$

$$\begin{aligned}
\frac{1}{r}\frac{\partial}{\partial r}(r \frac{\partial}{\partial r} J_0(\kappa_n^{(0)} \frac{r}{L})) &= -\frac{\kappa_n^{(0)}}{L} \frac{1}{r} \frac{\partial}{\partial r}(r J_1(\kappa_n^{(0)} \frac{r}{L})) \\
&= -\frac{\kappa_n^{(0)}}{L} \left(\frac{J_1(\kappa_n^{(0)} \frac{r}{L})}{r} + \frac{\kappa_n^{(0)}}{2L} \left(J_0(\kappa_n^{(0)} \frac{r}{L}) - J_2(\kappa_n^{(0)} \frac{r}{L}) \right) \right) = ... = -(\frac{\kappa_n^{(0)}}{L})^2 \\
\frac{1}{r}\frac{\partial}{\partial r}(r \frac{\partial}{\partial r} J_1(\kappa_n^{(1)} \frac{r}{L})) &= \frac{\kappa_n^{(1)}}{2L} \frac{1}{r} \frac{\partial}{\partial r}(r \left(J_0(\kappa_n^{(1)} \frac{r}{L}) - J_2(\kappa_n^{(1)} \frac{r}{L}) \right)) \\
&= \frac{\kappa_n^{(1)}}{2L} \frac{1}{r} \left(J_0(\kappa_n^{(1)} \frac{r}{L}) - J_2(\kappa_n^{(1)} \frac{r}{L}) \right) + \frac{\kappa_n^{(1)}}{2L} \frac{\partial}{\partial r} \left(J_0(\kappa_n^{(1)} \frac{r}{L}) - J_2(\kappa_n^{(1)} \frac{r}{L}) \right) \\
&= \frac{\kappa_n^{(1)}}{2L} \frac{1}{r} \left(J_0(\kappa_n^{(1)} \frac{r}{L}) - J_2(\kappa_n^{(1)} \frac{r}{L}) \right) + \frac{1}{2} \left(\frac{\kappa_n^{(1)}}{L} \right)^2 \left(-J_1(\kappa_n^{(1)} \frac{r}{L}) - \frac{1}{2} \left(J_1(\kappa_n^{(1)} \frac{r}{L}) - J_3(\kappa_n^{(1)} \frac{r}{L}) \right) \right) \\
&= \frac{\kappa_n^{(1)}}{2L} \frac{J_0(\kappa_n^{(1)} \frac{r}{L})}{r} - \frac{3}{4} \left(\frac{\kappa_n^{(1)}}{L} \right)^2 J_1(\kappa_n^{(1)} \frac{r}{L}) - \frac{\kappa_n^{(1)}}{2L} \frac{J_2(\kappa_n^{(1)} \frac{r}{L})}{r} + \frac{1}{4} \left(\frac{\kappa_n^{(1)}}{L} \right)^2 J_3(\kappa_n^{(1)} \frac{r}{L})
\end{aligned} \tag{B.35}$$

$$
\begin{aligned}
\frac{1}{r}\frac{\partial}{\partial r}(r\frac{\partial}{\partial r}J_m(\kappa_n^{(m)}\frac{r}{L})) &= \frac{\kappa_n^{(m)}}{2L}\frac{1}{r}\frac{\partial}{\partial r}(r\left(J_{m-1}(\kappa_n^{(m)}\frac{r}{L}) - J_{m+1}(\kappa_n^{(m)}\frac{r}{L})\right)) \\
&= \frac{\kappa_n^{(m)}}{2L}\frac{1}{r}\left(J_{m-1}(\kappa_n^{(m)}\frac{r}{L}) - J_{m+1}(\kappa_n^{(m)}\frac{r}{L})\right) + \frac{\kappa_n^{(m)}}{2L}\frac{\partial}{\partial r}\left(J_{m-1}(\kappa_n^{(m)}\frac{r}{L}) - J_{m+1}(\kappa_n^{(m)}\frac{r}{L})\right) \\
&= \frac{\kappa_n^{(m)}}{2L}\frac{1}{r}\left(J_{m-1}(\kappa_n^{(m)}\frac{r}{L}) - J_{m+1}(\kappa_n^{(m)}\frac{r}{L})\right) \\
&+ \left(\frac{\kappa_n^{(m)}}{2L}\right)^2\left(\left(J_{m-2}(\kappa_n^{(m)}\frac{r}{L}) - J_m(\kappa_n^{(m)}\frac{r}{L})\right) - \left(J_m(\kappa_n^{(m)}\frac{r}{L}) - J_{m+2}(\kappa_n^{(m)}\frac{r}{L})\right)\right) \\
&= \left(\frac{\kappa_n^{(m)}}{2L}\right)^2 J_{m-2}(\kappa_n^{(m)}\frac{r}{L}) + \frac{\kappa_n^{(m)}}{2L}\frac{J_{m-1}(\kappa_n^{(m)}\frac{r}{L})}{r} - 2\left(\frac{\kappa_n^{(m)}}{2L}\right)^2 J_m(\kappa_n^{(m)}\frac{r}{L}) \\
&- \frac{\kappa_n^{(m)}}{2L}\frac{J_{m+1}(\kappa_n^{(m)}\frac{r}{L})}{r} + \left(\frac{\kappa_n^{(m)}}{2L}\right)^2 J_{m+2}(\kappa_n^{(m)}\frac{r}{L}), \quad \text{for } m \geq 2
\end{aligned}
$$

Actually, the above second order derivatives are not necessary. Because Bessel function automatically satisfies Bessel equation

$$
\frac{1}{r}\frac{\partial}{\partial r}(r\frac{\partial}{\partial r}J_m(\kappa_n^{(m)}\frac{r}{L})) = \left(\frac{m^2}{r^2} - (\frac{\kappa_n^{(m)}}{L})^2\right) J_m(\kappa_n^{(m)}\frac{r}{L}) \tag{B.36}
$$

It can be checked straightforwardly that the RHS of above second order derivatives are actually quite simple, using the recursion relation

$$
J_{m+1}(x) + J_{m-1}(x) = 2mJ_m(x)/x \tag{B.37}
$$

which is essentially derived from the Bessel equation. This helps us to facilitate the conversion into coefficient matrix equations:

for $m \geq 1$, using Bessel Eq. B.36 and recursion relation Eq. B.37, we can simplify the SOC term a little bit,

$$\sum_{n=1}^{N_{max}} \left(k_z^2 + \frac{q^2}{4} + k_z q + v_3(k_z + \frac{q}{2}) + h + \left(\frac{\kappa_n^{(m)}}{L} \right)^2 \right) \frac{u_n}{\sqrt{\mathcal{N}_n^{(m)}}} J_m(\kappa_n^{(m)} \frac{r}{L})$$

$$-iv \sum_{l=1}^{N_{max}} \frac{\alpha_l}{\sqrt{\mathcal{N}_l^{(m+1)}}} \frac{\kappa_l^{(m+1)}}{L} J_m(\kappa_l^{(m+1)} \frac{r}{L})$$

$$-\Delta \sum_{n=1}^{N_{max}} \frac{v_n}{\sqrt{\mathcal{N}_n^{(m)}}} J_m(\kappa_n^{(m)} \frac{r}{L}) = E \sum_{n=1}^{N_{max}} \frac{u_n}{\sqrt{\mathcal{N}_n^{(m)}}} J_m(\kappa_n^{(m)} \frac{r}{L}) \tag{B.38}$$

$$iv \sum_{l=1}^{N_{max}} \frac{u_l}{\sqrt{\mathcal{N}_l^{(m)}}} \frac{\kappa_l^{(m)}}{L} J_{m+1}(\kappa_l^{(m)} \frac{r}{L})$$

$$+ \sum_{n=1}^{N_{max}} \left(k_z^2 + \frac{q^2}{4} + k_z q - v_3(k_z + \frac{q}{2}) - h + \left(\frac{\kappa_n^{(m+1)}}{L} \right)^2 \right) \frac{\alpha_n}{\sqrt{\mathcal{N}_n^{(m+1)}}} J_{m+1}(\kappa_n^{(m+1)} \frac{r}{L})$$

$$+\Delta \sum_{n=1}^{N_{max}} \frac{\beta_n}{\sqrt{\mathcal{N}_n^{(m+1)}}} J_{m+1}(\kappa_n^{(m+1)} \frac{r}{L}) = E \sum_{n=1}^{N_{max}} \frac{\alpha_n}{\sqrt{\mathcal{N}_n^{(m+1)}}} J_{m+1}(\kappa_n^{(m+1)} \frac{r}{L}) \tag{B.39}$$

$$\Delta \sum_{n=1}^{N_{max}} \frac{\alpha_n}{\sqrt{\mathcal{N}_n^{(m+1)}}} J_{m+1}(\kappa_n^{(m+1)} \frac{r}{L})$$

(B.40)

$$-\sum_{n=1}^{N_{max}}\left(k_z^2+\frac{q^2}{4}-k_zq-v_3(k_z-\frac{q}{2})+h+\left(\frac{\kappa_n^{(m+1)}}{L}\right)^2\right)\frac{\beta_n}{\sqrt{\mathcal{N}_n^{(m+1)}}}J_{m+1}(\kappa_n^{(m+1)}\frac{r}{L})$$
$$+iv\sum_{l=1}^{N_{max}}\frac{v_l}{\sqrt{\mathcal{N}_l^{(m)}}}\frac{\kappa_l^{(m)}}{L}J_{m+1}(\kappa_l^{(m)}\frac{r}{L})=E\sum_{n=1}^{N_{max}}\frac{\beta_n}{\sqrt{\mathcal{N}_n^{(m+1)}}}J_{m+1}(\kappa_n^{(m+1)}\frac{r}{L}) \tag{B.41}$$
$$-\Delta\sum_{n=1}^{N_{max}}\frac{u_n}{\sqrt{\mathcal{N}_n^{(m)}}}J_m(\kappa_n^{(m)}\frac{r}{L})$$
$$-iv\sum_{l=1}^{N_{max}}\frac{\beta_l}{\sqrt{\mathcal{N}_l^{(m+1)}}}\frac{\kappa_l^{(m+1)}}{L}J_m(\kappa_l^{(m+1)}\frac{r}{L})$$
$$-\sum_{n=1}^{N_{max}}\left(k_z^2+\frac{q^2}{4}-k_zq+v_3(k_z-\frac{q}{2})-h+\left(\frac{\kappa_n^{(m)}}{L}\right)^2\right)\frac{v_n}{\sqrt{\mathcal{N}_n^{(m)}}}J_m(\kappa_n^{(m)}\frac{r}{L})=E\sum_{n=1}^{N_{max}}\frac{v_n}{\sqrt{\mathcal{N}_n^{(m)}}}J_m(\kappa_n^{(m)}\frac{r}{L}) \tag{B.42}$$

for $m=0$, special care is needed for first order derivative, but the result can be recovered by replacing $m=0$ in the above equations.

Then using orthonormal condition, we have equations for the coefficients, $m \geq 0$,

$$\mathcal{H}_{11n}^{(m)} u_n - iv \sum_{l=1}^{N_{max}} \mathcal{A}_{nl}^{(m)} \alpha_l - \Delta v_n = E u_n \tag{B.43}$$

$$iv \sum_{l=1}^{N_{max}} \mathcal{B}_{nl}^{(m)} u_l + \mathcal{H}_{22n}^{(m)} \alpha_n + \Delta \beta_n = E \alpha_n \tag{B.44}$$

$$\Delta \alpha_n + \mathcal{H}_{33n}^{(m)} \beta_n + iv \sum_{l=1}^{N_{max}} \mathcal{B}_{nl}^{(m)} v_l = E \beta_n \tag{B.45}$$

$$-\Delta u_n - iv \sum_{l=1}^{N_{max}} \mathcal{A}_{nl}^{(m)} \beta_l + \mathcal{H}_{44n}^{(m)} v_n = E v_n \tag{B.46}$$

$$\mathcal{H}_{11n}^{(m)} = \left(k_z^2 + \frac{q^2}{4} + k_z q + v_3 (k_z + \frac{q}{2}) + h + \left(\frac{\kappa_n^{(m)}}{L} \right)^2 \right) \tag{B.47}$$

$$\mathcal{H}_{22n}^{(m)} = \left(k_z^2 + \frac{q^2}{4} + k_z q - v_3 (k_z + \frac{q}{2}) - h + \left(\frac{\kappa_n^{(m+1)}}{L} \right)^2 \right) \tag{B.48}$$

$$\mathcal{H}_{33n}^{(m)} = - \left(k_z^2 + \frac{q^2}{4} - k_z q - v_3 (k_z - \frac{q}{2}) + h + \left(\frac{\kappa_n^{(m+1)}}{L} \right)^2 \right) \tag{B.49}$$

$$\mathcal{H}_{44n}^{(m)} = - \left(k_z^2 + \frac{q^2}{4} - k_z q + v_3 (k_z - \frac{q}{2}) - h + \left(\frac{\kappa_n^{(m)}}{L} \right)^2 \right) \tag{B.50}$$

$$\mathcal{A}_{nl}^{(m)} = \frac{\frac{\kappa_l^{(m+1)}}{L} I_{nl}^{(1)}}{\sqrt{\mathcal{N}_l^{(m+1)}}\sqrt{\mathcal{N}_n^{(m)}}} \tag{B.51}$$

$$\mathcal{B}_{nl}^{(m)} = \frac{\frac{\kappa_l^{(m)}}{L} I_{nl}^{(2)}}{\sqrt{\mathcal{N}_l^{(m)}}\sqrt{\mathcal{N}_n^{(m+1)}}} \tag{B.52}$$

where

$$\int_0^L r J_m(\frac{\kappa_n^{(m)}}{L} r) J_m(\frac{\kappa_l^{(m+1)}}{L} r) dr = I_{nl}^{(1)} \tag{B.53}$$

$$\int_0^L r J_{m+1}(\frac{\kappa_n^{(m+1)}}{L} r) J_{m+1}(\frac{\kappa_l^{(m)}}{L} r) dr = I_{nl}^{(2)} \tag{B.54}$$

Using Eq. (2) in page 414 of the book "Introduction to Special Functions" by Zhuxi Wang and Dunren Guo

$$\int_0^x t J_\nu(at) J_\nu(bt) dt = \frac{x}{a^2 - b^2} \left(J_\nu(ax) \frac{dJ_\nu(bx)}{dx} - J_\nu(bx) \frac{dJ_\nu(ax)}{dx} \right) \tag{B.55}$$

for $\nu > -1$, which can be easily proved by considering two Bessel Equations

$$\begin{aligned} \frac{1}{t}\frac{d}{dt}(t\frac{dJ_\nu(at)}{dt}) + (a^2 - \frac{\nu^2}{t^2}) J_\nu(at) &= 0 \\ \frac{1}{t}\frac{d}{dt}(t\frac{dJ_\nu(bt)}{dt}) + (b^2 - \frac{\nu^2}{t^2}) J_\nu(bt) &= 0 \end{aligned}$$

Multiply the two equations by $tJ_\nu(bt)$ and $tJ_\nu(at)$ individually and subtract them and integrate it from 0 to x, to obtain

$$(a^2 - b^2) \int_0^x t J_\nu(at) J_\nu(bt) dt = \left(t J_\nu(at) \frac{dJ_\nu(bt)}{dt} - t J_\nu(bt) \frac{dJ_\nu(at)}{dt} \right) |_{t=0}^{t=x} \tag{B.56}$$

and it is easy to see the RHS is zero when $t = 0$, which concludes our proof of Eq. B.55. From this, we can easily have

$$
\begin{aligned}
I_{nl}^{(1)} &= \frac{L}{(\frac{\kappa_n^{(m)}}{L})^2 - (\frac{\kappa_l^{(m+1)}}{L})^2} \left(J_m(\kappa_n^{(m)}) \frac{dJ_m(\kappa_l^{(m+1)} r/L)}{dr}|_{r=L} - J_m(\kappa_l^{(m+1)}) \frac{dJ_m(\kappa_n^{(m)} r/L)}{dr}|_{r=L} \right) \\
&= -\frac{L}{(\frac{\kappa_n^{(m)}}{L})^2 - (\frac{\kappa_l^{(m+1)}}{L})^2} J_m(\kappa_l^{(m+1)}) \frac{\kappa_n^{(m)}}{2L} \left(J_{m-1}(\kappa_n^{(m)}) - J_{m+1}(\kappa_n^{(m)}) \right) \\
I_{nl}^{(2)} &= \frac{L}{(\frac{\kappa_n^{(m+1)}}{L})^2 - (\frac{\kappa_l^{(m)}}{L})^2} \left(J_{m+1}(\kappa_n^{(m+1)}) \frac{dJ_{m+1}(\kappa_l^{(m)} r/L)}{dr}|_{r=L} - J_{m+1}(\kappa_l^{(m)}) \frac{dJ_{m+1}(\kappa_n^{(m+1)} r/L)}{dr}|_{r=L} \right) \\
&= -\frac{L}{(\frac{\kappa_n^{(m+1)}}{L})^2 - (\frac{\kappa_l^{(m)}}{L})^2} J_{m+1}(\kappa_l^{(m)}) \frac{\kappa_n^{(m+1)}}{2L} \left(J_m(\kappa_n^{(m+1)}) - J_{m+2}(\kappa_n^{(m+1)}) \right)
\end{aligned}
$$

Then, we can further simplify coefficients of SOC term

$$
\begin{aligned}
\mathcal{A}_{nl}^{(m)} &= -(\frac{\sqrt{2}}{L})^2 \frac{1}{|J_{m+2}(\kappa_l^{(m+1)})|} \frac{1}{|J_{m+1}(\kappa_n^{(m)})|} \\
&\times \frac{\kappa_l^{(m+1)}}{L} \frac{L}{(\frac{\kappa_n^{(m)}}{L})^2 - (\frac{\kappa_l^{(m+1)}}{L})^2} J_m(\kappa_l^{(m+1)}) \frac{\kappa_n^{(m)}}{2L} \left(J_{m-1}(\kappa_n^{(m)}) - J_{m+1}(\kappa_n^{(m)}) \right) \\
&= -\frac{1}{L} \frac{\kappa_n^{(m)} \kappa_l^{(m+1)}}{(\kappa_n^{(m)})^2 - (\kappa_l^{(m+1)})^2} \frac{J_m(\kappa_l^{(m+1)}) \left(J_{m-1}(\kappa_n^{(m)}) - J_{m+1}(\kappa_n^{(m)}) \right)}{|J_{m+2}(\kappa_l^{(m+1)})| \cdot |J_{m+1}(\kappa_n^{(m)})|}, \quad \text{for } m \geq 1 \qquad \text{(B.57)} \\
&= -\frac{2}{L} \frac{\kappa_n^{(m)} \kappa_l^{(m+1)}}{(\kappa_n^{(m)})^2 - (\kappa_l^{(m+1)})^2} \frac{J_m(\kappa_l^{(m+1)}) \left(-J_{m+1}(\kappa_n^{(m)}) \right)}{|J_{m+2}(\kappa_l^{(m+1)})| \cdot |J_{m+1}(\kappa_n^{(m)})|}, \quad \text{for } m = 0. \qquad \text{(B.58)} \\
\mathcal{B}_{nl}^{(m)} &= -(\frac{\sqrt{2}}{L})^2 \frac{1}{|J_{m+1}(\kappa_l^{(m)})|} \frac{1}{|J_{m+2}(\kappa_n^{(m+1)})|} \\
&\times \frac{\kappa_l^{(m)}}{L} \frac{L}{(\frac{\kappa_n^{(m+1)}}{L})^2 - (\frac{\kappa_l^{(m)}}{L})^2} J_{m+1}(\kappa_l^{(m)}) \frac{\kappa_n^{(m+1)}}{2L} \left(J_m(\kappa_n^{(m+1)}) - J_{m+2}(\kappa_n^{(m+1)}) \right) \\
&= -\frac{1}{L} \frac{\kappa_n^{(m+1)} \kappa_l^{(m)}}{(\kappa_n^{(m+1)})^2 - (\kappa_l^{(m)})^2} \frac{J_{m+1}(\kappa_l^{(m)}) \left(J_m(\kappa_n^{(m+1)}) - J_{m+2}(\kappa_n^{(m+1)}) \right)}{|J_{m+1}(\kappa_l^{(m)})| \cdot |J_{m+2}(\kappa_n^{(m+1)})|} \qquad \text{(B.59)}
\end{aligned}
$$

where $m = 0$ term should be treated slightly differently, concerning the derivative rule for $J_m(x)$ in Eq. B.33 and B.34.

The matrix for coefficients is actually self-adjoint/Hermitian and in the diagonalization routine, only lower left part is referenced.

If we consider states with negative angular momentum, we need expansion as ($m \leq -1$, i.e. $|m| \geq 1$),

$$\begin{pmatrix} u(\mathbf{r}) \\ \alpha(\mathbf{r}) \\ \beta(\mathbf{r}) \\ v(\mathbf{r}) \end{pmatrix} = e^{ik_z z} \sum_{n=1}^{N_{max}} \begin{pmatrix} \frac{u_n}{\sqrt{\mathcal{N}_n^{(-|m|)}}} J_{-|m|}(\kappa_n^{(-|m|)} \frac{r}{L}) \\ \frac{\alpha_n}{\sqrt{\mathcal{N}_n^{(-|m|+1)}}} J_{-|m|+1}(\kappa_n^{(-|m|+1)} \frac{r}{L}) e^{i\theta} \\ \frac{\beta_n}{\sqrt{\mathcal{N}_n^{(-|m|+1)}}} J_{-|m|+1}(\kappa_n^{(-|m|+1)} \frac{r}{L}) e^{i\theta} \\ \frac{v_n}{\sqrt{\mathcal{N}_n^{(-|m|)}}} J_{-|m|}(\kappa_n^{(-|m|)} \frac{r}{L}) \end{pmatrix} \frac{e^{-i|m|\theta}}{\sqrt{2\pi}}$$

$$= e^{ik_z z} \sum_{n=1}^{N_{max}} \begin{pmatrix} \frac{u_n}{\sqrt{\mathcal{N}_n^{(|m|)}}} (-1)^{|m|} J_{|m|}(\kappa_n^{(|m|)} \frac{r}{L}) \\ \frac{\alpha_n}{\sqrt{\mathcal{N}_n^{(|m|-1)}}} (-1)^{|m|-1} J_{|m|-1}(\kappa_n^{(|m|-1)} \frac{r}{L}) e^{i\theta} \\ \frac{\beta_n}{\sqrt{\mathcal{N}_n^{(|m|-1)}}} (-1)^{|m|-1} J_{|m|-1}(\kappa_n^{(|m|-1)} \frac{r}{L}) e^{i\theta} \\ \frac{v_n}{\sqrt{\mathcal{N}_n^{(|m|)}}} (-1)^{|m|} J_{|m|}(\kappa_n^{(|m|)} \frac{r}{L}) \end{pmatrix} \frac{e^{-i|m|\theta}}{\sqrt{2\pi}}$$

where relation $J_{-m}(x) = (-1)^m J_m(x)$ and $\kappa_n^{(-m)} = \kappa_n^{(m)}$ has been used, and normalization is given by

$$\mathcal{N}_n^{(-|m|)} = \int_0^L J_{-|m|}(\kappa_n^{(-|m|)} \frac{r}{L}) J_{-|m|}(\kappa_n^{(-|m|)} \frac{r}{L}) r dr \tag{B.60}$$

$$= (-1)^{2|m|} \int_0^L J_{|m|}(\kappa_n^{(|m|)} \frac{r}{L}) J_{|m|}(\kappa_n^{(|m|)} \frac{r}{L}) r dr \tag{B.61}$$

$$= \frac{1}{2} L^2 \left(J_{|m|+1}(\kappa_n^{(|m|)}) \right)^2 \tag{B.62}$$

$$= \mathcal{N}_n^{(|m|)} \tag{B.63}$$

Following the above procedures, we obtain equations for coefficients ($m \leq -1$)

$$\mathcal{L}_{11n}^{(m)} u_n - iv \sum_{l=1}^{N_{max}} \mathcal{C}_{nl}^{(m)} \alpha_l - \Delta v_n = E u_n \tag{B.64}$$

$$iv \sum_{l=1}^{N_{max}} \mathcal{D}_{nl}^{(m)} u_l + \mathcal{L}_{22n}^{(m)} \alpha_n + \Delta \beta_n = E \alpha_n \tag{B.65}$$

$$\Delta \alpha_n + \mathcal{L}_{33n}^{(m)} \beta_n + iv \sum_{l=1}^{N_{max}} \mathcal{D}_{nl}^{(m)} v_l = E \beta_n \tag{B.66}$$

$$-\Delta u_n - iv \sum_{l=1}^{N_{max}} \mathcal{C}_{nl}^{(m)} \beta_l + \mathcal{L}_{44n}^{(m)} v_n = E v_n \tag{B.67}$$

where

$$\mathcal{L}_{11n}^{(m)} = \left(k_z^2 + \frac{q^2}{4} + k_z q + v_3 (k_z + \frac{q}{2}) + h + \left(\frac{\kappa_n^{(|m|)}}{L} \right)^2 \right) \tag{B.68}$$

$$\mathcal{L}_{22n}^{(m)} = \left(k_z^2 + \frac{q^2}{4} + k_z q - v_3 (k_z + \frac{q}{2}) - h + \left(\frac{\kappa_n^{(|m|-1)}}{L} \right)^2 \right) \tag{B.69}$$

$$\mathcal{L}_{33n}^{(m)} = -\left(k_z^2 + \frac{q^2}{4} - k_z q - v_3 (k_z - \frac{q}{2}) + h + \left(\frac{\kappa_n^{(|m|-1)}}{L} \right)^2 \right) \tag{B.70}$$

$$\mathcal{L}_{44n}^{(m)} = -\left(k_z^2 + \frac{q^2}{4} - k_z q + v_3 (k_z - \frac{q}{2}) - h + \left(\frac{\kappa_n^{(|m|)}}{L} \right)^2 \right) \tag{B.71}$$

$$\mathcal{C}_{nl}^{(m)} = \frac{\kappa_l^{(|m|-1)}}{L}\frac{\int_0^L r J_{|m|}(\kappa_n^{(|m|)}\frac{r}{L})J_{|m|}(\kappa_l^{(|m|-1)}\frac{r}{L})dr}{\sqrt{\mathcal{N}_l^{(|m|-1)}}\sqrt{\mathcal{N}_n^{(|m|)}}} \tag{B.72}$$

$$\mathcal{D}_{nl}^{(m)} = \frac{\kappa_l^{(|m|)}}{L}\frac{\int_0^L r J_{|m|-1}(\kappa_n^{|m|-1}\frac{r}{L})J_{|m|-1}(\kappa_l^{(|m|)}\frac{r}{L})dr}{\sqrt{\mathcal{N}_l^{(|m|)}}\sqrt{\mathcal{N}_n^{(|m|-1)}}} \tag{B.73}$$

which will be evaluated as before,

$$\mathcal{C}_{nl}^{(m)} = -\frac{1}{L}\frac{\kappa_n^{(|m|)}\kappa_l^{(|m|-1)}}{(\kappa_n^{(|m|)})^2-(\kappa_l^{(|m|-1)})^2}\frac{J_{|m|}(\kappa_l^{(|m|-1)})\left(J_{|m|-1}(\kappa_n^{(|m|)})-J_{|m|+1}(\kappa_n^{(|m|)})\right)}{|J_{|m|}(\kappa_l^{(|m|-1)})|\cdot|J_{|m|+1}(\kappa_n^{(|m|)})|}, \tag{B.74}$$

$$\mathcal{D}_{nl}^{(m)} = -\frac{1}{L}\frac{\kappa_l^{(|m|)}\kappa_n^{(|m|-1)}}{(\kappa_n^{|m|-1})^2-(\kappa_l^{(|m|)})^2}\frac{J_{|m|-1}(\kappa_l^{(|m|)})\left(J_{|m|-2}(\kappa_n^{|m|-1})-J_{|m|}(\kappa_n^{|m|-1})\right)}{|J_{|m|+1}(\kappa_l^{(|m|)})|\cdot|J_{|m|}(\kappa_n^{(|m|-1)})|}, \quad m\le -2 \tag{B.75}$$

$$= -\frac{2}{L}\frac{\kappa_l^{(|m|)}\kappa_n^{(|m|-1)}}{(\kappa_n^{|m|-1})^2-(\kappa_l^{(|m|)})^2}\frac{J_{|m|-1}(\kappa_l^{(|m|)})\left(-J_{|m|}(\kappa_n^{|m|-1})\right)}{|J_{|m|+1}(\kappa_l^{(|m|)})|\cdot|J_{|m|}(\kappa_n^{(|m|-1)})|}, \quad m=-1 \tag{B.76}$$

The self-adjoincy can be verified by interchanging n and l in $\mathcal{C}_{nl}^{(m)}$ and $\mathcal{D}_{nl}^{(m)}$.

From the numerical calculation, we observe the symmetry of $E\to -E$ when $m\to -m-1$ and $k_z\to -k_z$, assuming $m\ge 0$ here. In the following, we analytically prove this is indeed true.

1. To get started, we observe the relation of eigen matrix elements between the two classes of $m\ge 0$ and $m\le -1$. For clarity, I assume m to be non-negative. Of note is that $\mathcal{H}_{11n}^{(-m-1)}(-k_z)=-\mathcal{L}_{33n}^{(m)}(k_z)$, $\mathcal{H}_{22n}^{(-m-1)}(-k_z)=-\mathcal{L}_{44n}^{(m)}(k_z)$, $\mathcal{H}_{33n}^{(-m-1)}(-k_z)=-\mathcal{L}_{11n}^{(m)}(k_z)$, $\mathcal{H}_{44n}^{(-m-1)}(-k_z)=-\mathcal{L}_{22n}^{(m)}(k_z)$. And more lengthy derivation gives $\mathcal{A}_{nl}^{(-m-1)}=-\mathcal{D}_{ln}^{(m)}$, $\mathcal{B}_{nl}^{(-m-1)}=-\mathcal{C}_{ln}^{(m)}$, where Eq. B.114 has been used.

2. BdG equation has particle hole symmetry, Eq. C.26, which shall be written as

$$\begin{pmatrix} u_n \\ \alpha_n \\ \beta_n \\ v_n \end{pmatrix} \leftrightarrow \begin{pmatrix} \beta_n^* \\ v_n^* \\ u_n^* \\ \alpha_n^* \end{pmatrix} \tag{B.77}$$

   in basis expansion coefficients.

With these two properties, we write Eq. B.43 as

$$-\mathcal{L}_{33n}^{(m)}\beta_n^* + iv\sum_l \mathcal{D}_{ln}^{(m)}v_l^* - \Delta\alpha_n^* = E'\beta_n^*$$

where E' denotes the new eigenenergy after the symmetry operation. We then take the conjugate of the equation to obtain

$$\Delta\alpha_n + \mathcal{L}_{33n}^{(m)}\beta_n + iv\sum_l \mathcal{D}_{nl}^{(m)}v_l = -E'\beta_n$$

which is identical to Eq. B.66 by recognizing $E' = -E$. Similarly, Eq. B.44 changes to Eq. B.67, Eq. B.45 changes to Eq. B.64, and Eq. B.46 changes to Eq. B.65.

For concreteness, we check the special case with $N_{max} = 1$, $m = 0$, $L = 1$. We have the ansatz

$$\begin{pmatrix} u(\mathbf{r}) \\ \alpha(\mathbf{r}) \\ \beta(\mathbf{r}) \\ v(\mathbf{r}) \end{pmatrix} = \frac{e^{ik_z z}}{\sqrt{2\pi}} \begin{pmatrix} \frac{u}{\sqrt{\mathcal{N}_1^{(0)}}} J_0(\kappa_1^{(0)} r) \\ \frac{\alpha}{\sqrt{\mathcal{N}_1^{(1)}}} J_1(\kappa_1^{(1)} r) e^{i\theta} \\ \frac{\beta}{\sqrt{\mathcal{N}_1^{(1)}}} J_1(\kappa_1^{(1)} r) e^{i\theta} \\ \frac{v}{\sqrt{\mathcal{N}_1^{(0)}}} J_0(\kappa_1^{(0)} r) \end{pmatrix} \equiv \frac{e^{ik_z z}}{\sqrt{2\pi}} \begin{pmatrix} \frac{1}{A} J_0(ar) u \\ \frac{e^{i\theta}}{B} J_1(br) \alpha \\ \frac{e^{i\theta}}{B} J_1(br) \beta \\ \frac{1}{A} J_0(ar) v \end{pmatrix} \tag{B.78}$$

where we have abbreviated $[u_n, \alpha_n, \beta_n, v_n]$ into $[u, \alpha, \beta, v]$, $a = \kappa_1^{(0)} \approx 2.40483$, $b = \kappa_1^{(1)} \approx 3.83171$, and

$$\mathcal{N}_1^{(0)} = \int_0^1 J_0(\kappa_1^{(0)} r) J_0(\kappa_1^{(0)} r) r dr = \frac{1}{2} \left(J_1(\kappa_1^{(0)}) \right)^2 \equiv A^2 \approx 0.134757 \tag{B.79}$$

$$\mathcal{N}_1^{(1)} = \int_0^1 J_1(\kappa_1^{(1)} r) J_1(\kappa_1^{(1)} r) r dr = \frac{1}{2} \left(J_2(\kappa_1^{(1)}) \right)^2 \equiv B^2 \approx 0.081107 \tag{B.80}$$

Then we recast the eigen equation of BdG Hamiltonian into coefficient matrix, by using the following relations

$$
\begin{aligned}
-(\frac{1}{r}\frac{\partial}{\partial r}(r\frac{\partial}{\partial r})+\frac{1}{r^2}\frac{\partial^2}{\partial\theta^2})J_0(ar) &= a^2J_0(ar) && \text{(B.81)}\\
-(\frac{1}{r}\frac{\partial}{\partial r}(r\frac{\partial}{\partial r})+\frac{1}{r^2}\frac{\partial^2}{\partial\theta^2})J_1(br) &= b^2J_1(br) && \text{(B.82)}\\
-\lambda e^{-i\theta}(i\partial_r+\frac{1}{r}\partial_\theta)\left(J_1(br)e^{i\theta}\right) &= -\lambda e^{-i\theta}\left(i\frac{b}{2}(J_0(br)-J_2(br))e^{i\theta}+\frac{i}{r}J_1(br)e^{i\theta}\right)\\
&= -i\lambda\left(\frac{J_0(br)-J_2(br)}{2}+\frac{1}{r}J_1(br)\right)\\
&= -i\lambda\left(\frac{b}{2}\left(J_0(br)-J_2(br)\right)+\frac{1}{r}J_1(br)\right)\\
&= -i\lambda\left(\frac{b}{2}\left(J_0(br)-J_2(br)\right)+\frac{b}{2}\left(J_2(br)+J_0(br)\right)\right) && \text{(B.83)}\\
&= -i\lambda bJ_0(br) && \text{(B.84)}\\
ve^{i\theta}(-i\partial_r+\frac{1}{r}\partial_\theta)J_0(ar) &= \lambda e^{i\theta}(-i(-a)J_1(ar))\\
&= i\lambda ae^{i\theta}J_1(ar) && \text{(B.85)}
\end{aligned}
$$

where in order to get Eq. B.83 we have used Eq. B.37. With these simplifications, we plug Eq. B.78 into Eq. B.43,

B.27, B.28, B.29, to arrive at

$$\left(k_z^2+\frac{q^2}{4}+k_zq+\lambda(k_z+\frac{q}{2})+h+a^2\right)\frac{1}{A}J_0(ar)u-i\lambda b\frac{1}{B}J_0(br)\alpha-\Delta\frac{1}{A}J_0(ar)v = E\frac{1}{A}J_0(ar)u \quad \text{(B.86)}$$

$$i\lambda ae^{i\theta}\frac{1}{A}J_1(ar)u+\left(k_z^2+\frac{q^2}{4}+k_zq-\lambda(k_z+\frac{q}{2})-h+b^2\right)\frac{e^{i\theta}}{B}J_1(br)\alpha+\Delta\frac{e^{i\theta}}{B}J_1(br)\beta = E\frac{e^{i\theta}}{B}J_1(br)\alpha \quad \text{(B.87)}$$

$$\Delta\frac{e^{i\theta}}{B}J_1(br)\alpha-\left(k_z^2+\frac{q^2}{4}-k_zq-v_3(k_z-\frac{q}{2})+h+b^2\right)\frac{e^{i\theta}}{B}J_1(br)\beta+i\lambda e^{i\theta}\frac{1}{A}aJ_1(ar)v = E\frac{e^{i\theta}}{B}J_1(br)\beta \quad \text{(B.88)}$$

$$-\Delta\frac{1}{A}J_0(ar)u-i\lambda b\frac{1}{B}J_0(br)\beta-\left(k_z^2+\frac{q^2}{4}-k_zq+v_3(k_z-\frac{q}{2})-h+a^2\right)\frac{1}{A}J_0(ar)v = E\frac{1}{A}J_0(ar)v \quad \text{(B.89)}$$

We multiply both sides of Eq. B.86 and B.89 by $\int_0^1 \frac{1}{A}J_0(ar)rdr$ and Eq. B.87 and B.88 by $\int_0^1 \frac{1}{B}J_1(br)rdr$, we will have

$$\left(k_z^2+\frac{q^2}{4}+k_zq+\lambda(k_z+\frac{q}{2})+h+a^2\right)u-i\lambda\frac{b}{AB}\int_0^1 rdrJ_0(ar)J_0(br)\alpha-\Delta v = Eu \quad \text{(B.90)}$$

$$i\lambda\frac{a}{AB}\int_0^1 rdrJ_1(br)J_1(ar)u+\left(k_z^2+\frac{q^2}{4}+k_zq-\lambda(k_z+\frac{q}{2})-h+b^2\right)\alpha+\Delta\beta = E\alpha \quad \text{(B.91)}$$

$$\Delta\alpha-\left(k_z^2+\frac{q^2}{4}-k_zq-v_3(k_z-\frac{q}{2})+h+b^2\right)\beta+i\lambda\frac{a}{AB}\int_0^1 rdrJ_1(br)J_1(ar)v = E\beta \quad \text{(B.92)}$$

$$-\Delta u-i\lambda\frac{b}{AB}\int_0^r rdrJ_0(ar)J_0(br)\beta-\left(k_z^2+\frac{q^2}{4}-k_zq+v_3(k_z-\frac{q}{2})-h+a^2\right)v = Ev \quad \text{(B.93)}$$

which can be further casted into

$$\begin{pmatrix}\mathcal{H}_{11} & -i\lambda\mathcal{A} & 0 & -\Delta\\ i\lambda\mathcal{B} & \mathcal{H}_{22} & \Delta & 0\\ 0 & \Delta & \mathcal{H}_{33} & i\lambda\mathcal{B}\\ -\Delta & 0 & -i\lambda\mathcal{A} & \mathcal{H}_{44}\end{pmatrix}\begin{pmatrix}u\\ \alpha\\ \beta\\ v\end{pmatrix}=E\begin{pmatrix}u\\ \alpha\\ \beta\\ v\end{pmatrix} \quad \text{(B.94)}$$

where

$$\mathcal{H}_{11} = k_z^2 + \frac{q^2}{4} + k_z q + \lambda(k_z + \frac{q}{2}) + h + a^2 \tag{B.95}$$

$$\mathcal{H}_{22} = k_z^2 + \frac{q^2}{4} + k_z q - \lambda(k_z + \frac{q}{2}) - h + b^2 \tag{B.96}$$

$$\mathcal{H}_{33} = -\left(k_z^2 + \frac{q^2}{4} - k_z q - v_3(k_z - \frac{q}{2}) + h + b^2\right) \tag{B.97}$$

$$\mathcal{H}_{44} = -\left(k_z^2 + \frac{q^2}{4} - k_z q + v_3(k_z - \frac{q}{2}) - h + a^2\right) \tag{B.98}$$

$$\mathcal{A} = \frac{b}{AB}\int_0^1 r dr J_0(ar) J_0(br) \tag{B.99}$$

$$= \frac{b}{AB}\frac{1}{a^2 - b^2}(-J_0(b)\frac{dJ_0(ar)}{dr}|_{r=1}) \tag{B.100}$$

$$= \frac{ab}{AB}\frac{1}{a^2 - b^2} J_0(b) J_1(a) \tag{B.101}$$

$$\approx 2.0709759318690697 \tag{B.102}$$

$$\mathcal{B} = \frac{a}{AB}\int_0^1 r dr J_1(br) J_1(ar) \tag{B.103}$$

$$= \frac{a}{AB}\frac{1}{b^2 - a^2}(-J_1(a)\frac{dJ_1(br)}{dr}|_{r=1}) \tag{B.104}$$

$$= \frac{ab}{AB}\frac{1}{a^2 - b^2} J_1(a)\frac{1}{2}(J_0(b) - J_2(b)) \tag{B.105}$$

$$\approx 2.0709759318690693 \tag{B.106}$$

And $\mathcal{A} = \mathcal{B}$ at least to the accuracy of 10^{-15}.

Straightforwardly, we can check other special cases, by using Eq. B.57 and Eq. B.59.

- $m = 3$, $n = 5$, $l = 2$:

$$\mathcal{A} = -0.041749239919106576 \tag{B.107}$$

$$\mathcal{B} = -0.04174923991910716 \tag{B.108}$$

- $m = 1$, $n = 2$, $l = 2$:

$$\mathcal{A} = 0.081446190044653 \tag{B.109}$$

$$\mathcal{B} = 0.08144619004465767 \tag{B.110}$$

- $m = -3$, $n = 6$, $l = 2$:

$$\mathcal{A} = -0.04536913491022942 \tag{B.111}$$

$$\mathcal{B} = -0.045369134910227024 \tag{B.112}$$

- This means in Eq. B.57 and Eq. B.59, $\mathcal{A} = \mathcal{B}$ after interchanging n and l:

$$J_m(\kappa_l^{(m+1)})J_{m-1}(\kappa_n^{(m)}) = J_{m+1}(\kappa_n^{(m)})J_{m+2}(\kappa_l^{(m+1)}), \quad m \geq 1 \tag{B.113}$$

$$J_m(\kappa_l^{(m+1)}) = -J_{m+2}(\kappa_l^{(m+1)}) \tag{B.114}$$

where $\kappa_n^{(m)}$ is the nth non-zero root of the first kind of Bessel Function $J_m(x)$.

- Eq. B.114 can be proved easily with recursion relation and the definition of $\kappa_n^{(m)}$ for $m \geq 0$. Then apply the relation to J_{m+1} and multiply both sides of the equations, then Eq. B.113 follows naturally.

Appendix C

Time-dependent BdG formalism

In this appendix, we supplement the main results presented in Chapter 4 with more mathmatical derivations. We start from the Hamiltonian with the general form of spin-orbit coupling (SOC) $H_{SOC} = v_1\sigma_x k_x + v_2\sigma_y k_y + v_3\sigma_z k_z$ and Zeeman field in z-direction, $H = H_0 + H_{int}$, where (v_i are real constants, $i = 1, 2, 3$)

$$H_0 = \int d\mathbf{x} \begin{bmatrix} \psi_\uparrow^\dagger(\mathbf{x}) & \psi_\downarrow^\dagger(\mathbf{x}) \end{bmatrix} \begin{bmatrix} \xi_\mathbf{k} + v_3 k_z + h & v_1 k_x - i v_2 k_y \\ v_1 k_x + i v_2 k_y & \xi_k - v_3 k_z - h \end{bmatrix} \begin{bmatrix} \psi_\uparrow(\mathbf{x}) \\ \psi_\downarrow(\mathbf{x}) \end{bmatrix} \tag{C.1}$$

$$H_{int} = U_0 \int d\mathbf{x} \psi_\uparrow^\dagger(\mathbf{x}) \psi_\downarrow^\dagger(\mathbf{x}) \psi_\downarrow(\mathbf{x}) \psi_\uparrow(\mathbf{x}) \tag{C.2}$$

And we write Heisenberg equation of motion (EOM) as, ($\hbar = 1$) (remember that $[A, BC] = \{A, B\}C - B\{A, C\}$ for Fermions while $[A, BC] = [A, B]C + B[A, C]$ for Bosons)

$$\begin{aligned} i\frac{\partial}{\partial t}\psi_\uparrow(\mathbf{x}) &= (\xi_\mathbf{k} + v_3 k_z + h)\psi_\uparrow(\mathbf{x}) + (v_1 k_x - iv_2 k_y)\psi_\downarrow(\mathbf{x}) + U_0\psi_\downarrow^\dagger(\mathbf{x})\psi_\downarrow(\mathbf{x})\psi_\uparrow(\mathbf{x}) \\ &\approx (\xi_\mathbf{k} + v_3 k_z + h)\psi_\uparrow(\mathbf{x}) + (v_1 k_x - iv_2 k_y)\psi_\downarrow(\mathbf{x}) - \Delta(\mathbf{x})\psi_\downarrow^\dagger(\mathbf{x}) \qquad \text{(C.3)} \\ i\frac{\partial}{\partial t}\psi_\downarrow(\mathbf{x}) &= (\xi_\mathbf{k} - v_3 k_z - h)\psi_\downarrow(\mathbf{x}) + (v_1 k_x + iv_2 k_y)\psi_\uparrow(\mathbf{x}) - U_0\psi_\uparrow^\dagger(\mathbf{x})\psi_\downarrow(\mathbf{x})\psi_\uparrow(\mathbf{x}) \\ &\approx (\xi_\mathbf{k} - v_3 k_z - h)\psi_\downarrow(\mathbf{x}) + (v_1 k_x + iv_2 k_y)\psi_\uparrow(\mathbf{x}) + \Delta(\mathbf{x})\psi_\uparrow^\dagger(\mathbf{x}) \qquad \text{(C.4)} \end{aligned}$$

where approximation comes from mean-field approximation by defining order parameter $\Delta(\mathbf{x}) = -U_0\langle\psi_\downarrow\psi_\uparrow\rangle$. We solve the EOM in terms of Bogoliubov transformation,

$$\psi_\sigma(\mathbf{x}) = \frac{1}{V}\sum_\mathbf{k}\left[u_{\mathbf{k}\sigma}(\mathbf{x}, t)c_{\mathbf{k}\sigma} + v^*_{\mathbf{k}\bar{\sigma}}(\mathbf{x}, t)c^\dagger_{\mathbf{k}\bar{\sigma}} + \alpha_{\mathbf{k}\bar{\sigma}}(\mathbf{x}, t)c_{\mathbf{k}\bar{\sigma}} + \beta^*_{\mathbf{k}\sigma}(\mathbf{x}, t)c^\dagger_{\mathbf{k}\sigma}\right] \qquad \text{(C.5)}$$

where $\sigma = \uparrow, \downarrow$ and correspondingly $\bar{\sigma} = \downarrow, \uparrow$,

$$u_{\mathbf{k}\sigma}(\mathbf{x}, t) = u_{\mathbf{k}\sigma}(\mathbf{x})e^{-iE_{\mathbf{k}\sigma}t}, v_{\mathbf{k}\sigma}(\mathbf{x}, t) = v_{\mathbf{k}\sigma}(\mathbf{x})e^{-iE_{\mathbf{k}\sigma}t}, \alpha_{\mathbf{k}\sigma}(\mathbf{x}, t) = \alpha_{\mathbf{k}\sigma}(\mathbf{x})e^{-iE_{\mathbf{k}\sigma}t}, \beta_{\mathbf{k}\sigma}(\mathbf{x}, t) = \beta_{\mathbf{k}\sigma}(\mathbf{x})e^{-iE_{\mathbf{k}\sigma}t}$$

$$u^*_{\mathbf{k}\sigma}(\mathbf{x}, t) = u^*_{\mathbf{k}\sigma}(\mathbf{x})e^{+iE_{\mathbf{k}\sigma}t}, v^*_{\mathbf{k}\sigma}(\mathbf{x}, t) = v^*_{\mathbf{k}\sigma}(\mathbf{x})e^{+iE_{\mathbf{k}\sigma}t}, \alpha^*_{\mathbf{k}\sigma}(\mathbf{x}, t) = \alpha^*_{\mathbf{k}\sigma}(\mathbf{x})e^{+iE_{\mathbf{k}\sigma}t}, \beta^*_{\mathbf{k}\sigma}(\mathbf{x}, t) = \beta^*_{\mathbf{k}\sigma}(\mathbf{x})e^{+iE_{\mathbf{k}\sigma}t}$$

Denote

$$\begin{aligned} h_0^+ &= \xi_{\mathbf{k}} + v_3 k_z + h \\ h_0^- &= \xi_{\mathbf{k}} - v_3 k_z - h \\ \Lambda &= v_1 k_x - i v_2 k_y \end{aligned}$$

Then from Eq. C.3, we have

$$\begin{aligned} & i \sum_{\mathbf{k}} \left[\dot{u}_{\mathbf{k}\uparrow}(\mathbf{x}) c_{\mathbf{k}\uparrow} + \dot{v}^*_{\mathbf{k}\downarrow}(\mathbf{x}) c^\dagger_{\mathbf{k}\downarrow} + \dot{\alpha}_{\mathbf{k}\downarrow}(\mathbf{x}) c_{\mathbf{k}\downarrow} + \dot{\beta}^*_{\mathbf{k}\uparrow}(\mathbf{x}) c^\dagger_{\mathbf{k}\uparrow} \right] \\ = & \sum_{\mathbf{k}} \left[h_0^+ u_{\mathbf{k}\uparrow}(\mathbf{x}) c_{\mathbf{k}\uparrow} + h_0^+ v^*_{\mathbf{k}\downarrow}(\mathbf{x}) c^\dagger_{\mathbf{k}\downarrow} + h_0^+ \alpha_{\mathbf{k}\downarrow}(\mathbf{x}) c_{\mathbf{k}\downarrow} + h_0^+ \beta^*_{\mathbf{k}\uparrow}(\mathbf{x}) c^\dagger_{\mathbf{k}\uparrow} \right] \\ + & \sum_{\mathbf{k}} \left[\Lambda u_{\mathbf{k}\downarrow}(\mathbf{x}) c_{\mathbf{k}\downarrow} + \Lambda v^*_{\mathbf{k}\uparrow}(\mathbf{x}) c^\dagger_{\mathbf{k}\uparrow} + \Lambda \alpha_{\mathbf{k}\uparrow}(\mathbf{x}) c_{\mathbf{k}\uparrow} + \Lambda \beta^*_{\mathbf{k}\downarrow}(\mathbf{x}) c^\dagger_{\mathbf{k}\downarrow} \right] \\ + & \sum_{\mathbf{k}} \left[-\Delta u^*_{\mathbf{k}\downarrow}(\mathbf{x}) c^\dagger_{\mathbf{k}\downarrow} - \Delta v_{\mathbf{k}\uparrow}(\mathbf{x}) c_{\mathbf{k}\uparrow} - \Delta \alpha^*_{\mathbf{k}\uparrow}(\mathbf{x}) c^\dagger_{\mathbf{k}\uparrow} - \Delta \beta_{\mathbf{k}\downarrow}(\mathbf{x}) c_{\mathbf{k}\downarrow} \right] \end{aligned} \tag{C.6}$$

$$\begin{aligned} & i \sum_{\mathbf{k}} \left[\dot{u}_{\mathbf{k}\downarrow}(\mathbf{x}) c_{\mathbf{k}\downarrow} + \dot{v}^*_{\mathbf{k}\uparrow}(\mathbf{x}) c^\dagger_{\mathbf{k}\uparrow} + \dot{\alpha}_{\mathbf{k}\uparrow}(\mathbf{x}) c_{\mathbf{k}\uparrow} + \dot{\beta}^*_{\mathbf{k}\downarrow}(\mathbf{x}) c^\dagger_{\mathbf{k}\downarrow} \right] \\ = & \sum_{\mathbf{k}} \left[h_0^- u_{\mathbf{k}\downarrow}(\mathbf{x}) c_{\mathbf{k}\downarrow} + h_0^- v^*_{\mathbf{k}\uparrow}(\mathbf{x}) c^\dagger_{\mathbf{k}\uparrow} + h_0^- \alpha_{\mathbf{k}\uparrow}(\mathbf{x}) c_{\mathbf{k}\uparrow} + h_0^- \beta^*_{\mathbf{k}\downarrow}(\mathbf{x}) c^\dagger_{\mathbf{k}\downarrow} \right] \\ + & \sum_{\mathbf{k}} \left[\Lambda^\dagger u_{\mathbf{k}\uparrow}(\mathbf{x}) c_{\mathbf{k}\uparrow} + \Lambda^\dagger v^*_{\mathbf{k}\downarrow}(\mathbf{x}) c^\dagger_{\mathbf{k}\downarrow} + \Lambda^\dagger \alpha_{\mathbf{k}\downarrow}(\mathbf{x}) c_{\mathbf{k}\downarrow} + \Lambda^\dagger \beta^*_{\mathbf{k}\uparrow}(\mathbf{x}) c^\dagger_{\mathbf{k}\uparrow} \right] \\ + & \sum_{\mathbf{k}} \left[\Delta u^*_{\mathbf{k}\uparrow}(\mathbf{x}) c^\dagger_{\mathbf{k}\uparrow} + \Delta v_{\mathbf{k}\downarrow}(\mathbf{x}) c_{\mathbf{k}\downarrow} + \Delta \alpha^*_{\mathbf{k}\downarrow}(\mathbf{x}) c^\dagger_{\mathbf{k}\downarrow} + \Delta \beta_{\mathbf{k}\uparrow}(\mathbf{x}) c_{\mathbf{k}\uparrow} \right] \end{aligned} \tag{C.7}$$

From Eq. C.6, we have

$$
\begin{aligned}
i\dot{u}_{\mathbf{k}\uparrow}(\mathbf{x}) &= h_0^+ u_{\mathbf{k}\uparrow}(\mathbf{x}) + \Lambda\alpha_{\mathbf{k}\uparrow}(\mathbf{x}) - \Delta v_{\mathbf{k}\uparrow}(\mathbf{x}) \\
i\dot{v}^*_{\mathbf{k}\downarrow}(\mathbf{x}) &= h_0^+ v^*_{\mathbf{k}\downarrow}(\mathbf{x}) + \Lambda\beta^*_{\mathbf{k}\downarrow}(\mathbf{x}) - \Delta u^*_{\mathbf{k}\downarrow}(\mathbf{x}) \Rightarrow -i\dot{v}_{\mathbf{k}\downarrow}(\mathbf{x}) = (h_0^+)^* v_{\mathbf{k}\downarrow}(\mathbf{x}) + \Lambda^*\beta_{\mathbf{k}\downarrow}(\mathbf{x}) - \Delta^* u_{\mathbf{k}\downarrow}(\mathbf{x}) \\
i\dot{\alpha}_{\mathbf{k}\downarrow}(\mathbf{x}) &= h_0^+ \alpha_{\mathbf{k}\downarrow}(\mathbf{x}) + \Lambda u_{\mathbf{k}\downarrow}(\mathbf{x}) - \Delta\beta_{\mathbf{k}\downarrow}(\mathbf{x}) \\
i\dot{\beta}^*_{\mathbf{k}\uparrow}(\mathbf{x}) &= h_0^+ \beta^*_{\mathbf{k}\uparrow}(\mathbf{x}) + \Lambda v^*_{\mathbf{k}\uparrow}(\mathbf{x}) - \Delta\alpha^*_{\mathbf{k}\uparrow}(\mathbf{x}) \Rightarrow -i\dot{\beta}_{\mathbf{k}\uparrow}(\mathbf{x}) = (h_0^+)^* \beta_{\mathbf{k}\uparrow}(\mathbf{x}) + \Lambda^* v_{\mathbf{k}\uparrow}(\mathbf{x}) - \Delta^*\alpha_{\mathbf{k}\uparrow}(\mathbf{x}) \\
i\dot{u}_{\mathbf{k}\downarrow}(\mathbf{x}) &= h_0^- u_{\mathbf{k}\downarrow}(\mathbf{x}) + \Lambda^\dagger\alpha_{\mathbf{k}\downarrow}(\mathbf{x}) + \Delta v_{\mathbf{k}\downarrow}(\mathbf{x}) \\
i\dot{v}^*_{\mathbf{k}\uparrow}(\mathbf{x}) &= h_0^- v^*_{\mathbf{k}\uparrow}(\mathbf{x}) + \Lambda^\dagger\beta^*_{\mathbf{k}\uparrow}(\mathbf{x}) + \Delta u^*_{\mathbf{k}\uparrow}(\mathbf{x}) \Rightarrow -i\dot{v}_{\mathbf{k}\uparrow}(\mathbf{x}) = (h_0^-)^* v_{\mathbf{k}\uparrow}(\mathbf{x}) + (\Lambda^\dagger)^*\beta_{\mathbf{k}\uparrow}(\mathbf{x}) + \Delta^* u_{\mathbf{k}\uparrow}(\mathbf{x}) \\
i\dot{\alpha}_{\mathbf{k}\uparrow}(\mathbf{x}) &= h_0^- \alpha_{\mathbf{k}\uparrow}(\mathbf{x}) + \Lambda^\dagger u_{\mathbf{k}\uparrow}(\mathbf{x}) + \Delta\beta_{\mathbf{k}\uparrow}(\mathbf{x}) \\
i\dot{\beta}^*_{\mathbf{k}\downarrow}(\mathbf{x}) &= h_0^- \beta^*_{\mathbf{k}\downarrow}(\mathbf{x}) + \Lambda^\dagger v^*_{\mathbf{k}\downarrow}(\mathbf{x}) + \Delta\alpha^*_{\mathbf{k}\downarrow}(\mathbf{x}) \Rightarrow -i\dot{\beta}_{\mathbf{k}\downarrow}(\mathbf{x}) = (h_0^-)^* \beta_{\mathbf{k}\downarrow}(\mathbf{x}) + (\Lambda^\dagger)^* v_{\mathbf{k}\downarrow}(\mathbf{x}) + \Delta^*\alpha_{\mathbf{k}\downarrow}(\mathbf{x})
\end{aligned}
$$

where we have used $\Lambda^\dagger = v_1 k_x + i v_2 k_y$, $\Lambda^* = -(v_1 k_x + i v_2 k_y)$, $(\Lambda^\dagger)^* = -v_1 k_x + i v_2 k_y$ (note: $k = i\hbar\partial/\partial x$, $k^\dagger = k$, $k^* = -k$, so $k^\dagger = -k^*$).

Written in matrix form,

$$i\frac{\partial}{\partial t}\begin{pmatrix} u_{\mathbf{k}\uparrow}(\mathbf{x}) \\ \alpha_{\mathbf{k}\uparrow}(\mathbf{x}) \\ \beta_{\mathbf{k}\uparrow}(\mathbf{x}) \\ v_{\mathbf{k}\uparrow}(\mathbf{x}) \end{pmatrix} = \begin{pmatrix} h_0^+ & \Lambda & 0 & -\Delta \\ \Lambda^\dagger & h_0^- & \Delta & 0 \\ 0 & \Delta^* & -(h_0^+)^* & -\Lambda^* \\ -\Delta^* & 0 & -(\Lambda^\dagger)^* & -(h_0^-)^* \end{pmatrix} \begin{pmatrix} u_{\mathbf{k}\uparrow}(\mathbf{x}) \\ \alpha_{\mathbf{k}\uparrow}(\mathbf{x}) \\ \beta_{\mathbf{k}\uparrow}(\mathbf{x}) \\ v_{\mathbf{k}\uparrow}(\mathbf{x}) \end{pmatrix} \tag{C.8}$$

$$= \begin{pmatrix} \xi_{\mathbf{k}} + v_3 k_z + h & v_1 k_x - i v_2 k_y & 0 & -\Delta \\ v_1 k_x + i v_2 k_y & \xi_{\mathbf{k}} - v_3 k_z - h & \Delta & 0 \\ 0 & \Delta^* & -(\xi_{\mathbf{k}} - v_3 k_z + h) & v_1 k_x + i v_2 k_y \\ -\Delta^* & 0 & v_1 k_x - i v_2 k_y & -(\xi_{\mathbf{k}} + v_3 k_z - h) \end{pmatrix} \begin{pmatrix} u_{\mathbf{k}\uparrow}(\mathbf{x}) \\ \alpha_{\mathbf{k}\uparrow}(\mathbf{x}) \\ \beta_{\mathbf{k}\uparrow}(\mathbf{x}) \\ v_{\mathbf{k}\uparrow}(\mathbf{x}) \end{pmatrix} \tag{C.9}$$

$$i\frac{\partial}{\partial t}\begin{pmatrix} \alpha_{\mathbf{k}\downarrow}(\mathbf{x}) \\ u_{\mathbf{k}\downarrow}(\mathbf{x}) \\ v_{\mathbf{k}\downarrow}(\mathbf{x}) \\ \beta_{\mathbf{k}\downarrow}(\mathbf{x}) \end{pmatrix} = \begin{pmatrix} h_0^+ & \Lambda & 0 & -\Delta \\ \Lambda^\dagger & h_0^- & \Delta & 0 \\ 0 & \Delta^* & -(h_0^+)^* & -\Lambda^* \\ -\Delta^* & 0 & -(\Lambda^\dagger)^* & -(h_0^-)^* \end{pmatrix} \begin{pmatrix} \alpha_{\mathbf{k}\downarrow}(\mathbf{x}) \\ u_{\mathbf{k}\downarrow}(\mathbf{x}) \\ v_{\mathbf{k}\downarrow}(\mathbf{x}) \\ \beta_{\mathbf{k}\downarrow}(\mathbf{x}) \end{pmatrix} \tag{C.10}$$

$$= \begin{pmatrix} \xi_{\mathbf{k}} + v_3 k_z + h & v_1 k_x - i v_2 k_y & 0 & -\Delta \\ v_1 k_x + i v_2 k_y & \xi_{\mathbf{k}} - v_3 k_z - h & \Delta & 0 \\ 0 & \Delta^* & -(\xi_{\mathbf{k}} - v_3 k_z + h) & v_1 k_x + i v_2 k_y \\ -\Delta^* & 0 & v_1 k_x - i v_2 k_y & -(\xi_{\mathbf{k}} + v_3 k_z - h) \end{pmatrix} \begin{pmatrix} \alpha_{\mathbf{k}\downarrow}(\mathbf{x}) \\ u_{\mathbf{k}\downarrow}(\mathbf{x}) \\ v_{\mathbf{k}\downarrow}(\mathbf{x}) \\ \beta_{\mathbf{k}\downarrow}(\mathbf{x}) \end{pmatrix} \tag{C.11}$$

And normalization is given by $\int d\mathbf{x}\,[|u_{\mathbf{k}\sigma}(\mathbf{x})|^2 + |\alpha_{\mathbf{k}\sigma}(\mathbf{x})|^2 + |\beta_{\mathbf{k}\sigma}(\mathbf{x})|^2 + |v_{\mathbf{k}\sigma}(\mathbf{x})|^2] = 1$.

$$
\begin{aligned}
\Delta(\mathbf{x}) &= -U_0\langle\psi_\downarrow(\mathbf{x})\psi_\uparrow(\mathbf{x})\rangle \\
&= -U_0\frac{1}{V}\sum_{\mathbf{k}}\Big[u_{\mathbf{k}\downarrow}(\mathbf{x})v^*_{\mathbf{k}\downarrow}(\mathbf{x})\langle c_{\mathbf{k}\downarrow}c^\dagger_{\mathbf{k}\downarrow}\rangle + u_{\mathbf{k}\uparrow}(\mathbf{x})v^*_{\mathbf{k}\uparrow}(\mathbf{x})\langle c^\dagger_{\mathbf{k}\uparrow}c_{\mathbf{k}\uparrow}\rangle + \alpha_{\mathbf{k}\uparrow}(\mathbf{x})\beta^*_{\mathbf{k}\uparrow}(\mathbf{x})\langle c_{\mathbf{k}\uparrow}c^\dagger_{\mathbf{k}\uparrow}\rangle + \alpha_{\mathbf{k}\downarrow}(\mathbf{x})\beta^*_{\mathbf{k}\downarrow}(\mathbf{x})\langle c^\dagger_{\mathbf{k}\downarrow}c_{\mathbf{k}\downarrow}\rangle\Big] \\
&= -U_0\frac{1}{V}{\sum_{\mathbf{k}}}'\left[u_{\mathbf{k}\downarrow}(\mathbf{x})v^*_{\mathbf{k}\downarrow}(\mathbf{x})f(-E_{\mathbf{k}\downarrow}) + u_{\mathbf{k}\uparrow}(\mathbf{x})v^*_{\mathbf{k}\uparrow}(\mathbf{x})f(E_{\mathbf{k}\uparrow}) + \alpha_{\mathbf{k}\uparrow}(\mathbf{x})\beta^*_{\mathbf{k}\uparrow}(\mathbf{x})f(-E_{\mathbf{k}\uparrow}) + \alpha_{\mathbf{k}\downarrow}(\mathbf{x})\beta^*_{\mathbf{k}\downarrow}(\mathbf{x})f(E_{\mathbf{k}\downarrow})\right] \\
n_\uparrow(\mathbf{x}) &= \langle\psi^\dagger_\uparrow(\mathbf{x})\psi_\uparrow(\mathbf{x})\rangle \\
&= \frac{1}{V}\sum_{\mathbf{k}}\Big[|u_{\mathbf{k}\uparrow}(\mathbf{x})|^2\langle c^\dagger_{\mathbf{k}\uparrow}c_{\mathbf{k}\uparrow}\rangle + |v_{\mathbf{k}\downarrow}(\mathbf{x})|^2\langle c_{\mathbf{k}\downarrow}c^\dagger_{\mathbf{k}\downarrow}\rangle + |\alpha_{\mathbf{k}\downarrow}(\mathbf{x})|^2\langle c^\dagger_{\mathbf{k}\downarrow}c_{\mathbf{k}\downarrow}\rangle + |\beta_{\mathbf{k}\uparrow}(\mathbf{x})|^2\langle c^\dagger_{\mathbf{k}\uparrow}c_{\mathbf{k}\uparrow}\rangle\Big] \\
&= \frac{1}{V}{\sum_{\mathbf{k}}}'\left[|u_{\mathbf{k}\uparrow}(\mathbf{x})|^2 f(E_{\mathbf{k}\uparrow}) + |v_{\mathbf{k}\downarrow}(\mathbf{x})|^2 f(-E_{\mathbf{k}\downarrow}) + |\alpha_{\mathbf{k}\downarrow}(\mathbf{x})|^2 f(E_{\mathbf{k}\downarrow}) + |\beta_{\mathbf{k}\uparrow}(\mathbf{x})|^2 f(-E_{\mathbf{k}\uparrow})\right] \\
n_\downarrow(\mathbf{x}) &= \langle\psi^\dagger_\downarrow(\mathbf{x})\psi_\downarrow(\mathbf{x})\rangle \\
&= \frac{1}{V}\sum_{\mathbf{k}}\Big[|u_{\mathbf{k}\downarrow}(\mathbf{x})|^2\langle c^\dagger_{\mathbf{k}\downarrow}c_{\mathbf{k}\downarrow}\rangle + |v_{\mathbf{k}\uparrow}(\mathbf{x})|^2\langle c_{\mathbf{k}\uparrow}c^\dagger_{\mathbf{k}\uparrow}\rangle + |\alpha_{\mathbf{k}\uparrow}(\mathbf{x})|^2\langle c^\dagger_{\mathbf{k}\uparrow}c_{\mathbf{k}\uparrow}\rangle + |\beta_{\mathbf{k}\downarrow}(\mathbf{x})|^2\langle c^\dagger_{\mathbf{k}\downarrow}c_{\mathbf{k}\downarrow}\rangle\Big] \\
&= \frac{1}{V}{\sum_{\mathbf{k}}}'\left[|u_{\mathbf{k}\downarrow}(\mathbf{x})|^2 f(E_{\mathbf{k}\downarrow}) + |v_{\mathbf{k}\uparrow}(\mathbf{x})|^2 f(-E_{\mathbf{k}\uparrow}) + |\alpha_{\mathbf{k}\uparrow}(\mathbf{x})|^2 f(E_{\mathbf{k}\uparrow}) + |\beta_{\mathbf{k}\downarrow}(\mathbf{x})|^2 f(-E_{\mathbf{k}\downarrow})\right]
\end{aligned}
$$

This involves the full solution of $u_{\mathbf{k}\sigma}(\mathbf{x})$, $v_{\mathbf{k}\sigma}(\mathbf{x})$, $\alpha_{\mathbf{k}\sigma}(\mathbf{x})$, $\beta_{\mathbf{k}\sigma}(\mathbf{x})$, and $\frac{1}{V}{\sum_{\mathbf{k}}}'$ summation only involves $\mathbf{k} > 0$ (which is understood as requiring $k_x, k_y, k_z > 0$ simultaneously). However, the construction of BdG formalism is redundant, and

we can reduce half of computation by recognizing the one-to-one correspondence,

$$
\begin{array}{ccc}
E_{\mathbf{k}\uparrow} & \leftrightarrow & E_{\mathbf{k}\downarrow} \\
\begin{pmatrix} u_{\mathbf{k}\uparrow}(\mathbf{x}) \\ \alpha_{\mathbf{k}\uparrow}(\mathbf{x}) \\ \beta_{\mathbf{k}\uparrow}(\mathbf{x}) \\ v_{\mathbf{k}\uparrow}(\mathbf{x}) \end{pmatrix} & \leftrightarrow & \begin{pmatrix} \alpha_{\mathbf{k}\downarrow}(\mathbf{x}) \\ u_{\mathbf{k}\downarrow}(\mathbf{x}) \\ v_{\mathbf{k}\downarrow}(\mathbf{x}) \\ \beta_{\mathbf{k}\downarrow}(\mathbf{x}) \end{pmatrix}
\end{array}
$$

Therefore, we only need to solve the spin-up part, and remove the spin index, by denoting $u_{\mathbf{k}\uparrow}(\mathbf{x}) \equiv u_{\mathbf{k}}(\mathbf{x})$, $v_{\mathbf{k}\uparrow}(\mathbf{x}) \equiv v_{\mathbf{k}}(\mathbf{x})$, $\alpha_{\mathbf{k}\uparrow}(\mathbf{x}) \equiv \alpha_{\mathbf{k}}(\mathbf{x})$, $\beta_{\mathbf{k}\uparrow}(\mathbf{x}) \equiv \beta_{\mathbf{k}}(\mathbf{x})$, and $E_{\mathbf{k}\uparrow} \equiv E_{\mathbf{k}}$. Eq. C.9 becomes,

$$
i\frac{\partial}{\partial t}\begin{pmatrix} u_{\mathbf{k}}(\mathbf{x},t) \\ \alpha_{\mathbf{k}}(\mathbf{x},t) \\ \beta_{\mathbf{k}}(\mathbf{x},t) \\ v_{\mathbf{k}}(\mathbf{x},t) \end{pmatrix} = \begin{pmatrix} \xi_{\mathbf{k}} + v_3 k_z + h & v_1 k_x - i v_2 k_y & 0 & -\Delta(\mathbf{x}) \\ v_1 k_x + i v_2 k_y & \xi_{\mathbf{k}} - v_3 k_z - h & \Delta(\mathbf{x}) & 0 \\ 0 & \Delta^*(\mathbf{x}) & -(\xi_{\mathbf{k}} - v_3 k_z + h) & v_1 k_x + i v_2 k_y \\ -\Delta^*(\mathbf{x}) & 0 & v_1 k_x - i v_2 k_y & -(\xi_{\mathbf{k}} + v_3 k_z - h) \end{pmatrix} \begin{pmatrix} u_{\mathbf{k}}(\mathbf{x},t) \\ \alpha_{\mathbf{k}}(\mathbf{x},t) \\ \beta_{\mathbf{k}}(\mathbf{x},t) \\ v_{\mathbf{k}}(\mathbf{x},t) \end{pmatrix} \tag{C.12}
$$

which is

$$
E_{\mathbf{k}}\begin{pmatrix} u_{\mathbf{k}}(\mathbf{x}) \\ \alpha_{\mathbf{k}}(\mathbf{x}) \\ \beta_{\mathbf{k}}(\mathbf{x}) \\ v_{\mathbf{k}}(\mathbf{x}) \end{pmatrix} = \begin{pmatrix} \xi_{\mathbf{k}} + v_3 k_z + h & v_1 k_x - i v_2 k_y & 0 & -\Delta(\mathbf{x}) \\ v_1 k_x + i v_2 k_y & \xi_{\mathbf{k}} - v_3 k_z - h & \Delta(\mathbf{x}) & 0 \\ 0 & \Delta^*(\mathbf{x}) & -(\xi_{\mathbf{k}} - v_3 k_z + h) & v_1 k_x + i v_2 k_y \\ -\Delta^*(\mathbf{x}) & 0 & v_1 k_x - i v_2 k_y & -(\xi_{\mathbf{k}} + v_3 k_z - h) \end{pmatrix} \begin{pmatrix} u_{\mathbf{k}}(\mathbf{x}) \\ \alpha_{\mathbf{k}}(\mathbf{x}) \\ \beta_{\mathbf{k}}(\mathbf{x}) \\ v_{\mathbf{k}}(\mathbf{x}) \end{pmatrix} \tag{C.13}
$$

where spin-down part of contribution should be written out for the sake of self-consistency,

$$\begin{aligned}
\Delta(\mathbf{x}) &= -U_0 \frac{1}{V} \sum_{\mathbf{k}}{}' \left[u_{\mathbf{k}\uparrow}(\mathbf{x}) v^*_{\mathbf{k}\uparrow}(\mathbf{x}) f(E_{\mathbf{k}\uparrow}) + \alpha_{\mathbf{k}\uparrow}(\mathbf{x}) \beta^*_{\mathbf{k}\uparrow}(\mathbf{x}) f(-E_{\mathbf{k}\uparrow}) \right] \\
&\equiv -U_0 \frac{1}{V} \sum_{\mathbf{k}}{}' \left[u_{\mathbf{k}}(\mathbf{x}) v^*_{\mathbf{k}}(\mathbf{x}) f(E_{\mathbf{k}}) + \alpha_{\mathbf{k}}(\mathbf{x}) \beta^*_{\mathbf{k}}(\mathbf{x}) f(-E_{\mathbf{k}}) \right] \qquad \text{(C.14)} \\
n_\uparrow(\mathbf{x}) &= \frac{1}{V} \sum_{\mathbf{k}}{}' \left[|u_{\mathbf{k}\uparrow}(\mathbf{x})|^2 f(E_{\mathbf{k}\uparrow}) + |\beta_{\mathbf{k}\uparrow}(\mathbf{x})|^2 f(-E_{\mathbf{k}\uparrow}) \right] \\
&\equiv \frac{1}{V} \sum_{\mathbf{k}}{}' \left[|u_{\mathbf{k}}(\mathbf{x})|^2 f(E_{\mathbf{k}}) + |\beta_{\mathbf{k}}(\mathbf{x})|^2 f(-E_{\mathbf{k}}) \right] \qquad \text{(C.15)} \\
n_\downarrow(\mathbf{x}) &= \frac{1}{V} \sum_{\mathbf{k}}{}' \left[|v_{\mathbf{k}\uparrow}(\mathbf{x})|^2 f(-E_{\mathbf{k}\uparrow}) + |\alpha_{\mathbf{k}\uparrow}(\mathbf{x})|^2 f(E_{\mathbf{k}\uparrow}) \right] \\
&= \frac{1}{V} \sum_{\mathbf{k}}{}' \left[|v_{\mathbf{k}}(\mathbf{x})|^2 f(-E_{\mathbf{k}}) + |\alpha_{\mathbf{k}}(\mathbf{x})|^2 f(E_{\mathbf{k}}) \right] \qquad \text{(C.16)}
\end{aligned}$$

Denote

$$\begin{aligned}
m_{11}(\mathbf{k}) &= \xi_{\mathbf{k}} + v_3 k_z + h \\
m_{22}(\mathbf{k}) &= \xi_{\mathbf{k}} - v_3 k_z - h \\
m_{33}(\mathbf{k}) &= -\xi_{\mathbf{k}} + v_3 k_z - h \\
m_{44}(\mathbf{k}) &= -\xi_{\mathbf{k}} - v_3 k_z + h
\end{aligned}$$

For the homogeneous system we study here, we use plane-wave as the basis and wavefunctions take the following

form,

$$\begin{pmatrix} u_{\mathbf{k}}(\mathbf{x}) \\ \alpha_{\mathbf{k}}(\mathbf{x}) \\ \beta_{\mathbf{k}}(\mathbf{x}) \\ v_{\mathbf{k}}(\mathbf{x}) \end{pmatrix} = \begin{pmatrix} u_{\mathbf{k}} e^{+iqz/2} \\ \alpha_{\mathbf{k}} e^{+iqz/2} \\ \beta_{\mathbf{k}} e^{-iqz/2} \\ v_{\mathbf{k}} e^{-iqz/2} \end{pmatrix} e^{i\mathbf{k}\cdot\mathbf{x}} \tag{C.17}$$

Don't forget the momentum operator is yet to be operated upon plane-wave states. For instance,

$$\begin{aligned} E_{\mathbf{k}} u_{\mathbf{k}} e^{i(\mathbf{k}+\frac{q}{2}\mathbf{e}_z)\cdot x} &= m_{11}(\hat{\mathbf{k}}) u_{\mathbf{k}} e^{i(\mathbf{k}+\frac{q}{2}\mathbf{e}_z)\cdot x} + \Lambda(\hat{\mathbf{k}}) \alpha_{\mathbf{k}} e^{i(\mathbf{k}+\frac{q}{2}\mathbf{e}_z)\cdot x} - \Delta(\mathbf{x}) v_{\mathbf{k}} e^{i(\mathbf{k}-\frac{q}{2}\mathbf{e}_z)\cdot x} \\ &= m_{11}(\mathbf{k}+\frac{q}{2}\mathbf{e}_z) u_{\mathbf{k}} e^{i(\mathbf{k}+\frac{q}{2}\mathbf{e}_z)\cdot x} + (v_1 k_x - i v_2 k_y) \alpha_{\mathbf{k}} e^{i(\mathbf{k}+\frac{q}{2}\mathbf{e}_z)\cdot x} - \Delta(\mathbf{x}) v_{\mathbf{k}} e^{i(\mathbf{k}-\frac{q}{2}\mathbf{e}_z)\cdot x} \\ &\Downarrow \\ E_{\mathbf{k}} u_{\mathbf{k}} &= m_{11}(\mathbf{k}+\frac{q}{2}\mathbf{e}_z) u_{\mathbf{k}} + (v_1 k_x - i v_2 k_y) \alpha_{\mathbf{k}} - \Delta(\mathbf{x}) e^{-iqz} v_{\mathbf{k}} \end{aligned} \tag{C.18}$$

And similarly, we have other three terms,

$$E_{\mathbf{k}} \alpha_{\mathbf{k}} = (v_1 k_x + i v_2 k_y) u_{\mathbf{k}} + m_{22}(\mathbf{k}+\frac{q}{2}\mathbf{e}_z) \alpha_{\mathbf{k}} + \Delta(\mathbf{x}) e^{-iqz} \beta_{\mathbf{k}} \tag{C.19}$$

$$E_{\mathbf{k}} \beta_{\mathbf{k}} = \Delta^*(\mathbf{x}) e^{+iqz} \alpha_{\mathbf{k}} + m_{33}(\mathbf{k}-\frac{q}{2}\mathbf{e}_z) \beta_{\mathbf{k}} + (v_1 k_x + i v_2 k_y) v_{\mathbf{k}} \tag{C.20}$$

$$E_{\mathbf{k}} v_{\mathbf{k}} = -\Delta^*(\mathbf{x}) u_{\mathbf{k}} e^{+iqz} + (v_1 k_x - i v_2 k_y) \beta_{\mathbf{k}} + m_{44}(\mathbf{k}-\frac{q}{2}\mathbf{e}_z) v_{\mathbf{k}} \tag{C.21}$$

Putting everything together, we further have

$$\mathcal{M}\begin{pmatrix} u_{\mathbf{k}} \\ \alpha_{\mathbf{k}} \\ \beta_{\mathbf{k}} \\ v_{\mathbf{k}} \end{pmatrix} = E_{\mathbf{k}}\begin{pmatrix} u_{\mathbf{k}} \\ \alpha_{\mathbf{k}} \\ \beta_{\mathbf{k}} \\ v_{\mathbf{k}} \end{pmatrix} \tag{C.22}$$

where

$$\mathcal{M} = \begin{pmatrix} \xi_{\mathbf{k}+\frac{q}{2}\mathbf{e}_z} + v_3(k_z+\frac{q}{2}) + h & v_1k_x - iv_2k_y & 0 & -\Delta(\mathbf{x})e^{-iqz} \\ v_1k_x + iv_2k_y & \xi_{\mathbf{k}+\frac{q}{2}\mathbf{e}_z} - v_3(k_z+\frac{q}{2}) - h & \Delta(\mathbf{x})e^{-iqz} & 0 \\ 0 & \Delta^*(\mathbf{x})e^{+iqz} & -(\xi_{\mathbf{k}-\frac{q}{2}\mathbf{e}_z} - v_3(k_z-\frac{q}{2}) + h) & v_1k_x + iv_2k_y \\ -\Delta^*(\mathbf{x})e^{+iqz} & 0 & v_1k_x - iv_2k_y & -(\xi_{\mathbf{k}-\frac{q}{2}\mathbf{e}_z} + v_3(k_z-\frac{q}{2}) - h) \end{pmatrix}$$

and Eq. C.14, C.15, C.16 become

$$\Delta(z) = -e^{+iqz}U_0\frac{1}{V}{\sum_{\mathbf{k}}}'\left[u_{\mathbf{k}}v_{\mathbf{k}}^* f(E_{\mathbf{k}}) + \alpha_{\mathbf{k}}\beta_{\mathbf{k}}^* f(-E_{\mathbf{k}})\right] \tag{C.23}$$

$$n_\uparrow = \frac{1}{V}{\sum_{\mathbf{k}}}'\left[|u_{\mathbf{k}}|^2 f(E_{\mathbf{k}}) + |\beta_{\mathbf{k}}|^2 f(-E_{\mathbf{k}})\right] \tag{C.24}$$

$$n_\downarrow = \frac{1}{V}{\sum_{\mathbf{k}}}'\left[|v_{\mathbf{k}}|^2 f(-E_{\mathbf{k}}) + |\alpha_{\mathbf{k}}|^2 f(E_{\mathbf{k}})\right] \tag{C.25}$$

We shall further note the BdG equation has particle-hole symmetry, where equations are invariant under interchange of

$$\begin{array}{ccc} E_{\mathbf{k}} & \leftrightarrow & -E_{-\mathbf{k}} \\ \begin{pmatrix} u_{\mathbf{k}} \\ \alpha_{\mathbf{k}} \\ \beta_{\mathbf{k}} \\ v_{\mathbf{k}} \end{pmatrix} & \leftrightarrow & \begin{pmatrix} \beta^*_{-\mathbf{k}} \\ v^*_{-\mathbf{k}} \\ u^*_{-\mathbf{k}} \\ \alpha^*_{-\mathbf{k}} \end{pmatrix} \end{array} \tag{C.26}$$

For instance, we start from

$$m_{11}(\mathbf{k}+\frac{q}{2}\mathbf{e}_z)u_{\mathbf{k}} + (v_1k_x - iv_2k_y)\alpha_{\mathbf{k}} - \Delta(\mathbf{x})e^{-iqz}v_{\mathbf{k}} = E_{\mathbf{k}}u_{\mathbf{k}} \tag{C.27}$$

and we make the particle-hole interchange,

$$m_{11}(\mathbf{k}+\frac{q}{2}\mathbf{e}_z)\beta^*_{-\mathbf{k}} + (v_1k_x - iv_2k_y)v^*_{-\mathbf{k}} - \Delta(\mathbf{x})e^{-iqz}\alpha^*_{-\mathbf{k}} = -E_{-\mathbf{k}}\beta^*_{-\mathbf{k}} \tag{C.28}$$

and take the conjugate on both sides (note here every variable in the equation is complex number and there is no more operator involved, except $E_{\pm\mathbf{k}}$ is real),

$$\begin{array}{rcl} m_{11}(\mathbf{k}+\frac{q}{2}\mathbf{e}_z)^*\beta_{-\mathbf{k}} + (v_1k_x - iv_2k_y)^*v_{-\mathbf{k}} - \Delta^*(\mathbf{x})e^{+iqz}\alpha_{-\mathbf{k}} & = & -E_{-\mathbf{k}}\beta_{-\mathbf{k}} \\ & \Downarrow & \\ \left(\xi_{\mathbf{k}+\frac{q}{2}\mathbf{e}_z} + v_3(k_z+\frac{q}{2}) + h\right)\beta_{-\mathbf{k}} + (v_1k_x + iv_2k_y)v_{-\mathbf{k}} - \Delta^*(\mathbf{x})e^{+iqz}\alpha_{-\mathbf{k}} & = & -E_{-\mathbf{k}}\beta_{-\mathbf{k}} \end{array} \tag{C.29}$$

Then, we change the sign of momentum $\mathbf{k}$ and arrive at (note $\xi_{\mathbf{k}} = \xi_{-\mathbf{k}}$, $\xi_{\mathbf{k}} = \epsilon_{\mathbf{k}} - \mu = \frac{\hbar^2\mathbf{k}^2}{2m} - \mu$)

$$
\begin{aligned}
-\left(\xi_{-\mathbf{k}+\frac{q}{2}\mathbf{e}_z} + v_3(-k_z + \frac{q}{2}) + h\right)\beta_{\mathbf{k}} - (-v_1 k_x - iv_2 k_y)v_{\mathbf{k}} + \Delta^*(\mathbf{x})e^{+iqz}\alpha_{\mathbf{k}} &= E_{\mathbf{k}}\beta_{\mathbf{k}} \\
&\Downarrow \\
-\left(\xi_{\mathbf{k}-\frac{q}{2}\mathbf{e}_z} - v_3(k_z - \frac{q}{2}) + h\right)\beta_{\mathbf{k}} + (v_1 k_x + iv_2 k_y)v_{\mathbf{k}} + \Delta^*(\mathbf{x})e^{+iqz}\alpha_{\mathbf{k}} &= E_{\mathbf{k}}\beta_{\mathbf{k}} \qquad \text{(C.30)}
\end{aligned}
$$

which is identical to the third line in Eq. C.22. It is interesting to note that $m_{33}(\mathbf{k} - \frac{q}{2}\mathbf{e}_z) = -m_{11}(-\mathbf{k} + \frac{q}{2}\mathbf{e}_z)^*$ that has been used in the above derivation (also $m_{44}(\mathbf{k} - \frac{q}{2}\mathbf{e}_z) = -m_{22}(-\mathbf{k} + \frac{q}{2}\mathbf{e}_z)^*$). The sequence of operation is summerized as "take conjugate-negate k-negate equation" and order of operation does not matter (the proof can go backwards). Similarly, other equations in Eq. C.22 follow the particle-hole symmetry.

We can make use of the particle-hole symmetry to simplify Eq. C.23, C.24, C.25 into

$$
\begin{aligned}
\Delta(z) &= -e^{+iqz}\frac{U_0}{2}\frac{1}{V}\sum_{\mathbf{k}}\left[u_{\mathbf{k}}v_{\mathbf{k}}^* f(E_{\mathbf{k}}) + \alpha_{\mathbf{k}}\beta_{\mathbf{k}}^* f(-E_{\mathbf{k}})\right] && \text{(C.31)} \\
n_\uparrow &= \frac{1}{2}\frac{1}{V}\sum_{\mathbf{k}}\left[|u_{\mathbf{k}}|^2 f(E_{\mathbf{k}}) + |\beta_{\mathbf{k}}|^2 f(-E_{\mathbf{k}})\right] && \text{(C.32)} \\
n_\downarrow &= \frac{1}{2}\frac{1}{V}\sum_{\mathbf{k}}\left[|v_{\mathbf{k}}|^2 f(-E_{\mathbf{k}}) + |\alpha_{\mathbf{k}}|^2 f(E_{\mathbf{k}})\right] && \text{(C.33)}
\end{aligned}
$$

where $\frac{1}{V}\sum_{\mathbf{k}}$ runs over all momentum space, which will be convinient in numerical calculations. The factor of $1/2$ comes

from the following proof,

$$\Delta(z) = -e^{+iqz}U_0\frac{1}{V}\sum_{\mathbf{k}>0}\left[u_{\mathbf{k}}v^*_{\mathbf{k}}f(E_{\mathbf{k}}) + \alpha_{\mathbf{k}}\beta^*_{\mathbf{k}}f(-E_{\mathbf{k}})\right] \tag{C.34}$$

$$= -e^{+iqz}U_0\frac{1}{V}\sum_{\mathbf{k}<0}\left[u_{-\mathbf{k}}v^*_{-\mathbf{k}}f(E_{-\mathbf{k}}) + \alpha_{-\mathbf{k}}\beta^*_{-\mathbf{k}}f(-E_{-\mathbf{k}})\right] \tag{C.35}$$

where we just simply rewritten $\mathbf{k}$ as $-\mathbf{k}$ and sum over the other half of momentum space with $\mathbf{k} < 0$. Then, it's time to make use of particle-hole symmetry to rewrite Eq. C.35 as

$$\Delta(z) = -e^{+iqz}U_0\frac{1}{V}\sum_{\mathbf{k}<0}\left[\beta^*_{\mathbf{k}}\alpha_{\mathbf{k}}f(-E_{\mathbf{k}}) + v^*_{\mathbf{k}}u_{\mathbf{k}}f(E_{\mathbf{k}})\right] \tag{C.36}$$

which is identical to Eq. C.34 except for the momentum space summation. Together with Eq. C.34 and C.36, we arrive at Eq. C.31 where $\frac{1}{V}\sum_{\mathbf{k}}$ runs over all momentum space. Similar proof can be followed for Eq. C.32 and C.33.

C.1 Ground state solutions

We first start from ground state solutions using saddle point approach and assume a plane-wave form of order parameter (we assume Δ_0 is a real number)

$$\Delta(z) = \Delta_0 e^{+iqz} \tag{C.37}$$

instead of summing over quasiparticle contributions from Eq. C.31. Then Eq. C.22 is simplified into

$$\begin{pmatrix} m_{11}(\mathbf{k}+\frac{q}{2}\mathbf{e}_z) & v_1k_x - iv_2k_y & 0 & -\Delta_0 \\ v_1k_x + iv_2k_y & m_{22}(\mathbf{k}+\frac{q}{2}\mathbf{e}_z) & \Delta_0 & 0 \\ 0 & \Delta_0 & m_{33}(\mathbf{k}-\frac{q}{2}\mathbf{e}_z) & v_1k_x + iv_2k_y \\ -\Delta_0 & 0 & v_1k_x - iv_2k_y & m_{44}(\mathbf{k}-\frac{q}{2}\mathbf{e}_z) \end{pmatrix} \begin{pmatrix} u_{\mathbf{k}} \\ \alpha_{\mathbf{k}} \\ \beta_{\mathbf{k}} \\ v_{\mathbf{k}} \end{pmatrix} = E_{\mathbf{k}} \begin{pmatrix} u_{\mathbf{k}} \\ \alpha_{\mathbf{k}} \\ \beta_{\mathbf{k}} \\ v_{\mathbf{k}} \end{pmatrix} \tag{C.38}$$

where Δ_0, q, μ are determined from minimizing thermodynamic potential Ω under requirement of number conservation,

$$\frac{\partial\Omega}{\partial\Delta_0} = 0, \quad \frac{\partial\Omega}{\partial q} = 0, \quad -\frac{\partial\Omega}{\partial\mu} = n = \frac{1}{3\pi^2} \quad \text{(for 3D gas)} \tag{C.39}$$

where expression of Ω is found from previous paper [2013 New J. Phys. 15 075014]

$$\frac{\Omega}{V} = -\frac{|\Delta_0|^2 m}{4\pi\hbar^2 a_s} + \frac{1}{V}\sum_{\mathbf{k}}\left[\frac{\xi_{\mathbf{k}+q\mathbf{e}_z/2} + \xi_{-\mathbf{k}+q\mathbf{e}_z/2}}{2} - \frac{1}{4}\sum_{\eta=1}^{4}|E_{\mathbf{k}}^{\eta}| + \frac{|\Delta_0|^2}{2\epsilon_{\mathbf{k}}} - \frac{1}{2\beta}\sum_{\eta=1}^{4}\ln\left(1+\exp(-\beta|E_{\mathbf{k}}^{\eta}|)\right)\right] \tag{C.40}$$

and $E_{\mathbf{k}}^{\eta}$ are diagonalized from Eq. C.38 for given Δ_0, q, μ as variational parameters.

If the system we consider has $v_3 = 0$, then we can directly solve gap and number equations without resorting to Eq. C.39, since the expression for $E_{\mathbf{k}}^{\eta}$ can be analytically derived.

C.2 Time evolution

Once we have the saddle point solution of Δ_0, q, μ, we can determine the set of initial values $u_{\mathbf{k}}^{\eta}$, $\alpha_{\mathbf{k}}^{\eta}$, $\beta_{\mathbf{k}}^{\eta}$, $v_{\mathbf{k}}^{\eta}$ and $E_{\mathbf{k}}^{\eta}$ from Eq. C.38. Next, we study the time-dependent behaviour of order parameter and spin population, i.e. $\Delta(t)$, $n_{\uparrow}(t)$, $n_{\downarrow}(t)$,

by quenching h, v_1, v_2, v_3, or a_s. The set of evolution equation is given by (simplified from Eq. C.22),

$$\begin{pmatrix} m_{11}(\mathbf{k}+\frac{q}{2}\mathbf{e}_z) & v_1k_x - iv_2k_y & 0 & -\Delta(t) \\ v_1k_x + iv_2k_y & m_{22}(\mathbf{k}+\frac{q}{2}\mathbf{e}_z) & \Delta(t) & 0 \\ 0 & \Delta^*(t) & m_{33}(\mathbf{k}-\frac{q}{2}\mathbf{e}_z) & v_1k_x + iv_2k_y \\ -\Delta^*(t) & 0 & v_1k_x - iv_2k_y & m_{44}(\mathbf{k}-\frac{q}{2}\mathbf{e}_z) \end{pmatrix} \begin{pmatrix} u^\eta_{\mathbf{k}}(t) \\ \alpha^\eta_{\mathbf{k}}(t) \\ \beta^\eta_{\mathbf{k}}(t) \\ v^\eta_{\mathbf{k}}(t) \end{pmatrix} = i\frac{\partial}{\partial t} \begin{pmatrix} u^\eta_{\mathbf{k}}(t) \\ \alpha^\eta_{\mathbf{k}}(t) \\ \beta^\eta_{\mathbf{k}}(t) \\ v^\eta_{\mathbf{k}}(t) \end{pmatrix} \tag{C.41}$$

where according to Eq. C.31, C.32, C.33

$$\Delta(t) \equiv \Delta(z)e^{-iqz} \tag{C.42}$$

$$= -\frac{U_0}{2}\frac{1}{V}\sum_{\eta=1}^{4}\sum_{\mathbf{k}}\left[u^\eta_{\mathbf{k}}(t)v^{\eta*}_{\mathbf{k}}(t)f(E_{\mathbf{k}}(t)) + \alpha^\eta_{\mathbf{k}}(t)\beta^{\eta*}_{\mathbf{k}}(t)f(-E^\eta_{\mathbf{k}}(t))\right] \tag{C.43}$$

$$n_\uparrow(t) = \frac{1}{2}\frac{1}{V}\sum_{\eta=1}^{4}\sum_{\mathbf{k}}\left[|u^\eta_{\mathbf{k}}(t)|^2 f(E^\eta_{\mathbf{k}}(t)) + |\beta^\eta_{\mathbf{k}}(t)|^2 f(-E^\eta_{\mathbf{k}}(t))\right] \tag{C.44}$$

$$n_\downarrow(t) = \frac{1}{2}\frac{1}{V}\sum_{\eta=1}^{4}\sum_{\mathbf{k}}\left[|v^\eta_{\mathbf{k}}(t)|^2 f(-E_{\mathbf{k}}(t)) + |\alpha^\eta_{\mathbf{k}}(t)|^2 f(E^\eta_{\mathbf{k}}(t))\right] \tag{C.45}$$

and $E^\eta_{\mathbf{k}}(t)$ should be fixed at $t = 0$, because in the formulation of BdG theory, the population of quasiparticles do not change over time, but rather the wave-functions.

C.3 Case study: Rashba SOC with Zeeman field.

In this case study, we set $v_3 = 0$, $v_2 = v_2 = \lambda$, $T = 0$ and consequently we assume $q = 0$. The quasiparticle energy is written as $E^{\pm}_{\boldsymbol{k},\pm} = \pm\sqrt{\xi^2_{\boldsymbol{k}} + \Delta^2 + h^2 + \lambda^2 k^2_{\perp} \pm 2\sqrt{(h^2 + \lambda^2 k^2_{\perp})\xi^2_{\boldsymbol{k}} + h^2\Delta^2}}$, from which the number and gap equation can be derived as

$$n = \frac{1}{V}\sum_{\boldsymbol{k}} \left\{ 1 + \sum_{\alpha=\pm} \frac{-\xi_k}{2E_{k\alpha}} \left[1 + \alpha \frac{h^2 + \lambda^2 k^2_{\perp}}{\sqrt{(h^2 + \lambda^2 k^2_{\perp})\xi^2_{\boldsymbol{k}} + h^2\Delta^2}} \right] \right\} \tag{C.46}$$

$$\frac{m}{4\pi\hbar^2 a_s} = \frac{1}{V}\sum_{\boldsymbol{k},\alpha=\pm} \frac{-1}{4E_{\boldsymbol{k},\alpha}} \left[1 + \alpha \frac{h^2}{\sqrt{(h^2 + \lambda^2 k^2_{\perp})\xi^2_{\boldsymbol{k}} + h^2\Delta^2}} \right] + \frac{1}{V}\sum_{\boldsymbol{k}} \frac{1}{2\epsilon_{\boldsymbol{k}}} \tag{C.47}$$

In dimensionless form, we have

$$\begin{aligned} \frac{1}{3\pi^2} &= \frac{1}{4\pi^2}\int_0^{\infty} k_{\perp} dk_{\perp} \int_{-\infty}^{\infty} dk_z \\ &\quad \{1 - \frac{\xi_k}{2E_{k+}} \left[1 + \frac{h^2 + \lambda^2 k^2_{\perp}}{\sqrt{(h^2 + \lambda^2 k^2_{\perp})\xi^2_{\boldsymbol{k}} + h^2\Delta^2}} \right] - \frac{\xi_k}{2E_{k-}} \left[1 - \frac{h^2 + \lambda^2 k^2_{\perp}}{\sqrt{(h^2 + \lambda^2 k^2_{\perp})\xi^2_{\boldsymbol{k}} + h^2\Delta^2}} \right] \} \end{aligned}$$

$$\frac{1}{8\pi a_s k_F} = \frac{1}{4\pi^2}\int_0^{\infty} k_{\perp} dk_{\perp} \int_{-\infty}^{\infty} dk_z \left(\frac{1}{2(k^2_{\perp} + k^2_z)} - \frac{1}{4} \frac{\left[1 + \frac{h^2}{\sqrt{(h^2+\lambda^2 k^2_{\perp})(k^2_{\perp}+k^2_z-\mu)^2+h^2\Delta^2}} \right]}{E_{k+}} - \frac{1}{4} \frac{\left[1 - \frac{h^2}{\sqrt{(h^2+\lambda^2 k^2_{\perp})(k^2_{\perp}+k^2_z-\mu)^2+h^2\Delta^2}} \right]}{E_{k-}} \right)$$

from which we shall solve Δ and μ for given h, λ, a_s.

For the gap and number equations, we discuss about the numerical procedures in details here. The accuracy of momentum integrals is crucial to the precision of parameter values and phase boundaries in general. We first introduce

some notations.

$$\frac{1}{3\pi^2} = \frac{1}{4\pi^2}\int_0^\infty k_\perp dk_\perp \int_{-\infty}^\infty dk_z A(k_\perp,k_z) \quad \text{(C.48)}$$

$$= \frac{1}{4\pi^2}\int_0^\infty dk \int_{-1}^1 dx A(k,x) \quad \text{(C.49)}$$

$$\frac{1}{8\pi a_s k_F} = \frac{1}{4\pi^2}\int_0^\infty k_\perp dk_\perp \int_{-\infty}^\infty dk_z B(k_\perp,k_z) \quad \text{(C.50)}$$

$$= \frac{1}{4\pi^2}\int_0^\infty dk \int_{-1}^1 dx B(k,x) \quad \text{(C.51)}$$

where $k_\perp = k\sin\theta$, $k_z = k\cos\theta$, and

$$A(k_\perp,k_z) = 1-\frac{\xi_k}{2E_{k+}}\left[1+\frac{h^2+\lambda^2k_\perp^2}{\sqrt{(h^2+\lambda^2k_\perp^2)\xi_{\boldsymbol{k}}^2+h^2\Delta^2}}\right]-\frac{\xi_k}{2E_{k-}}\left[1-\frac{h^2+\lambda^2k_\perp^2}{\sqrt{(h^2+\lambda^2k_\perp^2)\xi_{\boldsymbol{k}}^2+h^2\Delta^2}}\right] \quad \text{(C.52)}$$

$$A(k,x) = k^2(1-\frac{\xi_k}{2E_{k+}}\left[1+\frac{h^2+\lambda^2k^2\sin^2\theta}{\sqrt{(h^2+\lambda^2k^2\sin^2\theta)\xi_{\boldsymbol{k}}^2+h^2\Delta^2}}\right]-\frac{\xi_k}{2E_{k-}}\left[1-\frac{h^2+\lambda^2k^2\sin^2\theta}{\sqrt{(h^2+\lambda^2k^2\sin^2\theta)\xi_{\boldsymbol{k}}^2+h^2\Delta^2}}\right]) \quad \text{(C.53)}$$

$$B(k_\perp,k_z) = \frac{1}{2(k_\perp^2+k_z^2)}-\frac{1}{4}\frac{\left[1+\frac{h^2}{\sqrt{(h^2+\lambda^2k_\perp^2)(k_\perp^2+k_z^2-\mu)^2+h^2\Delta^2}}\right]}{E_{k+}}-\frac{1}{4}\frac{\left[1-\frac{h^2}{\sqrt{(h^2+\lambda^2k_\perp^2)(k_\perp^2+k_z^2-\mu)^2+h^2\Delta^2}}\right]}{E_{k-}} \quad \text{(C.54)}$$

$$B(k,x) = k^2(\frac{1}{2k^2}-\frac{1}{4}\frac{\left[1+\frac{h^2}{\sqrt{(h^2+\lambda^2k^2\sin^2\theta)(k^2-\mu)^2+h^2\Delta^2}}\right]}{E_{k+}}-\frac{1}{4}\frac{\left[1-\frac{h^2}{\sqrt{(h^2+\lambda^2k^2\sin^2\theta)(k^2-\mu)^2+h^2\Delta^2}}\right]}{E_{k-}}) \quad \text{(C.55)}$$

where $x = \cos\theta$. We further have $A(k,x) = A(k,-x)$ and $B(k,x) = B(k,-x)$. Then, we rewrite gap and number

equation as,

$$\frac{1}{3\pi^2} = \frac{2}{4\pi^2}\int_0^1 dx\left(\int_0^{k_c} dkA(k,x) + \int_{k_c}^{\infty} dk\left(\frac{a_1(x)}{k^2}+\frac{a_2(x)}{k^4}+\frac{a_3(x)}{k^6}+...\right)\right) \quad \text{(C.56)}$$

$$= \frac{2}{4\pi^2}\int_0^1 dx\left(\int_0^{k_c} dkA(k,x) + \left(\frac{a_1(x)}{k_c}+\frac{a_2(x)}{3k_c^3}+\frac{a_3(x)}{5k_c^5}+...\right)\right) \quad \text{(C.57)}$$

$$\frac{1}{8\pi a_s k_F} = \frac{2}{4\pi^2}\int_0^1 dx\left(\int_0^{k_c} dkB(k,x) + \int_{k_c}^{\infty} dk\left(\frac{b_1(x)}{k^2}+\frac{b_2(x)}{k^4}+\frac{b_3(x)}{k^6}+...\right)\right) \quad \text{(C.58)}$$

$$= \frac{2}{4\pi^2}\int_0^1 dx\left(\int_0^{k_c} dkB(k,x) + \left(\frac{b_1(x)}{k_c}+\frac{b_2(x)}{3k_c^3}+\frac{b_3(x)}{5k_c^5}+...\right)\right) \quad \text{(C.59)}$$

where we have made use of the fact that both $A(k,x)$ and $B(k,x)$ scales as $1/k^2$ at large k. We determine the coefficients of $a_i(x)$ and $b_i(x)$ by calculating

$$y_1 = k_1^6 A(k_1,x) \quad \text{(C.60)}$$

$$y_2 = k_2^6 A(k_2,x) \quad \text{(C.61)}$$

$$y_3 = k_3^6 A(k_3,x) \quad \text{(C.62)}$$

and then at large momentum, they are related as

$$\begin{pmatrix} y_1 \\ y_2 \\ y_3 \end{pmatrix} = \begin{pmatrix} k_1^4 & k_1^2 & 1 \\ k_2^4 & k_2^2 & 1 \\ k_3^4 & k_3^2 & 1 \end{pmatrix} \begin{pmatrix} a_1 \\ a_2 \\ a_3 \end{pmatrix} \tag{C.63}$$

$$\begin{pmatrix} a_1 \\ a_2 \\ a_3 \end{pmatrix} = \begin{pmatrix} k_1^4 & k_1^2 & 1 \\ k_2^4 & k_2^2 & 1 \\ k_3^4 & k_3^2 & 1 \end{pmatrix}^{-1} \begin{pmatrix} y_1 \\ y_2 \\ y_3 \end{pmatrix} \tag{C.64}$$

$$= \frac{1}{det} \begin{pmatrix} \begin{vmatrix} k_2^2 & 1 \\ k_3^2 & 1 \end{vmatrix} & \begin{vmatrix} 1 & k_1^2 \\ 1 & k_3^2 \end{vmatrix} & \begin{vmatrix} k_1^2 & 1 \\ k_2^2 & 1 \end{vmatrix} \\ \begin{vmatrix} 1 & k_2^4 \\ 1 & k_3^4 \end{vmatrix} & \begin{vmatrix} k_1^4 & 1 \\ k_3^4 & 1 \end{vmatrix} & \begin{vmatrix} 1 & k_1^4 \\ 1 & k_2^4 \end{vmatrix} \\ \begin{vmatrix} k_2^4 & k_2^2 \\ k_3^4 & k_3^2 \end{vmatrix} & \begin{vmatrix} k_1^2 & k_1^4 \\ k_3^2 & k_3^4 \end{vmatrix} & \begin{vmatrix} k_1^4 & k_1^2 \\ k_2^4 & k_2^2 \end{vmatrix} \end{pmatrix} \begin{pmatrix} y_1 \\ y_2 \\ y_3 \end{pmatrix} \tag{C.65}$$

$$= \frac{1}{det} \begin{pmatrix} k_2^2 - k_3^2 & k_3^2 - k_1^2 & k_1^2 - k_2^2 \\ k_3^4 - k_2^4 & k_1^4 - k_3^4 & k_2^4 - k_1^4 \\ k_2^4 k_3^2 - k_2^2 k_3^4 & k_3^4 k_1^2 - k_3^2 k_1^4 & k_1^4 k_2^2 - k_1^2 k_2^4 \end{pmatrix} \begin{pmatrix} y_1 \\ y_2 \\ y_3 \end{pmatrix} \tag{C.66}$$

and $det = -(k_1^2 - k_2^2)(k_2^2 - k_3^2)(k_3^2 - k_1^2)$. Similiar expressions for

$$\begin{pmatrix} b_1 \\ b_2 \\ b_3 \end{pmatrix} = \frac{1}{det} \begin{pmatrix} k_2^2 - k_3^2 & k_3^2 - k_1^2 & k_1^2 - k_2^2 \\ k_3^4 - k_2^4 & k_1^4 - k_3^4 & k_2^4 - k_1^4 \\ k_2^4 k_3^2 - k_2^2 k_3^4 & k_3^4 k_1^2 - k_3^2 k_1^4 & k_1^4 k_2^2 - k_1^2 k_2^4 \end{pmatrix} \begin{pmatrix} z_1 \\ z_2 \\ z_3 \end{pmatrix} \tag{C.67}$$

where

$$z_1 = k_1^6 B(k_1, x) \tag{C.68}$$

$$z_2 = k_2^6 B(k_2, x) \tag{C.69}$$

$$z_3 = k_3^6 B(k_3, x) \tag{C.70}$$

We can take $k_1 = k_c \gg 1$, $k_2 = 1.5k_c \gg 1$, and $k_3 = 2k_c \gg 1$ for instance.

Then we take the initial values as $\Delta(0)$ and $\mu(0)$ and plug them back into

$$\begin{pmatrix} \xi_{\mathbf{k}} + h & \lambda(k_x - ik_y) & 0 & -\Delta(0) \\ \lambda(k_x + ik_y) & \xi_{\mathbf{k}} - h & \Delta(0) & 0 \\ 0 & \Delta(0) & -(\xi_{\mathbf{k}} + h) & \lambda(k_x + ik_y) \\ -\Delta(0) & 0 & \lambda(k_x - ik_y) & -(\xi_{\mathbf{k}} - h) \end{pmatrix} \begin{pmatrix} u_{\mathbf{k}}^\eta(0) \\ \alpha_{\mathbf{k}}^\eta(0) \\ \beta_{\mathbf{k}}^\eta(0) \\ v_{\mathbf{k}}^\eta(0) \end{pmatrix} = E_{\mathbf{k}}^\eta \begin{pmatrix} u_{\mathbf{k}}^\eta(0) \\ \alpha_{\mathbf{k}}^\eta(0) \\ \beta_{\mathbf{k}}^\eta(0) \\ v_{\mathbf{k}}^\eta(0) \end{pmatrix} \tag{C.71}$$

and straightforwardly diagonalize it for given momentum $\mathbf{k}$ and obtain wave-functions of $u_{\mathbf{k}}^\eta$, $\alpha_{\mathbf{k}}^\eta$, $\beta_{\mathbf{k}}^\eta$, $v_{\mathbf{k}}^\eta$ and eigenenergy $E_{\mathbf{k}}^\eta$ (check if it is the same as $E_{\mathbf{k}\pm}^\pm$). With the initial values (as benchmarks), we quench value of h and evolve the

functions according to

$$\begin{pmatrix} \xi_{\mathbf{k}}+h & \lambda(k_x-ik_y) & 0 & -\Delta(t) \\ \lambda(k_x+ik_y) & \xi_{\mathbf{k}}-h & \Delta(t) & 0 \\ 0 & \Delta^*(t) & -(\xi_{\mathbf{k}}+h) & \lambda(k_x+ik_y) \\ -\Delta^*(t) & 0 & \lambda(k_x-ik_y) & -(\xi_{\mathbf{k}}-h) \end{pmatrix} \begin{pmatrix} u^\eta_{\mathbf{k}}(t) \\ \alpha^\eta_{\mathbf{k}}(t) \\ \beta^\eta_{\mathbf{k}}(t) \\ v^\eta_{\mathbf{k}}(t) \end{pmatrix} = i\frac{\partial}{\partial t} \begin{pmatrix} u^\eta_{\mathbf{k}}(t) \\ \alpha^\eta_{\mathbf{k}}(t) \\ \beta^\eta_{\mathbf{k}}(t) \\ v^\eta_{\mathbf{k}}(t) \end{pmatrix} \tag{C.72}$$

where

$$\Delta(t) = -\frac{U_0}{2}\frac{1}{V}\sum_{\eta=1}^{4}\sum_{\mathbf{k}}\left[u^\eta_{\mathbf{k}}(t)v^{\eta*}_{\mathbf{k}}(t)f(E^\eta_{\mathbf{k}}(t=0)) + \alpha^\eta_{\mathbf{k}}(t)\beta^{\eta*}_{\mathbf{k}}(t)f(-E^\eta_{\mathbf{k}}(t=0))\right] \tag{C.73}$$

where we need to use renormalization $1/U_0 = m/(4\pi\hbar^2 a_s) - \sum_{\mathbf{k}} 1/2\epsilon_{\mathbf{k}}$.

For two dimensional system, the renormalization is given by

$$\begin{aligned} \frac{1}{U_0} &= -\frac{2\pi}{(2\pi)^2}\int_0^{k_c} kdk\frac{1}{E_b+2\epsilon_k} && \text{(C.74)} \\ &= -\frac{1}{2\pi}\frac{1}{4}\log(2k^2+E_b)|_0^{k_c} && \text{(C.75)} \\ &= -\frac{1}{8\pi}\log(1+\frac{2k_c^2}{E_b}) && \text{(C.76)} \end{aligned}$$

where I have used $\frac{1}{V}\sum_{\mathbf{k}} = \frac{1}{(2\pi)^2}\int_0^{k_c} kdk\int_0^{2\pi} d\theta$ and as for BdG matrix elements, $k_x = k\cos\theta$, $k_y = k\sin\theta$.

As a result of particle-hole symmetry, integration in $\Delta(t)$ can be reduced to radial direction only, since the relative phase between k_x and k_y would not matter.

$$\Delta(t) = -\frac{1}{2}\frac{1}{V}\sum_{\eta=1}^{4}\frac{1}{2\pi}\int_0^{k_c} kdk\left[u^\eta_{\mathbf{k}}(t)v^{\eta*}_{\mathbf{k}}(t)f(E^\eta_{\mathbf{k}}(t=0)) + \alpha^\eta_{\mathbf{k}}(t)\beta^{\eta*}_{\mathbf{k}}(t)f(-E^\eta_{\mathbf{k}}(t=0))\right]\frac{1}{-\frac{1}{8\pi}\log(1+\frac{2k_c^2}{E_b})} \tag{C.77}$$

To get accurate time-dependent results, the momentum integral meshgrid number is expected to be above 2000 points, and time step shall be around 0.0005.

C.4 Floquet spectrum

For a periodically driven Hamiltonian $\hat{H}(t)$ with period T, Floquet operator is defined as,

$$\hat{F} = \hat{\mathcal{T}} \exp\{-i \int_{T_i}^{T_i+T} dt \hat{H}(t)\} \tag{C.78}$$

where $\hat{\mathcal{T}}$ denotes time-order, and T_i is the initial time. The eigenvalue and eigenstates of $\hat{F}$ is given by

$$\hat{F}|\varphi_n\rangle = e^{-i\varepsilon_n T}|\varphi_n\rangle, \tag{C.79}$$

where $-\pi/T < \varepsilon_n < \pi/T$ is the quasi-energy.

The time-ordering operator can be written in terms of ordered product of exponentials in the infinite limit of number of terms

$$\begin{aligned}
\hat{F} &= \hat{\mathcal{T}} \exp\{-i \left(\int_{T_i}^{T_i+\Delta T} dt \hat{H}(T_i) + \int_{T_i+\Delta T}^{T_i+2\Delta T} dt \hat{H}(T_i+\Delta T) + ... + \int_{T_i+T-\Delta T}^{T_i+T} dt \hat{H}(T_i+T-\Delta T) \right)\} && \text{(C.80)} \\
&= \hat{\mathcal{T}} \exp\{-i\Delta T \left(\hat{H}(T_i) + \hat{H}(T_i+\Delta T) + ... + \hat{H}(T_i+T-\Delta T) \right)\} && \text{(C.81)} \\
&= \lim_{M\to\infty} \left(e^{-i\hat{H}(t_{M-1})\Delta T} e^{-i\hat{H}(t_{M-2})\Delta T} \dots e^{-i\hat{H}(t_0)\Delta T} \right) && \text{(C.82)} \\
&\approx \exp\{-i\hat{H}(T_i+T-\Delta T)\Delta T\} \exp\{-i\hat{H}(T_i+T-2\Delta T)\Delta T\} ... \exp\{-i\hat{H}(T_i)\Delta T\} && \text{(C.83)} \\
&\equiv \exp\{-i\hat{H}(t_{M-1})\Delta T\} \exp\{-i\hat{H}(t_{M-2})\Delta T\} ... \exp\{-i\hat{H}(t_0)\Delta T\} && \text{(C.84)}
\end{aligned}$$

where we have devided the time interval from T_i to $T_i + T$ into M moments $\Delta T = T/M$ and $t_j = T_i + jT/M$ and $j = 0, 1, ...M - 1$. Numerically, we will introduce a cutoff $M_{\max}$ for finite terms. We can make use of eigenvalue decomposition

$$H(t) = V(t)D(t)V(t)^\dagger \tag{C.85}$$

$$e^{-iH(t)\Delta t} = V(t)e^{-iD(t)\Delta t}V(t)^\dagger \tag{C.86}$$

(it is worth to note that this method is more stable than Taylor expansion to 2nd, 4th(RK) order, similiar to algorithm used in MATLAB function of expm or *exp* subroutine in the unsupported module of Eigen C++ library) then we have ,

$$F = \lim_{M\to\infty} \left(V(t_{M-1})e^{-iD(t_{M-1})\Delta t}V(t_{M-1})^\dagger V(t_{M-2})e^{-iD(t_{M-2})\Delta t}V(t_{M-2})^\dagger \dots V(t_0)e^{-iD(t_0)\Delta t}V(t_0)^\dagger\right) \tag{C.87}$$

where exponential of D is evaluated only for the diagonal terms, which are the eigenvalue terms.

If we have time-independent Hamiltonian H, then V and D are also time-independent and we shall have $V(t_{M-1})^\dagger V(t_{M-2}) = I$ and $V(t_{M-1}) = V(t_0) = V$. Then it follows that $F = V\left(\Pi_{j=0}^{M-1}e^{-iDT/M}\right)V^\dagger = Ve^{-iD\sum_{j=0}^{M-1}T/M}V^\dagger = Ve^{-iDT}V^\dagger = e^{-iHT}$ and its spectrum is given by $e^{-i\varepsilon_n T}$, where ε_n is the spectrum of H. However, note that from the spectrum of H, the result of $\log(e^{-i\varepsilon_n T})/(-iT)$ is not necessarily the same as ε_n because $|\varepsilon_n T|$ can have components larger than π and this fact leads to "spectrum folding" where spectrums belong to different branches in the complex plane are taken into account. The same thing applies to phase$(e^{-i\varepsilon_n T})/(-T)$ is not necessarily the same as ε_n. In order to circumvent this artifact for time-independent Hamiltonian, we need to restrict T to be small for large cutoff in H matrix, where the end results of high $\varepsilon_n T$ are restricted within the bounds of $[-\pi, \pi]$.

Appendix D

Partition Function for Superradient Phase

In this appendix, we supplement results presented in Sec. 5.4 with more mathematical derivations regarding the free energy per particle in the thermodynamic limit.

Using first quantized form of the Hamiltonian, we can write

$$H = \delta_R c^\dagger c + \sum_{j=1}^{N} \left[\frac{\hbar^2 \mathbf{k}^2}{2m} \mathcal{I}_j + \left(\frac{\hbar^2}{m} k_r k_z + \delta \right) \sigma_j^z + \frac{\Omega}{2} \frac{1}{\sqrt{V}} \left(\sigma_j^+ c + c^\dagger \sigma_j^- \right) \right] \tag{D.1}$$

where $\delta_R = \omega_c - \omega_R$ and $\mathcal{I}_j$ is identity matrix, $\sigma_j^\pm$ are raising and lowering operators for the j-th particle's spin state. The thermodynamic functions can be calculated from the canonical partition function, $Z(N,T) = \mathrm{Tr}[e^{-\beta H}]$. A convenient basis to calculate the trace of the partition function is the Glauber's coherent state $|\alpha\rangle$ for the photon field, then we have

$$Z(N,T) = \sum_{s_1=\uparrow,\downarrow} ... \sum_{s_N=\uparrow,\downarrow} \frac{V}{(2\pi)^3} \int d\mathbf{k}_1 ... \frac{V}{(2\pi)^3} \int d\mathbf{k}_N \int \frac{d^2\alpha}{\pi} \langle \mathbf{k}_1 s_1; ...; \mathbf{k}_N s_N | \langle \alpha | e^{-\beta H} | \alpha \rangle | \mathbf{k}_1 s_1; ...; \mathbf{k}_N s_N \rangle \tag{D.2}$$

where atomic field is denoted by atom index j and momentum $\mathbf{k}$ and spin $\sigma = \uparrow, \downarrow$. It follows then that the expectation value becomes,

$$\langle \alpha | e^{-\beta H} | \alpha \rangle = \exp \left\{ -\beta \delta_R |\alpha|^2 - \beta \sum_{j=1}^{N} h(\mathbf{k}_j) \right\} \tag{D.3}$$

$$h(\mathbf{k}_j) = (h_\uparrow(\mathbf{k}_j)|\mathbf{k}_j\uparrow\rangle\langle\mathbf{k}_j\uparrow| + h_\downarrow(\mathbf{k}_j)|\mathbf{k}_j\downarrow\rangle\langle\mathbf{k}_j\downarrow|) + \frac{\Omega}{2}\frac{1}{\sqrt{V}}\left(|\mathbf{k}_j\uparrow\rangle\langle\mathbf{k}_j\downarrow|\alpha + \alpha^*|\mathbf{k}_j\downarrow\rangle\langle\mathbf{k}_j\uparrow|\right) \tag{D.4}$$

where $h_\uparrow(\mathbf{k}) = \frac{\hbar^2\mathbf{k}^2}{2m} + \frac{\hbar^2}{m}k_r k_z + \delta$, $\quad h_\downarrow(\mathbf{k}) = \frac{\hbar^2\mathbf{k}^2}{2m} - \frac{\hbar^2}{m}k_r k_z - \delta$ and using the property $[h(\mathbf{k}_i), h(\mathbf{k}_j)] = 0$, we can reduce integrand of Eq. D.2 to

$$\begin{aligned}
\langle\mathbf{k}_1 s_1; ...; \mathbf{k}_N s_N|\langle\alpha|e^{-\beta H}|\alpha\rangle|\mathbf{k}_1 s_1; ...; \mathbf{k}_N s_N\rangle &= e^{-\beta\delta_R|\alpha|^2}\langle\mathbf{k}_1 s_1; ...; \mathbf{k}_N s_N|e^{-\beta\sum_{j=1}^N h(\mathbf{k}_j)}|\mathbf{k}_1 s_1; ...; \mathbf{k}_N s_N\rangle &\text{(D.5)}\\
&= e^{-\beta\delta_R|\alpha|^2}\langle\mathbf{k}_1 s_1; ...; \mathbf{k}_N s_N|\prod_{j=1}^N e^{-\beta h(\mathbf{k}_j)}|\mathbf{k}_1 s_1; ...; \mathbf{k}_N s_N\rangle &\text{(D.6)}\\
&= e^{-\beta\delta_R|\alpha|^2}\prod_{j=1}^N\langle\mathbf{k}_j s_j|e^{-\beta h(\mathbf{k}_j)}|\mathbf{k}_j s_j\rangle &\text{(D.7)}
\end{aligned}$$

From Eq. D.2 and Eq. D.7, we have

$$\begin{aligned}
Z(N,T) &= \sum_{s_1=\uparrow,\downarrow}...\sum_{s_N=\uparrow,\downarrow}\frac{V}{(2\pi)^3}\int d\mathbf{k}_1 ...\frac{V}{(2\pi)^3}\int d\mathbf{k}_N\int\frac{d^2\alpha}{\pi}e^{-\beta\delta_R|\alpha|^2}\left(\prod_{j=1}^N\langle\mathbf{k}_j s_j|e^{-\beta h(\mathbf{k}_j)}|\mathbf{k}_j s_j\rangle\right) &\text{(D.8)}\\
&= \int\frac{d^2\alpha}{\pi}e^{-\beta\delta_R|\alpha|^2}\left\{\frac{V}{(2\pi)^3}\int d\mathbf{k}_j \mathrm{Tr}_\sigma\exp\left[-\beta\begin{pmatrix} h_\uparrow(\mathbf{k}_j) & \frac{\Omega}{2}\frac{1}{\sqrt{V}}\alpha \\ \frac{\Omega}{2}\frac{1}{\sqrt{V}}\alpha^* & h_\downarrow(\mathbf{k}_j)\end{pmatrix}\right]\right\}^N &\text{(D.9)}
\end{aligned}$$

where the Trace is only for spin degrees of freedom. The eigenvalue of the 2×2 matrix is given by

$$\epsilon_j^\pm(\mathbf{k}_j) = \frac{\hbar^2\mathbf{k}_j^2}{2m} \pm \sqrt{\left(\frac{\hbar^2}{m}k_r k_{jz} + \delta\right)^2 + \left(\frac{\Omega}{2}\frac{1}{\sqrt{V}}\right)^2|\alpha|^2} \equiv \frac{\hbar^2\mathbf{k}_j^2}{2m} \pm |\mu(\mathbf{k}_j)| \tag{D.10}$$

Then from Eq. D.9 we have,

$$
\begin{aligned}
Z(N,T) &= \int \frac{d^2\alpha}{\pi} e^{-\beta\delta_R|\alpha|^2} \left[\frac{V}{(2\pi)^3} \int d\mathbf{k}_j \left(e^{-\beta\epsilon_j^+(\mathbf{k}_j)} + e^{-\beta\epsilon_j^-(\mathbf{k}_j)} \right) \right]^N && \text{(D.11)} \\
&= \int \frac{d^2\alpha}{\pi} e^{-\beta\delta_R|\alpha|^2} \left[\frac{V}{(2\pi)^3} \int d\mathbf{k} \exp(-\beta \frac{\hbar^2\mathbf{k}^2}{2m}) \left(e^{-\beta|\mu(\mathbf{k})|} + e^{\beta|\mu(\mathbf{k})|} \right) \right]^N && \text{(D.12)} \\
&= \int \frac{d^2\alpha}{\pi} e^{-\beta\delta_R|\alpha|^2} \left[\frac{V}{(2\pi)^3} \int d\mathbf{k} \exp(-\beta \frac{\hbar^2\mathbf{k}^2}{2m}) 2\cosh\beta \sqrt{\left(\frac{\hbar^2}{m} k_r k_z + \delta \right)^2 + \left(\frac{\Omega}{2} \frac{1}{\sqrt{V}} \right)^2 |\alpha|^2} \right]^N && \text{(D.13)} \\
&= \left[\frac{V}{(2\pi)^3} \int dk_x \int dk_y \exp(-\beta \frac{\hbar^2(k_x^2+k_y^2)}{2m}) \right]^N && \text{(D.14)} \\
&\times \int \frac{d^2\alpha}{\pi} e^{-\beta\delta_R|\alpha|^2} \left(\int dk_z \exp(-\beta \frac{\hbar^2 k_z^2}{2m}) 2\cosh(\beta \sqrt{\left(\frac{\hbar^2}{m} k_r k_z + \delta \right)^2 + \left(\frac{\Omega}{2} \frac{1}{\sqrt{V}} \right)^2 |\alpha|^2}) \right)^N && \text{(D.15)} \\
&= \left(\frac{V}{(2\pi)^3} \frac{2\pi m}{\hbar^2\beta} \right)^N 2 \int_0^\infty r e^{-\beta\delta_R r^2} dr \left(\int dk_z \exp(-\beta \frac{\hbar^2 k_z^2}{2m}) 2\cosh(\beta \sqrt{\left(\frac{\hbar^2}{m} k_r k_z + \delta \right)^2 + \left(\frac{\Omega}{2} \frac{1}{\sqrt{V}} \right)^2 r^2}) \right)^N && \text{(D.16)}
\end{aligned}
$$

In canonical ensemble and thermodynamic limit, free energy per particle is given by

$$
f(T,\Omega,\omega_c,\delta) = -\frac{1}{\beta} \lim_{N\to\infty} \frac{\log Z(N,T)}{N} \qquad \text{(D.17)}
$$

and we need to seek phase transition property by studying saddle point solution to F energy landscapes.

We shall make use of Laplace's method to further reduce the integrals. The formal statement of Lapace's method

is: Assume that $f(x)$ is a twice differentiable function on $[a,b]$ with $x_0 \in [a,b]$ the unique point such that $f(x_0) = \max_{[a,b]} f(x)$. Assume additionally that $f''(x_0) < 0$, then

$$\lim_{N\to+\infty} \left(\frac{\int_a^b e^{Nf(x)} dx}{e^{Nf(x_0)} \sqrt{\frac{2\pi}{-Nf''(x_0)}}} \right) = 1 \tag{D.18}$$

We denote,

$$\mathcal{S} = \int dk_z \exp(-\beta \frac{\hbar^2 k_z^2}{2m}) 2\cosh(\beta \sqrt{\left(\frac{\hbar^2}{m} k_r k_z + \delta\right)^2 + \left(\frac{\sqrt{N}\Omega}{2} \frac{1}{\sqrt{V}}\right)^2 \frac{|\alpha|^2}{N}}) \tag{D.19}$$

Then, partition function is formally written as

$$\begin{aligned} Z(N,T) &= \left(\frac{V}{(2\pi)^3} \frac{2\pi m}{\hbar^2 \beta}\right)^N 2 \int_0^\infty r e^{-N\frac{\beta\delta_R r^2}{N}} e^{N\log\mathcal{S}} dr & \text{(D.20)} \\ &= N \left(\frac{V}{(2\pi)^3} \frac{2\pi m}{\hbar^2 \beta}\right)^N \int_0^\infty dy \exp\left\{N\left[-\beta\delta_R y + \log\mathcal{S}\right]\right\} & \text{(D.21)} \end{aligned}$$

where we have denoted $y = \frac{|\alpha|^2}{N}$. By Laplace's method, the integral is given by

$$Z(N,T) = N \frac{1}{\sqrt{N}} \sqrt{\frac{2\pi}{-\phi''(y_0)}} \left(\frac{V}{(2\pi)^3} \frac{2\pi m}{\hbar^2 \beta}\right)^N \max_{0\le y\le\infty} \exp\left\{N\phi(y)\right\} \tag{D.22}$$

where y_0 is the point that gives maximum and $\phi(y) = -\beta\delta_R y + \log\mathcal{S}$. We note that,

$$\phi'(y) = -\beta\delta_R + \frac{\beta \int dk_z \exp(-\beta\frac{\hbar^2 k_z^2}{2m}) \sinh\left(\beta \sqrt{\left(\frac{\hbar^2}{m} k_r k_z + \delta\right)^2 + \left(\frac{\sqrt{N}\Omega}{2}\frac{1}{\sqrt{V}}\right)^2 y}\right) \frac{\left(\frac{\sqrt{N}\Omega}{2}\frac{1}{\sqrt{V}}\right)^2}{\sqrt{\left(\frac{\hbar^2}{m}k_r k_z+\delta\right)^2 + \left(\frac{\sqrt{N}\Omega}{2}\frac{1}{\sqrt{V}}\right)^2 y}}}{\mathcal{S}} \tag{D.23}$$

Putting $\phi'(y)=0$ we get an integral equation of $\eta=\sqrt{\left(\frac{\hbar^2}{m}k_rk_z+\delta\right)^2+\left(\frac{\sqrt{N}\Omega}{2}\frac{1}{\sqrt{V}}\right)^2}\,y$, and we shall denote $\tilde{\Omega}=\sqrt{N}\Omega\frac{1}{\sqrt{V}}=\sqrt{\rho}\Omega$ is the Tavis-Cummings coupling constant, an enhancement of coupling strength which scales as $\sqrt{N}$, but remains finite in the thermodynamic limit that $N\to\infty$, $V\to\infty$ such that $\rho=\frac{N}{V}$ is finite.

$$\delta_R\int dk_z\exp(-\beta\frac{\hbar^2k_z^2}{2m})2\cosh(\beta\eta)=\int dk_z\exp(-\beta\frac{\hbar^2k_z^2}{2m})\sinh(\beta\eta)\frac{\left(\frac{\sqrt{N}\Omega}{2}\frac{1}{\sqrt{V}}\right)^2}{\eta} \tag{D.24}$$

where k_z is yet to be integrated out. Then,

$$\begin{aligned}
-\beta f(\beta,\tilde{\Omega},\delta_R,\delta) &= \lim_{N\to\infty}\frac{1}{N}\log\left[N\frac{1}{\sqrt{N}}\sqrt{\frac{2\pi}{-\phi''(y_0)}}\left(\frac{V}{(2\pi)^3}\frac{2\pi m}{\hbar^2\beta}\right)^N\exp\left\{N\phi(y_0)\right\}\right] && \text{(D.25)}\\
&= \lim_{N\to\infty}\frac{\log\left(\sqrt{N}\sqrt{\frac{2\pi}{-\phi''(y_0)}}\right)}{N}+\log\left(\frac{V}{(2\pi)^3}\frac{2\pi m}{\hbar^2\beta}\right)+\phi(y_0) && \text{(D.26)}\\
&= \log\left(\frac{V}{(2\pi)^3}\frac{2\pi m}{\hbar^2\beta}\right)+\phi(y_0) && \text{(D.27)}\\
&= \log\left(\frac{V}{(2\pi)^3}\frac{2\pi m}{\hbar^2\beta}\right)-\beta\delta_Ry_0+\log\int dk_z\exp(-\beta\frac{k_z^2}{2})2\cosh(\beta\sqrt{\left(k_rk_z+\delta\right)^2+\left(\frac{\tilde{\Omega}}{2}\right)^2}\,y_0) && \text{(D.28)}
\end{aligned}$$

Second order derivative can be checked straightforwardly,

$$\phi''(y)=\frac{\frac{\partial Q}{\partial y}\mathcal{S}-Q^2}{\mathcal{S}^2} \tag{D.29}$$

where $Q \equiv \frac{\partial \mathcal{S}}{\partial y} = \beta \int dk_z \exp(-\beta \frac{\hbar^2 k_z^2}{2m}) \sinh\left(\beta \sqrt{\left(\frac{\hbar^2}{m} k_r k_z + \delta\right)^2 + \left(\frac{\sqrt{N}\Omega}{2} \frac{1}{\sqrt{V}}\right)^2 y}\right) \frac{\left(\frac{\sqrt{N}\Omega}{2} \frac{1}{\sqrt{V}}\right)^2}{\sqrt{\left(\frac{\hbar^2}{m} k_r k_z + \delta\right)^2 + \left(\frac{\sqrt{N}\Omega}{2} \frac{1}{\sqrt{V}}\right)^2 y}}$ and

$$
\begin{aligned}
\frac{\partial Q}{\partial y} &= \beta \left(\frac{\sqrt{N}\Omega}{2} \frac{1}{\sqrt{V}}\right)^2 \int dk_z \exp(-\beta \frac{\hbar^2 k_z^2}{2m}) \partial_y \left(\frac{\sinh\left(\beta \sqrt{\left(\frac{\hbar^2}{m} k_r k_z + \delta\right)^2 + \left(\frac{\sqrt{N}\Omega}{2} \frac{1}{\sqrt{V}}\right)^2 y}\right)}{\sqrt{\left(\frac{\hbar^2}{m} k_r k_z + \delta\right)^2 + \left(\frac{\sqrt{N}\Omega}{2} \frac{1}{\sqrt{V}}\right)^2 y}} \right) \\
&= \beta \left(\frac{\sqrt{N}\Omega}{2} \frac{1}{\sqrt{V}}\right)^4 \int dk_z \exp(-\beta \frac{\hbar^2 k_z^2}{2m}) \frac{\frac{\beta}{2} \cosh\left(\beta \sqrt{\left(\frac{\hbar^2}{m} k_r k_z + \delta\right)^2 + \left(\frac{\sqrt{N}\Omega}{2} \frac{1}{\sqrt{V}}\right)^2 y}\right) - \frac{\sinh\left(\beta \sqrt{\left(\frac{\hbar^2}{m} k_r k_z + \delta\right)^2 + \left(\frac{\sqrt{N}\Omega}{2} \frac{1}{\sqrt{V}}\right)^2 y}\right)}{2\sqrt{\left(\frac{\hbar^2}{m} k_r k_z + \delta\right)^2 + \left(\frac{\sqrt{N}\Omega}{2} \frac{1}{\sqrt{V}}\right)^2 y}}}{\left(\frac{\hbar^2}{m} k_r k_z + \delta\right)^2 + \left(\frac{\sqrt{N}\Omega}{2} \frac{1}{\sqrt{V}}\right)^2 y} \qquad \text{(D.30)} \\
&= \beta \left(\frac{\sqrt{N}\Omega}{2} \frac{1}{\sqrt{V}}\right)^4 \int dk_z \exp(-\beta \frac{\hbar^2 k_z^2}{2m}) \frac{\frac{\beta}{2} \cosh(\beta\eta) - \frac{\sinh(\beta\eta)}{2\eta}}{\eta^2} \qquad \text{(D.31)}
\end{aligned}
$$

In numerical calculations, we use dimensionless unit, by setting $\hbar = m = k_B = 1$ and choose a typical frequency $\omega = 1$MHz. Then it follows from the estimate, $k_r = 2\pi/\lambda$ and in dimensionless unit

$$k_r \sqrt{\hbar/(m\omega)} = \frac{2\pi}{773 \times 10^{-9} m} \sqrt{\frac{1.05 \times 10^{-34} J \cdot s}{(85 \times 1.67 \times 10^{-27} kg) \times (10^6 Hz)}} \approx 0.22$$

for a Rb atom. For K atom, $k_r \sim 0.33$; for Na atom, $k_r \sim 0.42$; for Li atom, $k_r \sim 0.77$. Temperature T is measured in $1/k_B$, $\tilde{\Omega} = \sqrt{\rho}\Omega$ and δ_R are measured in ω. Although $\delta_R = \omega_c - \omega_R$ can be either positive or negative, partition function Eq. D.2 can only be convergent when $\delta_R > 0$ (by analogy to positive electronic energy states) in the thermodynamic limit.

With the partition function, it is easy to compute the average photon number,

$$\langle \frac{c^\dagger c}{N} \rangle = \frac{\mathrm{Tr}[c^\dagger c e^{-\beta H}/N]}{Z(N,T)} \tag{D.32}$$

$$= \frac{|\alpha|^2}{N} \tag{D.33}$$

$$= y_0 \tag{D.34}$$

Thus, super-radiant phase occurs for $y_0 > 0$ where $|\alpha|^2$ would be an infinitely large value in the thermodynamic limit $N \to \infty$. Here we show average photon number in the parameter space of T and Ω .

If we consider the Hamiltonian without kinetic and SOC term, then

$$\begin{aligned}
Z(N,T) &= \int \frac{d^2\alpha}{\pi} e^{-\beta\delta_R|\alpha|^2} \left\{ \mathrm{Tr}_\sigma \exp\left[-\beta \begin{pmatrix} \delta & \frac{\Omega}{2}\frac{1}{\sqrt{V}}\alpha \\ \frac{\Omega}{2}\frac{1}{\sqrt{V}}\alpha^* & -\delta \end{pmatrix} \right] \right\}^N \\
&= \int \frac{d^2\alpha}{\pi} e^{-\beta\delta_R|\alpha|^2} \left[2\cosh\left(\beta\sqrt{\delta^2 + (\frac{\tilde{\Omega}}{2})^2 \frac{|\alpha|^2}{N}} \right) \right]^N \\
&= \int_0^\infty 2rdr e^{-\beta\delta_R r^2} \left[2\cosh\left(\beta\sqrt{\delta^2 + (\frac{\tilde{\Omega}}{2})^2 \frac{r^2}{N}} \right) \right]^N \\
&= N\int_0^\infty dy e^{-\beta N\delta_R y} \left[2\cosh\left(\beta\sqrt{\delta^2 + (\frac{\tilde{\Omega}}{2})^2 y} \right) \right]^N \\
&= N\int_0^\infty dy e^{N\left\{ -\beta\delta_R y + \log\left[2\cosh\left(\beta\sqrt{\delta^2 + (\frac{\tilde{\Omega}}{2})^2 y} \right) \right] \right\}}
\end{aligned} \tag{D.35}$$

Let's denote $\phi(y) = -\beta\delta_R y + \log\left[2\cosh\left(\beta\delta\sqrt{1+(\frac{\tilde{\Omega}}{2\delta})^2 y}\right)\right]$ and use Laplace's method to calculate Eq. D.35. Putting $\phi'(y) = 0$, it is easy to see that the max is taken at $\frac{\delta_R\delta}{\tilde{\Omega}^2/8}\eta = \tanh(\beta\delta\eta)$ where $\eta = \sqrt{1+(\frac{\tilde{\Omega}}{2\delta})^2 y}$. If $\tilde{\Omega}^2 < 8\delta_R\delta$, there is no phase transition even at zero temperature; however, if $\tilde{\Omega}^2 \geq 8\delta_R\delta$, there is a critical temperature T_c which is given by $\frac{\delta_R\delta}{\tilde{\Omega}^2/8} = \tanh(\frac{\delta}{k_B T_c})$. For $\beta > \beta_c$, the unique solution is given by a nonzero y_0 value that is determined by $\frac{\delta_R\delta}{\tilde{\Omega}^2/8}\sqrt{1+(\frac{\tilde{\Omega}}{2\delta})^2 y_0} = \tanh(\beta\delta\sqrt{1+(\frac{\tilde{\Omega}}{2\delta})^2 y_0})$. (This derivation agrees with the paper PRA 7, 831(1973). Eq. 32)

If we set $k_r = 0$, it recovers the Dicke phase diagram (which is equivalent to setting both kinetic energy and k_r to 0, in which case kinetic energy does not contribute to the super-radient phase transition). However, for non-zero k_r value, the phase boundary displays a non-monochromatic relation in $\Omega - T$.

Bibliography

[1] H. K. Onnes, "The nobel prize in physics 1913," *www.nobelprize.org/nobel_prizes/physics/laureates*/1913/, Nobel Media AB 2014.

[2] H. K. Onnes, "Investigations into the properties of substances at low temperatures, which have led, amongst other things, to the preparation of liquid helium.," *Nobelprize.org. Nobel Lecture*, December 13, 1913.

[3] J. M. Leinaas and J. Myrheim, "On the theory of identical particles," *Il Nuovo Cimento B (1971-1996)*, vol. 37, no. 1, pp. 1–23, 1977.

[4] E. Robert and R. Robert, "Quantum physics of atoms, molecules," *Solids, Nuclei, and Particles (2nd ed.). pp. 272–3.*, 1985.

[5] D. Griffiths, "Introduction to quantum mechanics (2nd ed.).," *pp. 183–4.*, 2005.

[6] W. Pauli", "The connection between spin and statistics," *Physical Review*, vol. 58, no. 8, pp. 716–722, 1940.

[7] Bose, "Plancks gesetz und lichtquantenhypothese / quantum theory of the monatomic ideal gas, part ii," *Zeitschrift für Physik*, vol. 26, no. 1, pp. 178–181, 1924.

[8] A. Einstein, "Elektron und allgemeine relativitätstheorie / the electron and the general theory of relativity," *Physica*, vol. 5, pp. 330–334, 1925.

[9] A. Einstein, "hysikalisch-mathematische klasse," *Sitzungsberichte der Preussischen Akademie der Wissenschaften*, p. 3, 1925.

[10] K. B. Davis", "Bose-einstein condensation in a gas of sodium atoms," *Physical Review Letters*, vol. 75, no. 22, pp. 3969–3973, 1995.

[11] C. C. Bradley", "Evidence of bose-einstein condensation in an atomic gas with attractive interactions," *Physical Review Letters*, vol. 75, no. 9, pp. 1687–1690, 1995.

[12] M. Anderson, J. Ensher, M. Matthews, C. Wieman, and E. Cornell, "Observation of bose-einstein condensation in a dilute atomic vapor," *Science*, vol. 269, no. 5221, pp. 198–201, 1995.

[13] M. Greiner, O. Mandel, T. Esslinger, T. W. Hansch, and I. Bloch, "Quantum phase transition from a superfluid to a mott insulator in a gas of ultracold atoms," *Nature*, vol. 415, pp. 39–44, 01 2002.

[14] N. Goldman, G. Juzeliūnas, P. Öhberg, and I. B. Spielman, "Light-induced gauge fields for ultracold atoms," *Reports on Progress in Physics*, vol. 77, no. 12, p. 126401, 2014.

[15] T. Bourdel", "Experimental study of the bec-bcs crossover region in lithium 6," *Physical Review Letters*, vol. 93, no. 5, 2004.

[16] J. Kinast", "Evidence for superfluidity in a resonantly interacting fermi gas," *Physical Review Letters*, vol. 92, no. 15, 2004.

[17] M. Greiner, C. A. Regal, and D. S. Jin, "Emergence of a molecular bose-einstein condensate from a fermi gas," *Nature*, vol. 426, pp. 537–540, 12 2003.

[18] M. Bartenstein", "Crossover from a molecular bose-einstein condensate to a degenerate fermi gas," *Physical Review Letters*, vol. 92, no. 12, 2004.

[19] M. W. Zwierlein", "Condensation of pairs of fermionic atoms near a feshbach resonance," *Physical Review Letters*, vol. 92, no. 12, 2004.

[20] D. Jaksch", "Cold bosonic atoms in optical lattices," *Physical Review Letters*, vol. 81, no. 15, pp. 3108–3111, 1998.

[21] M. P. A. Fisher", "Boson localization and the superfluid-insulator transition," *Physical Review B*, vol. 40, no. 1, pp. 546–570, 1989.

[22] M. V. Berry, "Exact aharonov-bohm wavefunction obtained by applying dirac's magnetic phase factor," *European Journal of Physics*, vol. 1, no. 4, p. 240, 1980.

[23] M. Berry, "Quantal phase factors accompanying adiabatic changes," *Proceedings of the Royal Society of London A: Mathematical, Physical and Engineering Sciences*, vol. 392, no. 1802, pp. 45–57, 1984.

[24] C. A. Mead", "The geometric phase in molecular systems," *Reviews of Modern Physics*, vol. 64, no. 1, pp. 51–85, 1992.

[25] Y. J. Lin, R. L. Compton, K. Jimenez-Garcia, J. V. Porto, and I. B. Spielman, "Synthetic magnetic fields for ultracold neutral atoms," *Nature*, vol. 462, pp. 628–632, 12 2009.

[26] Y.-J. Lin, R. L. Compton, K. Jimenez-Garcia, W. D. Phillips, J. V. Porto, and I. B. Spielman, "A synthetic electric force acting on neutral atoms," *Nat Phys*, vol. 7, pp. 531–534, 07 2011.

[27] Y.-J. Lin", "Bose-einstein condensate in a uniform light-induced vector potential," *Physical Review Letters*, vol. 102, no. 13, 2009.

[28] B. DeMarco and D. Jin, "Onset of fermi degeneracy in a trapped atomic gas," *Science*, vol. 285, no. 5434, pp. 1703–1706, 1999.

[29] R. P. Feynman, "Simulating physics with computers," *International Journal of Theoretical Physics*, vol. 21, no. 6, pp. 467–488, 1982.

[30] L. Huang, Z. Meng, P. Wang, P. Peng, S.-L. Zhang, L. Chen, D. Li, Q. Zhou, and J. Zhang, "Experimental realization of two-dimensional synthetic spin-orbit coupling in ultracold fermi gases," *Nat Phys*, vol. 12, pp. 540–544, 06 2016.

[31] P. Wang", "Spin-orbit coupled degenerate fermi gases," *Physical Review Letters*, vol. 109, no. 9, 2012.

[32] L. W. Cheuk", "Spin-injection spectroscopy of a spin-orbit coupled fermi gas," *Physical Review Letters*, vol. 109, no. 9, 2012.

[33] C. Chin", "Feshbach resonances in ultracold gases," *Reviews of Modern Physics*, vol. 82, no. 2, pp. 1225–1286, 2010.

[34] Y.-j. Lin, K. Jimenez-Garcia, and I. B. A. Spielman, "spin-orbit coupled bose-einstein condensate," *Nature*, vol. 2011, pp. 83–86.

[35] Y.-j. Lin, R. L. Compton, K. Jimenez-Garcia, W. D. Phillips, J. V. Porto, and I. B. A. Spielman, "synthetic electric force acting on neutral atoms," *Nat. Phys*, vol. 2011, pp. 531–534.

[36] V. Galitski and I. B. Spielman, "Spin-orbit coupling in quantum gases," *Nature*, vol. 2013, pp. 49–54.

[37] E. Jaynes and F. Cummings, "Comparison of quantum and semiclassical radiation theories with application to the beam maser," in *IEEE Proc.*, (*51*), pp. 89–109, **1963**.

[38] G. Rempe, H. Walther, and N. Klein, "Observation of quantum collapse and revival in a one-atom maser," *Phys. Rev. Lett*, vol. 1987, pp. 353–356.

[39] J. Ye, D. W. Vernooy, and H. J. Kimble, "Trapping of single atoms in cavity qed," *Phys. Rev. Lett*, vol. 1999, pp. 4987–4990.

[40] F. Brennecke, T. Donner, S. Ritter, T. Bourdel, M. Kohl, and T. Esslinger, "Cavity qed with a bose-einstein condensate," *Nature*, vol. 2007, pp. 268–271.

[41] Y. Colombe, T. Steinmetz, G. Dubois, F. Linke, D. Hunger, and J. Reichel, "Strong atom-field coupling for bose-einstein condensates in an optical cavity on a chip," *Nature*, vol. 2007, pp. 272–276.

[42] K. Baumann, C. Guerlin, F. Brennecke, and T. Esslinger, "Dicke quantum phase transition with a superfluid gas in an optical cavity," *Nature*, vol. 2010, pp. 1301–1306.

[43] H. Chen, Y. Zhang, X. Yao, Z. Wu, X. Zhang, Y. Zhang, and M. Xiao, "Parametrically amplified bright-state polariton of four- and six-wave mixing in an optical ring cavity," *Sci. Rep*, vol. 2014.

[44] R. H. Dicke, "Coherence in spontaneous radiation processes," *Phys. Rev*, vol. 1954, pp. 99–110.

[45] L. Dong, L. Jiang, H. Hu, and H. Pu, "Finite-momentum dimer bound state in a spin-orbit-coupled fermi gas," *Physical Review A*, vol. 87, no. 4, 2013.

[46] L. Dong, L. Jiang, and H. Pu, "Fulde–ferrell pairing instability in spin–orbit coupled fermi gas," *New Journal of Physics*, vol. 15, no. 7, p. 075014, 2013.

[47] H. Hu, L. Dong, Y. Cao, H. Pu, and X.-J. Liu, "Gapless topological fulde-ferrell superfluidity induced by an in-plane zeeman field," *Physical Review A*, vol. 90, no. 3, 2014.

[48] Y. Dong, L. Dong, M. Gong, and H. Pu, "Dynamical phases in quenched spin–orbit-coupled degenerate fermi gas," *Nature Communications*, vol. 6, pp. 6103 EP –, 01 2015.

[49] L. Dong, L. Zhou, B. Wu, B. Ramachandhran, and H. Pu, "Cavity-assisted dynamical spin-orbit coupling in cold atoms," *Physical Review A*, vol. 89, no. 1, 2014.

[50] L. Dong, C. Zhu, and H. Pu, "Photon-induced spin-orbit coupling in ultracold atoms inside optical cavity," *Atoms*, vol. 3, no. 2, pp. 182–194, 2015.

[51] C. Zhu, L. Dong, and H. Pu, "Effects of spin-orbit coupling on jaynes-cummings and tavis-cummings models," *Physical Review A*, vol. 94, no. 5, 2016.

[52] C. Zhu, L. Dong, and H. Pu, "Harmonically trapped atoms with spin–orbit coupling," *Journal of Physics B: Atomic, Molecular and Optical Physics*, vol. 49, no. 14, p. 145301, 2016.

[53] Z. q. Yu and H. Zhai *Phys. Rev. Lett.*, vol. 107, 2011.

[54] J. P. Vyasanakere and V. B. Shenoy *Phys Rev B*, vol. 83, p. 094515, 2011.

[55] P. Wang, Z. q. Yu, Z. Fu, J. Miao, L. Huang, S. Chai, H. Zhai, and J. Zhang *Phys. Rev. Lett.*, vol. 109, 2012.

[56] J. y. Zhang, S. c. Ji, Z. Chen, L. Zhang, Z. d. Du, B. Yan, G. s. Pan, B. Zhao, Y. j. Deng, H. Zhai, S. Chen, and J. w. Pan *Phys Rev. Lett.*, vol. 109, 2012.

[57] B. Ramachandhran, B. Opanchuk, X. j. Liu, H. Pu, P. D. Drummond, and H. Hu *Phys. Rev. A*, vol. 85, 2012.

[58] Q. Zhu, C. Zhang, and B. Wu *Europhys Lett.*, vol. 100, 2012.

[59] B. M. Anderson, G. Juzeliunas, V. M. Galitski, and I. B. Spielman *Phys. Rev. Lett.*, vol. 108, 2012.

[60] Y. Li, X. Zhou, and C. Wu *Phys. Rev. B*, vol. 85, 2012.

[61] J. P. Vyasanakere, S. Zhang, and V. B. Shenoy *Phys Rev. B*, vol. 84, 2011.

[62] T. l. Ho and S. Zhang *Phys Rev. Lett.*, vol. 107, 2011.

[63] C. Wang, C. Gao, C. m. Jian, and H. Zhai *Phys Rev. Lett.*, vol. 105, 2010.

[64] S. k. Yip *Phys Rev. A*, vol. 83, 2011.

[65] L. D. Landau and E. M. j. a. Lifshit?s?, *Statistical physics*. London Pergamon Press, 1958. Translation of Statisticheskai?a? fizika.

[66] J. Bardeeen, L. N. Cooper, and J. R. Schrieffer *Phys Rev.*, vol. 106, 1957.

[67] A. Sedrakian, J. Mur-Petit, A. Polls, and H. Muther *Phys Rev. A*, vol. 72, 2005.

[68] P. Fulde and R. A. Ferrell *Phys Rev.*, vol. 135, 1964.

[69] A. I. Larkin and Y. N. Ovchinnikov *Sov Phys. JETP*, vol. 20, 1965.

[70] R. Casalbuoni and G. Nardulli *Rev Mod. Phys*, vol. 76, 2004.

[71] L. Dong, L. Jiang, H. Hu, and H. Pu *Phys Rev. A*, vol. 87, 2013.

[72] A. V. Chaplik and L. I. Magarill *Phys Rev. Lett.*, vol. 96, 2006.

[73] M. Iskin and A. L. Subasi *Phys Rev. Lett.*, vol. 107, 2011.

[74] M. Iskin and A. L. Subasi *Phys Rev. A*, vol. 84, p. 043621, 2011.

[75] S. Takei, C. h. Lin, B. M. Anderson, and V. Galitski *Phys Rev. A*, vol. 85, p. 023626, 2012.

[76] L. Jiang, X. J. Liu, and H. hui vol. 84, 2011.

[77] K. v. Klitzing", "New method for high-accuracy determination of the fine-structure constant based on quantized hall resistance," *Physical Review Letters*, vol. 45, no. 6, pp. 494–497, 1980.

[78] R. B. Laughlin", "Quantized hall conductivity in two dimensions," *Physical Review B*, vol. 23, no. 10, pp. 5632–5633, 1981.

[79] D. J. Thouless", "Quantized hall conductance in a two-dimensional periodic potential," *Physical Review Letters*, vol. 49, no. 6, pp. 405–408, 1982.

[80] F. Wilczek, "**5**," *Nature Phys*, vol. 614, 2009.

[81] C. Nayak, S. H. Simon, A. Stern, M. Freedman, and S. D. Sarma *Rev Mod. Phys*, vol. 80, 2008.

[82] J. P. Vyasanakere, S. Zhang, and V. B. Shenoy *Phys Rev. B*, vol. 84, 2011.

[83] C. A. R. S. de Melo, M. Randeria, and J. R. Engelbrecht in *Bose-Einstein Condensation*, pp. 355–392, 3202 (1993); M. Randeria, in , edited by A. Griffin, D.

W. Snoke, and S. Stringari, (Cambridge University Press, Cambridge, England p: Rev. Lett. **71**, 1995.

[84] H. Hu, X. j. Liu, and P. Drummond *Europhys Lett.*, vol. 74, 2008.

[85] H. T. C. Stoof, K. B. Gubbels, and D. B. M. Dickerscheid, *Ultracold Quantum Fields*. Springer, 2009.

[86] M. Gong, S. Tewari, and C. Zhang *Phys Rev. Lett.*, vol. 107, 2011.

[87] H. Hu, L. Jiang, X. j. Liu, and H. Pu *Phys Rev. Lett.*, vol. 107, 2011.

[88] H. Hu and X. j. Liu *Phys Rev. A*, vol. 73, 2006.

[89] D. Sheehy and L. Radzihovsky *Phys Rev. B*, vol. 75, 2007.

[90] G. Orso *Phys Rev. Lett.*, vol. 98, 2007.

[91] H. Hu, X. j. Liu, and P. D. Drummond *Phys Rev. Lett.*, vol. 98, 2007.

[92] M. Tezuka and M. Ueda *Phys Rev. Lett.*, vol. 100, 2008.

[93] R. Liao, Y. Yi-Xiang, and W. M. Liu *Phys Rev. Lett.*, vol. 108, 2012.

[94] V. B. Shenoy, "arxiv:1211," vol. 1831, 2012.

[95] L. Dong, L. Jiang, and H. Pu *New J Phys.*, vol. 15, 2013.

[96] B. M. Anderson, G. Juzeliūnas, V. M. Galitski, and I. B. Spielman *Phys. Rev. Lett.*, vol. 108, 2012.

[97] B. M. Anderson, I. B. Spielman, and G. Juzeliūnas *Phys Rev. Lett.*, vol. 111, 2013.

[98] L. Dong, L. Jiang, H. Hu, and H. Pu *Phys Rev. A*, vol. 87, 2013.

[99] Z. Zheng, M. Gong, X. Zou, C. Zhang, and G. c. Guo *Phys Rev. A*, vol. 87, 2013.

[100] F. Wu, G. c. Guo, W. Zhang, and W. Yi *Phys Rev. Lett.*, vol. 110, 2013.

[101] X. j. Liu and H. Hu *Phys Rev. A*, vol. 87, 2013.

[102] M. Z. Hasan and C. L. Kane *Rev Mod. Phys*, vol. 82, 2010.

[103] X. l. Qi and S. c. Zhang *Rev Mod. Phys*, vol. 83, 2011.

[104] J. D. Sau, R. M. Lutchyn, S. Tewari, and S. D. Sarma *Phys Rev. Lett.*, vol. 104, 2010.

[105] Y. Oreg, G. Refael, and F. von Oppen *Phys Rev. Lett.*, vol. 105, 2010.

[106] X. Wan, A. M. Turner, A. Vishwanath, and S. Y. Savrasov *Phys Rev. B*, vol. 83, 2011.

[107] A. A. Burkov and L. Balents *Phys Rev. Lett.*, vol. 107, 2011.

[108] G. Xu, H. Weng, Z. Wang, X. Dai, and Z. Fang *Phys Rev. Lett.*, vol. 107, 2011.

[109] J. D. Sau and S. Tewari *Phys Rev. B*, vol. 86, 2012.

[110] Y. Xu, R. Chu, and C. Zhang *arXiv:*, vol. 1310.4100.

[111] A. P. Schnyder, S. Ryu, A. Furusaki, and A. W. W. Ludwig *Phys Rev. B*, vol. 78, 2008.

[112] X. j. Liu, L. Jiang, H. Pu, and H. Hu *Phys Rev. A*, vol. 85, 2012.

[113] M. Endres, T. Fukuhara, D. Pekker, M. Cheneau, P. Schauβ, C. Gross, E. Demler, S. Kuhr, and I. Bloch, "The "higgs" amplitude mode at the two-dimensional superfluid/mott insulator transition,," *Nature*, vol. 487, 2012.

[114] T. Kinoshita, T. Wenger, and D. A. q. N. c. Weiss *Nature*, vol. 440, pp. 900–903, 2006.

[115] M. Gring, M. Kuhnert, T. Langen, T. Kitagawa, B. Rauer, M. Schreitl, I. Mazets, D. Smith, E. Demler, and J. Schmiedmayer, "Relaxation and prethermalization in an isolated quantum system,," *Science*, vol. 337, pp. 1318–1322, 2012.

[116] L. Sadler, J. Higbie, S. Leslie, M. Vengalattore, and D. Stamper-Kurn, "Spontaneous symmetry breaking in a quenched ferromagnetic spinor bose condensate," *Nature*, vol. 443, 2006.

[117] W. Zurek, U. Dorner, and P. Zoller, "Dynamics of a quantum phase transition,," *Phys Rev. Lett.*, vol. 95, 2005.

[118] S. Hofferberth, I. Lesanovsky, B. Fischer, T. Schumm, and J. Schmiedmayer, "Non-equilibrium coherence dynamics in one-dimensional bose gases," *Nature*, vol. 449, pp. 324–327, 2007.

[119] A. Polkovnikov, K. Sengupta, A. Silva, and M. Vengalattore, "Nonequilibrium dynamics of closed interacting quantum systems,," *Phys Mod. Phys*, vol. 83, 2011.

[120] A. Sommer, M. Ku, G. Roati, and M. Zwierlein, "Universal spin transport in a strongly interacting fermi gas," *Nature*, vol. 472, pp. 201–204, 2011.

[121] C. Chin, R. Grimm, P. Julienne, and E. Tiesinga, "Feshbach resonances in ultracold gases,," *Rev Mod. Phys*, vol. 82, 2010.

[122] L. Sanchez-Palencia and M. Lewenstein, "Disordered quantum gases under control," *Nature Physics*, vol. 6, pp. 87–95, 2010.

[123] A. Volkov and S. Kogan, "Collisionless relaxation of the energy gap in superconductors,," *Soviet Physics JETP*, vol. 38, 1974.

[124] R. Barankov, L. Levitov, and B. Spivak, "Collective rabi oscillations and solitons in a time-dependent bcs pairing problem,," *Phys Rev. Lett.*, vol. 93, 2004.

[125] A. Andreev, V. Gurarie, and L. Radzihovsky, "Nonequilibrium dynamics and thermodynamics of a degenerate fermi gas across a feshbach resonance,," *Phys Rev. Lett.*, vol. 93, 2004.

[126] E. Yuzbashyan, O. Tsyplyatyev, and B. Altshuler, "Relaxation and persistent oscillations of the order parameter in fermionic condensates,," *Phys Rev. Lett.*, vol. 96, 2006.

[127] E. Yuzbashyan and M. Dzero, "Dynamical vanishing of the order parameter in a fermionic condensate,," *Phys Rev. Lett.*, vol. 96, 2006.

[128] R. Barankov and L. Levitov, "Synchronization in the bcs pairing dynamics as a critical phenomenon,," *Phys Rev. Lett.*, vol. 96, 2006.

[129] A. Bulgac and S. Yoon, "Large amplitude dynamics of the pairing correlations in a unitary fermi gas,," *Phys Rev. Lett.*, vol. 102, 2009.

[130] E. Yuzbashyan, B. Altshuler, V. Kuznetsov, and V. Z, "Nonequilibrium cooper pairing in the nonadiabatic regime,," *Phys Rev. B*, vol. 72, 2005.

[131] M. Cambiaggioa, A. Rivas, and M. Saracenoa, "Integrability of the pairing hamiltonian,," *Nuclear Physics A*, vol. 624, pp. 157–167, 1997.

[132] V. Kuznetsov, "Quadrics on real riemannian spaces of constant curvature: Separation of variables and connection with gaudin magnet," vol. 1992.

[133] M. Foster, M. Dzero, V. Gurarie, and E. Yuzbashyan, "Quantum quench in a $p+ip$ superfluid: Winding numbers and topological states far from equilibrium,," *Phys Rev. B*, vol. 88, 2013.

[134] M. Foster, V. Gurarie, M. Dzero, and E. Yuzbashyan, "Quench-induced floquet topological p-wave superfluids,," *Phys Rev. Lett.*, vol. 113, 2014.

[135] J. Gaebler, J. Stewart, J. Bohn, and D. p.-w. F. m. Jin *Phys Rev. Lett.*, vol. 98, 2007.

[136] J. Levinsen, N. R. Cooper, and G. V. Shlyapnikov, "Topological $p_x + ip_y$ superfluid phase of fermionic polar molecules,," *Phys Rev. A*, vol. 84, 2011.

[137] R. A. Williams, L. J. LeBlanc, K. Jimenez-Garcia, M. C. Beeler, A. R. Perry, W. D. Phillips, and I. B. Spielman, "Synthetic partial waves in ultracold atomic collisions,," *Science*, vol. 335, 2012.

[138] Y. Lin, K. Jimenez-Garca, and I. S.-o.-c. B.-E. c. Spielman, "Nature **471**," pp. 83–86, 2011.

[139] J. Zhang, S. Ji, Z. Chen, L. Zhang, Z. Du, B. Yan, G. Pan, B. Zhao, Y. Deng, H. Zhai, S. Chen, and J. Pan, "Collective dipole oscillations of a spin-orbit coupled bose-einstein condensate," *Phys. Rev Lett*, vol. 109, 2012.

[140] P. Wang, Z. Yu, Z. Fu, J. Miao, L. Huang, S. Chai, H. Zhai, and J. Zhang, "Spin-orbit coupled degenerate fermi gases," *Phys. Rev. Lett.*, vol. 109, 2012.

[141] L. Cheuk, A. Sommer, Z. Hadzibabic, T. Yefsah, W. Bakr, and M. Zwierlein, "Raman-induced interactions in a single-component fermi gas near an s-wave feshbach resonance," *Phys Phys. Rev*, vol. 111, 2013.

[142] C. Qu, C. Hamner, M. Gong, C. Zhang, and P. Engels, "Observation of zitterbewegung in a spin-orbit coupled bose-einstein condensate,," *Phys Rev. A*, vol. 88, 2013.

[143] C. Hamner, C. Qu, Y. Zhang, J. Chang, M. Gong, C. Zhang, and P. Engels, "Dicke-type phase transition in a spin-orbit-coupled bose-einstein condensate,," *Nat Commun.*, vol. 5, 2014.

[144] M. Gong, S. Tewari, and C. B.-b. Zhang, "crossover and topological phase transition in 3d spin-orbit coupled degenerate fermi gases,," *Phys Rev. Lett.*, vol. 107, 2011.

[145] M. Gong, G. Chen, S. Jia, and C. Zhang, "Searching for majorana fermions in 2d spin-orbit coupled fermi superfluids at finite temperature,," *Phys Rev. Lett.*, vol. 109, 2012.

[146] M. Sato, Y. Takahashi, and S. Fujimoto, "Non-abelian topological order in *s*-wave superfluids of ultracold fermionic atoms," *Phys Rev. Lett.*, vol. 103, 2009.

[147] J. Zhou, W. Zhang, and W. Yi, "Topological superfluid in a trapped two-dimensional polarized fermi gas with spin-orbit coupling,," *Phys Rev. A*, vol. 84, 2011.

[148] H. Hu, B. Ramachandhran, H. Pu, and X. Liu, "Spin-orbit coupled weakly interacting bose-einstein condensates in harmonic traps,," *Phys Rev. Lett.*, vol. 108, 2012.

[149] X. Liu, L. Jiang, H. Pu, and H. Hu, "Probing majorana fermions in spin-orbit-coupled atomic fermi gases,," *Phys Rev. A*, vol. 85, 2012.

[150] K. Seo, L. Han, and C. Sa de Melo, "Topological phase transitions in ultracold fermi superfluids: The evolution from bardeen-cooper-schrieffer to bose-einstein-condensate superfluids under artificial spin-orbit fields,," *Phys Rev. A*, vol. 85, 2012.

[151] M. Iskin and A. Subasi, "Stability of spin-orbit coupled fermi gases with population imbalance,," *Phys Rev. Lett.*, vol. 107, 2011.

[152] H. Hu, L. Jiang, X. Liu, and H. Pu, "Probing anisotropic superfluidity in atomic fermi gases with rashba spin-orbit coupling,," *Phys Rev. Lett.*, vol. 107, 2011.

[153] L. Jiang, X. Liu, H. Hu, and H. Pu, "Rashba spin-orbit-coupled atomic fermi gases," *Phys Rev. A*, vol. 84, 2011.

[154] L. Dong, L. Jiang, and H. Pu, "Fulde-ferrell pairing instability in spin-orbit coupled fermi gas,," *New J Phys.*, vol. 15, 2013.

[155] C. Qu, Z. Zheng, M. Gong, Y. Xu, L. Mao, X. Zou, G. Guo, and C. Zhang, "Topological superfluids with finite-momentum pairing and majorana fermions,," *Commun.*, vol. 4, 2013.

[156] W. Zhang and W. Yi, "Topological fulde-ferrell-larkin-ovchinnikov states in spin-orbit-coupled fermi gases,," *Nat Commun.*, vol. 4, 2013.

[157] X. Liu and H. Hu, "Topological fulde-ferrell superfluid in spin-orbit-coupled atomic fermi gases,," *Phys Rev. A*, vol. 88, 2013.

[158] C. Chen, "Inhomogeneous topological superfluidity in one-dimensional spin-orbit-coupled fermi gases,," *Phys Rev. Lett.*, vol. 111, 2013.

[159] J. Vyasanakere, S. Zhang, and V. B.-b. Shenoy, "crossover induced by a synthetic non-abelian gauge field,," *Phys Rev. B*, vol. 84, 2011.

[160] S. Ghosh, S. Vyasanakere, and V. Shenoy, "Trapped fermions in a synthetic non-abelian gauge field,," *Phys Rev. A*, vol. 84, 2011.

[161] J. Liu, Q. Han, L. B. Shao, and Z. D. Wang, "Exact solutions for a type of electron pairing model with spin-orbit interactions and zeeman coupling,," *Phys Rev. Lett.*, vol. 107, 2011.

[162] K. Martiyanov, V. Makhalov, and A. Turlapov, "Observation of a two-dimensional fermi gas of atoms,," *Phys Rev. Lett.*, vol. 105, 2010.

[163] V. Martiyanov, K. Makhalov, and A. Turlapov, "Ground-state pressure of quasi-2d fermi and bose gases,," *Phys Rev. Lett.*, vol. 112, 2014.

[164] B. Fröhlich, M. Feld, E. Vogt, M. Koschorreck, W. Zwerger, and M. Köhl, "Radiofrequency spectroscopy of a strongly interacting two-dimensional fermi gas,," *Phys Rev. Lett.*, vol. 106, 2011.

[165] P. Dyke, E. Kuhnle, S. Whitlock, H. Hu, M. Mark, S. Hoinka, M. Lingham, P. Hannaford, and C. Vale, "Crossover from 2d to 3d in a weakly interacting fermi gas,," *Phys Rev. Lett.*, vol. 106, 2011.

[166] M. Bartenstein, A. Altmeyer, S. Riedl, S. Jochim, C. Chin, H. Denschlag, and R. Grimm, "Collective excitations of a degenerate gas at the bec-bcs crossover,," *Phys Rev. Lett.*, vol. 92, 2004.

[167] A. Altmeyer, S. Riedl, C. Kohstall, J. Wright, R. Geursen, M. Bartenstein, C. Chin, H. Denschlag, and R. Grimm, "Precision measurements of collective oscillations in the bec-bcs crossover,," *Phys Rev. Lett.*, vol. 98, 2007.

[168] E. Alba, X. Fernandez-Gonzalvo, J. Mur-Petit, J. Pachos, and J. Garcia-Ripoll, "Seeing topological order in time-of-flight measurements,," *Phys Rev. Lett.*, vol. 107, 2011.

[169] J. Sau, R. Sensarma, S. Powell, I. Spielman, and S. Sarma, "Chiral rashba spin textures in ultracold fermi gases,," *Phys Rev. B*, vol. 83, 2011.

[170] P. Wang, W. Yi, and G. Xianlong, "Topological phase transition in the quench dynamics of a one-dimensional fermi gas," preprint, 2014.

[171] C. F. Chan and M. P. s. Gong, "phase diagram, and edge modes in the topological fulde-ferrell-larkin-ovchinnikov phase,," *Phys Rev. B*, vol. 89, 2014.

[172] M. Bauer, M. Parish, and T. Enss, "Universal equation of state and pseudogap in the two-dimensional fermi gas,," *Phys Rev. Lett.*, vol. 112, 2014.

[173] S. Haroche and J. m. Raimond, *Exploring the Quantum.* New York: Oxford, 2006.

[174] F. Brennecke, T. Donner, S. Ritter, T. Bourdel, M. Kohl, and T. Esslenger, "Nature," vol. 450, 2007.

[175] Y. Colombe, T. Steinmetz, G. Dubois, F. Linke, D. Hunger, and J. Reichel, "Nature **450**," vol. 272, 2007.

[176] S. Slama, S. Bux, G. Krenz, C. Zimmermann, and P. W. Courteille *Phys Rev. Lett.*, vol. 98, 2007.

[177] D. Schmidt, H. Tomczyk, S. Slama, and C. Zimmermann, "Beyond the dicke quantum phase transition with a bose-einstein condensate in an optical ring resonator," *arXiv:*, vol. 1311.2156.

[178] S. Gupta, K. L. Moore, K. W. Murch, and D. M. Stamper-Kurn *Phys Rev. Lett.*, vol. 99, 2007.

[179] K. Baumann, C. Guerlin, F. Brennecke, and T. Esslinger *Nature*, vol. **464**, 1301, 2010.

[180] N. Brahms, T. Botter, S. Schreppler, D. W. C. Brooks, and D. M. Stamper-Kurn *Phys Rev. Lett.*, vol. 108, 2013.

[181] M. Lewenstein, A. Sanpera, V. Ahufinger, B. Damski, A. S. De, and U. Sen *Adv Phys.*, vol. 56, 2007.

[182] I. B. Mekhov and H. Ritsch *J. Phys B: At Mol. Opt*, vol. 45, 2012.

[183] Y. j. Lin, K. Jimenez-Garcia, and I. B. Spielman *Nature (London)* **471***, 83 (2011);*, vol. 7, 2011.

[184] L. W. Cheuk, A. T. Sommer, Z. Hadzibabic, T. Yefsah, W. S. Bakr, and M. W. Zwierlein *Phys Rev. Lett.*, vol. 109, 2012.

[185] M. J. Edmonds, M. Valiente, G. Juzeliunas, L. Santos, and P. Öhberg *Phys Rev. Lett.*, vol. 110, 2013.

[186] K. M. Birnbaum, A. Boca, R. Miller, A. D. Boozer, T. E. Northup, and H. J. Kimble *Nature*, vol. 436, pp. 87–90, 2005.

[187] B. Wu", "Nonlinear landau-zener tunneling," *Physical Review A*, vol. 61, no. 2, 2000.

[188] E. J. Mueller", "Superfluidity and mean-field energy loops: Hysteretic behavior in bose-einstein condensates," *Physical Review A*, vol. 66, no. 6, 2002.

[189] S. Burger", "Superfluid and dissipative dynamics of a bose-einstein condensate in a periodic optical potential," *Physical Review Letters*, vol. 86, no. 20, pp. 4447–4450, 2001.

[190] B. Wu", "Landau and dynamical instabilities of the superflow of bose-einstein condensates in optical lattices," *Physical Review A*, vol. 64, no. 6, 2001.

[191] G. Watanabe", "Swallowtail band structure of the superfluid fermi gas in an optical lattice," *Physical Review Letters*, vol. 107, no. 27, 2011.

[192] B. P. Venkatesh", "Band-structure loops and multistability in cavity qed," *Physical Review A*, vol. 83, no. 6, 2011.

[193] B. Wu and Q. Niu *Phys Rev. A*, vol. 61, 2011.

[194] J. M. Zhang, W. M. Liu, and D. L. Zhou *Phys Rev. A*, vol. 78, 2011.

[195] B. Wu and Q. Niu, "Phys," *Rev. A*, vol. 64, 2001.

[196] A. Kossakowski, "On quantum statistical mechanics of non-hamiltonian systems," *Rep. Math. Phys.*, vol. 1972, pp. 247–274.

[197] G. Lindblad, "On the generators of quantum dynamical semigroups," *Commun. Math. Phys*, vol. 1976, pp. 119–130.

[198] C. Emary and T. Brandes *Phys Rev. E*, vol. 67, 2003.

[199] B. M. Garraway *Phil Trans. R*, vol. 369, 2011.

[200] Y. K. Wang and F. T, "Hioe," *Phys Rev. A*, vol. 7, 1973.

[201] K. B. Davis, M. O. Mewes, M. R. Andrews, N. J. van Druten, D. S. Durfee, D. M. Kurn, and W. Ketterle, "Bose-einstein condensation in a gas of sodium atoms," *Phys. Rev. Lett.*, vol. 75, pp. 3969–3973, Nov 1995.

[202] B. Paredes, A. Widera, V. Murg, O. Mandel, S. Folling, I. Cirac, G. V. Shlyapnikov, T. W. Hansch, and I. Bloch, "Tonks-girardeau gas of ultracold atoms in an optical lattice," *Nature*, vol. 429, pp. 277–281, 05 2004.

[203] T. Kinoshita, T. Wenger, and D. Weiss, "Observation of a one-dimensional tonks-girardeau gas," *Science*, vol. 305, no. 5687, pp. 1125–1128, 2004.

[204] Z. Hadzibabic, P. Kruger, M. Cheneau, B. Battelier, and J. Dalibard, "Berezinskii-kosterlitz-thouless crossover in a trapped atomic gas," *Nature*, vol. 441, pp. 1118–1121, 06 2006.

[205] M. Greiner", "Probing the excitation spectrum of a fermi gas in the bcs-bec crossover regime," *Physical Review Letters*, vol. 94, no. 7, 2005.

[206] Y. J. Lin, K. Jimenez-Garcia, and I. B. Spielman, "Spin-orbit-coupled bose-einstein condensates," *Nature*, vol. 471, pp. 83–86, 03 2011.

[207] P. Baldi, P. Sadowski, and D. Whiteson, "Searching for exotic particles in high-energy physics with deep learning," *Nature Communications*, vol. 5, pp. 4308 EP –, 07 2014.

[208] P. Mehta and D. J. Schwab, "An exact mapping between the variational renormalization group and deep learning," *arXiv:1410.3831*, 10 2014.

[209] S. Lloyd, M. Mohseni, and P. Rebentrost, "Quantum algorithms for supervised and unsupervised machine learning," 07 2013.

[210] S. Lloyd, M. Mohseni, and P. Rebentrost, "Quantum principal component analysis," *Nat Phys*, vol. 10, pp. 631–633, 09 2014.

[211] J. Carrasquilla and R. G. Melko, "Machine learning phases of matter," *Nat Phys*, vol. advance online publication, pp. –, 02 2017.

[212] J. Liu", "Self-learning monte carlo method," *Physical Review B*, vol. 95, no. 4, 2017.

[213] G. Torlai", "Learning thermodynamics with boltzmann machines," *Physical Review B*, vol. 94, no. 16, 2016.

[214] L. Huang", "Accelerated monte carlo simulations with restricted boltzmann machines," *Physical Review B*, vol. 95, no. 3, 2017.

[215] D.-L. Deng, X. Li, and S. D. Sarma, "Exact machine learning topological states," 09 2016.

[216] K. Ch'ng, J. Carrasquilla, R. G. Melko, and E. Khatami, "Machine learning phases of strongly correlated fermions," 09 2016.

[217] P. Broecker, J. Carrasquilla, R. G. Melko, and S. Trebst, "Machine learning quantum phases of matter beyond the fermion sign problem," 08 2016.

[218] G. Carleo and M. Troyer, "Solving the quantum many-body problem with artificial neural networks," *Science*, vol. 355, no. 6325, pp. 602–606, 2017.

[219] E. P. L. van Nieuwenburg, Y.-H. Liu, and S. D. Huber, "Learning phase transitions by confusion," *Nat Phys*, vol. advance online publication, pp. –, 02 2017.

[220] L. Wang", "Discovering phase transitions with unsupervised learning," *Physical Review B*, vol. 94, no. 19, 2016.

[221] E. M. Stoudenmire and D. J. Schwab, "Supervised learning with quantum-inspired tensor networks," 05 2016.

[222] H. W. Lin and M. Tegmark, "Why does deep and cheap learning work so well?," 08 2016.

[223] J. Chen, S. Cheng, H. Xie, L. Wang, and T. Xiang, "On the equivalence of restricted boltzmann machines and tensor network states," 01 2017.

[224] R. Melko and M. Stoudenmire, "https://physicsml.github.io/pages/papers.html."